KfK 2881
Oktober 1979

# Progress Report

## Teilinstitut Nukleare Festkörperphysik des Instituts für Angewandte Kernphysik 1.6.1978 - 31.5.1979

Editors:
K.-P. Bohnen, M. Kobbelt
Institut für Angewandte Kernphysik

Kernforschungszentrum Karlsruhe

K E R N F O R S C H U N G S Z E N T R U M  K A R L S R U H E

Institut für Angewandte Kernphysik

KfK 2 8 8 1

# P R O G R E S S  R E P O R T

Teilinstitut Nukleare Festkörperphysik
des Instituts für Angewandte Kernphysik

1.6.1978 - 31.5.1979

Editors:

K.-P. Bohnen and M. Kobbelt

Kernforschungszentrum Karlsruhe GmBH, Karlsruhe

Kernforschungszentrum Karlsruhe GmbH
ISSN 0303-4003
ISSN 0171-2381

Abstract

This Progress Report of the Teilinstitut Nukleare Festkörperphysik covers the work done at the Institute during the period from June 1st, 1978 to May 31st, 1979.

The main research areas presently under investigation are underlined by the arrangement of the report: structure and dynamics of solids, electronic structure and magnetism of solids, and the development and investigation of novel materials. Some technical developments important in carrying out this research are included as well.

Zusammenfassung

Dieser Progress Report des Teilinstituts Nukleare Festkörperphysik erfaßt den Zeitraum vom 1. Juni 1978 - 31. Mai 1979. Die Darstellung betont die Hauptforschungsgebiete, auf denen das Institut zur Zeit tätig ist. Diese sind: Struktur und Dynamik von Festkörpern, Elektronenstruktur und Magnetismus von Festkörpern und die Entwicklung und Untersuchung neuartiger Materialien. Einige technische Entwicklungen, die für diese Forschungsarbeiten wichtig sind, wurden ebenfalls in den Bericht aufgenommen.

# E D I T O R I A L

This Progress Report of the Teilinstitut Nukleare Festkörperphysik covers the work done at the Institute during the period from June 1st, 1978 to May 31st, 1979.

The main research areas presently under investigation are underlined by the arrangement of the report: structure and dynamics of solids, electronic structure and magnetism of solids, and the development and investigation of novel materials. Some technical developments important in carrying out this research are included as well.

Work submitted for publication or already published is accounted for in a short version or as an abstract. First results of current investigations are described more extensively. Neutron scattering work by guest groups, not related to the research area of this Institute, has not been included in the report. An account of it will be given in a separate report.

The report is supplemented by a list of the Institute's staff members, their publications in the period of reporting, and a list of the neutron spectrometers available in the research reactor FR2.

Finally, we would like to thank M. Müller for the typing of this report.

# P R E F A C E

The Teilinstitut Nukleare Festkörperphysik of the Institut für Angewandte Kernphysik (IAK I) developed from the use of nuclear methods in solid state research. Its special methods are elastic and inelastic neutron scattering, Mössbauer-spectroscopy, and irradiation of solids with ions from a 3 MV Van de Graaff accelerator. With the development of its research program toward specific problems in solid state research, the institute has supplemented its experimental equipment with facilities for ion implantations, thin film preparation by sputtering and evaporation, back-scattering and channelling, magnetization- and $T_c$-measurements, crystal growing, X-ray diffraction, and electron beam annealing. This tendency toward non-nuclear methods will get additional enhancement in the coming years, because the Karlsruhe research reactor (FR2) will not be operated beyond 1981. Preparations are in progress to transfer the most modern instruments now installed at the FR2 to the French reactors Orphée in Saclay and Siloé and Mélusine at Grenoble, which will allow continuation of part of the neutron scattering activity. As major investment for this instrument transfer the analyzer of a triple axis spectrometer is nearly finished in construction. An electron loss spectrometer is built up in cooperation with the Institut für Festkörperforschung in Jülich. A chemical vapor deposition unit for growing single crystals of refractory compounds has been put in operation. The plans to transfer the ion implantation facility together with a 2 MV accelerator to a new experimental hall near the 3 MV accelerator, for irradiation with all three accelerators in common target stations, proceed. The hall will start to be built late this or early next year.

The Institute has now (October 1979) 24 scientists as professional staff. The number of guest scientists, graduate and Ph.D. students increased by a factor of 2 to about 20. IAK I shares with its sister institute IAK II (Teilinstitut Kernphysik) a common infrastructure consisting of a mechanical and an electronic workshop, a maintenance group for the 3 MV accelerator, and a group responsible for experimental computers and data processing. Development activitites of the latter two groups are included in this progress report.

In the Research & Development Program and in the Annual Report of the Nuclear Research Center as a whole, the research program of IAK I is subdivided into the following three topics (titles for 1979):

11.02.02 Structure and Dynamics of Solids

11.02.03 Electronic Structure of Solids and Magnetism

10.02.03 Ion Implantation and Channelling

The list of contents of this report differs from the listing above by an extra chapter for Theory and the listing of activities in Ion Implantation and Channelling together with those in materials development under the common title Materials Research. There are also the extra chapters Data Processing and Development of Instruments.

The main effort of the IAK I research is still concentrated on high $T_c$ superconducting materials. This includes band structure calculations and theoretical investigations in lattice dynamics and electron-phonon-coupling. Experimental work is done in inelastic neutron scattering for the determination of phonon dispersion and density of states, in preparation of bulk samples and (mostly metastable) superconducting films or layers by sputtering, evaporation and ion implantation, and in investigations of superconducting materials by backscattering, channelling, X-ray diffraction, and other methods mentioned in this report.

In the chapter Dynamics and Structure of Solids the reader may see some heterogeneity in research topics concerning the work in non-superconductors. This is due in part to the engaged collaboration of the IAK I staff with external research groups from universities and other institutions. On some other research topics the institute is interested because they are related to the general know-how of the Institute.

The investigations under the heading Electronic Structure and Magnetism are concentrated on alloys of transition and rare-earth metals which allow Mößbauer-spectroscopy with $^{61}Ni$, $^{155}Gd$, and $^{151}Eu$. This work aims at a better understanding of local moment formation and magnetic coupling in metals. An essential basis for part of it is the supply of short-living $^{61}Ni$ Mößbauer sources from the Karlsruhe cyclotron. Magnetic neutron scattering is performed on spin glasses, crystal field excitations and on Jahn-Teller distorted crystal structures.

W. Schmatz

# CONTENTS

## 1. INVESTIGATIONS ON THE DYNAMICS AND STRUCTURE OF SOLIDS

# 1. INVESTIGATIONS ON THE DYNAMICS AND STRUCTURE OF SOLIDS

## 1.1 Lattice Dynamics in the Pseudobinary System NbN - TiC

*L. Pintschovius, P. Rödhammer[a], A.N. Christensen[b] and R. Currat[c]*

[a] *Fachbereich Physik, Universität Konstanz, D-7750 Konstanz*

[b] *Institute of Inorganic Chemistry, University of Aarhus, Denmark*

[c] *Institut Laue-Langevin, F-38042 Grenoble, France*

Within the transition metal compounds (TMC's) with NaCl-structure the highest superconducting transition temperatures $T_c$ have been found in the pseudobinary systems NbN - NbC and NbN - TiC. Since in other TMC's a close correlation between $T_c$ and the occurence of marked anomalies in the acoustic phonon dispersion has been observed, we extended our investigations of the dispersion curves to a crystal with a composition close to that which gives the highest $T_c$, i.e. $Nb_{.8}Ti_{.2}N_{.8}C_{.1}$.

Our sample had a volume of 0.4 $cm^3$ and a $T_c$ = 15.4 K. The measurements were performed at room temperature on the triple-axis-spectrometers TAS1 at the FR2 Karlsruhe and IN8 at the HFR Grenoble. Because our sample was a solid solution there was considerable disorder concerning the atomic masses, the scattering lengths and probably the force constants. This resulted in a strong incoherent background and a pronounced broadening of the phonon lines. The line shapes often exhibited a double peak structure which made it difficult to evaluate phonon frequencies in the usual way (see Fig. 1). Having no theory to extract the information contained in the line shapes we resorted to define phonon frequencies as averages of the intensity distributions. Similar line shapes have been observed in non-stoichiometric niobium nitride /1/ and have been analysed in the same way which enables a direct comparison of the data.

The phonon dispersion is plotted in Fig. 2. The comparison with the dispersion curves of compounds with higher and lower valence electron concentration, e.g. $NbN_{.83}$ and $NbC_{.98}$ respectively, shows that the phonon dispersion of our sample resembles closely that of $NbN_{.83}$. In particular, the most pronounced anom-

aly occurs at the X-point. However, the phonon frequencies around the X-point are somewhat higher in $Nb_{.8}Ti_{.2}N_{.8}C_{.1}$ than in $NbN_{.83}$; this can only partly be attributed to the differences in the average atomic masses. Thus our results show that the maximum of $T_c$ as a function of composition in NbN-TiC alloys is not associated with a further enhancement of the phonon anomalies present in $NbN_{.86}$.

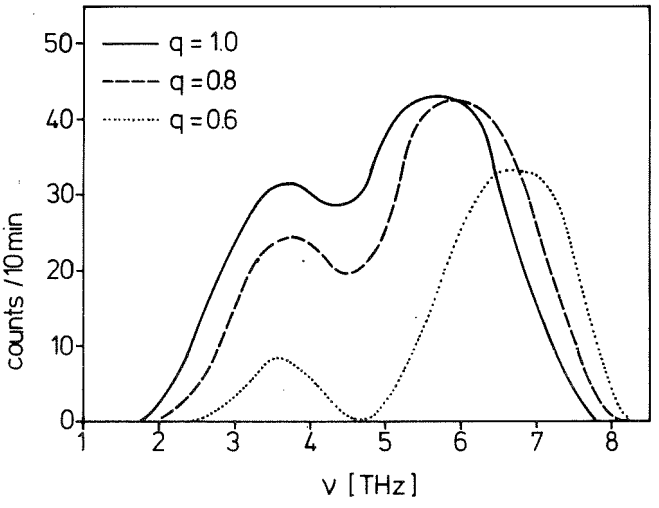


Fig. 1
Normalized intensity distributions of LA-phonons in the <100>-direction measured at the reciprocal lattice point (511). The data were not corrected for resolution effects.

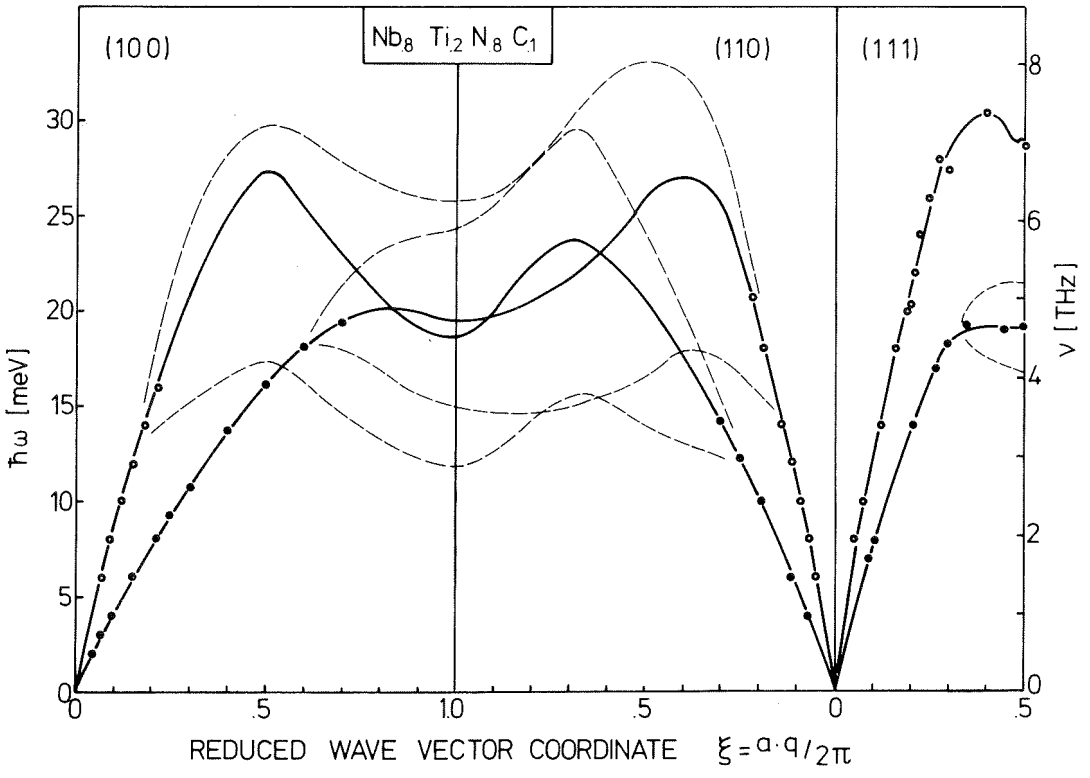


Fig. 2 Acoustic phonon dispersion of $Nb_{.8}Ti_{.2}N_{.8}C_{.1}$ at room temperature. Data points have been ommitted in cases of extreme broadening of the phonon groups as indicated by the dashed lines. In these cases the full lines represent average frequencies.

Reference

/1/ W. Reichardt, in Prog. Rep. Teilinst. Nukl. Festkörperphysik, Ges. f. Kernforschung, KfK 2670, 7(1978) and W. Reichardt and B. Scheerer, this volume, p. 4

## 1.2 Phonon Anomalies in VN and their Electronic Origin

*W. Weber, P. Rödhammer[a], L. Pintschovius, W. Reichardt, F. Gompf and A.N. Christensen[b]*

[a] *Fachbereich Physik, Universität Konstanz, D-7750 Konstanz*

[b] *Department of Inorganic Chemistry, Aarhus University, Dk-8000 Aarhus, Denmark*

Phys. Rev. Lett., in press

Abstract

Phonon dispersion and density of states measurements are presented for VN, a cubic transition metal compound with 10 valence electrons. The acoustic phonons differ strongly from those observed in 9 valence-electron compounds; in particular the prominent soft-mode region has moved from the interior to the boundary of the Brillouin zone. Using the theory of Varma and Weber we find that these changes arise primarily from a rigid-band-like increase in the Fermi energy.

## 1.3 Phonons in $NbN_{.83}$

*W. Reichardt, B. Scheerer*

In our former investigations on the dispersion curves of $NbN_{.83}$ /1/ we showed that there is a strong depression of the phonon branches in the vicinity of the X-point accompanied by a considerable broadening of the phonon groups in this region. Due to this broadening and the small size of the sample we were not able to obtain complete information about the LA branch in the <100>-direction.

As this branch plays a crucial role concerning present theoretical attempts to explain the origin of the phonon anomalies in the refractory compounds /2/ /3/ we repeated some of our former measurements and extended them with a somewhat larger sample ($.4cm^3$). Measurements on the LA <100> and the TA <110> branches which meet at the X-point were performed at four different positions in the reciprocal lattice in order to eliminate contributions of the rather numerous spurions. Fig. 1 gives a synthesis of the former and newly obtained results. The points in the vicinity of the X-point represent the centers of mass of the rather broad phonon groups whereas the dashed lines mark the extend of the broadening. Our results indicate that the strong depression of the LA <100> branch already starts at q $\sim$.5. The solid curves are obtained from a fit of the double shell model to the experimental data. Fig. 2 shows the line shapes of the phonon groups for the TA <110>-direction between q = .5 and the zone boundary. It is seen that near the X-point the lineshapes can no longer be described by a Gaussian or a Lorentzian, but rather look like being composed of two broad peaks.

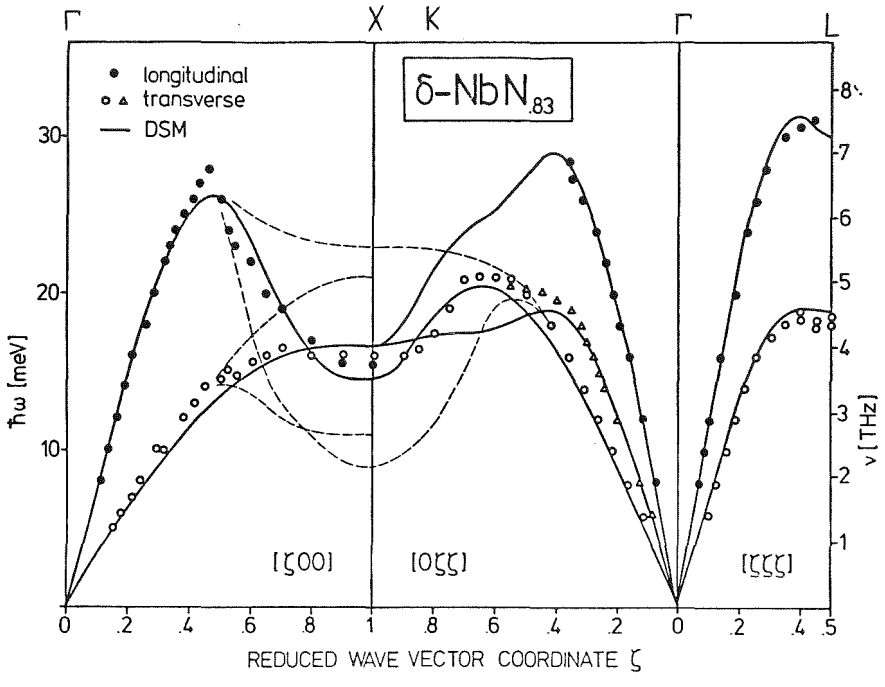


Fig. 1

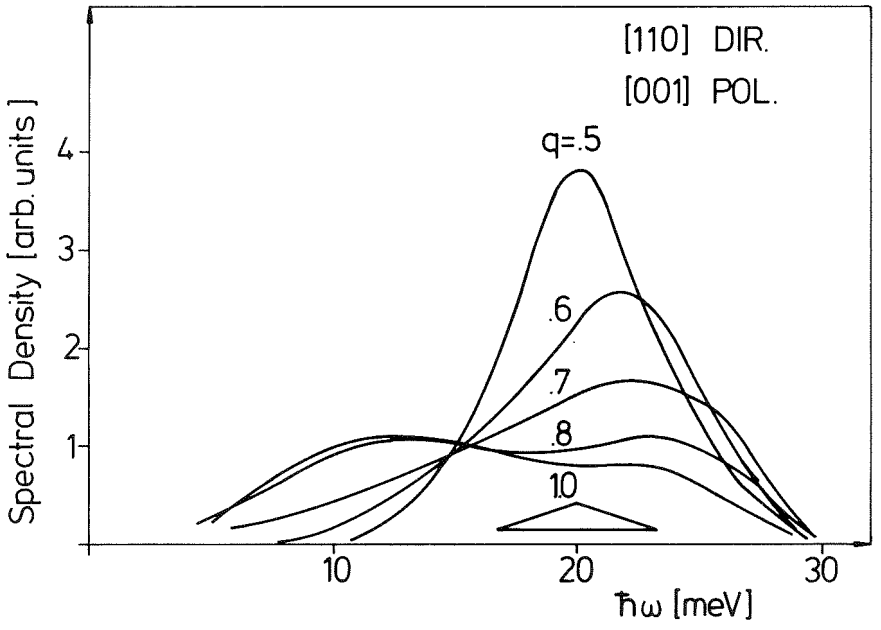


Fig. 2 Const. Q intensity profiles for the TA-branch (pol.<001>) in the <110> direction extracted from const. E-scans after corrections for spectrometer luminosity and energy dependent factors in the one-phonon cross-section.

References

/1/ W. Reichardt, in Prog. Rep. Teilinstitut Nukl. Festkörperphysik, KfK 2670, 7 (1978)

/2/ C.M. Varma and W. Weber, Phys. Rev. Letters 39, 1094 (1977)

/3/ W. Hanke, J. Hafner and H. Bilz, Phys. Rev. Letters 37, 1560 (1976)

## 1.4 Studies on the Lattice Distortion in NbN Caused by Vacancies

*M. Müllner[a], W. Reichardt, A.N. Christensen[b]*

[a] *Institut für Kernphysik, Universität Frankfurt*

[b] *Institut of Inorganic Chemistry, University of Aarhus, Denmark*

Our previous measurements of the individual Debye Waller factors of $NbN_{.95}$ at room temperature have yielded very large values of the mean square atomic amplitudes $\langle u^2 \rangle$ which were inconsistent with the values calculated from

inelastic neutron scattering data /1/. We tentatively explained these discrepancies by a strong lattice distortion caused by both Nb- and N-vacancies leading to appreciable static contributions to the Debye Waller coefficients.

In order to substantiate this explanation of our results we performed additional measurements as a function of temperature. Neutron diffraction patterns of $NbN_{.95}$ powder were taken at temperatures 20, 100, 200, and 294 K on the diffractometer ND3 ($\lambda$ = 1.0156(2) Å) at the reactor FR2. In the region of $20^{\circ} \leq 2\theta \leq 110^{\circ}$ 16 reflections were measured and analysed with Rietveld's profile refinement program /2/. Fitting 6 parameters we got R-factors ≤ 2% for the reflection intensities.

Fig. 1 illustrates the temperature dependence of the individual mean square amplitudes $\langle u^2 \rangle$ of $NbN_{.95}$. In the temperature range between 20 K and 300 K $\langle u^2 \rangle_N$ remains nearly constant (∿.025 $Å^2$) whereas $\langle u^2 \rangle_{Nb}$ rises from .021 $Å^2$ to .028 $Å^2$; below 200 K the heavier Nb atoms vibrate with a smaller amplitude than the lighter N atoms; above this temperature this behaviour is inverted. The values at room temperature agree with the data of our earlier experiment within the accuracy of the experiments.

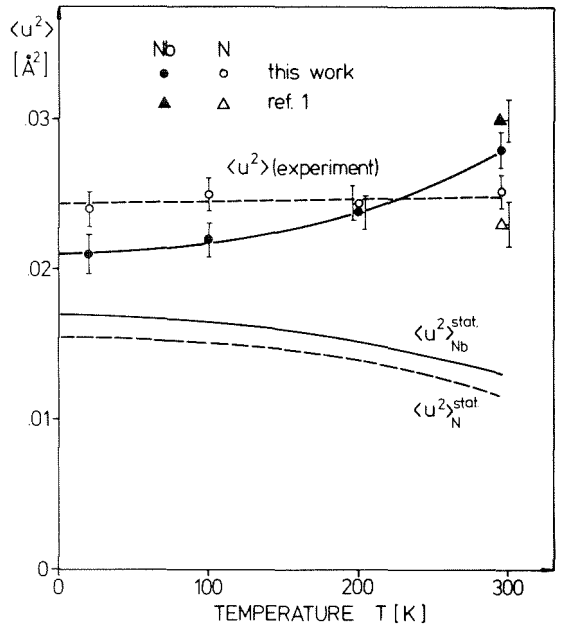


Fig. 1
Mean square amplitudes of Nb and N in $NbN_{.95}$ as a function of temperature.

For a preliminary analysis of these results we have calculated the dynamical part of the mean square amplitudes $\langle u^2 \rangle^{dyn}$ both from a model fitted to the experimental dispersion curves of $NbN_{.84}$ /3/ and from the generalized phonon density of states of $NbN_{.95}$ obtained from a neutron scattering experiment on a powder sample /4/ under the assumption that the phonon density of states does not change with temperature. A preliminary inelastic neutron scattering experiment performed at two different temperatures /5/ justifies this assumption. Average values for $\langle u^2 \rangle^{dyn}$ obtained by the two calculation methods mentioned above were subtracted from the individual mean square amplitudes determined from the experiment in order to determine the static part $\langle u^2 \rangle^{stat}$. The results are indicated in Fig. 1 by the two lower curves. Within the accuracy of this analysis determined both by the errors of the experiment and uncertainties intro-

duced by the corrections for the dynamical contributions the static mean square amplitudes are the same for both components. They increase slightly with decreasing temperature, which seems to imply that the distortions caused by the vacancies in the lattice are temperature dependent.

As these changes with temperature are of a similar magnitude as the errors in the determination of $\langle u^2 \rangle^{stat}$ further measurements above room temperature are needed to obtain a definite answer to this question.

References

/1/ W. Reichardt, B. Scheerer and A.N. Christensen, Progress Report of the Teilinstitut Nukleare Festkörperphysik, Ges. f. Kernforschung Karlsruhe, KfK 2538 (1977) 11

/2/ H.M. Rietveld, J. Appl. Cryst. 2 (1969) 65

/3/ W. Reichardt, in Progress Report of the Teilinstitut Nukleare Festkörperphysik, Kernforschungszentrum Karlsruhe, KfK 2670 7 (1978)

/4/ F. Gompf, W. Reichardt and A.N. Christensen, in Progress Report of the Teilinstitut Nukleare Festkörperphysik, Ges. f. Kernforschung Karlsruhe, KfK 2357 11 (1976)

/5/ F. Gompf, private communication

## 1.5 Investigations of the Phonon Density of States of $MoC_x$

*N. Nücker, W. Reichardt*

α-$MoC_x$ with the NaCl-structure exists only at carbon concentrations $.65 < x < .75$ and temperatures above 1960 C /1/. By rapid quenching from high temperatures the B1-structure can be retained. The (non-existing) stoichiometric compound has 10 valence electrons (VE's) like NbN. Superconducting transition temperatures above 14 K have been observed /2/. For the refractory compounds one can conclude from the empirical correlation between particular features in the phonon dispersion curves and the number of VE's that the lattice dynamics of $MoC_x$ should be similar to that of NbN.

We have performed an inelastic scattering experiment on the time-of-

flight spectrometer TOF 3 at the FR2 using a polycrystalline sample of $MoC_x$ ($T_c$ = 12K) for the determination of the phonon density of states. Sample preparation is described elsewhere /3/. Neutron diffraction experiments showed the pure B1 phase without detectable traces of $Mo_2C$ but in addition there was a considerable amount of free carbon left from the preparation process. This amount of free carbon still has to be determined quantitatively by chemical analysis and from the diffraction pattern. We performed an additional inelastic scattering experiment on graphite. These results will be used to correct our MoC data for the carbon contamination. A preliminary analysis of the diffration data gave x $\sim$ .7.

So far we have performed only a crude analysis of the inelastic scattering data without corrections for the free carbon content. Nevertheless the essential features of the vibrational spectrum of $MoC_x$ can already be seen at this state of the analysis. In Fig. 1 the acoustic part of the generalized phonon density of states of $\alpha$-$MoC_{\sim.7}$ is compared to that of $NbN_{.95}$. Although the spectrum of $MoC_{\sim.7}$ is considerably harder than that of $NbN_{.95}$ the shapes of the two distributions are rather similar. From this we must conclude that also in $MoC_{\sim.7}$ there is a strong depression of the phonon branches in the vicinity of the X-point. The shoulder in the MoC-distribution at 16 meV may be partly caused by

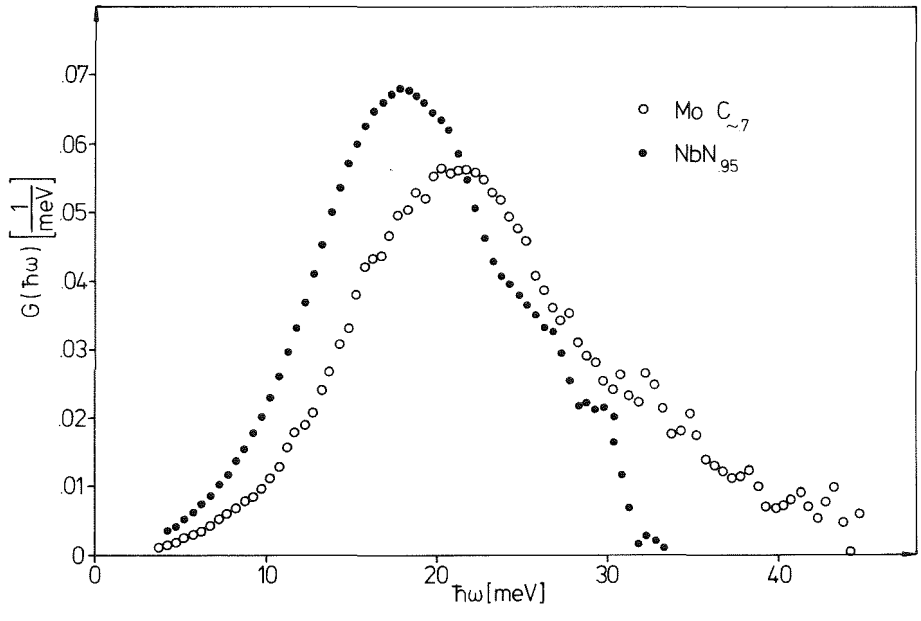


Fig. 1 Comparison between the acoustic parts of the generalized phonon densities of states of $MoC_{\sim.7}$ and $NbN_{.95}$.

the contribution of the free carbon as the phonon density of states of graphite has a maximum in this region.

At present a new sample without free carbon is available. It is intended to perform additional measurements on this sample in order to remove possible uncertainties caused by the carbon contaminations.

References

/1/ E. Rudy, S. Windisch, A.J. Stosick, and I.R. Hoffman, Trans. AIME 239, 1247 (1967)

/2/ R.H. Willens, E. Buehler and B.T. Matthias, Phys. Rev. 159, 327 (1967)

/3/ C. Politis, this report, p. 133

## 1.6 Phonon Dispersion of NbO

*P. Roedhammer*[a], *W. Reichardt, J. Hufnagl*[a]

[a]*Fachbereich Physik, Universität Konstanz, D-7750 Konstanz*

NbO belongs to the family of the refractory compounds; it has nominally 11 valence electrons per molecule (VE) and a superconducting transition temperature ($T_c$) of 1.6 K /1/. In contrast to the refractory carbides and nitrides with rocksalt structure NbO contains three formula units in the cubic unit cell. This structure originates from the rocksalt lattice by removing the Nb-atom and the O-atom from the corners and the center of the cubic cell, respectively. As a consequence of this the Brillouin zone (BZ) is simple cubic. Nevertheless, we expect that the dispersion curves of NbO bare some resemblance to those of the related compounds with rocksalt structure. Our investigation of the lattice dynamics of NbO is of particular interest in view of the proposed correlation between the electronic band structure - the topology of the Fermi surface - and anomalies in the phonon dispersion curves. Furthermore, the results may help to clarify the role of vacancies in stabilizing the rocksalt structure in this class of materials.

Measurements were performed on the triple axis spectrometer TAS 1 at the FR2 using a sample of two coaligned single crystals with a total volume of about 0.3 $cm^3$. The results so far obtained are shown in Fig. 1 as plotted in the BZ of the rocksalt structure (4 times larger than the actual BZ) in order to facilitate the comparison with the dispersion curves of other refractory compounds. The true zone boundaries are at q = 0.5 for all three symmetry directions. At this q-value gaps occur in the dispersion curves in the <011> - and <110> directions as is obvious for the TA branch in <110> - direction. The magnitude of this gap is consistent with model calculations to be described in the next section. In the vicinity of the L-point the TA phonon groups became very broad. This is most likely caused by contributions of some optical branch.

The dispersion curves of ZrC ($T_c$<0.05 K, 8 VE) /2/ and $NbN_{.83}$ ($T_c$ = 12 K, 10 VE for the stoichiometric case) /3/ are indicated in Fig. 1 by the dashed and dotted lines, respectively. Comparison with the presently available data suggests that the dispersion curves of NbO exhibit some similarity to those of NbN with regard to the depression of the phonon branches at the X-point.

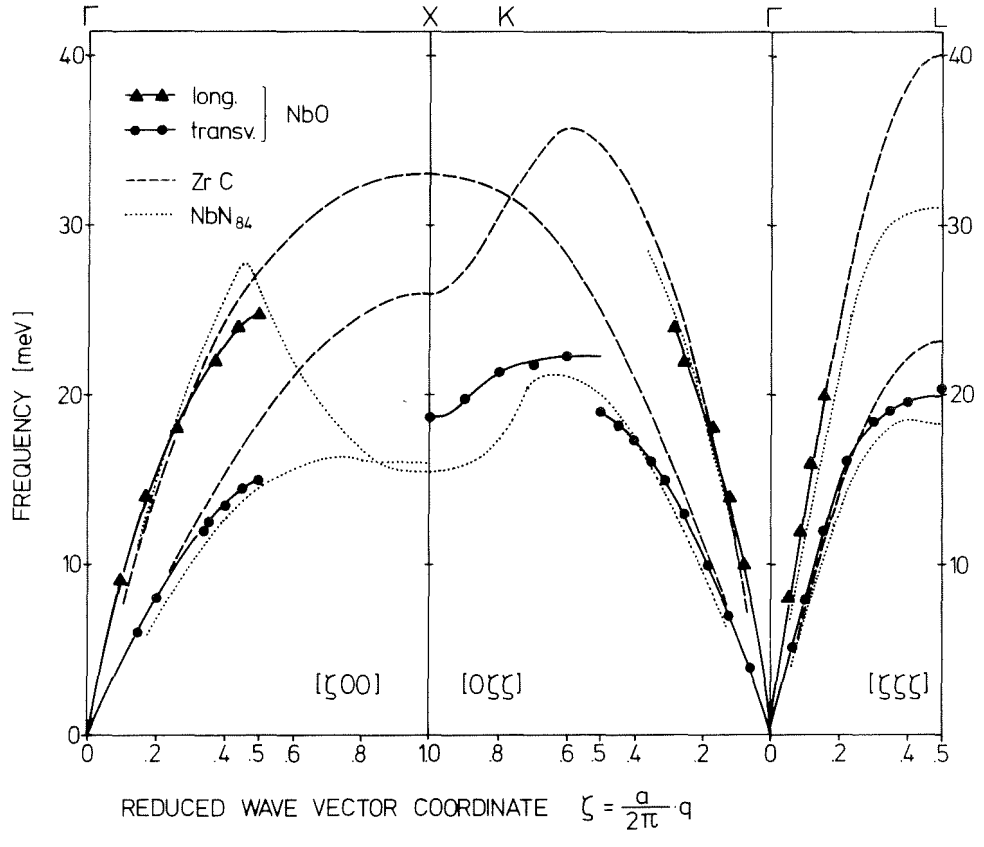


Fig. 1 Dispersion curves of NbO in the main symmetry directions plotted in the BZ of the rocksalt structure. The full lines are merely a guide to the eye. For comparison the results for ZrC /2/ and $NbN_{.83}$ are indicated by the dashed and dotted lines, respectively.

References

/1/ B.W. Roberts, Properties of Selected Superconductive Materials, NBS Technical Note 983, 46 (1978)

/2/ H.G. Smith, N. Wakabayashi, and M. Mostoller, in Superconductivity in d- and f-band Metals, edited by D.H. Douglass, Plenum Press, New York, 223 (1976)

/3/ W. Reichardt, B. Scheerer, this report, p.4

## 1.7 Influence of Ordered Vacancies on the Phonon Dispersion of the Refractory Compounds

*W. Reichardt*

The refractory compounds of Type AB with rocksalt structure show a strong tendency to form vacancies both in the A and the B sublattice. In some compounds like $V_8C_7$ and NbO the vacancies are ordered. Strictly speaking these compounds have no longer the rocksalt structure but a structure with larger dimensions of the unit cell and the Bravais lattice is no longer fcc. In order to show their relationship to the refractory compounds without vacancies it seems reasonable to consider the lattices with ordered vacancies as rocksalt structures with a superstructure which also emphasizes their connection with those cases where only short range ordering of vacancies exists.

The refractory compounds are presently of particular interest because unusual structures occur in the dispersion curves caused by electron-phonon coupling. In order to be able to distinguish these effects from the "trivial" influence of the superstructure we started model calculations for simple systems with ordered vacancies.

For this aim a computer program was written which calculates the phonon dispersion curves of a cubic structure with 8 atomic positions in the unit cell on the basis of a Born v. Kármán (BvK) model. In particular the following cases can be delt with: $A_4B_4$ (identical to rocksalt structure) - $A_4B_3$,$A_3B_4$ (i.e. vacancies in the A or the B sublattice) - $A_3B_3$ (NbO structure).

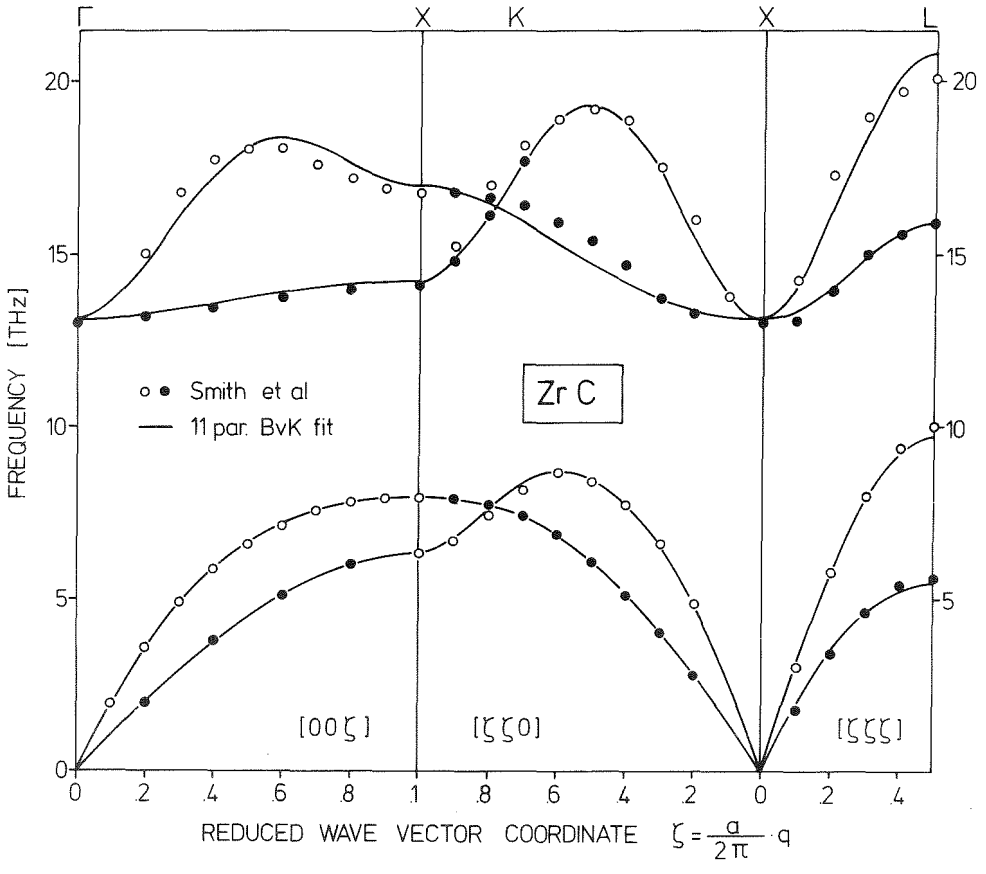


Fig. 1 Fit of an 11 parameter Born v. Kármán model to the experimental data of ZrC /1/.

In order to use reasonable interatomic forces in our calculations we took ZrC as a model substance which has no anomalies of electronic origin in the dispersion curves. An 11 parameter BvK model was fitted to the experimental dispersion curves /1/ which gave an excellent agreement with the experimental results (Fig. 1). With these force constants the dispersion curves of hypothetical $Zr_4C_3$, $Zr_3C_4$, and $Zr_3C_3$ compounds were calculated. The results for some branches in the <100>-direction are shown in Fig. 2. They are plotted in an enlarged Brillouin zone which corresponds to that of the related rocksalt structure in order to facilitate the comparison with the results for the compound without vacancies. Besides the well-sized gaps at q = .5 and a depression of some branches at the zone boundary there is an overall decrease of the phonon frequencies. In real structures the latter effect will be compensated to some extent by the reduction ot the interatomic distances caused by the vacancies which leads to an increase of the interatomic force constants.

Further investigations with other force models for the refractory compounds are necessary in order to find out to which extent these results depend on the particular choice of force constants in our model.

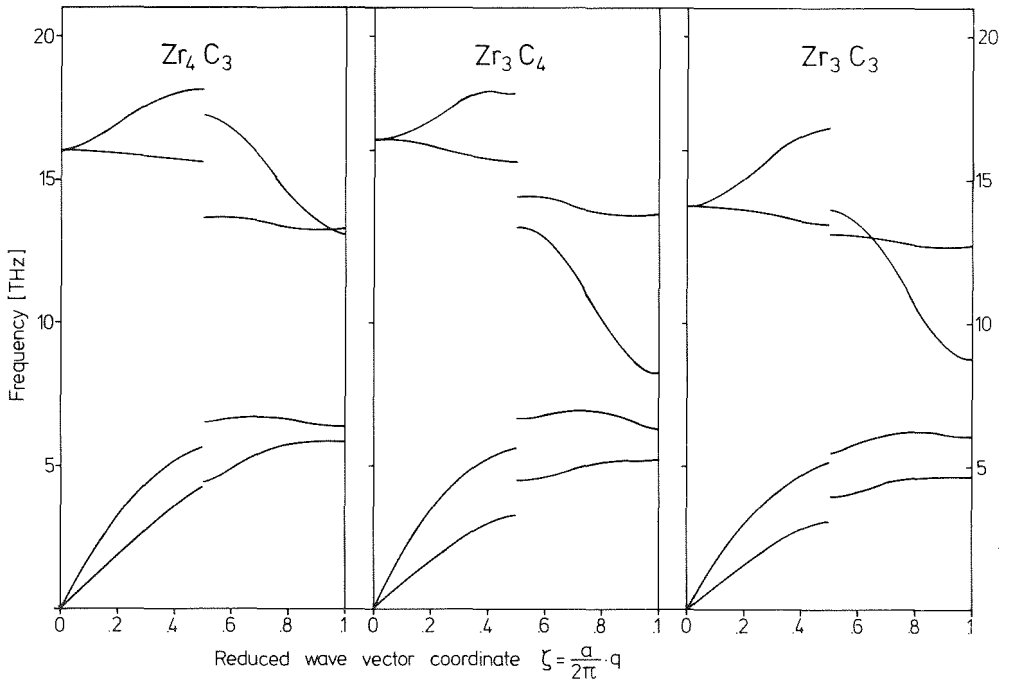


Fig. 2 Dispersion curves in the <100>-direction of hypothetical zirconium carbide compounds with different kinds of ordered vacancies calculated with the force-constants of ZrC.

Reference

/1/ H.G. Smith, N. Wakabayashi, and M. Mostoller, in Superconductivity in d- and f-band Metals, edited by d.H. Douglass, Plenum Press, New York, 223 (1976)

## 1.8 Born v. Kármán Model for A15-Compounds

*W. Reichardt*

Extensive investigations on the phonon density of states of A15-compounds ($A_3B$) have been performed by inelastic neutron scattering using powder samples /1/, whereas only scarce information is available about the phonon dispersion curves /2/ /3/ due to the lack of suitable single crystals. Recently, calculations of the dispersion curves of several A15 compounds have been performed on

a microscopic basis by Achar and Barsch /4/ /5/. Although the phonon densities of states determined from these microscopic models bare some similarity to our experimental results in Ref./1/ there exist fundamental discrepancies since the model calculations predict high frequency bands which we did not observe in our experiments. Within this theory these bands are mainly caused by vibrations of the transition metals within the chains. On the other hand, the theoretical preditions seem to be supported by recent neutron scattering /6/ and optical /7/ experiments where scattering intensities were observed for $V_3Si$ at 58 and 55 meV respectively, which is well above the high frequency cutoff (< 50 meV) of our experimental phonon density of states.

In order to help to an understanding of these discrepancies we have developed a computer program which allows to calculate the phonon dispersion curves of A15-compounds on the basis of a Born v. Kármán model. At present either general or axially symmetric forces can be used up to the fourth neighbor interaction. An extension to include further neighbors is easily possible. The model parameters can be determined from experimental dispersion curves by a least square fit procedure.

Preliminary calculations have been performed for $V_3Si$ and $Nb_3Sn$ at 300 K. For the determination of the model parameters we proceeded as follows: Due to the limited experimental information we assumed axially symmetric interactions up to the third neighbors which include interactions between A-atoms within the chain, nearest neighbor A-B interactions and coupling between the chains. The model parameters for $V_3Si$ were obtained by a fit to the elastic constants /8/, to the $\Gamma_{12}$ frequency determined by Wipf et al /9/ and to the center of gravity of the high frequency peak of the phonon density of states assuming that this peak is due to Si-vibrations. Based on the empirical finding that the interatomic forces of A15-compounds with the same number of valence electrons are very similar /1/ we applied the force constants of $V_3Si$ also to $Nb_3Sn$ only slightly modifying the A-B interactions in order to account for the stronger elastic anisotropy in $Nb_3Sn$ compared to $V_3Si$. This modification bares some arbitrariness as the same changes in the low frequency acoustic modes could be obtained by similar modifications in the interchain force constants.

The generalized phonon densities of states $G(\hbar\omega)$ for $V_3Si$ and $Nb_3Sn$ calculated with these models are compared with the results of Ref. 1 in Figs. 1 a and 1 b. Although the agreement with the experimental results is not perfect the essential features in the frequency distributions are well reproduced. In particular no bands appear above the experimental high frequency cutoffs. In Fig. 2 the low frequency dispersion curves obtained from our model for $Nb_3Sn$

are compared with the available phonon data /2/ /3/. Considering the simplicity of our calculations the agreement is quite satisfactory.

Although our present model is certainly too crude to describe the details of the phonon dispersion curves of the A15-compounds we believe that the basic features of our analysis are essentially correct, which are a rather strong interchain coupling (ca. 27000 dyn/cm) and a A-B interaction (ca. 35000 dyn/cm) of similar magnitude as the intrachain A-A interaction (ca. 40000 dyn/cm). (The cited values refer to the longitudinal force-constants).

The main discrepancies between the calculation of Achar and Barsch and our phenomenological model are clearly caused by the much larger intrachain interaction in the microscopic model leading to a $\Gamma_{12}$ frequency which is more than twice as large as the experimental value of Wipf et al /9/.

Fig. 1a

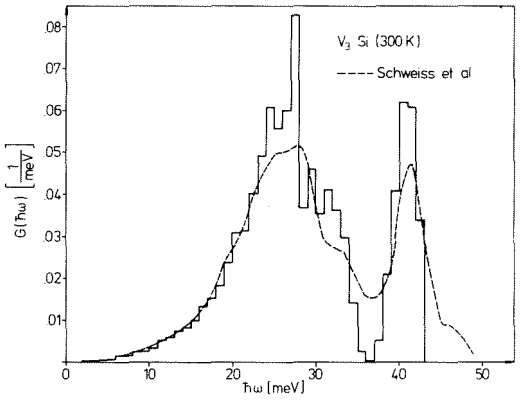


Fig. 1b

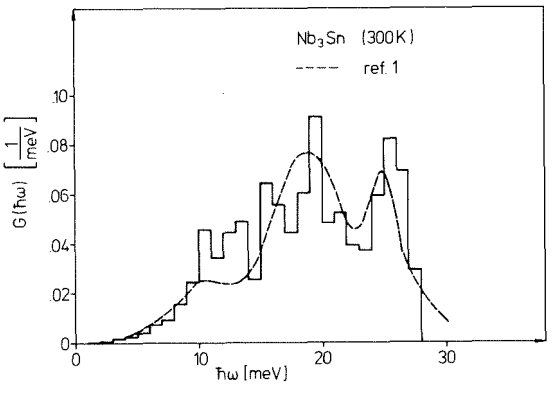


Fig. 1a and 1b: Histograms of the generalized phonon densities of states of $V_3Si$ and $Nb_3Sn$ at 300 K calculated from Born v. Kármán models for 165 q-values in the irreducible part of the Brillouin zone. Dashed lines represent experimental data of Ref. 1.

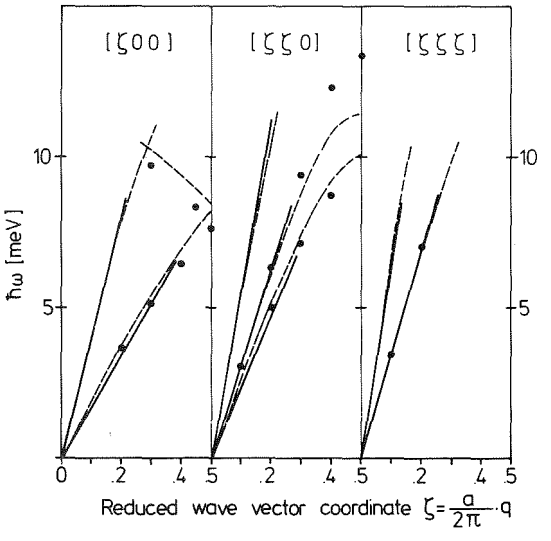


Fig. 2
Acoustic modes of $Nb_3Sn$ at 300 K as calculated from the model described in the text (dashed lines). Experimental data were taken from Refs. 2 and 3. Full lines indicate the slopes of the phonon branches at the Γ-point calculated from the elastic constants.

References

/1/ B.P. Schweiss, B. Renker, E. Schneider, and W. Reichardt in Superconductivity in d- and f-Band Metals, edited by D.H. Douglass, Plenum Press, New York, 189 (1976)

/2/ J.D. Axe and G. Shirane, Phys. Rev. B 8, 1965 (1973)

/3/ G. Shirane and J.D. Axe, Phys. Rev. B 18, 3742 (1978)

/4/ B.N.N. Achar and G.R. Barsch, Phys. Lett. 59A, 65 (1976)

/5/ B.N.N. Achar and G.R. Barsch, Solid State Comm. 30, 419 (1979)

/6/ H.G. Smith et al, in Progress Report Solid State Division, ORNL - 5486, 172 (1979)

/7/ S. Schicktanz, R. Kaiser, W. Spengler, Solid State Comm. 28, 935 (1978)

/8/ L.R. Testardi and T.B. Bateman, Phys. Rev. 154, 402 (1967)

/9/ H. Wipf et al, Phys. Rev. Letters 41, 1752 (1978)

## 1.9 Temperature Dependence of the Phonon Density of States of $Nb_3(Ge_{.8}Nb_{.2})$

*W. Reichardt, N. Nücker, B. Scheerer*

Neutron scattering experiments on a series of A15-compounds have shown that a considerable phonon softening occurs over a large part of the frequency spectrum when the samples are cooled to liquid nitrogen temperature /1/. The

observed softening increased with increasing superconducting transition temperature ($T_c$) of the compound.

$Nb_3Ge$ samples prepared by sputtering or chemical vapor deposition have $T_c$ values up to 23 K and correspondingly we expect a rather strong temperature dependence of the phonon density of states. By chemical methods only nonstoichiometric samples can be obtained which have $T_c$ values of about 6 K. It seemed of interest whether the observed correlations between the amount of phonon softening and $T_c$ also holds if the variations of $T_c$ are not caused by changes in the constituents but by lattice defects in one and the same compound.

Previously we reported about measurements of the phonon density of states at room temperature of niobium germanium performed on a sample of composition $Nb_3(Ge_{.8}Nb_{.2})$ ($T_c$ = 6.5 K) /2/. We have extended these measurements to T = 77 K. Fig. 1 shows a comparison between the results at 77 K and 296 K. Only a rather small softening is observed in the frequency range below about 18 meV. These changes are similar to those observed in $V_3Ge$ which has a $T_c$ of 6.2 K /1/.

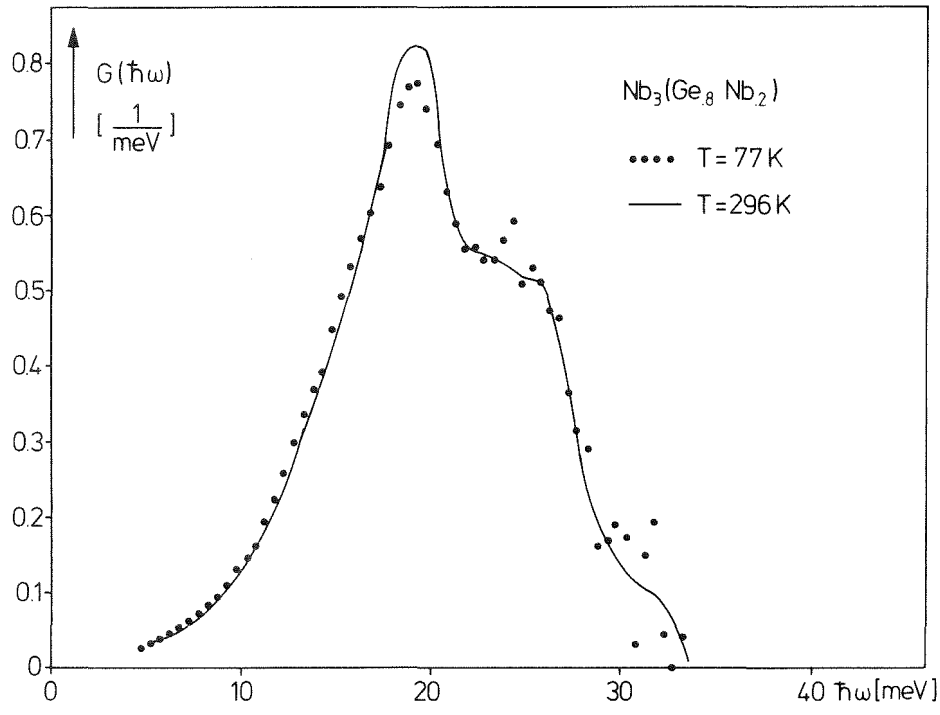


Fig. 1 Generalized Phonon Density of States of $Nb_3(Ge_{.8}Nb_{.2})$ at 77 K and 296 K.

References

/1/ B.P. Schweiss, B. Renker, E. Schneider and W. Reichardt, in Superconductivity in d- and f-Band Metals, edited by D.H. Douglass, Plenum Press, New York, 189 (1976)

/2/ N. Nücker and W. Reichardt, in Prog. Rep. Teilinst. Nukl. Festkörperphysik, Kernforschungszentrum Karlsruhe, KfK 2670, 9 (1978)

## 1.10 Acoustic Phonon Dispersion in $Mo_6Se_8$

*B. Renker, B.P. Schweiss[a], J.B. Suck[b] and R. Flükiger[c]*

[a] *Institut für Kristallographie und Mineralogie der Universität Frankfurt, 6000 Frankfurt a. M. 1*

[b] *Institut Laue Langevin, F-38042 Grenoble*

[c] *Département de Physique de la Matière Condensée, Université de Genève, CH-1211 Genève 4*

$Mo_6Se_8$ belongs to the class of Chevrel phase superconductors ($T_c$ = 6.5K). This binary compound provides a good starting point for the investigation of ternary Mo = chalcogenides some of which exhibit extremely high critical fields (up to 70 T) and reasonable values of transition temperatures (15K). The structure of $Mo_6Se_8$ is rhombohedral, space group R3 with lattice parameters a = 6.658Å and $\alpha = 91.58^{\circ}$ (room temperature). A phase transition on cooling has not been observed. Starting point of our investigations were phonon density of states measurements where similar to other high $T_c$ Chevrel phase compounds a considerable softening of phonon frequencies on cooling has been observed /1/. Here we report results of acoustic phonon measurements at 300 K and 5 K on a $Mo_6Se_8$ single crystal. Measurements proved to be extremely difficult since our sample ( $\sim .1cm^3$) contained at least three crystallites. Two of which were of similar orientation with an angular offset of about 2 degrees. The third one with a size of about one fourth of the sample showed a completely different orientation. A structure observed in the phonon peaks could be clearly attributed to the two neighbouring crystallites. Since the angle $\alpha$ differs only by $1.58^{\circ}$ from $90^{\circ}$, effort was taken to investigate the high symmetry directions of the cubic system although in our case the direction <110> and <1$\bar{1}$0> for instance are not identical. The crystal was oriented such that the scattering plane contained the (430) and (5$\bar{3}$0) reciprocal lattice points both of which have favourable structure factors. Fig. 1 shows the results obtained so far: Some indications for a phonon softening were observed in the <1$\bar{1}$0> direction where independent results obtained at the FR2 and the HFR reactor indicate a broader dip around $q \simeq .5\ q_{max}$. The phonon energy corresponds well to that part of the $G(\hbar\omega)$ spectrum where a pronounced anomalous temperature effect had been observed before. Phonons measured along <111>, <100> and <001> respectively showed a normal temperature dependence. The transversal branch along <110> is somewhat steeper

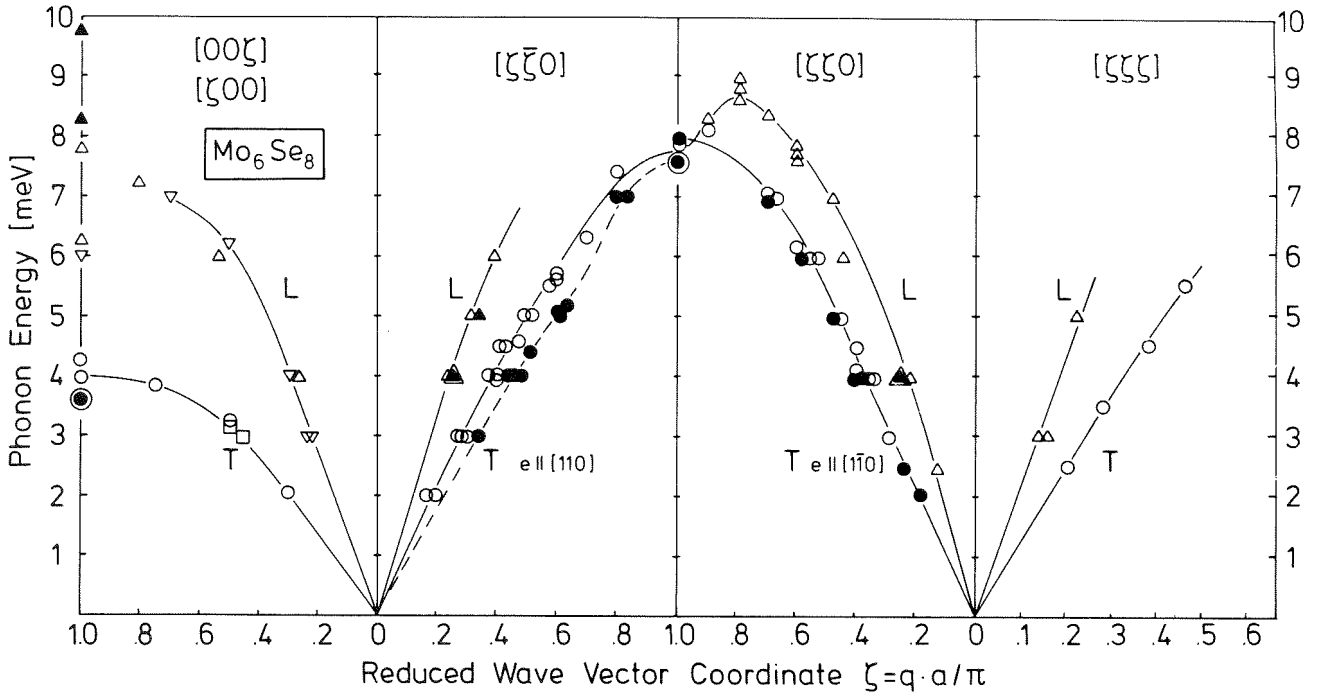


Fig. 1 Results of acoustic phonon measurements in $Mo_6Se_8$ for some selected directions for 300 K and 5 K. Open symbols refer to the 300 K and full symbols to the 5 K results. Within experimental error no differences between measuring results in <00ζ> (symbols = Δ, O) and <ζ00> direction (symbols ▽,□) were observed. Since the sample was of poor quality different runs with different orientations of the crystal have been undertaken in order to eliminate spurious peaks. The phonon softening most pronounced for the TA <ζζ̄0> branch was clearly observed in all cases for both const. $\hbar\omega$ and const. q scans.

than that one along <1$\bar{1}$0>. There are also - but less pronounced - indications for a phonon softening. An anomalous temperature effect which has been observed first in the G($\hbar\omega$) spectra of superconducting molybdenum chalcogenides has been explained by the assumption of a strong electron phonon coupling. The question arises whether the anomaly observed in the TA <1$\bar{1}$0> branch may be explained by a fermi surface nesting effect. Some arguments therefore can be found from recent band structure calculations /2/ which seem to show regions with parallel tangents in <110> direction and $q \simeq .5\ q_{max}$. Effort was taken to look also for an anomaly in the LA branch, but due to the poor quality of the sample sufficiently accurate measurements were not possible at low temperatures. Additional difficulties arise from the fact that the room temperature results seem to indicate the hybridisation with an optical branch close to this wave vector. The slope of the LA branch which has been measured at both temperatures does not signalize a phonon softening.

References

/1/ P. Schweiß, B. Renker and J.B. Suck, J. de Physique, suppl. no. 8, Tome 39, C6 - 356 (1978)

/2/ O.K. Andersen, W. Klose and H. Nohl, Phys. Rev. B 17, 1209 (1978)

## 1.11 Comparison of the Experimentally Determined Phonon Density of States of $LaB_6$ with a Lattice Dynamical Model Calculation

*F. Gompf, G. Schell and H. Winter*

In Ref. /1/ we gave preliminary results of inelastic neutron scattering experiments on $LaB_6$. The time-of-flight spectra were marked by unsatisfactory statistics due to the high absorption cross section of the boron ($B^{10}$) atoms. Nevertheless, from the results obtained with an incident energy of 5.0 meV some low frequency excitations could be determined.

In Fig. 1 we show the phonon density of states extracted from this data. Inspite of the bad statistics of the experiment certain sharp peaks at about 13, 36, 65 and perhaps around 95 meV could be located. Above 100 meV the intensity of the scattered neutrons is so weak that higher frequencies cannot be determined.

In order to interprete the phonon density of states we have developed a Born von Kármán model taking into account central forces and nearest neighbour boron-boron and metal-boron interactions only. The two force constants involved have been determined by fitting the position of the energetically highest $A_{1g}$-"breathing"-mode to Raman results /2/ and the position of the energetically lowest (translational) mode to our measurements, that is to 13 meV. The breathing mode has been selected because its energy is not affected by bond bending forces probably existing in the hexaborides but not treated within the frame of our model. Our results are: $f_{B-B}=16\cdot10^4$dyn/cm in accordance with the value of Ref. /2/ ($14\cdot10^4$dyn/cm) and $f_{La-B}=0.075\ f_{B-B}$. Note that this value of $f_{La-B}$ can be accounted for by assuming only electrostatic interaction between a La-atom and its nearest neighbour boron atoms originating from the charge transfer of two electrons /3/ from each metal atom to the boron sublattice.

The phonon density of states calculated with this model is shown in Fig. 1. The measured peaks coincide with those calculated. The vibrational types of those modes are visualized in Fig. 2. Only the rotational peak at 26 meV does not fit to its measured counterpart at 36 meV indicating the importance of additional bond bending forces.

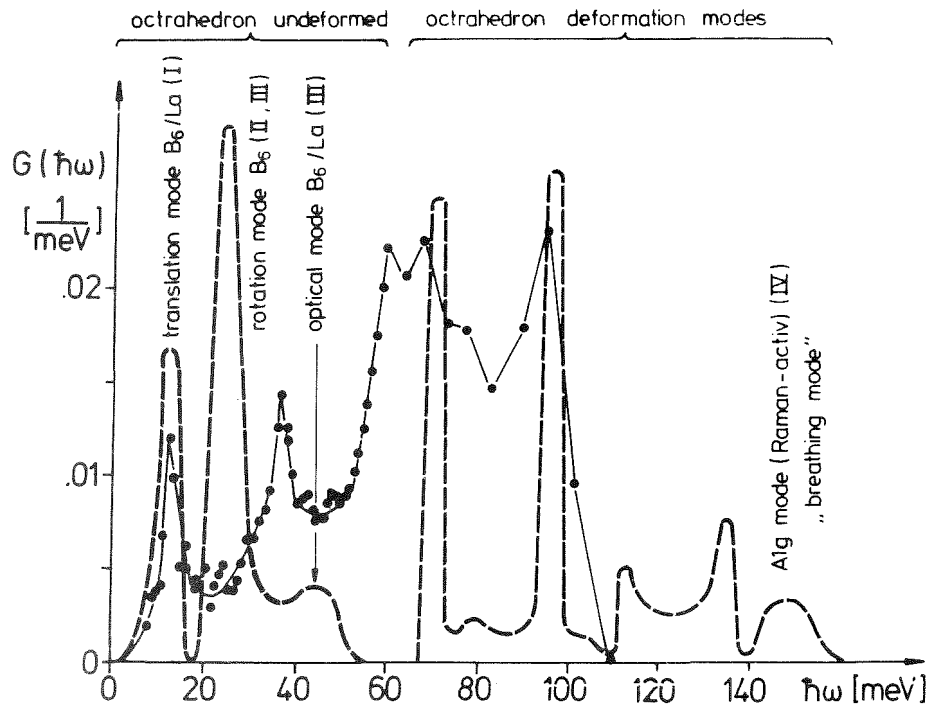


Fig. 1 Comparison of the experimentally determined phonon density of states of $LaB_6$ (•-•-•) with the lattice dynamical model calculation (---).

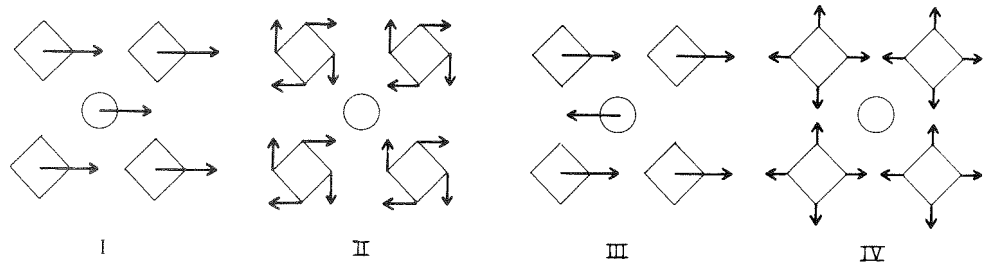


Fig. 2 Types of vibrational modes used in the model calculation.

Presently our model is being improved by the addition of bond bending forces. We also expect a better determination of the high frequency modes from measurements on an enriched sample of $B^{11}$ which will be performed in the near future.

The influence of the individual modes on the superconducting transition temperature is discussed on page 59 in this volume.

References

/1/ F. Gompf, in "Progress Report Teilinstitut Nukleare Festkörperphysik", Ges. f. Kernforschung, KFK 2670, 17 (1978)

/2/ H. Scholz, W. Bauhofer, and K. Ploog, Solid State Commun. 18, 1539 (1976)

/3/ H.C. Longuet-Higgins and M. de V. Roberts, Proc. Roy. Soc. (London) A224, 336 (1954)

## 1.12 Comparison of the Phonon Density of States of $Be_{22}Re$ ($T_c$ = 9.75 K) with that of Be ($T_c$ = 0.028 K).

*F. Gompf and S. Jönsson*[a]

[a] *MPI Stuttgart, Institut für Werkstoffwissenschaften*

Among the family of the h.c.p. metals, Be is the lightest element and was found to have a $T_c$ of only 0.028 K. It posesses a complex electronic structure and peculiarities in the phonon dispersion curves. This makes it difficult to develop a good lattice dynamical model from which the phonon density of states can be calculated.

$Be_{22}X$ compounds (X = Mo, W, Tc, Re) are known to have a complex fcc structure with 8 formula units per unit cell and are all superconductors. $Be_{22}Re$ for instance can be characterized by several outstanding features such as high atomic density, low specific heat and a high transition temperature of $T_c$ = 9.75 K /1/. Despite of the low concentration of the transition metal atoms and the large mass difference to the host atoms a strong influence on $T_c$ of the transition metal ions has been demonstrated by Bucher et al. /2/ who measured a pronounced isotope effect in $Be_{22}Mo$.

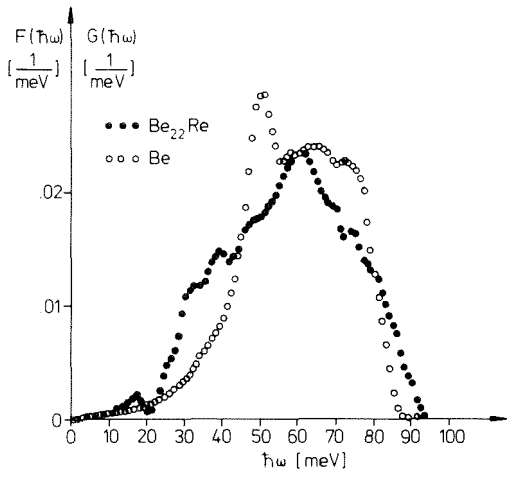


Fig. 1 a
Comparison of $F(\hbar\omega)$ for Be with $G(\hbar\omega)$ of $Be_{22}Re$ (for explanation see text).

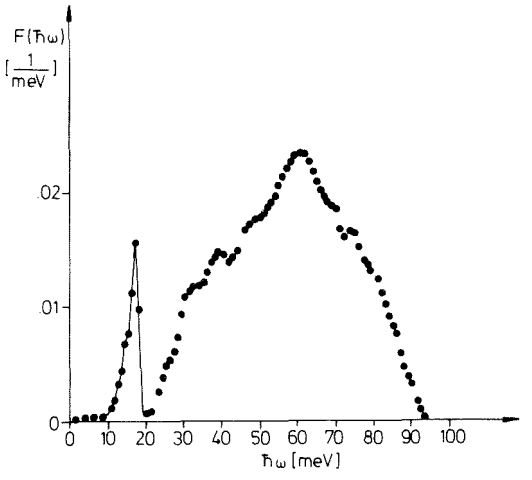


Fig. 1 b
The true phonon density of states for $Be_{22}Re$.

For a better understanding of the low frequency transition metal modes we performed room temperature measurements on Be and $Be_{22}Re$ using inelastic neutron scattering on TOF II and TOF III, multidetector time-of-flight spectrometers with incident neutron energies of 5 and 27 meV, respectively. The phonon density of states for $Be_{22}Re$ and for Be deduced from these scattering data are shown in Fig. 1 a. For $Be_{22}Re$ we get of course a generalized phonon density of states $G(\omega) = F_1(\omega) \cdot \sigma_1/M_1 + F_2(\omega) \cdot \sigma_2/M_2$. Since $(\sigma/M)_{Be} = 14.7\ (\sigma/M)_{Re}$ and with the atomic ratio of 22:1 we get a Re contribution to $G(\hbar\omega)$ of about $3^{o}/oo$ which means that the generalized phonon density of states reflects mainly the Be modes.

In comparison to Be the high frequency modes in $Be_{22}Re$ are notably moved to higher frequencies while between 20 and 60 meV the Be modes in $Be_{22}Re$ are much softer. The transition metal modes presumably appear in the region below 21 meV separated through a gap from the rest of the spectrum (see enlargement in Fig. 2). This can be understood by assuming a resonance mode like behaviour of the Re atoms when vibrating against clusters of Be atoms in their highly symmetric environment. If we subtract the areas of both spectra up to the gap, there is a surplus for the $Be_{22}Re$ spectrum (shaded area in Fig. 2) which is about $3^{o}/oo$ of the total density area as expected from the ratio of $\sigma_{Be} \cdot M_{Re}/22 \cdot \sigma_{Re} \cdot M_{Be}$. After multiplying this Re-area with 14.7 and normalizing the total spectrum to unity we arrive at the true phonon density of states which is shown in Fig. 1 b.

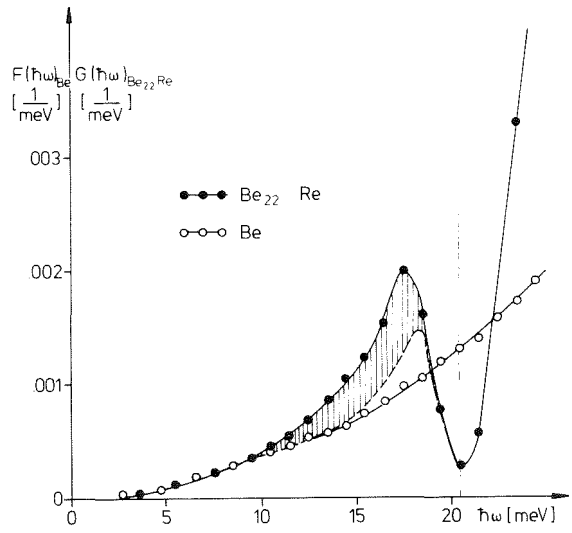


Fig. 2
Region of Re vibrations in the generalized phonon density of states $G(\hbar\omega)$ for $Be_{22}Re$ (shaded area)

From both spectra we deduced the specific heat as a function of temperature which is shown in Fig. 3. For Be the agreement with experimental results of Hill et al /3/ is excellent. For $Be_{22}Re$ the specific heat has only been measured up to 18 K /1/ whereas our data begin at 20 K. In order to still be able to make a comparison we calculated the Debye temperature $\Theta_D$ as a function of temperature which is shown in Fig. 4. $\Theta_D$ steadily continues Buchers values, has a deep minimum at about 40 K and yields a room temperature value of 860 K. To demonstrate the correctness of our assumption concerning the region of the transition metal modes we additionally show the $\Theta_D$-curve for the uncorrected $G(\hbar\omega)$ of $Be_{22}Re$ (dash-dotted line).

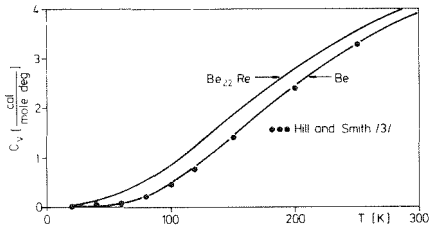


Fig. 3
Specific heat for Be and $Be_{22}Re$ as deduced from their vibration spectra.

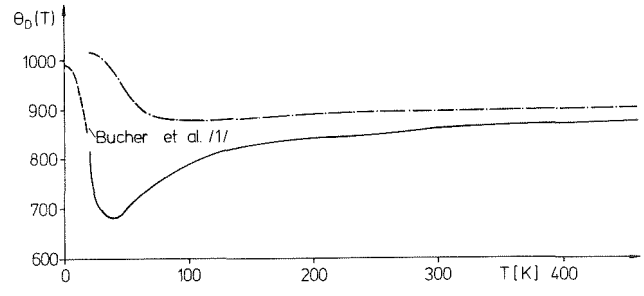


Fig. 4
The Debye temperature of $Be_{22}Re$ as calculated from the specific heat data of Bucher et al /1/ (---), the generalized phonon density of states (-·-·-) and the true density of states (——).

References

/1/ E. Bucher, F. Heiniger, J. Müller and P. Spitzli, Phys. Letters 19, 263 (1965)

/2/ E. Bucher and C. Palmy, Phys. Letters 24 A, (1967) 340

/3/ R.W. Hill and P.L. Smith, Phil. Mag. 44 (1953) 636

## 1.13 Neutron Scattering Studies of a Structural Phase Transition in La $Ag_{1-x}$ $In_x$ compounds.

*K. Knorr[a], B. Renker, B. Lüthi[b], W. Assmus[b] and R. Tacke[b]*

[a] *Inst. f. Physik, Johannes Gutenberg Universität Mainz, D-6500 Mainz*

[b] *Phys. Inst., Universität Frankfurt, D-6000 Frankfurt*

Recently a structural phase transition has been reported for $LaAg_{1-x}In_x$ compounds. The dependence of the transition temperature on the In-concentration x has been explained within the frame work of a Martensitic transition /1/ /2/. The present work reports investigations of the structural phase transition by means of thermal neutron scattering.

Elastic scattering results:

The cubic to tetragonal distortion has been studied in detail. At the transition a splitting of Bragg peaks caused by the growing of domains with the new tetragonal structure is observed. In addition new reflexes occur at the M points of the Brillouin zones corresponding to a doubling of the unit cell axes.

Fig. 1 shows the behaviour of the lattice constant a at the transition for samples with x = .2 and .11, respectively. The jump in the lattice parameter together with a hysteresis of about 5 K observed in elastic scans when the transition is passed from above or below $T_c$ indicates a first order phase transition.

Inelastic scattering results:

Acoustic phonon dispersion curves have been measured for the <100>, <110>, and <111> directions for concentrations X = 0, .11, .25 and in particular for the TA <110> branch at various temperatures (Fig. 2 and 3). It turns out clearly that the phase transition is triggered by a softening of the TA <110> phonon at the M-point.

For LaAg which does not exhibit a transition the TA <110> phonon branch is anomally soft at the zone boundary but it does never reach down to $\hbar\omega \simeq 0$. We find over a large temperature region a critical exponent $\beta = \frac{1}{2}$ as demonstrated by the $(\hbar\omega)^2$ over T plot in Fig. 4. Since no 4-dimensional resolution corrections have been applied the data for $\hbar\omega < 1.5$ meV have only qualitative character. In particular the rounding off in the vicinity of the transition may be due to the difficulty to separate the phonon intensity from the critical scattering.

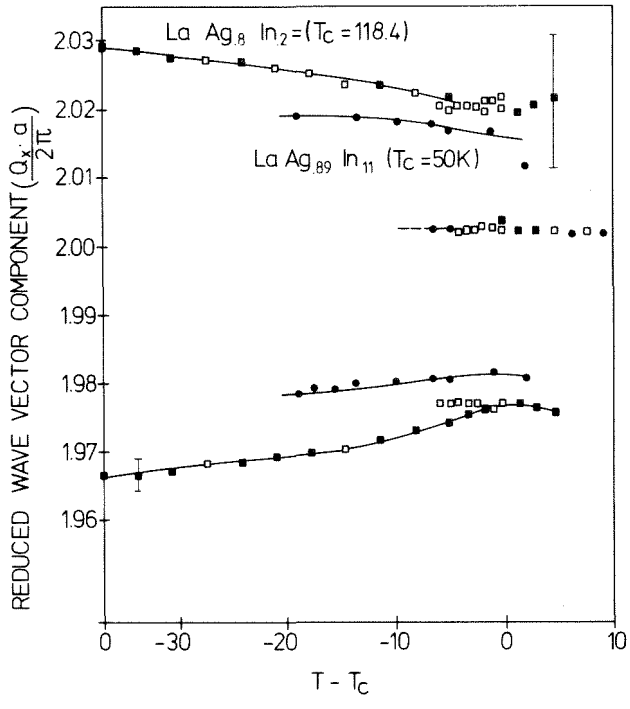


Fig. 1
Splitting of the cubic lattice parameter a at the transition for compounds $LaAg_{.8}In_{.2}$ and $LaAg_{.89}In_{.11}$. Full symbols refer to heating up and open symbols to cooling down of the sample.

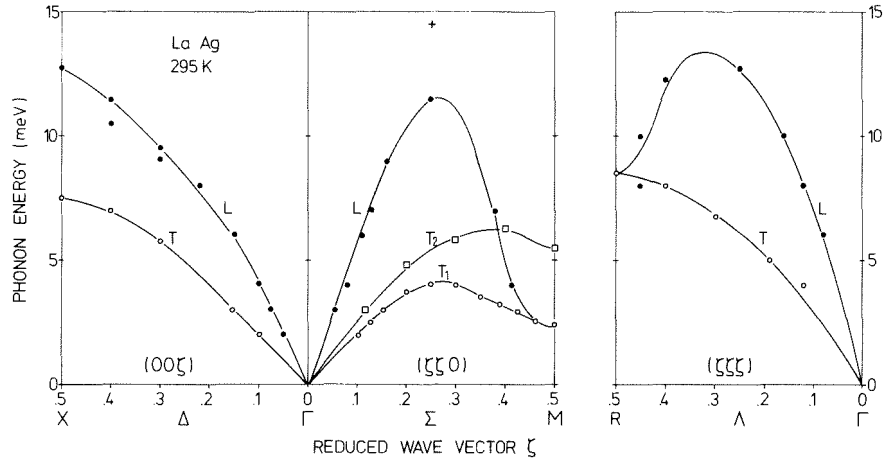


Fig. 2 Acoustic phonon dispersion along the <100>, <110> and <111> directions for pure LaAg at room temperature. The $T_1$ <110> phonon with polarisation $\vec{e}$ = <1$\bar{1}$0> is anomally soft near the M-point. This behaviour is still more pronounced for samples with 11 and 20 at. % In-concentration.

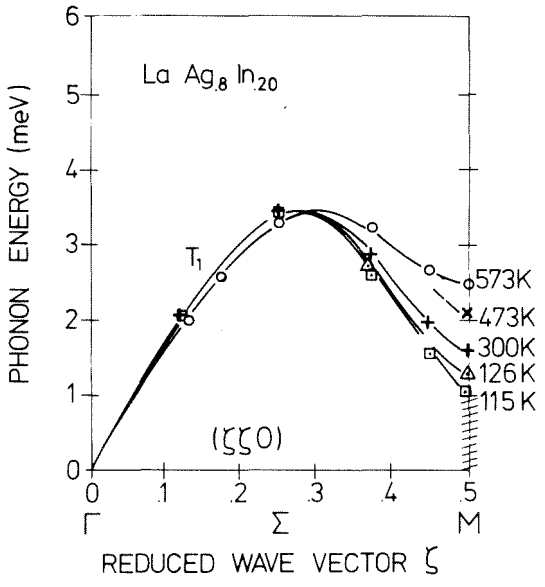


Fig. 3
Temperature dependence of the $T_1$ <110> soft phonon branch for $LaAg_{8}In_{2}$. The hatched region marks the presence of critical scattering.

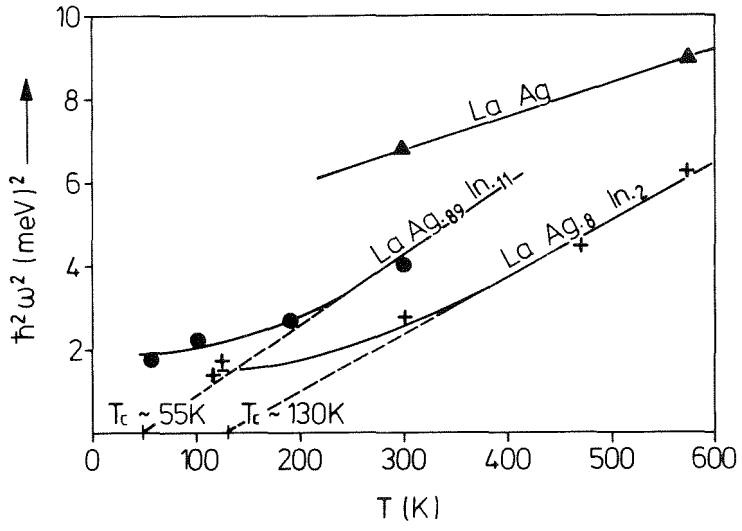


Fig. 4 Temperature dependence of the soft phonon frequency at the M-point as obtained for samples with various In concentrations. The results are qualitative since no four dimensional resolution corrections have been applied.

References

/1/ H. Ihrig, D.T. Virgen, J. Kübler, S. Methfessel, Phys. Rev. B 8 , 4525 (1973)

/2/ W. Assmus, R. Takke, R. Sommer, B. Lüthi, J. Phys. C 11, L 575 (1978)

## 1.14 Acoustic Phonons in $UAl_2$

*B. Renker, K. Käfer and J. Burkin*[a]

[a] *Institut für Materialforschung, IMF I*

The compound $UAl_2$ can be characterized as a spin fluctuation system with absence of magnetic ordering down to 80 mK /1/. The physics can be understood by the presence of a narrow 5f band near the Fermi level responsible for a large value of $\gamma$ ( $\sim$ 90 m J/K$^2$ Mol) in the electronic contribution to the specific heat.

Recent compressibility data seem to show a remarkable change in the compressibility between 4 K and 300 K /2/. Thus we have undertaken a study of the lattice dynamical properties of $UAL_2$ by means of phonon measurements using the technique of inelastic neutron scattering.

The sample (single crystal of $\sim$ 1 $cm^3$ volume) was prepared by slowly cooling down of the melt. The resultant ingot contained several larger crystallites which could be localized on a diffractometer and separated mechanically. Measurements were performed at 300 K and 5 K on a triple axis instrument.

$UAl_2$ possesses $Cu_2Mg$ structure (Laves phase). The symmetry is cubic (fcc) and the unit cell containes 24 atoms. Its primitive cell containes 2U and 4Al atoms. From a total of 18 phonon branches only parts of the acoustical ones have been measured.

For a general view we show the generalized phonon density of states (Fig. 1) uncorrected for multi-phonon contributions, as obtained by the scattering from a polycrystalline sample. The region below 12 meV (about $\frac{1}{6}$ of the total area) contains predominantly the acoustic vibrations. From the phonon measurements there are some indications for a low optical branch around 10 meV which may be the lowest optical branch that involves mainly vibrations of the heavy U atoms. The high frequency region above $\sim$ 20 meV finally containes predominantly vibrations of the light Al atoms.

The measured phonon dispersion curves along the high symmetry direction of the cubic system are shown in Fig. 1 for 300 K and 5 K. The largest temperature effect is found for the LA ‹100› branch where a hardening of $\sim$ 12 % is observed. Almost no changes are observed for the other branches. In particular any indications of phonon anomalies have not been found in this system. Thus from the present data we may conclude that none of the unusual electronic properties of this compound leads to remarkable effects in the phonon dispersion. The electronic density of states might be high, but in view of our results we conclude that there is no sharp structure in the density of states near the Fermi Level.

Finally we have calculated the following values of the elastic constants from the slopes of the dispersion curves: $C_{11}$ = 18.6±1.6 (22.2±1.9), $C_{44}$ = 7.8±.6 (7.1±.6), $C_{12}$ = 4.6±1.2 (4.2±1.2). The values in brackets refer to the 5 K results. From these values a decrease in the compressibility of $\sim$ 9 % between 300 K and 4 K is found which seems quite normal.

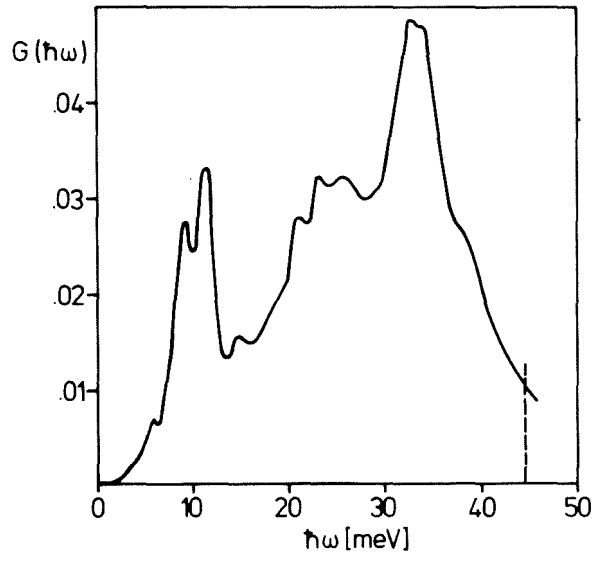


Fig. 1
Generalized phonon density of states G(hω) of $UAl_2$. The cutoff at high energies results from a normalization of the underlying area. Corrections for multi phonon contributions which have not been applied will shift this cutoff value to higher energies.

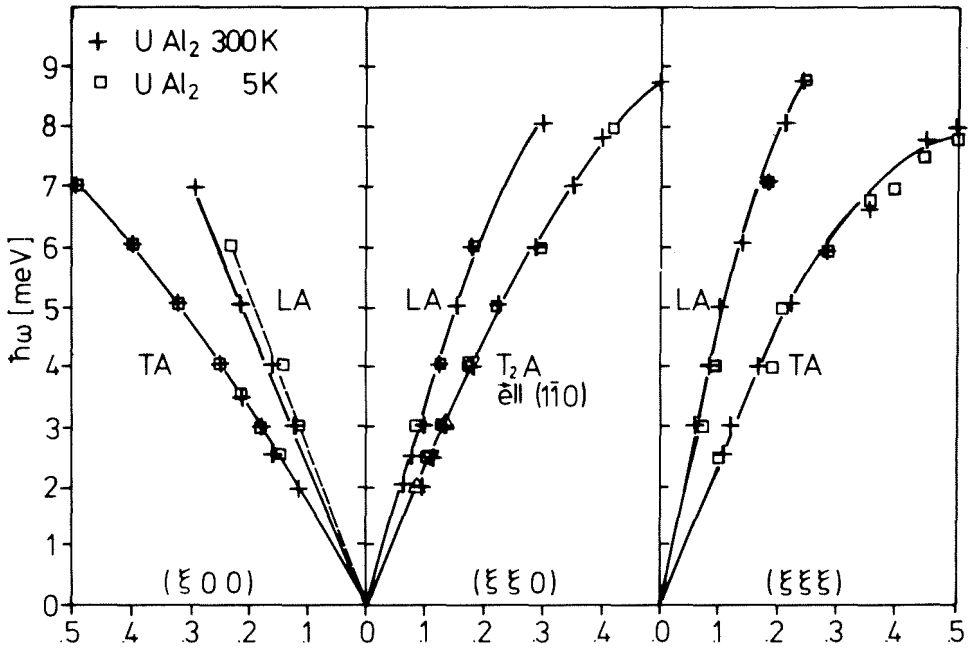


Fig. 2 Acoustic phonon branches along the main symmetry directions for 300 K and 5 K.

References

/1/ J.M. Fournier, Solid State Comm. 29, 111 (1979)

/2/ J.M. Fournier, J. Beille, to be published

## 1.15 Phonon Density of States of $LaAl_2$

*N. Nücker and M. Löwenhaupt*[a]

[a] *KFA Jülich*

Our former measurements of the phonon density of states of $LaAl_2$ at low temperatures /1/ showed frequencies up to 33 meV. Since the acoustical modes are clearly separated from the optical ones, the ratio of the optical to acoustic density can be calculated. In a neutron scattering experiment the constituents of $LaAl_2$ contribute according to their $\sigma/M$ ratios, i.e. 0.067 barn/g for Lanthanum and 0.056 barn/g for Aluminium. Therefore 37 % of the phonon density of states are expected to be acoustic modes associated with the heavier mass of Lanthanum. From low temperature experiment we obtained a considerably higher value of 45 % for optical phonons indicating that some optical modes had not been observed in the previous experiment. A reinvestigation at room temperature with a polycrystalline sample of $LaAl_2$ showed some intensity at about 50 meV. To ensure that this intensity was not due to some hydrogen contamination we repeated the experiment with two single crystals which were spun around two orthogonal axis during the course of the experiment in order to yield the same phonon sampling as a polycrystalline sample. Fig. 1 compares the time-of-flight spectra of both experiments in a logarithmical scale. Obviously both spectra contain intensities around 50 meV. The phonon density of states derived from these spectra is shown in Fig. 2. Now the acoustical part is 36 % of the entire phonon density of states as expected. In the frequency range below 33 meV the distribution agrees rather well with the previous result taken at 20 K indicating that temperature effects are small in $LaAl_2$.

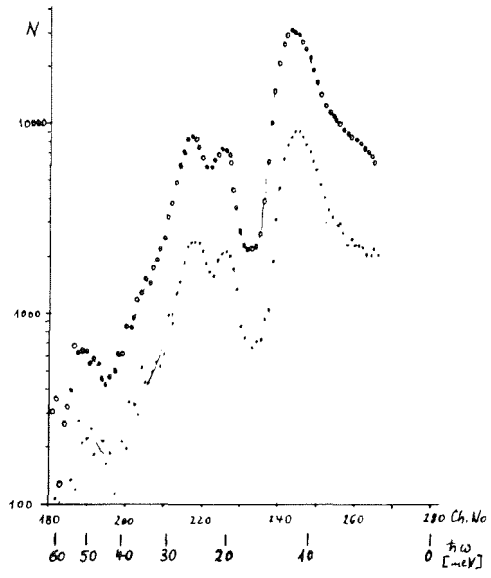


Fig. 1
Time of flight spectrum of $LaAl_2$ ($E_o$ = 27 meV, T = 300 K) polycrystal, single crystal.

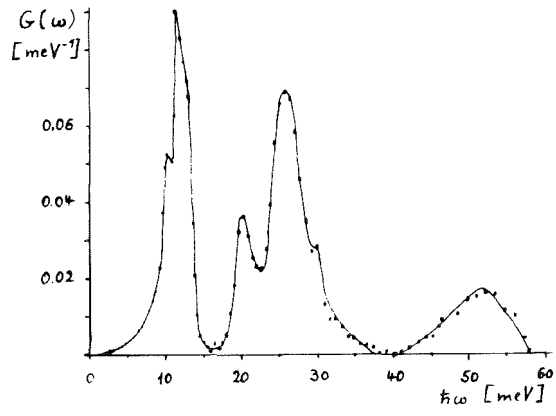


Fig. 2
Phonon density of states of $LaAl_2$

Reference

/1/ K. Knorr and N. Nücker, in Progr. Rep. Teilinst. Nukl. Festkörperphysik, Ges. f. Kernforschung, KFK 2357 (1976)

## 1.16 Comparison of the Lattice Dynamics of $CeSn_3$ and $LaSn_3$

*L. Pintschovius, E. Holland-Moritz[a], D. Wohlleben[a], S. Star[b] and J. Liebertz[b]*

[a] *II. Phys. Inst. der Universtität Köln*

[b] *Inst. f. Krist. der Universität Köln*

Magnetic neutron scattering experiments /1/ revealed that $CeSn_3$ belongs to the class of intermediate valence (IV) compounds: The valence state of the

Ce ions lies somewhat in between that of $Ce^{3+}$ and $Ce^{4+}$. As the ionic radius differs considerably for the different valence states, those phonon modes which lead to a volume change of the IV-ion, are expected to be strongly coupled to the valence fluctuations.

The first observation of anomalies in the phonon dispersion of an IV-system has been reported by Mook et al. /2/ for $Sm_{0.75}Y_{0.25}S$. These authors found a softening and a pronounced broadening of certain phonon modes, especially of the LA branch in the 111-direction. However, the sample was an alloy and therefore it cannot be excluded that the anomalies are to some extent caused by disorder.

$CeSn_3$ is an intermetallic compound which crystallizes in the $Cu_3Au$-structure. $LaSn_3$ has the same structure, but the La ions are in a stable configuration (3+). We therefore used $LaSn_3$ as a reference system. Our samples had a volume of about 2 $cm^3$ and a mosaic spread of less than $0.5^o$. The experiments were carried out on the triple axis spectrometers TAS 1 and TAS 2 at the FR2 Karlsruhe and IN3 at the HFR Grenoble. All measurements were made at room temperature.

We have tried to analyze the data for $CeSn_3$ on the basis of a Born-von-Kármán model. The essential features of the phonon dispersion can be reproduced by a very simple model with 3 parameters only which is a first hint that the lattice dynamics of this compound is not much affected by the valence fluctuations. At the moment we do not know how many parameters are needed to get a quantitative agreement between calculation and experiment. For the best fit so far obtained forces up to fourth nearest neighbors have been included (see Fig.1).

We feel that the best way to estimate the influence of the valence fluctuations on the phonon dispersion of $CeSn_3$ is a comparison with the phonon dispersion of $LaSn_3$. The present data indicate that the lattice dynamics of both compounds is nearly identical (see Fig. 2) so that the effect of the valence fluctuations has to be small.

In order to examine whether the valence fluctuations lead to a line broadening the acoustic branches were investigated with high resolution. In most cases the observed linewidth did not exceed the instrumental linewidth as calculated from a resolution program. In the other cases a similar difference between the experimental and the calculated linewidth was observed for $LaSn_3$ too. We presume that these differences are at least partly due to the neglect of the vertical collimation in calculating the linewidth. Anyhow a possible line broadining is at least one order of magnitude smaller ($\Delta\omega/\omega < 5$ %) than that found in $Sm_{.75}Y_{.25}S$ and is therefore in the range of the broadening due to the normal electron phonon coupling.

Meanwhile we became aware of an independent investigation of the phonon dispersion of $CeSn_3$ by Stassis et al. /3/. Their preliminary results published for the <100>-direction differ in some details from ours. However, both investigations arrive at the conclusion that the influence of the valence fluctuations is not obvious.

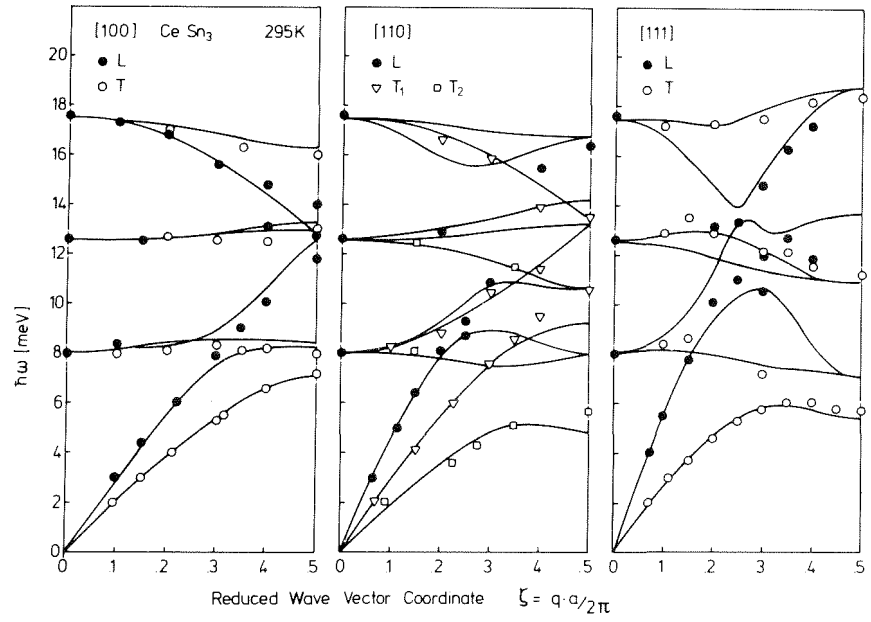


Fig. 1 Phonon dispersion of $CeSn_3$ at room temperature. Lines are a result of a fit based on a 14 parameter Born-von-Kármán model.

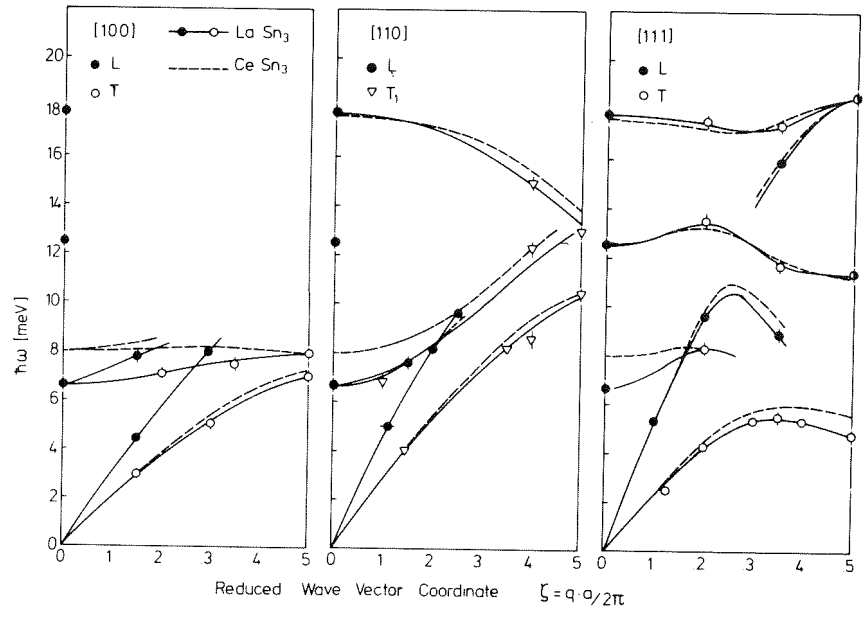


Fig. 2 Phonon dispersion of $LaSn_3$. Full lines are a guide to the eye. Dashed lines represent the data for $CeSn_3$.

References

/1/ E. Holland-Moritz, Thesis, Köln 1978

/2/ H.A. Mook, R.M. Nicklow, T. Penney, F. Holtzberg and M.W. Shafer, preprint

/3/ C. Stassis, C.K. Loong and R.M. Nicklow, in Progr. Rep. O.R.N.L.-5486, Solid State Division, April 1979, p.166

## 1.17 Investigations of the Polymeric Metal $(SN)_x$

*L. Pintschovius and R. Pynn*[a]

[a] *Institut Laue-Langevin, F-38042 Grenoble, France*

In the last year two papers have been published, a review article and a contributed paper to the Proceedings of the Conference on Low Dimensional Conductors in Dubrovnik. The titles and abstracts of these publications are as following:

Polysulfur Nitride, $(SN)_x$, the First Example of a Polymeric Metal

*L. Pintschovius*

Coll. and Polymer Science 256, 883 (1978)

Abstract

Polymeric sulfur nitride, $(SN)_x$ is an unusual substance, which although composed of non-metallic elements exhibits metallic properties and even becomes superconducting at very low temperatures (0.3 K). The bonds between the polymeric chains are much weaker than within the chains. Therefore all electrical and mechanical properties are highly anisotropic. The preparation and crystal structure is described and a review is given of the physical investigations, especially of the electrical and optical properties and of the lattice dynamics. Parallels are drawn to the properties of organic polymers.

Kohn Anomalies in the Phonon Dispersion of Polysulfur Nitride, $(SN)_x$

*L. Pintschovius and R. Pynn*

In Quasi One-Dimensional Conductors, Lecture Notes in Physics, Proc. Int. Conf. Dubrovnik 1978, S. Barisic et al. (ed.), Springer-Verlag, Berlin 1979, p. 421

Abstract

The phonon dispersion of $(SN)_x$ has been investigated by inelastic neutron scattering. The longitudinal acoustic branch in the chain direction has been examined with particular care to see whether it exhibits a Kohn anomaly. Two small dips have been found at $q = 0.14 \cdot 2\pi/b$ and $q = 0.25 \cdot 2\pi/b$. These values agree well with the predictions of a band structure calculation performed by Rudge and Grant. No significant change of the dips has been observed on cooling to 80 K. This indicates that their size is limited by the curvature of the Fermi surface and not by its thermal smearing-out.

## 1.18 Phonon Dispersion of Brominated Polysulfur Nitride, $(SNBr_{.35})_x$

*L. Pintschovius and M. Kobbelt*

Recently it has been found /1/ that the physical properties of $(SN)_x$ can be considerably modified by reaction with halogens, i.e. $Br_2$, $I_2$ and $AsF_5$. So far the product resulting from a reaction with bromine has been investigated most thoroughly. The chemical formula can be written as $(SN\ Br_y)_x$ with $y \sim 0.4$. The color of this substance is dark blue instead of gold for the pristine material and the conductivity in the chain direction is about ten times as high, i.e. $\sigma_{\parallel} \sim 2 \cdot 10^4\ \Omega^{-1}cm^{-1}$/2/. Both facts clearly indicate that the electronic properties have substantially changed upon bromination. However, it is still a matter of controversy if the bromine atoms enter into the $(SN)_x$ lattice or if they sit only in the interfiber regions. An investigation of the lattice dynamics should give further information on how tight the bromine atoms are linked to the $(SN)_x$

lattice and on how far the bonding forces are changed.

Measurements of low frequency phonons in $(SNBr_{.35})_x$ at room temperature were performed on the triple -axis- spectrometer TAS 1 at the FR2 Karlsruhe. The volume of our crystal was very large as compared to others grown by the current techniques, e.g. 0,08 $cm^3$, but this is still fairly small for inelastic neutron scattering. The sample was encapsuled in a quartz container which was pumped to $10^{-2}$Torr, filled with gaseous bromine and then pumped again. From the increase in weight we deduce the formula of our sample to be $(SNBr_{.35})_x$. Upon bromination the mosaic spread parallel and perpendicular to the chain direction increased from $1.3^o$ to $2^o$ and $6^o$ to $10^o$, respectively.

In accordance with the results of Street et al. /2/, but in contrast to the findings of other authors /1/ /3/, the unit cell parameters did not change noticeably upon bromination. From the increase in the linewidth of the $\bar{1}02$-reflection we deduce a decrease of the fiber diameter to about 20 Å, again in accordance with ref. /2/.

As can be seen from Fig. 1, the dispersion curves of brominated $(SN)_x$ agree in most cases within experimental uncertainties with those of the pristine $(SN)_x$. This supports the picture that at least most of the bromine atoms are not incorporated into the $(SN)_x$ lattice. Both the intrachain and the interchain forces seem to be scarcely modified. Merely the small softening of the LA branch in the $\bar{1}02$-direction by about 10 % indicates a certain decrease of the interchain forces between the $\bar{1}02$-layers. This fits to the findings of optical investigations which revealed that the electronic properties of brominated $(SN)_x$ are more anisotropic than those of the original material.

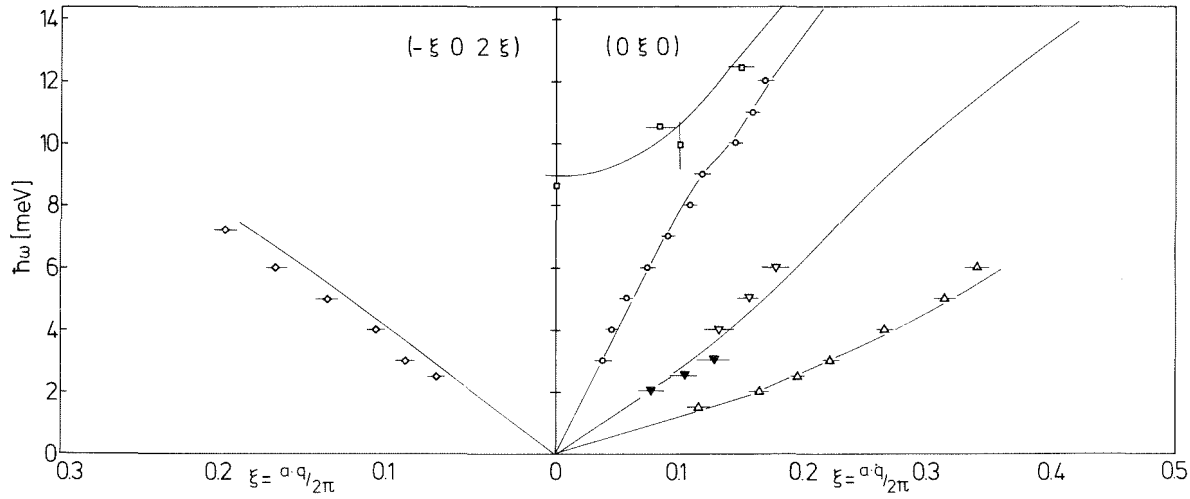


Fig. 1 Dispersion of low frequency phonons of $(SNBr_{.35})_x$ in the chain direction (right) and in one direction perpendicular to the chains (left) at room temperature. Full lines represent the dispersion curves of unbrominated $(SN)_x$. Different symbols refer to measurements in different Brillouin zones.

References

/1/ C.A. Bernard, A. Herold, M. Lelaurian and G. Robert, C.R. Acad. Sc. Paris, C 283, 625 (1976)

/2/ W.D. Gill, W. Bludau, R.H. Geiss, P.M. Grant, R.L. Greene, J.S. Mayerle and G.B. Street, Phys. Rev. Lett. 38, 1305 (1977)

/3/ L. Iqbal, R.M. Baughman, J. Kleppinger and A.G. MacDiarmid, in Synthes. and prop. of low-dimens. mat., Annals of the New York Acad. of Sciences; New York 1977, p. 775

## 1.19 Inelastic Neutron Scattering on $YCo_3H_3$

*R. Feile[a], N. Nücker, K.H.J. Buschow[b]*

[a] *Institut für Physik der Universität Mainz*

[b] *Philips Research Laboratories Eindhoven*

$YCo_3H_3$ appears to be a good system for hydrogen storage applications. As can be seen from Fig. 1 the hydrogen saturation pressure reaches a plateau at about x=2. It is reasonable to assume that in the range from x=2 to x=3.4 equivalent interstitial sites are being filled. Because of the relative high pressure at this plateau the binding energy of the hydrogen must be small. The strong dependence of the plateau on the temperature can be used to store and recuperate hydrogen in the system. The small hysteresis between the population and the depopulation process is an indication for a very fast H-diffusion.

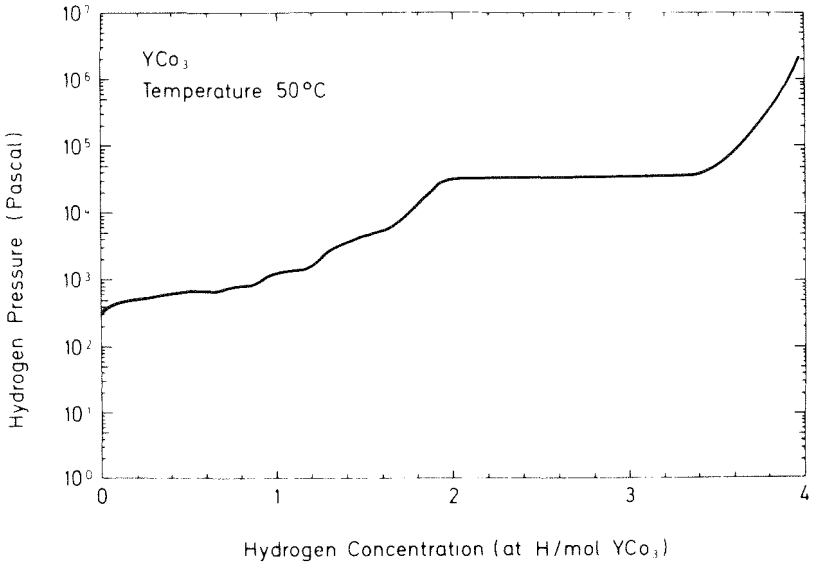


Fig. 1
Hydrogen saturation pressure of $YCo_3H_x$

In order to get a first view of the microscopic properties of this system neutron inelastic scattering experiments were performed at the TOF 3-spectrometer at the FR2 Karlsruhe on a sample with x=3. The incident neutron energy was 26.85 meV. Fig. 2 shows the time of flight spectrum which was corrected for background scattering.

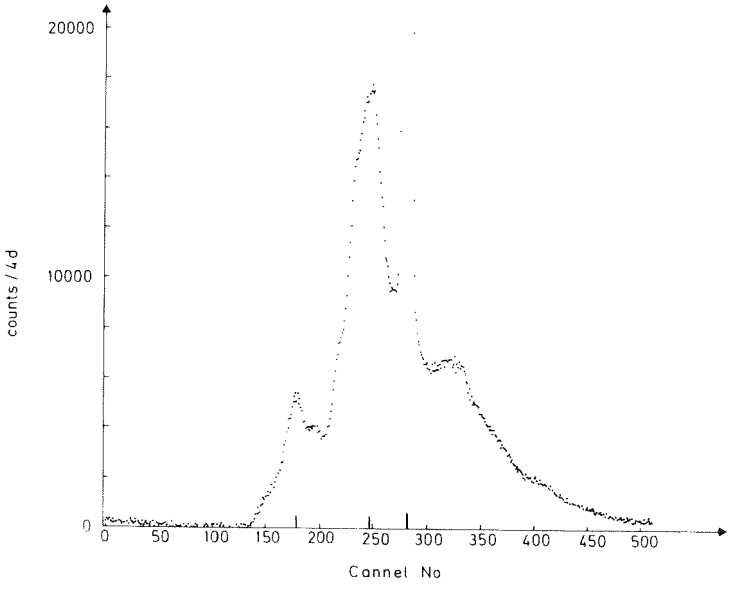


Fig. 2 Time of flight spectrum of $YCo_3H_3$

The elastic line is to be seen at channel 280. On the energy gain side of the spectrum two pronounced peaks are found. The peak centered at channel 248 corresponds to an energy of about 10 meV and is thought to be due to the vibration of the host lattice. The second peak at channel 179 is assigned to localized vibrations of the hydrogen in the interstitials. The corresponding energy of about 65 meV is low in comparison to other metals with dissolved hydrogen. /1/ /2/ Probably this fact is related to shallow potential wells of the interstitials which in turn may lead to the relative high hydrogen saturation pressure. More detailed investigations including a study of the diffusion from quasielastic neutron scattering are under way.

References

/1/ M.A. Saad, Atomkernenergie 14. Jg. H. 6 (1969)

/2/ T. Springer in Hydrogen in Metals I, ed. G. Alefeld, J. Völkl (1978)

## 1.20 Stress-Induced Changes in the Phonon Spectrum of Silicon

*J. Estel[a], J. Kalus[a] and L. Pintschovius*

[a] *Universität Bayreuth*

Our investigations of the effect of uniaxial pressure on the phonon dispersion of silicon /1,2/ have been continued by measurements of the energy shifts in the TA-branch in the ⟨111⟩-direction. The experiments were performed on the triple-axis-spectrometer TAS1 at the FR2 Karlsruhe. The results are plotted in Fig. 1. They are very similar to those obtained for the TA-branch in the <100>-direction /1/.

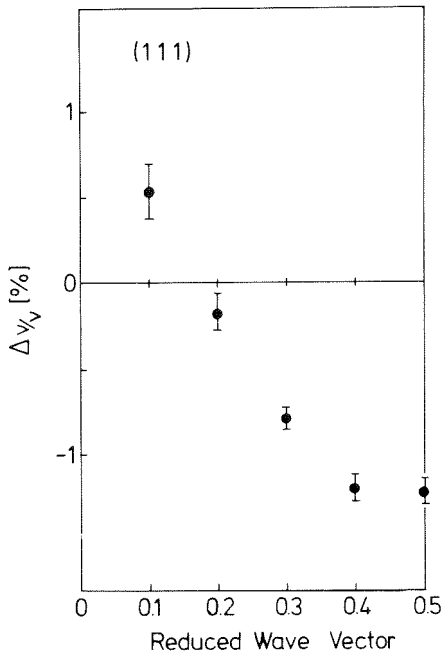


Fig. 1
Frequency shifts $(\nu(p)-\nu(0))/\nu(o)$ caused by uniaxial pressure of p = 10.2 kbar in the <111>-direction for TA phonons propagating in the direction of the stress.

References

/1/ J. Prechtel, J. Kalus, E. Lüscher, L. Pintschovius and R. Gosh, Phys. Stat. sol., in press.

/2/ J. Estel, J. Kalus, R. Scherm and L. Pintschovius, in Progr. Rep. Teilinst. Nukl. Festkörperphysik, Ges. f. Kernforschung, KFK 2670, 24 (1978).

## 1.21 Lattice Vibrations in Amorphous Boron

*F. Gompf and N. Nücker*

All of the various crystalline modifications of elemental boron are built up from icosahedral subunits which contain twelve boron atoms /1/. Lattice dynamical studies of rhombohedral α-B and β-B by Weber et al. /2/ have shown that the bonding can be divided into intra- and intericosahedral contributions. A comparison of the amorphous and β-rhombohedral Raman spectra of boron by Lannin /3/ yields similarities in peak frequencies that are consistent with similar short range order in both materials. This seems to indicate that the B-12 icosahedron also manifests itself in the amorphous state.

To extend these findings and also to help clarify the type of binding between such units in the amorphous state we performed an inelastic neutron scattering experiment on a 98 % $B^{11}$ enriched powder sample. (The $B^{10}$-isotope has an extreme high neutron absorption cross section.) The experiment was carried out at room temperature with TOF III (a multidetector time-of-flight spectrometer) using an incident neutron energy of 27 meV.

The phonon density of states deduced from these scattering data is shown in Fig. 1a. To interprete the different vibration maxima we also show the calculated one-phonon density of states of β-B from Weber et al /2/ (solid line in Fig. 1b) and the experimental results by Richter et al. /4/ (dashed line) which were obtained from first order Raman scattering.

We compare our results with Weber et al /2/ who divide the phonons in crystalline boron into three groups:

(i) The inter-icosahedral modes: These are frequencies higher than 120meV where atoms of neighbouring icosahedra vibrate against each other. For β-B there are two such modes, one at 135 meV and another around 155 meV. As can be seen from Fig. 1a we find intensity contributions from intericosahedral-like modes above 120 meV. If this hump is caused by frequencies centered around 135 and 155 meV as registered in the Raman data cannot be decided from this measurement.

(ii) The intra-icosahedral modes: Their frequencies should extend from about 68 to 112 meV which we also find for the amorphous modification.

(iii) The librational modes due to the rotation of the whole icosahedron: In Weber's model they have low frequencies in the range of 20 to 30 meV. We don't find a peak in this energy region. But we find for amorphous boron, as well as Richter in his spectrum of β-boron, a peak at 46 meV which could very well be

caused by such librational modes.

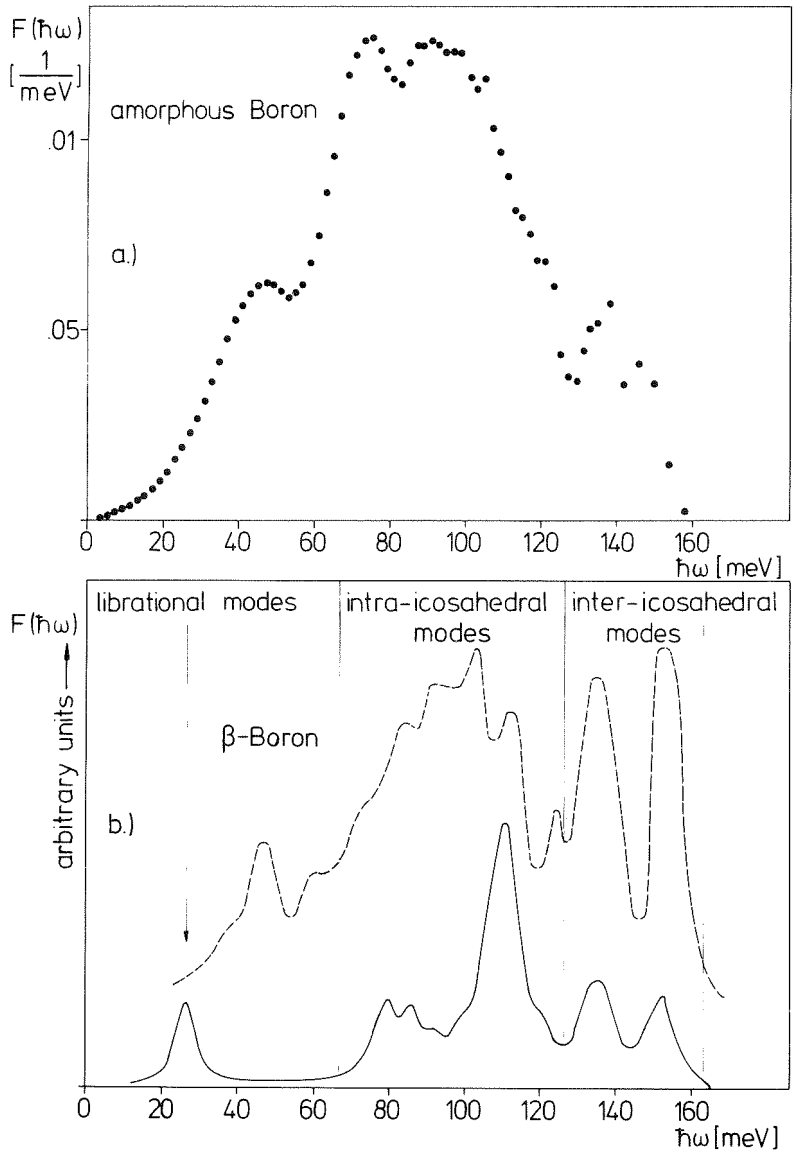


Fig. 1 Phonon density of states for a) amorphous boron, b) β-rhombohedral boron (lattice dynamical model calculation by Weber et al. /2/ - solid line and first order Raman scattering by Richter et al. /4/ - dashed line).

The similarities between the spectra of β-B and its amorphous modification strongly suggest that a tightly linked network of icosahedral units is also present in the amorphous phase.

References

/1/ Boron and Refractory Borides (Edited by V.J. Matkovich) New York (1977).

/2/ W. Weber and M.F. Thorpe, J. Phys. Chem. Solids 36, 967 (1975)

/3/ J.S. Lannin, Solid State Commun. 25, 363 (1978)

/4/ W. Richter, A. Hansen and H. Binnenbruch, phys. stat. sol (b) 60, 461 (1973)

## 1.22 Phonon Spectra of Amorphous Red and Orthorhombic Black Phosphorus.

*F. Gompf and J. Lannin*[a]

[a] *Pennsylvania State Univ., Dep. of Phys., U.S.A.*

The structure of semiconducting black phosphorus is orthorhombic with lattice parameters of a = 4,3763Å, b = 10,4780Å and c = 3,3136Å with eight atoms per unit cell. Orthorhombic black P (o-black P) has a typical layer structure with a large ratio of next neighbour interlayer to intralayer distances of 1.61. This suggests a pronounced two dimensional (2d) character of this compound.

The semiconducting amorphous red phosphorus (a-red P) has only been poorly studied. Raman scattering and infrared absorption experiments of /1/ show that its structure is not build up from simple structural units. Ref /1/ suggested that there exists a more local layer-like atomic arrangement. Thus a-red P should correspond more nearly to a locally quasi-2d amorphous solid.

To help clarify some of these interesting properties of both P modifications we have performed inelastic neutron scattering experiments at TOFII, a multi detector time-of-flight spectrometer with an incident neutron energy of 5 meV. The phonon densities of states $F(h\omega)$ for both modifications were deduced from the scattering data and partially corrected for resolution of the spectrometer.

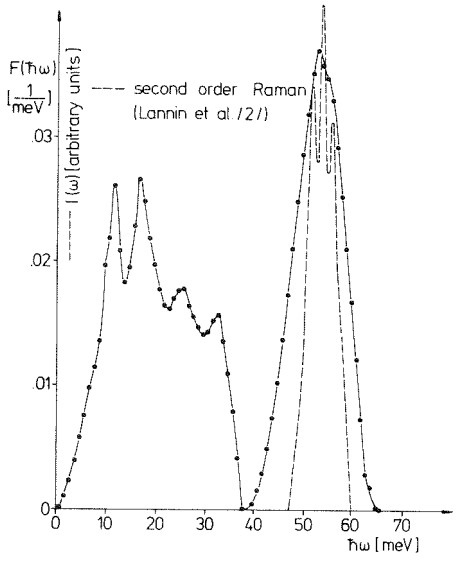


Fig. 1
Phonon density of states of orthorhombic black phosphorus.

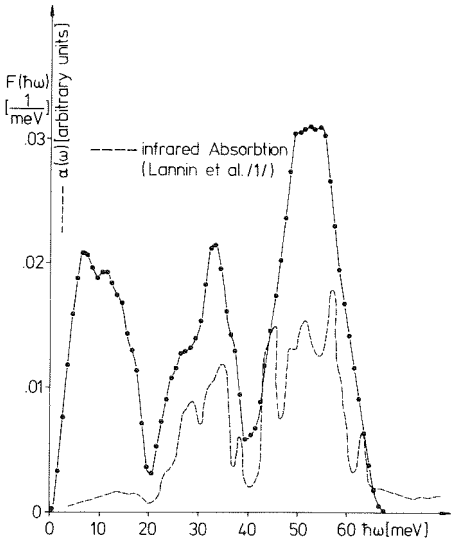


Fig. 2
Phonon density of states of amorphous red phosphorus.

Fig. 1 shows F(ħω) for o-black P. The very structured spectrum can be divided into two parts:

(i) A lower part with four sharp peaks at 10.5, 16.5, 25.5 and 32.5 meV which together make up about 50 % of the modes in F(ħω).

(ii) A higher part which is separated by a gap at around 39 meV. For this energy range the resolution of our spectrometer is rather poor so that any possible structure could not be detected. The broken line in Fig. 1 shows the second order Raman spectrum of o-black P from /2/ at 300K. It coincides nicely with the position of our higher optical modes and reveals a detailed structure. The difference in width, however, cannot be explained by difference in resolution. Unfortunately in this measurement the lower part of the spectrum could not be detected.

Fig. 2 shows the phonon density of states of a-red P. The spectrum may be divided into three parts which are separated by gaps at 20.5 meV and 40.5meV:

(i) About one quarter of the modes of F(ħω) make up the low frequency part of the spectrum. It has two peaks at 7 and 11.5 meV and shows a pronounced shift towards smaller frequencies in comparison to o-black P. This shift seems to be responsible for the gap at 20.5 meV.

(ii) A second quarter of modes in F(ħω) is given by the middle part of the spectrum with a shoulder at 26 meV and a peak at 33 meV. There are corre-

sponding peaks in the o-black P modification.

(iii) The high optical modes are separated by a gap at 40.5 meV and contribute about 50 % of the modes in $F(\hbar\omega)$. Both gap and peak are practically identical with the ones found in o-black P.

The broken line in Fig. 2 gives the infrared absorption, $\alpha(\omega)$ from Ref. /2/ for a-red P. The gap at 20.5 meV, the maxima in the middle part of the spectrum and the center of the high frequency band correspond well to the neutron data. Again the resolution for the high optical modes is not good enough to show details while the low lying part of the spectrum cannot be detected by infrared absorption.

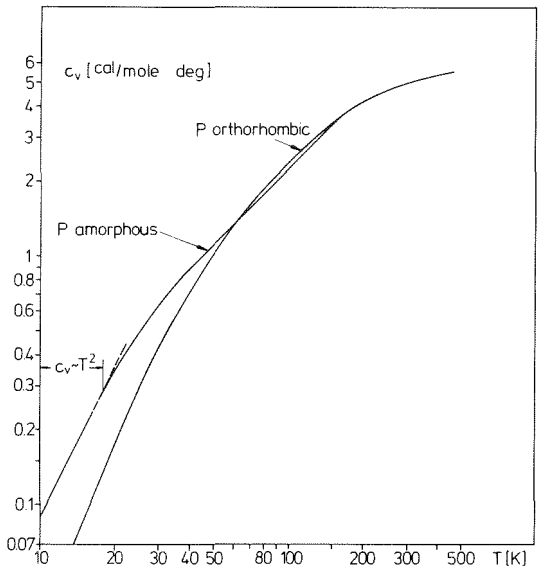


Fig. 3
Lattice specific heat for orthorhombic black and amorphous red phosphorus as deduced from their phonon densities of states.

From the phonon densities of states we calculated the lattice specific heat $c_v$ which is shown in a log $c_v$ versus T plot in Fig. 3. Similar to some other layer lattice structures a-red P shows a region where $c_v \sim T^2$ holds which is a sign for the 2d behaviour of this substance and nicely confirms the assumptions of Ref. /2/.

References

/1/ J.S. Lannin and B.V. Shanabrook, Solid State Commun. 28 (1978) 497.

/2/ J.S. Lannin and B.V. Shanabrook, 14th Intern. Conf. Phys. of Semiconductors, Edingburgh (1978)

## 1.23 Inelastic Neutron Scattering by a Very Low Energy Librational $A_2$ Mode in $K_2SnCl_6$

*K. Vogt[a], W. Reichardt, W. Prandl[a]*

[a]*Institut für Kristallographie der Universität Tübingen, D-7400 Tübingen*

$K_2SnCl_6$ crystallizes at high temperatures in the cubic space group Fm3m. Its crystal structure (Fig. 1) is closely related to the perovskite structure: starting from Fig. 1 one can obtain the perovskite structure by filling the empty spaces between $[MX_6]$-octahedra along the crystallographic axes a, b, and c with additional M atoms. In this process, of course, the compensation of charges has to be taken into account properly.

A system of strong intensity and fairly narrow diffuse streaks along $a^*$, $b^*$ and $c^*$ was observed on X-ray photographs /1/. An analysis of the phonon eigenvectors /1/ showed that the streaks arise from $A_2$ librational modes of the $[SnCl_6]$-octahedra with wave vectors q along the Δ path (between the Γ(000) and the X(100) point of the Brillouin zone). On cooling, $K_2SnCl_6$ undergoes at least two phase transitions /1/ /2/: at 261 K an orthorhombic phase is formed with superstructure reflections at the X point. At 255 K another transition takes the crystal into a monoclinic phase.

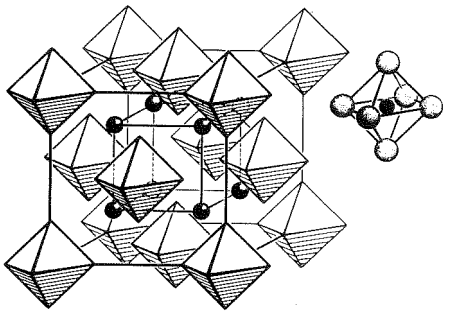

Fig. 1
The $A_2$ $MX_6$ structure
(A = K; M = Sn)

The neutron inelastic measurements are intended to provide some information about the relation between the librational mode and the lattice instabilities. All measurements, we report about here, were made at room temperature in the cubic phase.

The elastic constants of these fairly soft crystals were determined from the slopes of the TA<100>, TA<110>, LA<100>, and LA<110> branches. The results are:

$$c_{11} = 2.10 \times 10^{11} \text{ dyn/cm}^2$$
$$c_{12} = 1.21 \times 10^{11} \text{ dyn/cm}^2$$
$$c_{44} = 0.78 \times 10^{11} \text{ dyn/cm}^2.$$

Haussühl determined the $c_{ij}$ from ultrasonic measurements: there is good agreement between the two methods /3/.

The small variation of the X-ray intensity along the diffuse streaks is an indication that the scattering is due to <001> planes which are nearly uncorrelated among each other. The rapid decrease of intensity in a direction perpendicular to the streaks will give information about the coupling within the planes. We therefore have done two sets of measurements: one with the 5k3-streak in the scattering plane (Fig. 2), the second one with the 53l-streak perpendicular to the scattering plane (Fig. 3). From Fig. 2 it is clear, that

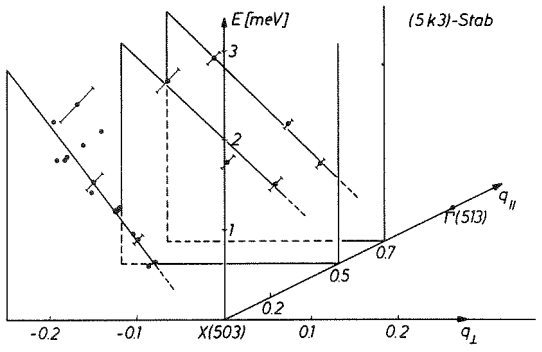


Fig. 2
Dispersion surface within the vicinity of the diffuse streak (5k3) lying in the scattering plane.

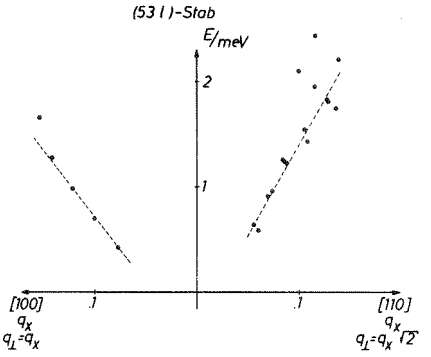


Fig. 3
The diffuse streak (53l) is ⊥ to the scattering plane. Energy of the librational mode E(q) with $q_{\perp}$ to the streak.

the dispersion surface, for $q_{\parallel}$ between Γ and X, has indeed the form of a trough with a V-shaped cross section. For $q_{\perp}$=0, i.e. right in the center of the streak, we observe a single peak at E = 0 in constant-Q-scans: this means that the energy gap is less than the instrumental resolution (0.6 meV). From constant-E-scans along Γ-X (with E = 0), on the other hand, we conclude that E > 0: there is a smooth intensity maximum at the X-point which can only be explained by a decrease of the (positive) mode energy at this point, since the inelastic structure factor is constant along Γ-X.

With the second set of measurements (Fig. 3) we tried to find out whether there is an anisotropy in $E(q_{\perp})$: there is a fourfold axis of symmetry parallel to Γ-X. Thus the directions $q_{\perp}$ ||<100> and $q_{\perp}$ ||<110> are not symmetrically equivalent. We find that $E(q_{\perp})$ is isotropic around the streak as long as E is linear in $q_{\perp}$. There is, however, anisotropy at higher energies: with $q_{\perp}$ ||<110> the mode merges

into a TA<110> branch. With q ||<100> , however, we cannot trace the mode to beyond $|q_{100}| = 0.25$.

The results in Figs. 2 and 3 have been corrected for resolution effects. At $q_{\parallel} = 0.5$ and 0.7 the energy extrapolates to $E \simeq 0$ for $q_{\perp} = 0$. At the X-point, however, E seems to extrapolate towards $E(q_{\perp} = 0) < 0$.

A fairly simple model may be used to interprete the observed E(q). Rigid octahedra are assumed which may, for a given <001> layer, only librate around the <001> axis. Assume torsional springs of strength D between the four nearest neighbours within one layer, and a local anisotropy for every individual octahedron represented by a torsional spring E. In addition there is a coupling (with strength F) between the reference octahedron and the 8 next nearest octahedra in the layers at $z = \pm \left[00\frac{1}{2}\right]$.

We then obtain

$$\hbar^2\omega^2(q_x q_y q_z) = \frac{4D}{\Theta}\left\{1 - \frac{1}{2}\left[\cos\frac{q_x+q_y}{2} + \cos\frac{q_x-q_y}{2}\right] + \frac{E}{4D} + \frac{F}{D}\left[\cos\frac{q_x}{2} + \cos\frac{q_y}{2}\right]\cdot\cos\frac{q_z}{2}\right\}$$

where $\Theta$ is the moment of inertia. This relation allows a good description of the experimental data including the variation of E along the center of the streak. Both from our experimental results and from this model the softening of the librational $A_2$ mode at the X-point is assumed to be the reason for the lattice instability.

This work was supported by the Federal Minister of Research (BMFT project Nr. 03 - 41 A 03 P / 03 - 45 A 03 I).

References

/1/ H. Boysen, J. Ihringer, W. Prandl, W. Yelon, Sol. State Commun. 20, (1976) 1019; J. Ihringer (1979), Acta Cryst., im Druck

/2/ W. Kugler, Diplomarbeit, Tübingen 1978

/3/ S. Haussühl, private communication

1.24 Hydrogen Bonds in Schlippe's Salt: Refinement of the Crystal Structures of $Na_3SbS_4 \cdot 9H_2O$ by X-ray Diffraction and $Na_3SbS_4 \cdot 9D_2O$ by Neutron Diffraction at Room Temperature

*K. Mereiter[a], A. Preisinger[a] and H. Guth*

[a]*Institut für Mineralogie, Kristallographie und Strukturchemie, Technische Universität Wien, A-1060 Wien, Austria*

Abstract

The room-temperature crystal structure of Schlippe's salt, space group $P2_13$, $Z = 4$, has been refined for $Na_3SbS_4 \cdot 9H_2O$, $a = 11.957(3)$ Å, from X-ray data to $R_F = 0.022$, and for $Na_3SbS_4 \cdot 9D_2O$, $a = 11.959(3)$ Å, from neutron data to $R_F = 0.058$. X-ray and neutron results are in good agreement. Within experimental error, no structural isotope effect between the H and D compounds is observed. Finite groups of distorted, face-sharing Na coordination octahedra, $[(H_2O)_3Na(H_2O)_3Na(H_2O)_3NaS_3]$ (point symmetry 3), and $SbS_4$ tetrahedra (point symmetry 3) share common corners via three of their four S atoms to form a three-dimensional framework. Average bond lengths are Na-O = 2.39, Na-S = 3·00, Sb-S = 2·33 Å. $D_2O$ molecules with D-O = 0·93-0.97 Å and D-O-D = 107-108° form an extensive hydrogen-bond system. Six different bonds are observed: one O-D···O(O···O = 2.81 Å), four approximately linear O-D···S(O···S = 3·29-3.36, D···S = 2.34-2.40 Å); the sixth D atom forms a bifurcated bond with two S atoms [D(6)···S = 2.86 Å]. According to Raman spectra, all D as well as H atoms are involved in hydrogen bonding.

1.25 Hydrogen Bonds in Schlippe's Salt, $Na_3SbS_4 \cdot 9H_2O$ and $Na_3SbS_4 \cdot 9D_2O$: Diffraction and Spectroscopic Studies in the Temperature Range of 75 K to 295 K.

*K. Mereiter[a], A. Preisinger[a], H. Guth, G. Heger, K. Hiebl[b] and W. Mikenda[c]*

[a] *Institut für Mineralogie, Kristallographie und Strukturchemie, Technische Universität Wien, Austria*

[b] *Institut für Physikalische Chemie, Universität Wien, Austria*

[c] *Institut für Organische Chemie, Universität Wien, Austria*

Abstract

The work on the crystal structure of Schlippe's salt, done by X-ray and neutron diffraction studies at room temperature (Mereiter, Preisinger and Guth, 1979; Acta Crystallogr. B35, 19 - 25), has now been supplemented by the neutron diffraction study of $Na_3SbS_4 \cdot 9D_2O$ at 105 K and by Raman and $^1$H-NMR spectroscopic investigations in the temperature range of 75 - 295 K. For $Na_3SbS_4 \cdot 9D_2O$ at 105 K, the space group is $P2_13$, a = 11.878 Å, Z = 4. Least-squares refinement of the neutron data converged to R(F) = 0.043 for 857 observed reflections. Compared with the structure at room temperature, there are minor changes in atomic coordinates; thermal vibrations are strongly reduced at 105 K. Observed bond lengths within the $SbS_4$ tetrahedron and the $D_2O$ molecules are slightly larger at 105 K than at room temperature (bond lengths not corrected for thermal motion); Na-O,S and hydrogen bonds decrease in length. Average bond lengths at 105 K are Sb-S= 2.333, Na-O=2.377, O-D=0.963 Å. $^1$H-NMR spectra show the usual doublet pattern of water molecules with an average intramolecular H-H distance of 1.546 Å at 90 K. At low temperatures an additional intermolecular spin-spin coupling could be observed. Raman spectra of both the H and the D compounds of Schlippe's salt are well resolved at low temperatures. The observed O-H(D) stretching frequencies, $\bar{\nu}$(O-H) = 3309 - 3422, $\bar{\nu}$(O-D) = 2448 - 2550 $cm^{-1}$, show that all hydrogen bonds of Schlippe's salt - one O-H(D)...O, four approximately linear O-H(D)...S and one fairly symmetric bifurcated O-H(D)...S,S bond - are nearly equal in strength.

## 1.26 Investigation by Neutron Diffraction of Phase Transitions in Stressed Austenitic CrNi Steel

*Volkhard Jung*

For the knowledge of the material behavior under stress it is of interest, to investigate the process of phase transformation in stressed austenitic CrNi steel samples. This material is taken for reactor tanks.

The disadvantage of the X-ray diffraction method lies in the fact that only a very thin layer of material (6...23 µm) can be analysed. Depending on the penetration depth different fractions will result of the three phase components, i.e. fcc, hcp and bcc, respectively, as can be seen from the results of measurements at CrNi steel samples /1/. If the fractions of the different phases in a bulk sample have to be determined, however, it is necessary to abandon X-ray diffraction in favor of neutron diffraction. In this case, the phase fractions are averaged over the bulk sample and the content of different phases can be measured in the whole irradiated volume. Samples of austenitic 18/8 % CrNi steel were annealed at 1050°C for half an hour and cooled down very slowly (∿15h). These samples were stretched by 2, 12.5, 25 and 47 percent, respectively.

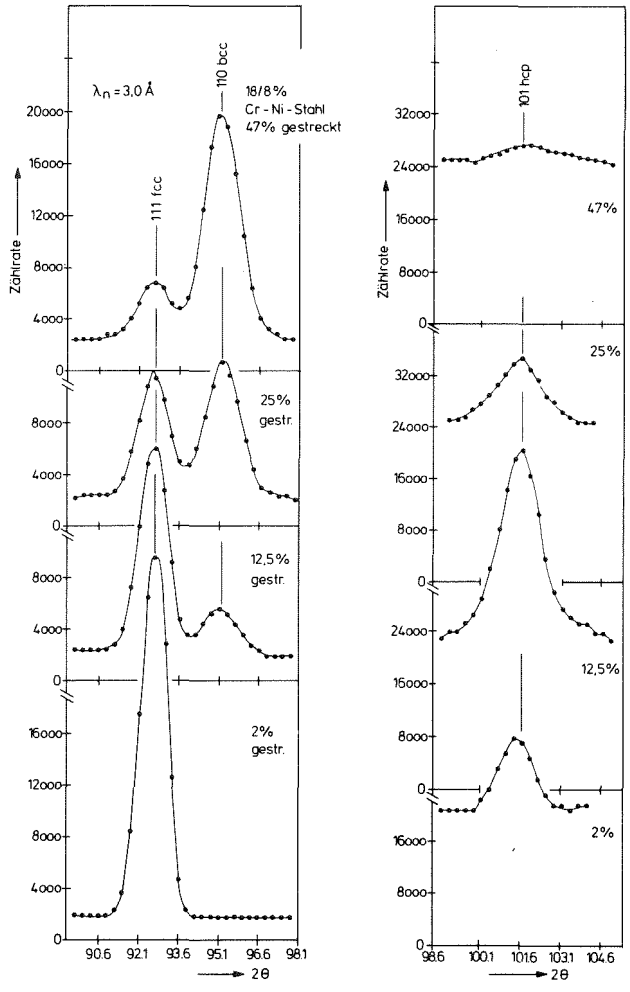


Neutron diffraction spectra were taken for the 111 fcc, 110 bcc and 101 hcp reflections at a wave length of 3.0 Å. As shown in Fig. 1, the hexagonal phase is generated at a low stress value (2 %) without any contribution of the bcc phase. At higher elongation (12.5 %), the hcp phase reaches its maximum and the bcc phase becomes important.

At 25 % elongation, the hcp phase drops to the value of the 2 % elongation, while the fcc and bcc fractions are about equal. At 47 % elongation, the hcp phase has nearly vanished, and the

Fig. 1
Neutron diffraction spectra of the 111 fcc, 110 bcc and 101 hcp reflexes at $\lambda_n$ = 3.0 Å taken from 18/8% CrNi steel samples at different elongation by 2, 12.5, 25 and 47 %, respectively.

ratio of fcc and bcc fractions at 12.5 % elongation is reversed at this highest elongation.

In order to determine the exact values of the phase content it is necessary, as in the X-ray method too, to measure the texture of the different fractions.

The measured intensities of the three reflections, <111> fcc, <110> bcc and <101> hcp, respectively, taken in the plane vertical to the stress-direction have to be corrected by the angular distribution of intensity of reflections taken in a plane of the stress direction. These corrected values result in the phase content (fcc, bcc and hcp) in the total irradiated volume of the samples.

Further measurements were carried out on cold rolled sheets with 18/8 % CrNi and with 18/10.4 % CrNi, 0.5 % Ti/0.5 % Mo (inhibited phase transitions). The preferred orientation of the <111> fcc and the <110> bcc planes is determined.

Reference

/1/ M.W. Bowkett and D.R. Haries:
Martensitic Transformations in Cold Rolled En 58 B (Type 321) Austenitic Stainless Steel, AERE-R-9093, Harwell, April 1978.

# 2. THEORY

## 2.1 Diffusion Mechanism and Structure of α-AgI

*W. Schommers*

In order to obtain information about the microscopic mechanism in superionic conductors, we have to answer the following question: How does a many-particle system with strong anharmonicities behave in a periodical potential? In the case of α-AgI the $Ag^+$ ions represent the many-particle system with strong anharmonicities, whereas the periodical potential is given by a well-defined bcc lattice formed by the $I^-$ ions. The silver subsystem is highly disordered and the silver ions move through the iodine lattice with high mobility. Molecular-dynamics (MD) calculations are important in studying many-particle systems with strong anharmonicities, since anharmonicity is treated without approximations. The essential features of the MD-model used here are discussed in detail in Refs. /1/ - /3/. In this paper we want to discuss two aspects: (i) the structure, and (ii) the diffusion mechanism of the $Ag^+$ subsystem.

The MD calculations were performed at T = 585 K. First, we have neglected the Coulomb interaction. In this case we have a many-particle system consisting of weak disks in a periodical potential. For this model we get the pair correlation function g(r) which is shown in Fig. 1b. The position of the prepeak in g(r) is very close to the repulsion diameter (1.8 Å) of the weak disks. Therefore, the characteristics of the prepeak should be given by the Born-Mayer potential. The long-range oscillatory part in g(r) is due to the interaction of the weak disks with the periodical potential. The weak disks move through the lattice with relative high mobility (see Fig. 2a): The diffusion constant is $17 \cdot 10^{-5}$ $cm^2/sec$. The diffusion constant is given by the slope of the linear part of the mean-square displacement $\langle r^2(t) \rangle$.

With the presence of the Coulomb interaction we observe in g(r) two effects (see Fig. 1a): (i) the prepeak at 1.8 Å disappears. This means that the Coulomb energy keeps the $Ag^+$ ions apart, (ii) the $Ag^+$ subsystem tends to crystallize. Comparison with Fig. 1c shows that the peaks in g(r) of the $Ag^+$ subsystem are strongly correlated to the peaks in g(r) of the iodine lattice; even the details are reflected in the $Ag^+$ subsystem. This quasi-crystallization is accompanied

with a decrease of mobility of the $Ag^+$ ions (see Fig. 2a). The diffusion constant is now $2.86 \cdot 10^{-5}$ $cm^2/sec$. This value is close to that obtained experimentally /4/ ($\sim 2.6 \cdot 10^{-5}$ $cm^2/sec$). The correlation effects due to the Coulomb interaction (tendency to crystallize and decrease of mobility) are also typical features of an electron gas at low density in a solid and are known as Wigner-crystallization.

In order to obtain more information about the diffusion mechanism, we have to consider the microscopic square displacements $r_i^2(t)$, $i = 1, \ldots, N_+$. $N_+$ is the particle number of the $Ag^+$ ions. The results show (typical examples are represented in Fig. 2b) that there occur well-defined jump-diffusion processes. We observe a "local" motion within restricted regions of space. The distances between these regions are approximately given by the maxima of g(r) (see Fig. 1a). Furthermore, it turns out that the flight time $\tau_F$ is shorter than the residence time $\tau_R$ and we obtain: $\tau_R/\tau_F = 3.5 \pm 0.7$. This is in good agreement with the experimentally observed value of $3.0 \pm 0.6$ /5/.

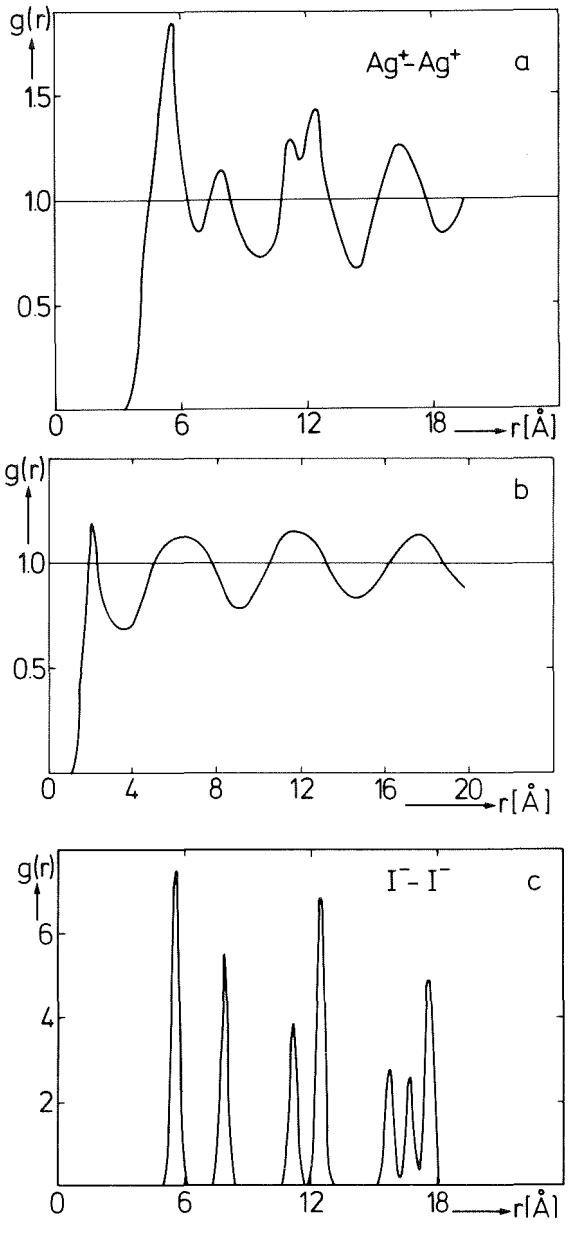


Fig. 1
(a,c) pair correlation function for α-AgI

(b) pair correlation function for weak disks

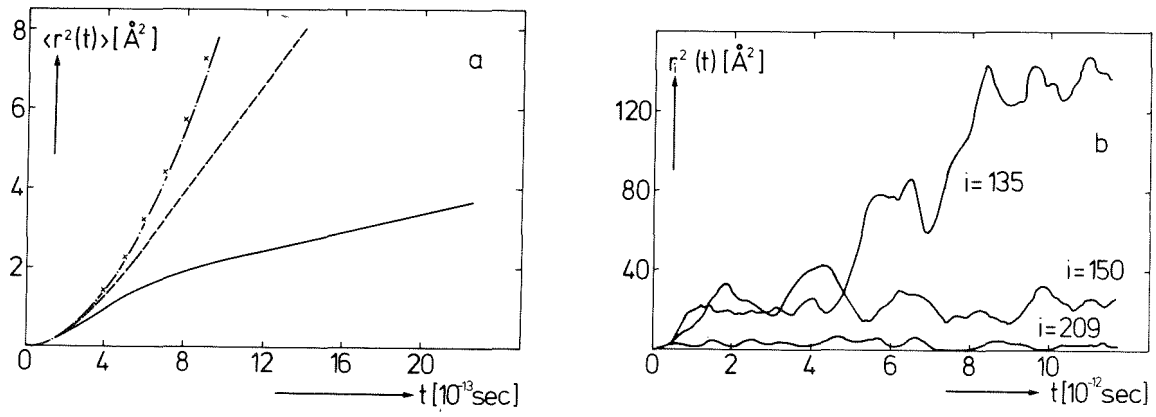


Fig. 2 (a) mean square displacements: ——— α-AgI, ---- weak disks, -·-·- weak disks without the presence of the lattice, xxx perfect gas

(b) microscopic square displacements for the $Ag^+$ ions (typical examples for the ions 135, 150, 209)

References

/1/ W. Schommers, Phys. Rev. Lett. 38, 1536 (1977)

/2/ W. Schommers, Phys. Rev. B 17, 2057 (1978)

/3/ W. Schommers, in press (Proceedings of the International Conference on "Fast Ion Transport in Solids", Fontana, USA)

/4/ A. Kvist and R. Tarneberg, Z. Naturforsch. 25 A, 257 (1978)

/5/ J.B. Boyce et al., Phys. Rev. Lett. 38, 1362 (1977)

## 2.2 Determination of the Pair Potential for Liquid Gallium from the Pair Correlation Function

*W. Schommers*

In a canonical ensemble all thermodynamical functions of a classical homogeneous system are dependent only on the pair correlation function g(r) provided that a pure pair interaction exists. This makes g(r) an essential quantity in statistical physics.

In Ref. /1/ we proposed a method which allows to calculate the pair potential from the experimentally determined g(r) without using any parameters. There

are other theoretical attempts (Born-Green, Percus-Yevick, method by Ailawadi and Naghizadeh /2/) to extract information about the pair potential from the knowledge of g(r). In contrast to the simple metal pseudo-potential theory all these methods are applicable without modifications to transition metals. We started to determine the pair potential for liquid gallium at 305 K by means of these methods using a structure factor which has been measured with high accuracy by Narten /3/.

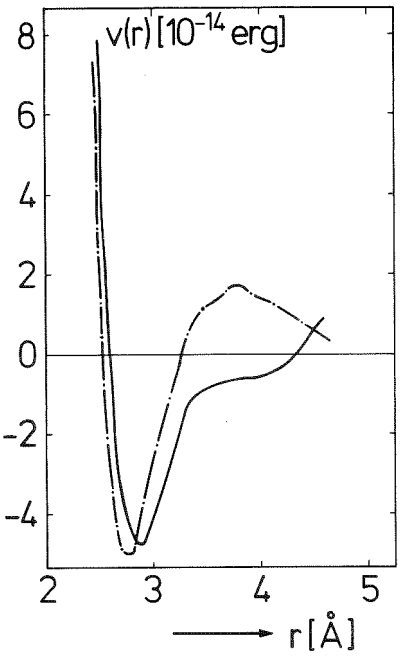


Fig. 1
Pair Potential for Liquid Gallium
-·-·- the first approximation (see Ref. /1/)
——— the final potential (after 12 iterations)

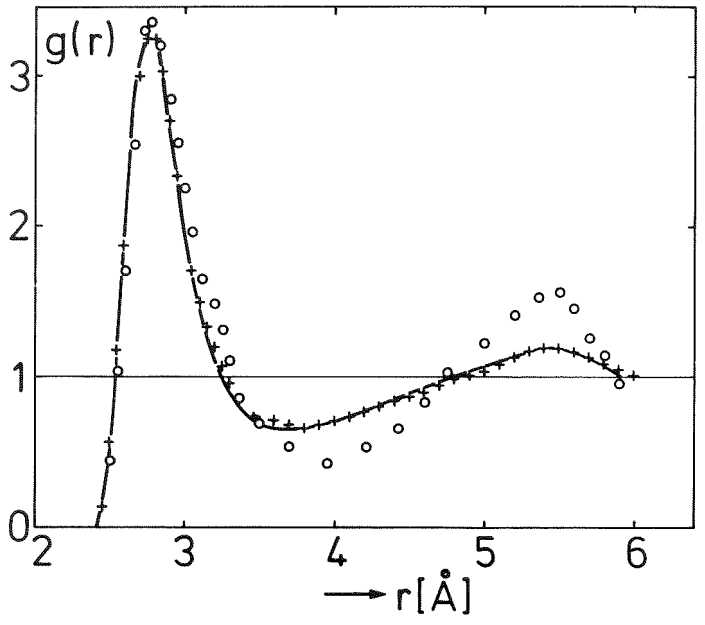


Fig. 2 Pair Correlation Function g(r) for Liquid Ga
xxx experimental /3/
ooo obtained from molecular-dynamics by means of the first approxiamtion (see Fig. 1)
— obtained from molecular-dynamics by means of the final potential (see Fig. 1)

The pair potential v(r) which has been calculated from the method described in Ref. /1/ is shown in Fig. 1. This pair potential yields a g(r) which is shown in Fig. 2. As can be seen the deviations of the calculated from the experimental g(r) are small. The next step is to calculate the pair potential by means of the other methods in order to test their applicability.

References

/1/ W. Schommers, Phys. Lett. A 43, 157 (1973)

/2/ M.K. Ailawadi and J. Naghizadeh, Solid State Commun. 20, 45 (1976)

/3/ A.H. Narten, J. Chem. Phys. 56, 1185 (1972)

## 2.3 Influence of Spin Fluctuations on the Superconducting Transition Temperature in Nb, V, and VN

*H. Rietschel and H. Winter*

Ferromagnetic spin fluctuations ("paramagnons") are known to counteract superconductivity /1/. However, it has commonly been assumed /1/ that for the superconducting transition metals the influence of paramagnons on $T_c$ is negligible.

This assumption is in contrast to our results presented here. For the elements Nb and V and for the compound VN we numerically solved the linearized Eliashberg equations /1/ taking into account both phonons and paramagnons /2/ - /5/.

In Fig. 1, the resulting $T_c$ as a function of the parameters S and $\kappa$ is shown for the three materials. Here, S is the Stoner factor related to the particle-hole t-matrix $t(q,\omega)$ /4/, and $\kappa$ is defined by $\kappa$ = (q-dependent interaction)/(total interaction) at $q = 0$ for the electron-electron interaction entering $t(q,\omega)$. Two values for $\kappa$ have been used: $\kappa = 0$ described an upper limit to the paramagnon effects /3/ while $\kappa = 0.3$ has proved to be appropriate for the description of the paramagnon contribution $\lambda_{spin}$ to the mass enhancement $m^*/m$ in Pd /3/.

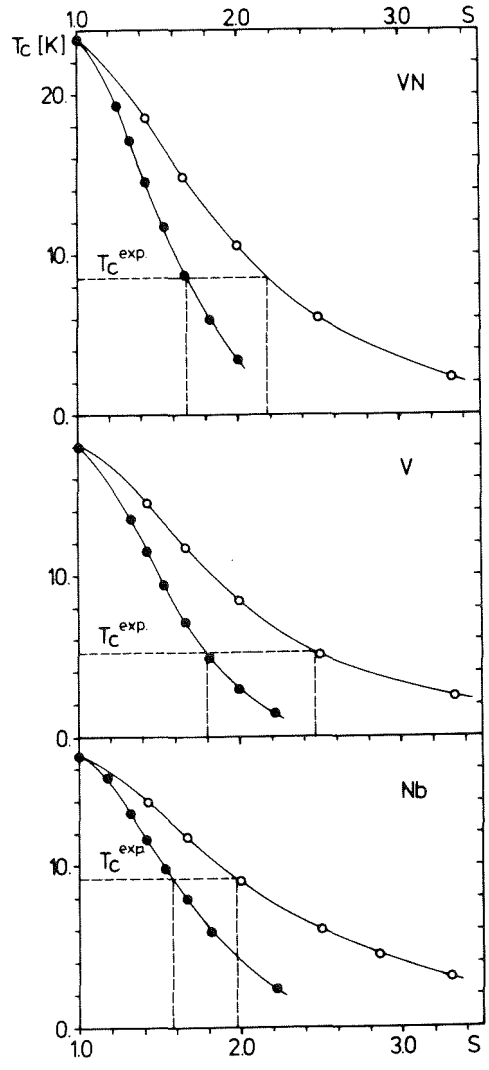


For S = 1 (no paramagnons), $T_c$ is significantly too high for all three superconductors. This observation has been made by other groups, too, but has not yet been related to the omission of spin fluctuations. Equating $T_c(S)$ to the experimental $T_c$ defines for each $\kappa$ a value for S labelled $S_{T_c}(\kappa)$. The ranges for S limited by $S_{T_c}(0)$ and $S_{T_c}(0.3)$ are rather narrow. Nevertheless, the values S=1.72 and S=2.34 for Nb and V, resp., which have been reported in /6/, lie within these ranges, thus demonstrating that already medium Stoner factors $S \sim 2$ may lead to a substantial reduction of $T_c$. For VN, an experimental estimate $S \sim 2.5$ has been reported in /7/ which lies slightly above the S range. For $\lambda_{spin}$ we found $\lambda_{spin} = 0.21$ for Nb, 0.34 for V and 0.27 for VN. These values turned out to be almost independent of $\kappa$.

Fig. 1
$T_c$ as a function of S for $\kappa = 0$ (closed circles) and 0.3 (open circles) in Nb, V, and VN

References

/1/ G. Gladstone, M.A. Jensen and J.R. Schrieffer, in "Superconductivity", Vol. 2, edited by R.D. Parks, Marcel Dekker, Inc., New York (1969)

/2/ N.F. Berk and J.R. Schrieffer, Phys. Rev. Lett. 17, 433 (1966)

/3/ J.R. Schrieffer, J. Appl. Phys. 39, 642 (1968)

/4/ W.H. Butler, H.G. Smith and N. Wakabayashi, Phys. Rev. Lett. 39,1004 (1977)

/5/ H. Rietschel, Z. Physik B30, 271 (1978)

/6/ J.F. Janak, Phys. Rev. B16, 255 (1977)

/7/ F.I. Ajami and R.K. MacCrone, J. Phys. Chem. Solids 36, 7 (1975)

## 2.4 The Eliashberg Function and the Superconducting $T_c$ of Transition Metal Hexaborides

*G. Schell, H. Winter and H. Rietschel*

Among the compounds $MeB_6$ which consist of two simple cubic sublattices formed by the metal atoms and boron octahedra, superconductivity is observed in the systems $LaB_6$ ($T_c$ = .45K) and $YB_6$ ($T_c$ = 7.1K). Because this class of materials can be considered as a model for more complicated structures consisting of clusters of atoms (e.g. the Chevrel phases), it is interesting to calculate the relative contributions of the different phonon modes to the Eliashberg function $\alpha^2F(\omega)$ and to answer the question whether the coupling to a particular vibrational mode is predominantly responsible for superconductivity.

For the calculation of $\alpha^2F(\omega)$ we use the Gyorffy formula /1/:

$$\alpha^2F(\omega) = \sum_{\kappa,\vec{q},s,i} \frac{\eta_s}{6\, M_s\, N} \left|\vec{e}^{\,s,i}_{\vec{q},\kappa}\right|^2 \frac{\delta(\omega-\omega_{\vec{q},\kappa})}{\omega} \qquad (1)$$

where $\vec{q}$, $\kappa$ label the wave vectors and phonon branches, and s, i the type and number of atoms within a unit cell in equivalent positions, N being the number of $\vec{q}$-points in the Brillouin-Zone. The electronic parameters $\eta_s$ are given by the phaseshifts $\delta_l$ and the local densities of states $n_l$:

$$\eta_s = \frac{2\, m\, \varepsilon_F}{\pi^2\, n(\varepsilon_f)\, h^2} \sum_l 2(l+1)\, \sin^2(\delta_l-\delta_{l+1}) \frac{n_l^s\, n_{l+1}^s}{n_l^{(o)s}\, n_{l+1}^{(o)s}} \qquad (2)$$

In (1) and (2) we give the local version of Gyorffy's formula for brevity, whereas in this work $\alpha^2F(\omega)$ has been calculated using a nonlocal extension /2/.

The $\eta_s$ have been obtained applying the selfconsistent symmetrized cluster approach /3/ which allows calculations for systems consisting of 176 scatterers. With the choice of appropriate boundary conditions the whole energy range between the deep lying 5p semicore levels of e.g. La, the intra- and intercluster bonding states /4/ and the f-levels above the Fermi energy have been described by continuous density of states curves. The results are in good agreement with recent APW bandstructure work /5/, ESCA- /6/, and X-ray emission experiments /7/. Fig. 1 shows the total electronic density of states for $LaB_6$. Table 1 lists the electronic quantities entering equation (2).

Table 1

| Compound | $LaB_6$ $\varepsilon_F$=.77Ryd $n(\varepsilon_F)$=9.33Ryd$^{-1}$ | | | | | | | $YB_6$ $\varepsilon_F$=.86Ryd $n(\varepsilon_F)$=8.14Ryd$^{-1}$ | | | | | | |
|---|---|---|---|---|---|---|---|---|---|---|---|---|---|---|
| Component | La | | | | B | | | Y | | | | B | | |
| $\eta_s$ (eV/Å$^2$) | .633 | | | | .390 | | | .998 | | | | .435 | | |
| $\delta_l$ | 1.46 | 2.15 | .34 | .03 | .51 | .65 | .01 | 1.79 | 2.45 | .55 | .01 | .46 | .72 | .01 |
| $n^s_l/n^{(0)s}_l$ | .47 | .55 | .50 | 1.2 | .21 | .51 | 1.3 | .66 | .42 | .55 | 1.03 | .32 | .37 | 1.32 |

Table 2

| Phonon-Energy (meV) | Type of Vibration | Contribution to $\lambda$ |
|---|---|---|
| 13 | Translational Modes of the Metal- and Boron-Sublattices | .11 |
| 36 | Torsional Modes of the Octahedra | .12 |
| 45 | Optical Modes of the Metal- and Boron-Sublattices | .09 |
| 65<br>90 | Vibrations of the Boron-Sublattice Connected with Deformations of the Octahedra | .07 |

The phonon properties have been calculated using a Born-von-Kármán model described on page 22 in this volume. The peaks in the phonon density of states are connected with certain types of vibrations (at the Γ-point) quoted in Table 2 together with their contributions to Mc Millan's $\lambda$. The evaluation of the non-local version of equation (1) turned out to be of great importance because $\lambda$ is reduced in $LaB_6$ by about 25 % as compared to the local result.

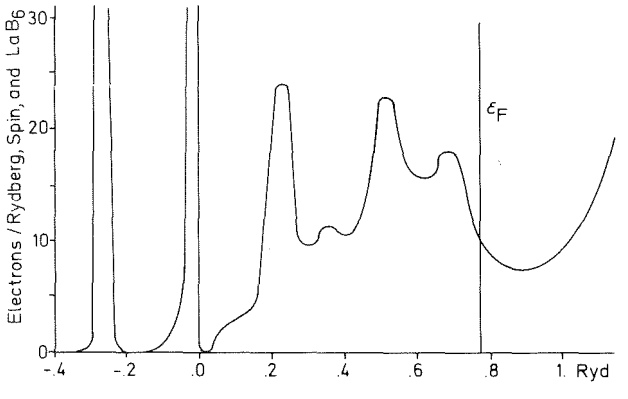


Fig. 1 Electronic density of states in $LaB_6$

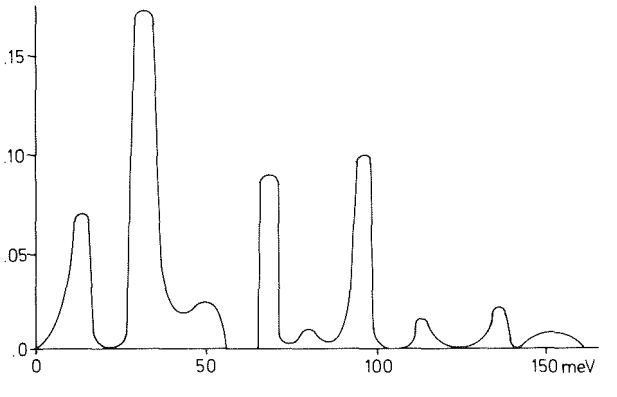


Fig. 2 Eliashberg function of $LaB_6$

The Eliashberg function for $LaB_6$ is shown in Fig. 2. We see that the translational and torsional modes give comparable contributions to $\lambda$ and dominate the deformation modes of the octahedra. Two features cause the large difference in the $T_c$s of $YB_6$ and $LaB_6$: $\eta^Y$ is larger than $\eta^{La}$ due to its more pronounced d-character on account of the higher Fermi level and the frequency of the translational mode is lower in $YB_6$ by a factor of $\sim.75$ /8/.

References

/1/ I.R. Gomersall and B.L. Gyorffy, J. Phys. F: Metal Phys. 4, 1204 (1974)

/2/ H. Rietschel, Z. Physik B30, 271 (1978)

/3/ G. Ries and H. Winter, J. Phys. F: Metal Phys. 9, 1589 (1979)

/4/ H.C. Longuet-Higgins and M. de V. Roberts, Proc. Roy. Soc. (London) A224, 336 (1954)

/5/ A. Hasegawa and A. Yanase, J. Phys. F: Metal Phys. 7, 1245 (1977)

/6/ M. Aono, S. Kawai, S. Kono, M. Okusawa, T. Sagawa, and Y. Takehana, J. Phys. Chem. Solids 37, 215 (1976)

/7/ I.I. Lyakhovskaya, T.M. Zimkina, and V.A. Fomichev, Sov. Phys. - Solid St. 12, 138 (1970)

/8/ F. Gompf, in Progress Report Teilinstitut Nukleare Festkörperphysik, Ges. f. Kernforschung, KfK 2670, contribution 1.9 (1978)

## 2.5 Lattice Dynamics of NbC and NbN

*W. Weber*

The tight binding theory of Varma and Weber /1/ is used to calculate the phonon dispersion curves for NbC and NbN. For this purpose, the method is generalized to include more than one particle per unit cell. Various first principles electronic band structure calculations /2/ have been used to determine the matrix elements of an empirical tight binding Hamiltonian used in the formalism. The gradients of this matrix elements have been found from overlap calculations using self-consistent atomic and ionic wave-functions and potentials.

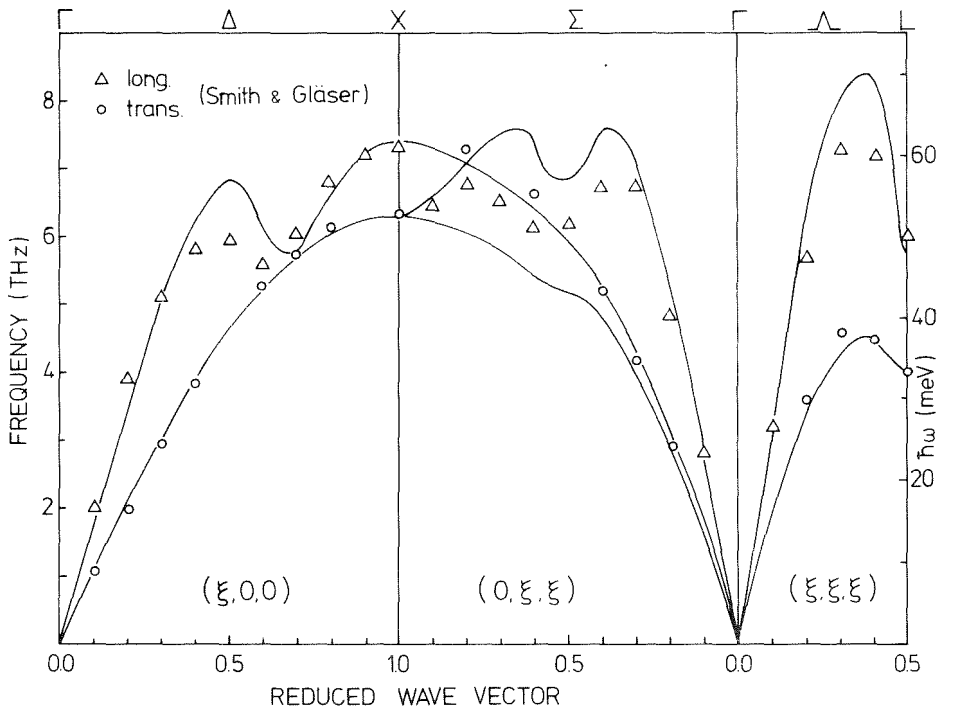


Fig. 1 Acoustic phonon dispersion curves of NbC as calculated with the band structure of Schwarz (Ref. 2). Experimental values are taken from Ref.1.

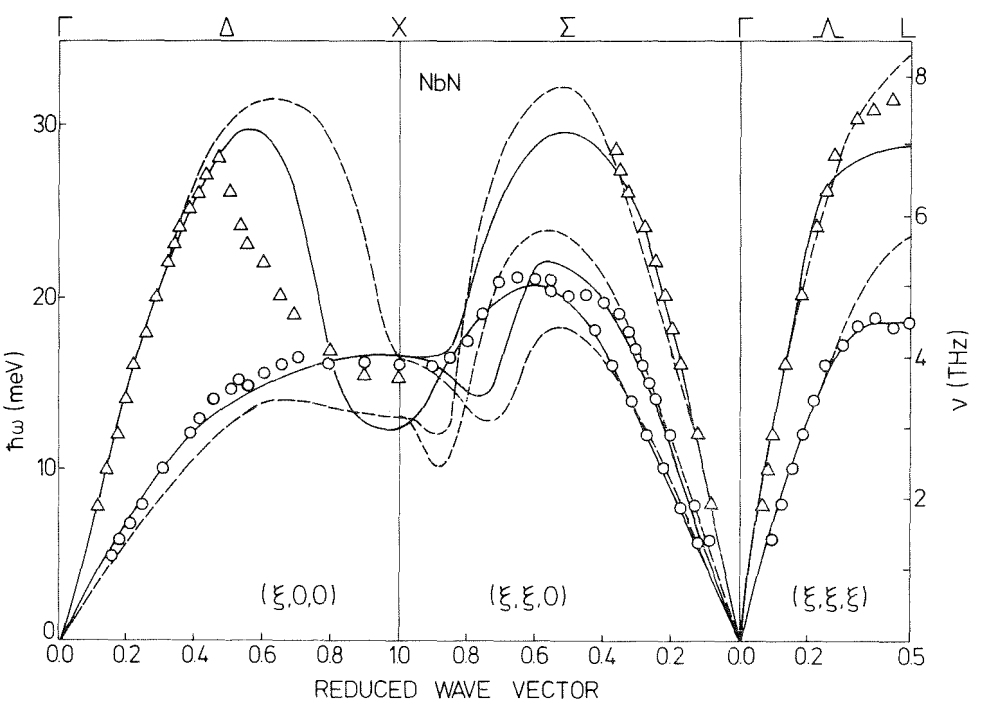


Fig. 2 Acoustic phonon dispersion curves of NbN. Experimental values for $NbN_{0.83}$ from Ref. 4. Dashed lines show predicted curves for fully stoichiometric NbN. Solid lines represent calculations which take into account the non-stoichiometry.

For NbC, very good agreement with experiment /3/ is obtained (see Fig. 1), irrespective which of the three electronic band structures were used in our calculations. Especially, all anomalies in the phonon dispersion are correctly reproduced. However, in each calculation, the anomaly in the LA branch along the $\Delta$ direction appears at somewhat different positions. This can be traced back to slightly different shapes of the electronic bands near the Fermi energy. Best accordance with experiment is obtained using the band structure of Schwarz.

In Fig. 2, our results for NbN are compared to the experimental results of Reichardt and Scheerer /4/ for a $NbN_{0.83}$ sample. The dashed lines represent calculations assuming a fully stoichiometric NbN crystal. These calculations have been performed previous to the neutron scattering work.

The main differences to the NbC dispersion are i) the shift of the anomalies along $\Delta$ and $\Sigma$ directions to the X point of the Brillouin zone, ii) the disappearance of the anomaly at the L point, iii) the broad depression of the TA branches along $\Delta$ and $\Sigma$. All these features have been correctly predicted by our calculation. They arise essentially from a rigid-band-like increase of the Fermi energy when compared to NbC. In order to study the effects of nonstoichiometry, we have lowered the Fermi energy for NbN to some extent. Then, the agreement with experiment was further improved (see Fig. 2, solid lines).

Altogether, our study confirms the observations of Ref. 1, that the anomalies in the phonon dispersion curves are related to the topology of the electronic bands near the Fermi energy.

Part of this work was performed at MPI f. Festkörperforschung, Stuttgart.

References

/1/ C.M. Varma and W. Weber, Phys. Rev. Letters 39, 1094 (1977) and Phys. Rev. B19, 6142 (1979)

/2/ K.H. Schwarz, J. Phy. C 10, 195 (1977); M. Gupta and A.J. Freeman, in Superconductivity in d- and f-Band Metals, 2nd Rochester Conf. (Ed. D.H. Douglass), Plenum Press, New York, 1976, p. 313; B.M. Klein, D.A. Papaconstantopulous, and L.L. Boyer, ibid., p 339.

/3/ H.G. Smith and W. Gläser, Phys. Rev. Letters 25, 1611 (1970)

/4/ W. Reichardt and B. Scheerer, this volume, p.4

## 2.6 Phonon Linewidths and Phonon Anomalies in Nb and NbC

*W. Weber*

In most pure metals, the dominant contribution to the phonon linewidths at low temperatures arises from electron-phonon coupling. This "intrinsic" linewidth $\gamma_{qj}$ of a phonon of frequency $\omega_{qj}$ (q wavevector, j branch index) is a measure of how strongly electrons at the Fermi surface are coupled via a particular phonon. Therefore, the linewidths $\gamma_{qj}$ are related /1/ to quantities which determine the superconducting properties of a material, e.g. the Eliashberg function

$$\alpha^2 F(\omega) \quad \propto \quad \sum_{qj} \quad \gamma_{qj} \quad / \quad \omega_{qj} \quad \delta(\omega-\omega_{qj}).$$

Since probably all materials with high superconducting transition temperatures $T_c$ show phonon anomalies, it has been an often discussed problem in how far these anomalies are related to superconductivity. We have developed a theory /2/ which allows to calculate phonon dispersion curves and phonon linewidths for transition metals and compounds using a tight-binding Hamiltonian for the electronic band structure and for the electron-phonon coupling. In this theory, the term $D_2^C$ has been shown to be the source of the anomalies. $D_2^C$ incorporates all contributions to the phonon dynamical matrix from virtual scattering between electronic states close to the Fermi energy $E_F$ ($\sim \pm$ 0.5 eV).

For Nb, $-D_2^C$ shows a large, asymmetric peak at the anomaly position in the $\Delta$ direction (see Fig. 1). Almost the same structure is found for $\gamma$. A similar correlation between $-D_2^C$ and $\gamma$ appears along the $\Sigma$ direction. We note that our results for $\gamma$ agree well with calculations of Butler et al /1/ using a different formalism.

In NbC, the correlation between $\gamma$ and $-D_2^C$ is even more dramatic. Here the curves of $\gamma$ and $-D_2^C$ show much sharper structure than in Nb. The anomalies are much more pronounced; similarly, in the anomalous regions, $\gamma$ may exceed the average linewidth by more than an order of magnitude (see Fig. 2), as compared to about a factor of two in Nb (see Fig. 1).

The extremely anisotropic nature of the electron-phonon coupling in NbC is manifest in two respects: i) only the few anomalous phonons couple strongly between electronic states at $E_F$ and give the dominant contributions to $\alpha^2(\omega)\ F(\omega)$; ii) only relatively few electronic states at the Fermi surface are involved in this strong coupling, the other states are coupled rather modestly.

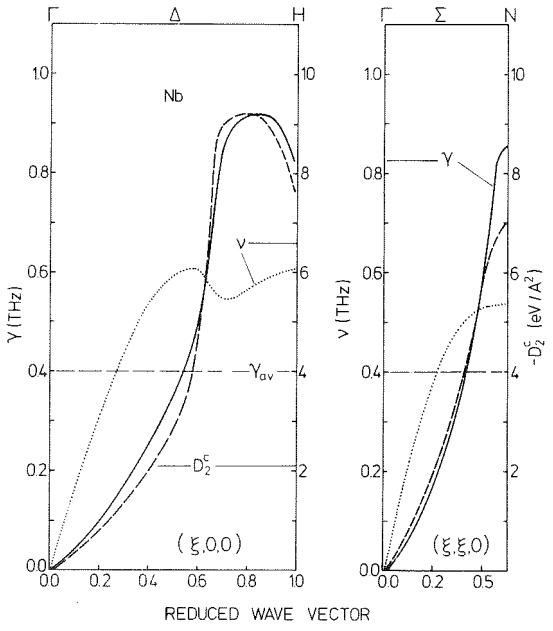


Fig. 1
Phonon linewidths $\gamma$, $-D_2^c$ and phonon frequencies $\nu$ for longitudinal polarisation along two symmetry directions in Nb. $\gamma_{av}$ denotes the average value of all phonon linewidths in the Brillouin zone. The units for $\gamma$ are those used in Ref. 2.

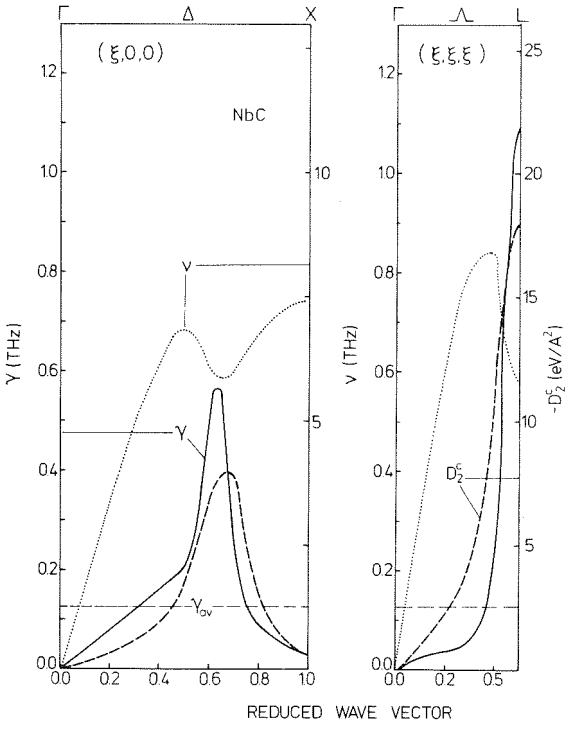


Fig. 2
Longitudinal acoustic phonons $\nu$, linewidths $\gamma$ and $-D_2^c$ along two symmetry directions in NbC. Also shown is $\gamma_{av}$.

References

/1/ W.M. Butler, H.G. Smith, and N. Wakabayashi, Phys. Rev. Letters 39, 1004 (1977)

/2/ C.M. Varma and W. Weber, Phys. Rev. Letters 39, 1094 (1977) and Phys. Rev. B19, 6142 (1979)

## 2.7 On the Electronic Structure of $Nb_3Sn$ and $V_3Si$

*L.F. Mattheiss[a] and W. Weber*

*[a]visiting scientist from Bell Laboratories, USA.*

Many A-15 materials exhibit various interesting physical properties; e.g., very large values of the electronic density of states N(o) at the Fermi energy $E_F$ and the highest superconducting transition temperatures $T_c$ found so far. At low temperatures, some of them, e.g., $Nb_3Sn$ and $V_3Si$ undergo structural transitions from the cubic into a tetragonal phase - without much effect on $T_c$. These properties have been connected with the fact that the Nb or V atoms form three sets of non-intersecting chains along <100> directions.

In order to gain better physical understanding of the electronic structure of these materials, we have performed a tight binding analysis of the self-consistent APW band-structure calculations of Klein et al /1/. For this purpose, we have developed a program to generate a nonorthogonal tight binding (NTB) Hamiltonian matrix in the two-center-approximation, applicable to <u>any</u> given crystal structure - thereby allowing <u>any</u> number of s, p or d orbitals at an atom site. In addition, a general fitting procedure was developed including a unique symmetry assignment scheme of all eigenvalues of the Hamiltonian.

For the A-15 compounds, we found it necessary to use a 62 orbital basis, including s and p orbitals for the transition metal atoms. For $V_3Si$ and $Nb_3Sn$ we obtained fits with rms errors of 3.0 and 1.8 mRy, respectively. In both materials $E_F$ lies close to a peak of the electronic density of states (see Fig. 1). This peak is caused by two extremely flat bands starting from a $\Gamma_{12}$ state. The states in these bands are composed to ∿60% of $d_{3z^2-r^2}$ and to ∿15% of $p_z$ Nb or V orbitals (z defined along the chain directions). These orbitals exhibit strong σ-type interaction both along the chains and between different chains - leading to strong p-d hybridisation effects. Our result is in contrast to an earlier study /2/ using a limited basis set without metal p orbitals, where the $d_{x^2-y^2}$ orbitals were found to be dominant with very weak δ-type interaction along the chains.

We also studied the influence of the tetragonal distortion on the electronic structure. The effects of interatomic distance changes on the NTB matrix elements were included using a linear interpolation based on 1nn and 2nn cubic matrix elements.

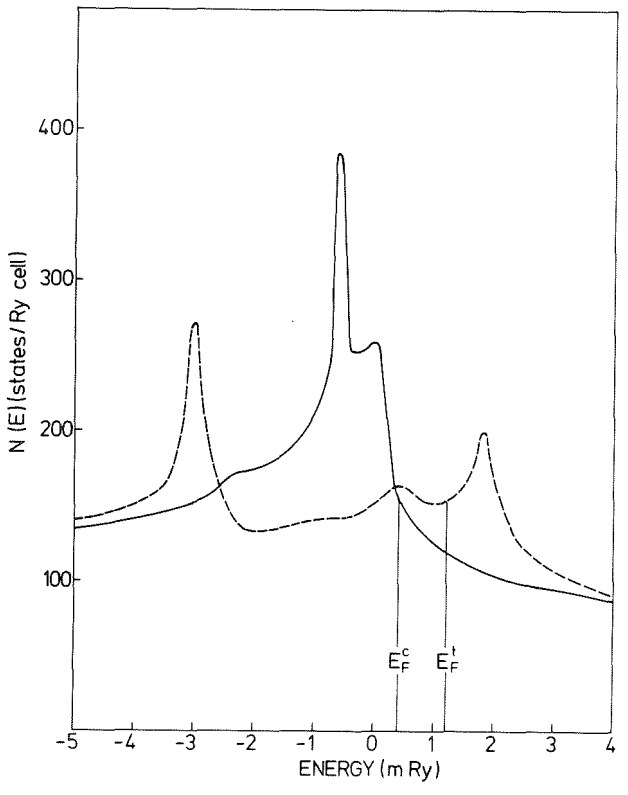


Fig. 1
Electronic densities of states near $E_F$ for cubic $Nb_3Sn$ (solid line) and tetragonally distorted $Nb_3Sn$ (dashed line).

In the A15 structure, a tetragonal distortion results not only in the change of the lattice parameters, but also in a sublattice distortion; i.e. in two of the three metal atom chains occurs a pairing of atoms /3/. This dimerization corresponds to a frozen optic phonon of $\Gamma_{12}$ symmetry in the cubic structure. It is found that the mere tetragonal distortion does not affect the bands very much. However, the dimerization of the chains causes an asymmetry in the pdσ interaction which splits the $\Gamma_{12}$ bands by ∿6mRy. As a consequence, the sharp peak in the electron density of states just below $E_F$ splits into two parts (see Fig. 1).
This causes a decrease in the sum of all occupied one-electron energies as compared to the cubic case. The value of N(o) has not been altered very much.

This joint venture has been performed with each of the authors staying for a while at the other's home base.

References

/1/ B.M. Klein, L.L. Boyer, D.A. Papaconstantopoulos, and L.F. Mattheiss, Phys. Rev. B18, 6411 (1978)

/2/ L.F. Mattheiss, Phys. Rev. B12, 2161 (1975)

/3/ G. Shirane and J.D. Axe, Phys. Rev. B4, 2957 (1971)

# 3. ELECTRONIC STRUCTURE AND MAGNETISM OF SOLIDS

## 3.1 Jahn - Teller Distorted Crystal Structure in $Rb_2 Cr_{1-x} Mn_x Cl_4$ $(0 \leq x \leq 1)$

*G. Münninghoff[a], E. Hellner[a], W. Treutmann[a], and G. Heger*

[a] *Fachbereich Geowissenschaften der Universität Marburg*

$Rb_2Me^{2+}Cl_4$ compounds with paramagnetic 3d transition metal ions $Me^{2+}$ are of special interest due to their quasi two-dimensional magnetic behaviour. Antiferromagnetic examples predominate, e.g. $Rb_2MnCl_4$, having a crystal structure of the $K_2NiF_4$ type (space group I4/mmm) /1/ (see Fig. 1). Jahn-Teller instable $d^4$ or $d^9$ cations cause a distortion of the $Me^{2+}Cl_6$ octahedra. An antiferrodistortive ordering of these tetragonally elongated octahedra in the <001> planes leads to a symmetry reduced crystal structure and to ferromagnetic interactions within the planes, e.g. in $Rb_2CrCl_4$. This correlation between crystal structure and magnetic behaviour was predicted for $K_2CuF_4$ by Khomski & Kugel /2/. To study the crystallographic distortion of the $K_2NiF_4$ structure and the magnetic transition from the antiferromagnetic $Rb_2MnCl_4$ to the ferromagnetic $Rb_2CrCl_4$, neutron diffraction measurements on single crystals of the mixed system $Rb_2Cr_{1-x}Mn_xCl_4$ are performed.

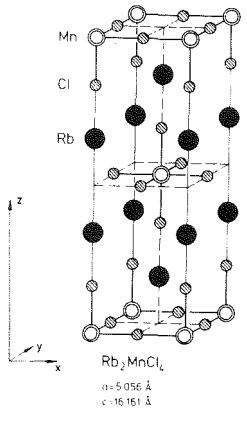


Fig. 1
Crystal structure of $Rb_2MnCl_4$ ($K_2NiF_4$ type)

As representative of the Jahn-Teller distorted case we studied a sample of $Rb_2Cr_{0.99}Mn_{0.01}Cl_4$ at room temperature. The symmetry reduction leads to a space group of Bbcm (Cmca-No.64- in the convention of the International Tables for X-ray Crystallography). The superstructure cell is two times larger than that of the $K_2NiF_4$ type: $a' \simeq a\sqrt{2} = 7.262(4)$ Å; $b' \simeq a\sqrt{2} = 7.262(4)$ Å; $c' = c = 15.773(8)$ Å. The structure refinement (R=0.043 with $R = \Sigma \big| |F_o| - |F_c| \big| / \Sigma |F_o|$ (reliability factor)) revealed the following (Cr,Mn) - Cl distances: 2.74(2) Å (2x); 2.40(2) Å (2x); 2.43(1) Å (2x). The tetragonally elongated $(Cr,Mn)Cl_6$ octahedra are ordered in an antiferrodistortive manner with their long axis in the <001> plane.

The influence of the Jahn-Teller instable $Cr^{2+}$ ion on the undistorted $Rb_2MnCl_4$ lattice at room temperature has been studied

for various concentrations by crystal structure analysis in the space group I4/mmm. So far $Rb_2Cr_{1-x}Mn_xCl_4$ compounds with x=0.01/0.08/0.53/0.63/0.83/0.91/0.97 have been investigated. The real deviations of the $Cl^-$ ions from their mid-position between the (Cr,Mn) ions cannot be described in I4/mmm due to space group symmetry. The long and short (Cr,Mn)-Cl distances within the <001> planes however, cause an unusually large mean square displacement of the $Cl^-$ ions in bond direction. The mean square displacement components of the in-plane $Cl^-$ are shown in Fig. 2. With growing Cr content a drastic increase of the in-bond component $U_{22}$ is visible.

Our results on $Rb_2Cr_{1-x}Mn_xCl_4$ indicate a continuous distortion of the $(Cr,Mn)Cl_6$ octahedra over the whole composition range.

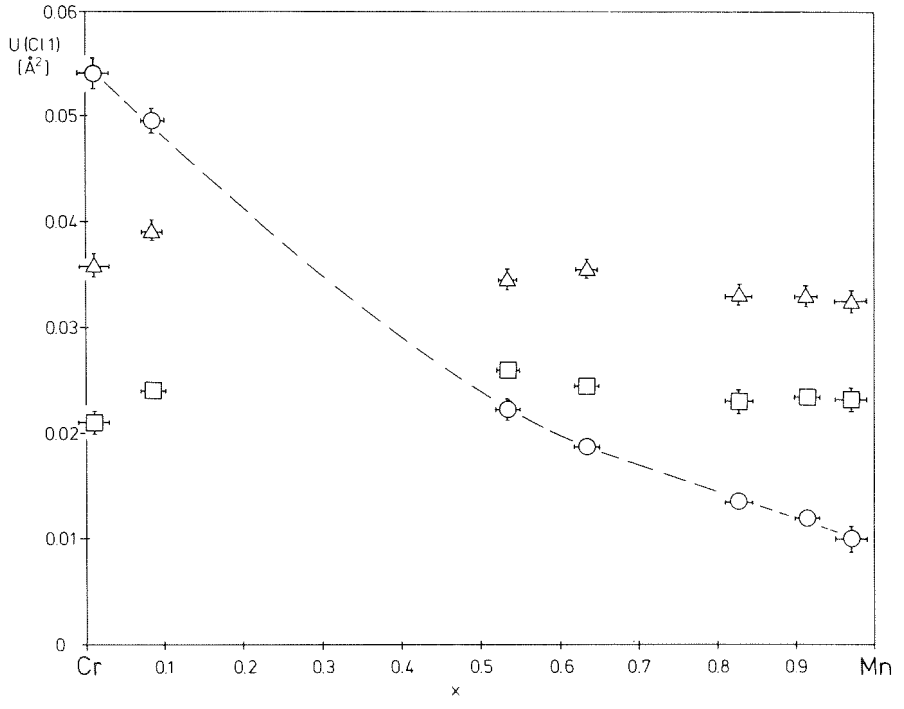


Fig. 2 The dependence of the mean square displacements $U_{ij}$ of Cl(1) on the $Cr^{2+}$ concentration in $Rb_2Cr_{1-x}Mn_xCl_4$ (refinement in I4/mmm)
□ : $U_{11}$; O : $U_{22}$; Δ : $U_{33}$

References

/1/ A. Epstein, E. Gurewitz, J. Makowsky, and Shaked, Phys. Rev. B2, 3703 (1970).

/2/ D.J. Khomskii and K.J. Kugel, Solid State Commun. 13, 763 (1973)

## 3.2 Mössbauer Spectroscopy of Compounds $NiFe_{2-t}Al_tO_4$ with Spinell Structure

*G. Czjzek, J. Fink, F. Götz, V. Oestreich, H. Schmidt, J.J. Bara[a], and Z.M. Stadnik[a]*

[a] *Institute of Physics, Jagiellonian University, Cracow, Poland*

In investigations of complex magnetic compounds such as ferrimagnetic oxides containing two or more different types of magnetic ions it is often useful to observe the changes of the magnetic properties when nonmagnetic ions are substituted for some of the magnetic ions. Thus, for the ferrimagnetic spinell $NiFe_2O_4$ information on the Fe-Fe exchange interactions on one sublattice (octahedrally coordinated B sites) could be obtained by replacing $Ni^{2+}$ by diamagnetic $Zn^{2+}$ /1/ whereas the properties of the pure compound are rather insensitive to this interaction as they are dominated by other interactions /2/. Similarly, new information could be obtained by substituting $Al^{3+}$ for $Fe^{3+}$ /3/.

We have now extended the studies reported in Ref. /3/ by Mössbauer spectroscopy with $^{57}Fe$ and $^{61}Ni$ at 4.2K in zero field as well as in magnetic fields up to 6 Tesla in several samples of the general formula $NiFe_{2-t}Al_tO_4$ ($0.2 \leq t \leq 1.9$). Some typical spectra are shown in Fig. 1. For the $^{57}Fe$ spectra the contributions from tetrahedral A sites and octahedral B sites are clearly separated. From the intensity ratios of the two components we deduce the fractions of A and B sites occupied by Fe ions in essential agreement with the results described in Ref. /3/. The Mössbauer spectra of $^{61}Ni$ are not nearly as well resolved, particularly those obtained in zero field. The spectra in a field of 6 T, shown in Fig. 1b, however, clearly show that all Ni ions occupy octahedral B sites for samples with Al concentrations corresponding to $t \leq 1.25$.

For higher Al concentrations the Mössbauer spectra in magnetic fields become quite complex. In particular, the lines corresponding to nuclear transitions with $\Delta M = 0$ do not disappear. This is clearly seen in the spectra of $^{57}Fe$, but also for $^{61}Ni$ we obtain significantly better fits when we assume a finite intensity of the lines corresponding to the $\Delta M = 0$ transitions. Since the intensity of these lines vanishes when the hyperfine field acting on the nuclei is parallel to the direction of observation, we conclude that the magnetic moments in these compounds are canted with respect to the applied field which was directed parallel to the direction of observation. Considerable broadening of the outer lines which for an applied field of 6 T cannot be fitted any more by a single Lorentz absorp-

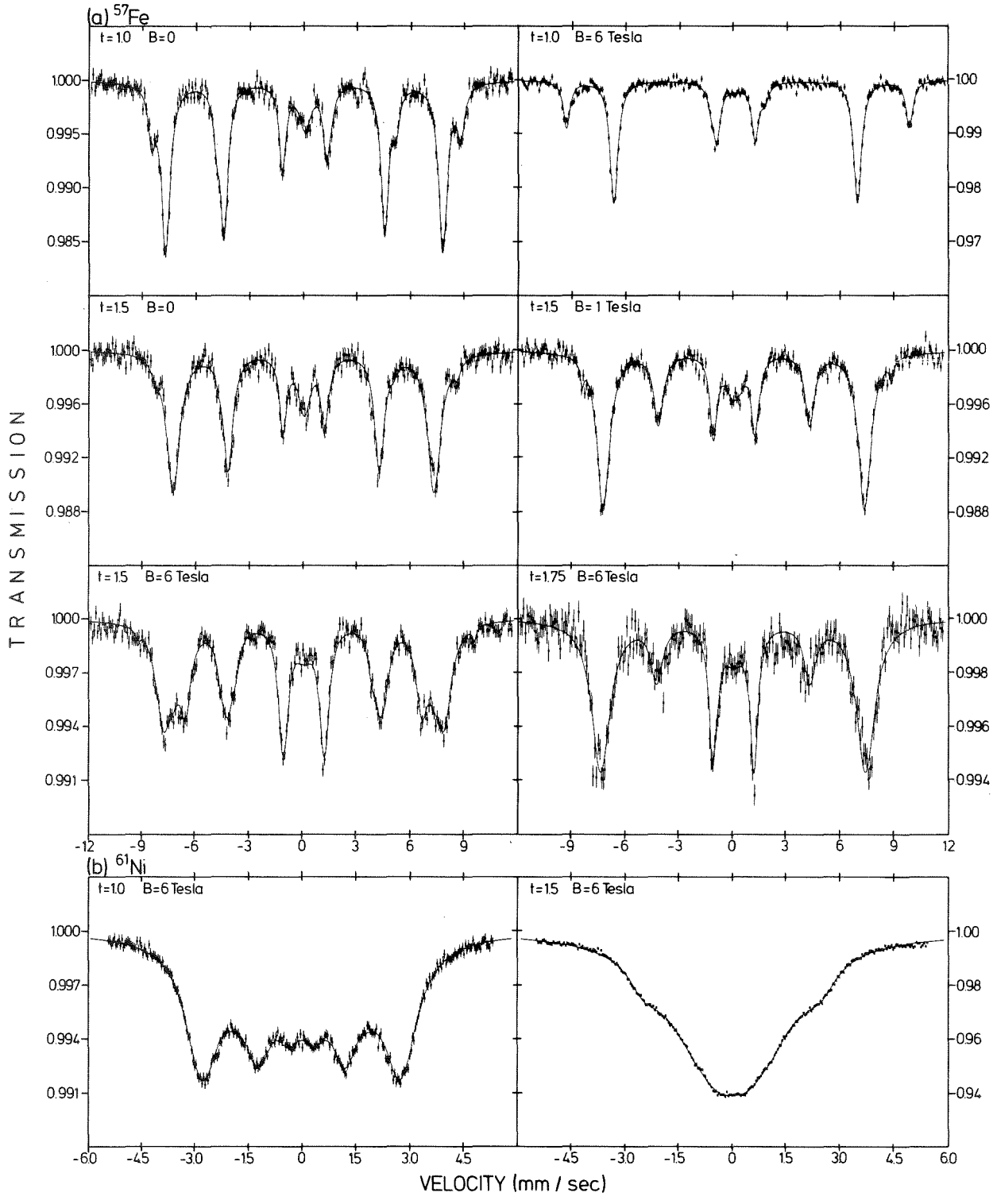


Fig. 1 Mössbauer absorption spectra (a) of $^{57}Fe$ and (b) of $^{61}Ni$ in several compounds $NiFe_{2-t}Al_tO_4$ with spinell structure. All spectra were taken at 4.2 K. Values of the Al content t and of the applied field B are shown for the individual spectra.

tion line indicates the presence of Fe atoms with different canting angles. This finding can be rationalized in terms of the local canting model worked out theoretically by A. Rosencwaig /4/. An analysis of our experimental results in terms of this model is expected to yield quantitative results on the exchange interactions prevailing in these compounds.

References

/1/ G.A. Petitt, Solid State Commun. 13, 1611 (1973)

/2/ J.-P. Morel, J. Phys. Chem. Solids 28, 629 (1967)

/3/ J.J. Bara, A.T. Pedziwiatr, Z.M. Stadnik, A. Szytuła, J. Todorović, Z. Tomkowicz, and W. Zarek, phys. stat. sol. (a) 44, 325 (1977)

/4/ A. Rosencwaig, Can. J. Phys. 48, 2857 (1970)

## 3.3 Magnetic Neutron Scattering from a Tetranuclear Copper (II) Complex

*P. v. Blanckenhagen, H. Weitzel[a], L. Merz[a] and W. Haase[a]*

[a] *Institut für Physikalische Chemie, TH Darmstadt*

Structural investigations of alkoxobridged copper (II) complexes $[((C_2H_5)_2\ N\ CH_2CH_2\ O)\ N\ C\ O\ Cu]_4$ show the existence of cuban type clusters with a $Cu_4O_4$ core. The temperature dependence of the magnetic susceptibility shows a maximum at 35 K and thus indicates overall antiferromagnetic spin coupling between the copper ions of the tetranuclear Cu-clusters /1/.

The four copper (II) ions in the clusters are situated in an almost tetrahedral arrangement with $S_4$ point symmetry. The magnetic interactions between these copper ions can be described by two isotropic exchange integrals and due to these interactions the electronic ground state is splitted into five energy levels.

The level scheme for the magnetic excitations as derived from these susceptibility data should be proved by neutron scattering experiments.

The inelastic neutron scattering experiments were done with the spectrometers MAG 1 and MAG 2 using incoming neutron energies of 13.6 and 3.55 meV, re-

spectively. The sample temperature was varied between 4.5 and 300 K. The observed peaks in the energy spectra (Fig. 1) may be due to magnetic or nuclear scattering. From the temperature dependence of the peak intensities (Fig. 2) we conclude, that the peak at 9.2 meV is due to transitions from magnetic ground state to an excited state. The other peaks observed may be caused by vibrations. Further investigations of the dependence of the peak intensities upon the momentum transfers are necessary for the identification of other magnetic levels and for the determination of the full level scheme.

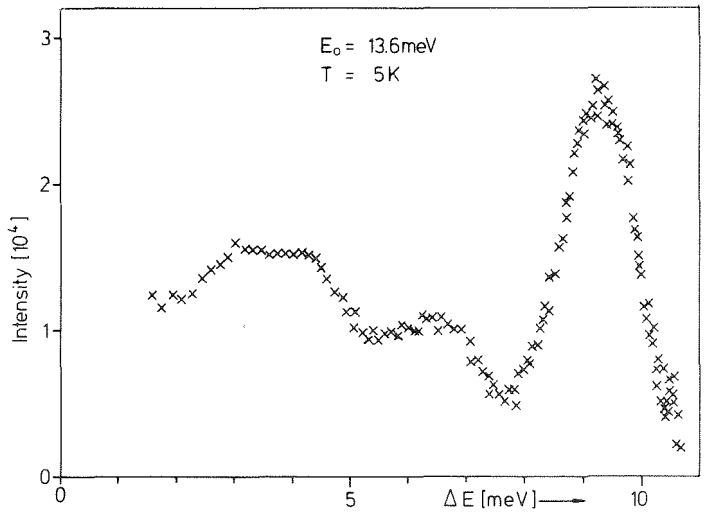


Fig. 1
Energy spectra for neutrons scattered from $[Et_2N(CH_2)_2O\ Cu\ N\ C\ O]_4$

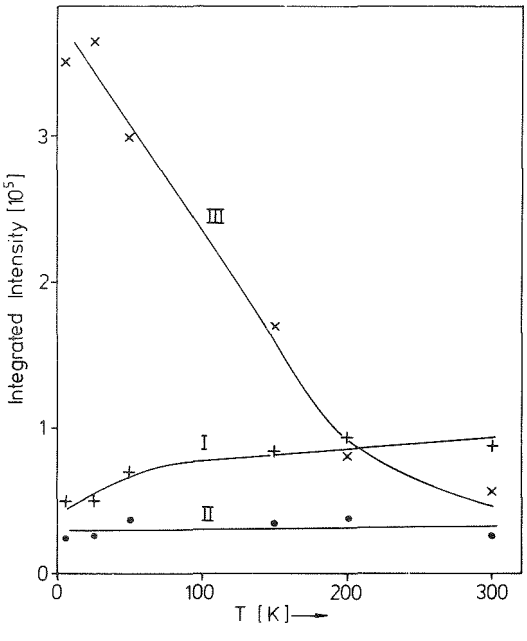


Fig. 2 Temperature dependence of the neutron intensity at different energy transfers:
I : 3.6 meV; II : 6.6 meV; III : 9.2 meV

Reference

/1/ L. Merz and W. Haase, J. Chem. Soc. Dalton Trans. (1978) 1594-1598.

## 3.4 Spin Relaxation in the Amorphous Spin Glass $Al_2Mn_3Si_3O_{12}$

*1. W. Nägele[a], P. v. Blanckenhagen, K. Knorr[a], and J.B. Suck[b]*

*[a]Institut für Kristallographie, Universität Tübingen*

*[b]Institut Max von Laue - Paul Langevin, Grenoble, France*

*Z. Phys. B 33, 251 (1979)*

Abstract

Neutron scattering measurements on the amorphous spin glass $Al_2Mn_3Si_3O_{12}$ have been made using the time-of-flight method. The scattering law $S(Q,\omega)$ reveals a quasielastic line with temperature and Q-dependent linewidth and an elastic line with constant intensity between 15 and 294 K. The linewidth of the quasielastic scattering diminishes with decreasing temperature following an Arrhenius law at least down to 15 K. Deviations from this exponential form are strictly correlated with an increase of the elastic intensity below 15 K. We favour the opinion that this effect is caused by the instrumental resolution rather than by the onset of spin glass freezing.

*2. W. Nägele[a], P. v. Blanckenhagen, and A. Heidemann[b]*

*[a]Institut für Kristallographie, Universität Tübingen*

*[b]Institut Max von Laue - Paul Langevin, Grenoble, France*

*Submitted to J. Magn. Magn. Mat.*

Abstract

Neutron scattering experiments on the amorphous spin glass $Al_2Mn_3Si_3O_{12}$ with energy resolutions from 0.5 to 0.0006 meV reveal an exponential dependence of the relaxation time on reciprocal temperature points to the possibility that the spin glass behaviour in this compound is due to a relaxation phenomenon. In this paper we report on results obtained with high resolution triple-axis and backscattering neutron spectrometers.

Note added: The second work reports measurements of the quasielastic scattering law with the triple axis spectrometer MAG 2 at the cold source of the FR2 and with the backscattering spectrometer IN 10 at the HFR Grenoble. The results of these experiments with higher energy resolution show that the temperature dependence of the width of the quasielastic line may be described by an Arrhenius law down to 3.5 K and that no significant deviation from this law appears near the freezing temperature of the spin glass.

## 3.5 The Distribution of Electric Field Gradients in Random Amorphous Solids: An Analytic Approximation.

*G. Czjzek, J. Fink, F. Götz, H. Schmidt, J.M.D. Coey[a], A. Liénard[a], and J.-P. Rebouillat[a]*

*[a]Transitions de Phases, C.N.R.S. Grenoble, France*

Mössbauer spectra of amorphous solids are generally characterized by a well defined quadrupole splitting. The electric field gradient (EFG) whose interaction with the nuclear quadrupole moment gives rise to the quadrupole splitting is determined by the angular distribution of electric charges surrounding the nucleus. Thus, an analysis of the quadrupole spectra yields new information about the structure of amorphous solids supplementary to diffraction data which are primarily determined by the radial distribution function and allow only indirect inferences on angular distributions.

Cochrane et al /1/ have shown that point charge calculations of the EFG based on a computer-generated structural model yield energy level distributions in good agreement with those observed experimentally. In the present work we attempt to find an analytic approximation for the distribution of the parameters determining the quadrupole splitting for a random amorphous structure. Based on the experimentally determined radial distribution functions which show that the atomic arrangement surrounding any probe atom can be considered roughly as a sequence of spherical shells we define randomness by

(i) random distribution of angular atomic coordinates in any shell, and

(ii) absence of correlations between the atomic distributions in different shells.

We have realized proposition (i) by constructing statistical ensembles of atomic shells on a computer. For every shell of median radius $r_s$ a random atomic distribution was obtained with help of a random number generator. The atoms were treated as hard spheres of radius $r_A$, and in constructing a shell a new atomic position was accepted only if no overlap occurred with any of the atoms whose positions had been tossed before. For every shell the components $V_{ik}$ of the field gradient tensor were calculated in a point charge model, setting the charge carried by each atom equal to one. The distribution functions of the $V_{ik}$ obtained for any ensemble were quite well approximated by a Gaussian distribution: $P(...V_{ik}...) = N \cdot \exp\{-\Sigma V_{ik}^2/2\sigma^2\}$. The values $\sigma$ decrease very rapidly with increasing $r_s$. In the range from $r_s = 2r_A$ until $r_s = 6r_A$ we found approximately $\sigma(r_s) \propto r_s^{-2.3}$. By proposition (ii) the distribution function for a random solid in the sense defined here is given by the folded distribution functions for the individual shells. Thus, the total distribution function of the $V_{ik}$ again is approximately Gaussian with $\sigma^2_{total} = \sum_{shells} \sigma^2(shell)$. The rapid decrease of $\sigma$ with $r_s$ guarantees the convergence of the sum. Deviations from the Gaussian approximation which can be associated with excluded-volume effects are quite pronounced for the first coordination shell ($r_s = 2r_A$) whereas they become negligible for larger values of $r_s$. They can be accounted for by adding in the exponential a term proportional to $[\mathrm{Det}(V_{ik})]^{2/3}$ with a factor which is different for positive and negative values of the determinant.

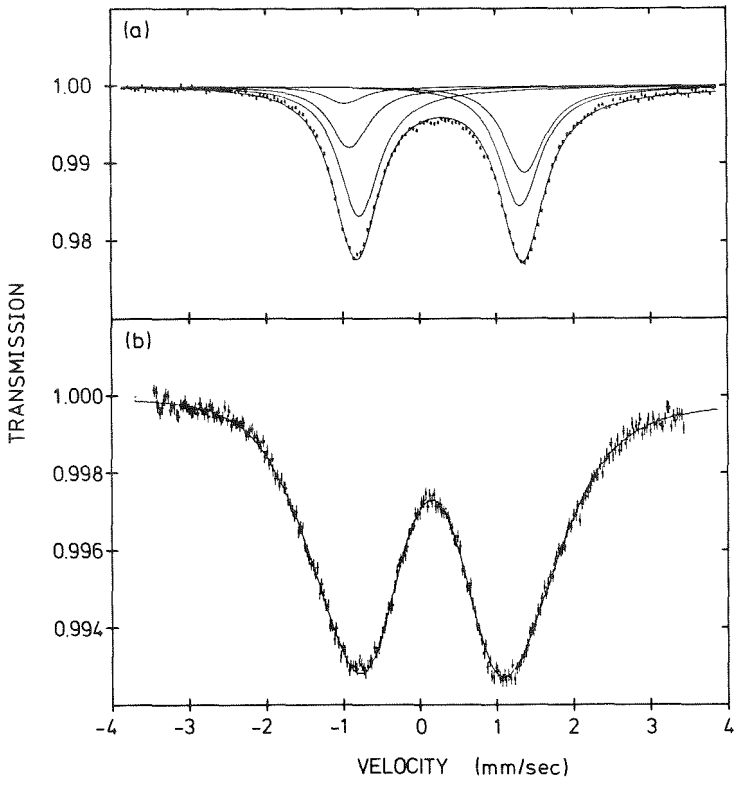


Zu 3.5:

Fig. 1
Mössbauer absorption spectra of $^{155}Gd$: (a) in crystalline $GdNi_5$. In this compound with hexagonal structure all Gd ions occupy equivalent lattice sites and all $^{155}Gd$ nuclei experience the same electric field gradient. (b) In amorphous $Gd_{0.2}Ni_{0.8}$. The continuous curve is a fit with the distribution function described in the text.

The experimentally observed quadrupole splitting is determined by only two parameters (the trace is zero) related to the eigenvalues of the EFG tensor. They are conventionally chosen as $V_{zz}$ and the asymmetry parameter $\eta=(V_{xx}-V_{yy})/V_{zz}$ with $0 \leq \eta \leq 1$. /2/. From the distribution functions of the tensor components described above the distribution function $P(V_{zz}, \eta)$ which is relevant for the experimental spectrum can be derived. We have tested our results by comparison with the Mössbauer spectrum measured with $^{155}Gd$ in an amorphous alloy $Gd_{.2}Ni_{.8}$ at 45 K (above $T_c$ = 39 K).

A fit of our distribution function including the term which describes excluded-volume effects to the experimental data is shown in Fig. 1b.

References

/1/ R.W. Cochrane, R. Harris, M. Plischke, D. Zobin, and M.J. Zuckermann, Phys. Rev. B5, 1969 (1975)

/2/ B.D. Dunlap in Mössbauer Effect Data Index 1970, ed. by J.G. Stevens (New York, Plenum, 1972), p. 25

## 3.6 Magnetic Interactions in PrEu and PrGd Alloys

*F. Götz, G. Czjzek, J. Fink, H. Schmidt and P. Fulde*[a]

[a] *MPI Stuttgart*

For the Van Vleck paramagnet Praseodymium (dhcp structure) the ratio of exchange interaction to crystal field energy is close to the critical value required for the occurence of a magnetic moment. By alloying magnetic impurities into Pr, the exchange interactions can be changed locally and a long-range polarization around each impurity may be expected. We have investigated dilute alloys of Pr with Eu and with Gd by magnetization measurements and by Mössbauer spectroscopy.

At low temperatures the susceptibility of the alloys in small applied fields (0.1 to 0.5 T) is higher than that of pure Pr, but as a significant magnetic moment is induced in the Pr matrix by higher applied fields the alloy

magnetization is reduced compared to that of the pure metal. The difference between the magnetization of the alloys and that of pure Pr was found to be qualitatively similar for PrEu and PrGd alloys of equal concentration. From these data we can derive a crude estimate for the exchange integral between Pr and Gd, $J_{PrGd} \sim 4$ K; the exchange coupling strength between Pr and Eu is larger by a factor of 2 to 3.

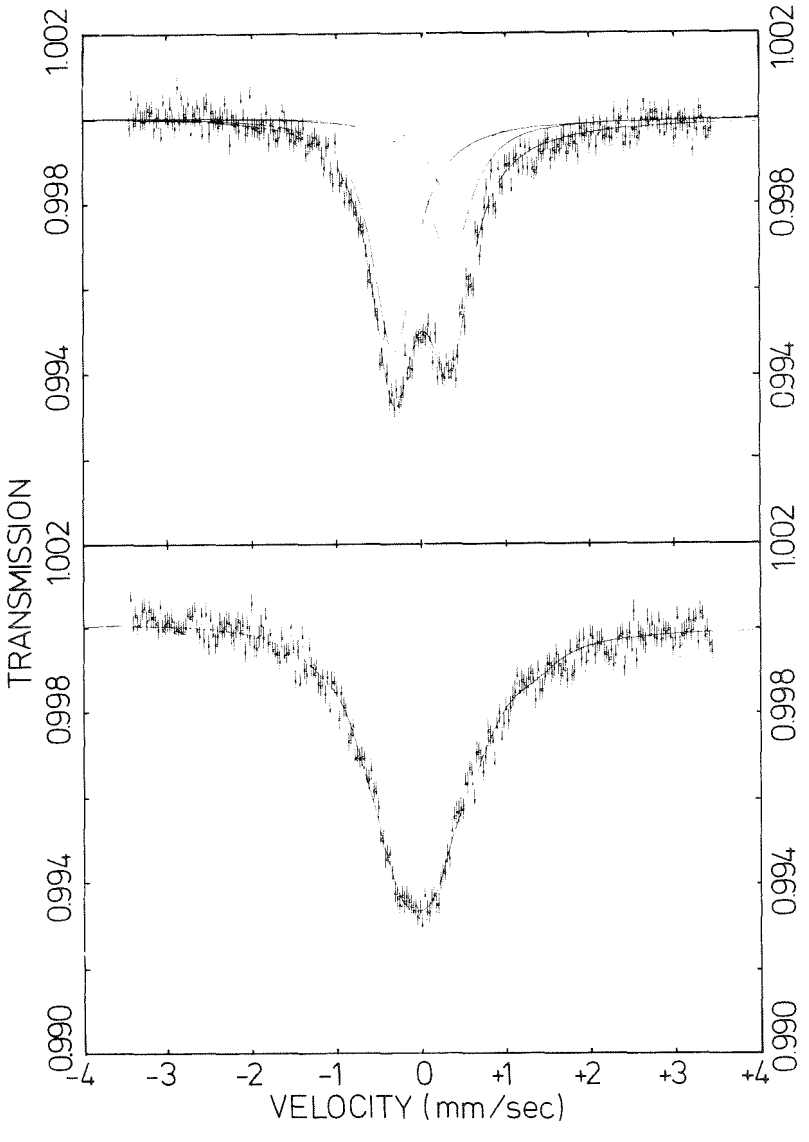


Fig. 1 Mössbauer spectra of $Pr_{.982}Gd_{.018}$ in zero applied field. The upper spectrum at 10 K exhibits quadrupole splitting only whereas at 1.2 K also a magnetic hyperfine field of (19.7±0.4) Tesla at an angle of 90° with respect to the c-axis is acting on all Gd nuclei. The solid lines are transmission integral fits to the data.

$^{151}$Eu Mössbauer spectra for low Eu concentrations ($\lesssim$ 1.2 %) exhibit magnetic splitting at low temperatures (<10 K) which can be ascribed to slow electronic relaxation. The temperature dependence of the hyperfine field for alloys with higher Eu concentrations ($\gtrsim$ 2 %) indicates either antiferromagnetic ordering or spin-glass freezing.

From the quadrupole splitting of the $^{155}$Gd Mössbauer spectra of PrGd alloys (see Fig. 1) the axial crystal field parameter $B_2^o$ was estimated to be $B_2^o$ = 2.4 K for both lattice sites. At low temperatures the spectra of all absorbers (1.8, 3.4, and 8.1 at % Gd) show magnetic hyperfine splitting, thus indicating the onset of magnetic ordering or spin-glass freezing. For the concentrations investigated, the temperatures where the splitting sets in are about 2 to 3 K higher than the spin-glass freezing temperatures derived by Sarkissian /1/ from susceptibility measurements.

A model assuming each magnetic impurity to be surrounded by an antiparallel polarization cloud due to ferromagnetic spin-spin coupling can qualitatively explain the experimental results.

Reference

/1/ B.V.B.Sarkissian, Sol. State Comm. 27, 57 (1978)

## 3.7 Magnetic Interactions in Compounds $GdT_2Si_2$ (T = Mn,Fe,Co,Ni).

*K. Łatka[a], H. Schmidt, V. Oestreich, F. Götz, and G. Czjzek*

[a] *Guest scientist from the Institute of Physics, Jagiellonian University, Craców, Poland*

The metallic compounds of the general formula $RT_2X_2$ (R = rare earth, T = transition metal, X = Si,Ge) which all crystallize in the same body-centered tetragonal structure (I4/mmm) are well suited for systematic studies of the magnetic interactions between ions of the rare earths and of the transition metals in metallic solids. Continuing and extending an investigation of compounds $DyT_2Si_2$ /1/ we have started a study of the series $GdT_2Si_2$ (T = Mn,Fe,Co,Ni) by measurements of the magnetization in the temperature range 1.8K≤T≤290K in fields up to 6 Tesla and by Mössbauer spectroscopy (with $^{155}$Gd, $^{61}$Ni, and $^{57}$Fe).

The results of the magnetization measurements are summarized in table 1. For $GdMn_2Si_2$ the temperature dependence of the susceptibility shows the characteristics of a ferrimagnet with a Néel temperature near 65K. The Mn moment of about $6\mu_B$ estimated from $\chi(T)$ in the temperature range from 100 to 300 K is in agreement with that obtained from the saturation magnetization if we add $7\mu_B$ per Gd ion to the value measured at 2 K.

Table 1

| Compound | $p_{eff}$ [$\mu_B$] | $\Theta$ [K] | $T_N$ [K] | $\langle B_{SF} \rangle$ [T] | $B_{SF/P}$ [T] | $E_{AA}/k_B$ [K] | $E_{AB}/k_B$ [K] | $B_A$ [Tesla] |
|---|---|---|---|---|---|---|---|---|
| $GdMn_2Si_2$ | * | ∿-300 | 65(3) | - | - | - | - | - |
| $GdFe_2Si_2$ | 8.18 | +3 | 8.4(0.2) | 0.3 | 2.5 | 6 | 3 | 0.01 |
| $GdCo_2Si_2$ | 8.19 | -29 | 45(4) | 0.7 | 35 | 8 | 37 | 0.02 |
| $GdNi_2Si_2$ | 7.97 | -1 | 15.0(0.2) | 2.5 | 12 | 7 | 8 | 1 |

*$p_{eff}(Mn) \sim 6\mu_B$ if $p_{eff}(Gd) = 7.94\mu_B$

For the other compounds a Curie-Weiss law $\chi(T) = p_{eff}^2 / 3k_B (T-\Theta)$ was found at high temperatures with an effective moment $p_{eff}$ close to the theoretical value $7.94\mu_B$ for Gd alone. Mössbauer spectra of $^{57}Fe$ in $GdFe_2Si_2$ and of $^{61}Ni$ in $GdNi_2Si_2$ show no magnetic hyperfine splitting for all temperatures down to 1.2K. This result confirms that the 3d moment in these compounds is zero. At low temperatures these compounds order antiferromagnetically. The magnetization curves obtained below the Néel temperature are typical for weakly anisotropic antiferromagnets, as shown in Fig. 1 (data obtained at 2K). As our measurements were performed with polycrystalline materials, the spin-flop transition does not occur abruptly at a sharply defined field $B_{SF}$, but is spread over a range of fields whose average is listed in table 1. For $GdFe_2Si_2$ the transition to the paramagnetic state at the field $B_{SF/P}$ occurs in the field range accessible to us. For the other compounds the transverse susceptibility $\chi_\perp$ determined in the spin-flop phase was used to estimate the values of $B_{SF/P}$.

Although an exact derivation of the interaction energies is not possible as the magnetic structures of the compounds investigated are not known, the most relevant interaction energies can be estimated on the basis of a simple 2-sublattice molecular field approach. As shown in table 1, the intra-sublattice energy $E_{AA}$, given in this model by $E_{AA} = 0.5k_B (T_N+\Theta)$, is practically independent of the 3d element T, whereas the intersublattice energy $E_{AB} = 0.5k_B (T_N-\Theta)$ shows

considerable variation. The results for $E_{AB}$ are confirmed by the values of $B_{SF/P}$ deduced from the low-temperature magnetization curves. (In this simple model $B_{SF/P}$ is proportional to $E_{AB}$). These results point to a magnetic structure consisting of ferromagnetic Gd planes perpendicular to the c-axis which are stacked in some sequence giving net antiferromagnetic order. A structure of this type has been found in $NdFe_2Si_2$ /2/.

The anisotropy field $B_A$ can be deduced from the spin-flop field since $B_{SF}$ is approximately given by $(2 \cdot B_A \cdot B_{mol})^{1/2}$ where $B_{mol}$ is the molecular field. The difference between the small anisotropy fields in the compounds with Fe and Co and the rather large value for the Ni compound is easily explained by different orientations of the magnetic moments as derived from $^{155}Gd$ Mössbauer spectra. In the compounds with Fe and Co the moments are nearly perpendicular to the c-axis. During the spin-flop the moments remain near to some direction in the a-b-plane, an easy plane with small anisotropy. In $GdNi_2Si_2$, on the other hand, the angle between the Gd moments and the c-axis is approximately $30^{\circ}$. Flopping then involves changes of this angle, and just the dipolar contribution to $B_A$ yields a relatively strong anisotropy.

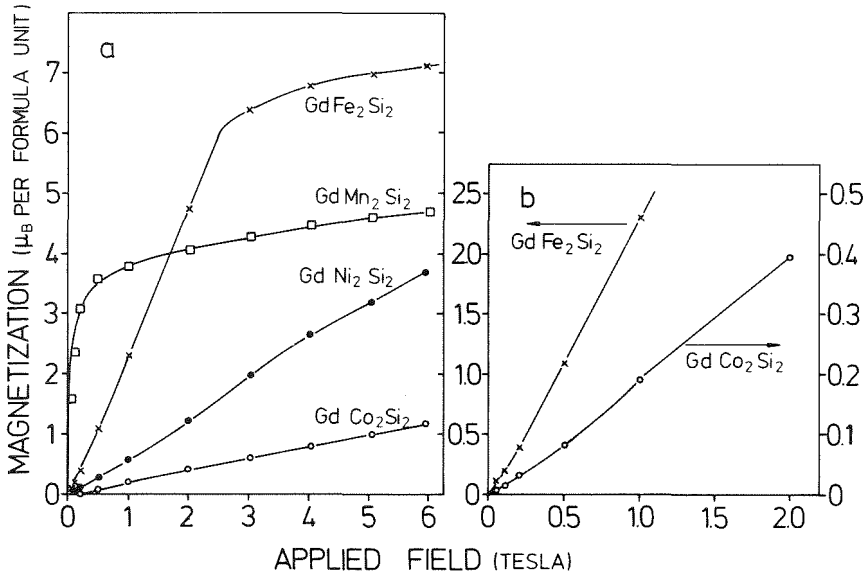


Fig. 1 Magnetization curves of the compounds $GdT_2Si_2$ at 4.2 K. (a) Shows the data for all compounds investigated in the full range of fields up to 6 Tesla. (b) Low-field results for $GdFe_2Si_2$ and $GdCo_2Si_2$.

References

/1/ E.A. Görlich, A.Z. Hrynkiewicz, K. Łatka, R. Kmieć, A. Szytuła, and K. Tomala, J. Phys. (Paris) Colloque, 40, C2-656 (1979)

/2/ H. Pinto and H. Shaked, Phys. Rev. B7, 3261 (1973)

## 3.8 Crystal Field Levels in $La_{.92}Ho_{.08}Al_2$ and $Y_{.92}Ho_{.08}Al_2$

*P. v. Blanckenhagen*

In previous work we have studied the magnetic neutron scattering from (RE) $Al_2$ compounds /1/ /2/. For $HoAl_2$ no crystal field levels have been observed in the paramagnetic state. The magnetic scattering appears as broad quasielastic line, which results from the fast relaxation of the magnetic moments. This relaxational behaviour may be due to the exchange interaction between neighbouring Ho ions or between Ho ions and the conduction electrons /3/. In the first case one would expect a reduction of the relaxation rate by a substitution of the Ho ions by non-magnetic La- or Y-ions.

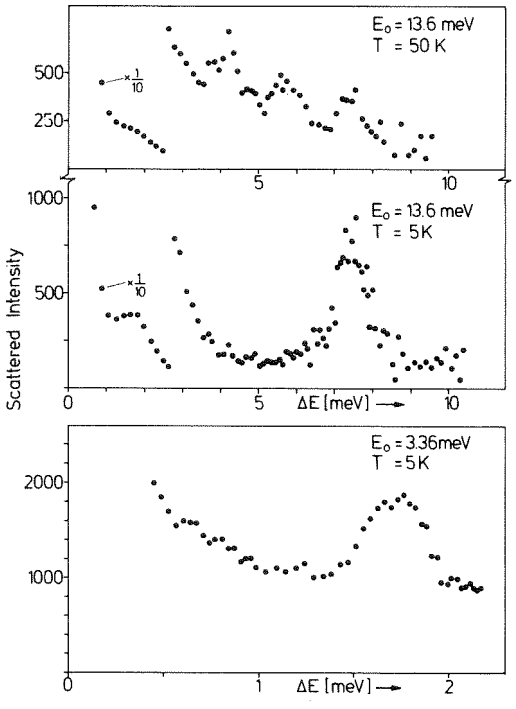


The experiments were performed with the spectrometers MAG 1 and MAG 2 in the time-of-flight mode of operation with energies of the incident neutron beams of 13.6 and 3.55 meV, respectively.

In $La_{.92}Ho_{.08}Al_2$ as well as in $Y_{.92}Ho_{.08}Al_2$ crystal field transitions have been observed (Fig. 1).

The energy levels are different in $Y_{.92}Ho_{.08}Al_2$ and in $La_{.92}Ho_{.08}Al_2$. The results for $Y_{.92}Ho_{.08}Al_2$ can be explained with the crystal electric field parameters of $HoAl_2$ as derived from magnetization data: W = 0.15 and x = 0.32 /4/. Whereas the substitution of Ho by Y reduces only the relaxation rate the substitution of Ho by La also changes the crystal electric field. In the last case the data measured as yet do not allow a determination of x and W.

Fig. 1
Energy spectra of neutrons scattered from $Y_{.92}Ho_{.08}Al_2$. The spectra are calculated from the time-of-flight spectra after subtraction of the background. Peaks due to crystal field transitions are at 1.7, 4.2, 5.7 and 7.4 meV.

References

/1/ P. v. Blanckenhagen, H. Happel, K. Knorr and A. Murani in Prog. Rep. Teilinstitut Nukl. Festkörperphysik, Ges. f. Kernforschung, KFK 2357, 71 (1976)

/2/ P. v. Blanckenhagen, H. Happel and K. Knorr J. Mag. Mag. Mat. 9, 20 (1978)

/3/ K.W. Becker, P. Fulde and J. Keller, Z. Physik B 28, 9 (1977)

/4/ B. Barbara, J.X. Boucherte, M.F. Rossignol and J. Schweizer in Proc. Conf. Neutron Scattering, Gatlinbury (USA), 452 (1976)

# 4. MATERIALS RESEARCH

## 4.1 Disorder Analysis in Ion Implanted Aluminum through Energy Dependent Channelling Measurements

*T. Hussain*[a] *and G. Linker*

[a]*On leave from Physics Department, University of Dacca, Bangladesh.*

The channeling effect together with backscattering measurements using energetic ions is a convenient tool for a qualitative defect analysis in ion implanted semiconductors and metals. Though the disorder of ion implanted metals has not been as widely studied as was done in semiconductors, from the present understanding of this field it is clear that ion-induced disorder in metals is different to that in semiconductors. In ion-implanted metals instead of a disorder peak (which is normally observed in implanted semiconductors) generally a monotonous increment of the dechanneling yield with depth is observed indicating the presence of extended defects like dislocations, interstitial clusters, grain boundaries with associated strains etc. These disorder regions in many cases extend to depths beyond the ions projected range. According to the suggestions given by Quéré /1/ the energy dependence of the dechanneling cross-section may give information about the nature of defects.

Here the results from energy dependent channeling analysis of aluminum single crystals implanted with S, Ca, Cu, Ga, Ge and Cs are reported. Channeling measurements have been performed along the <100> direction with a well collimated beam of $^4He^+$ particles and energies in the range of 1.0 - 3.0 MeV have been used. Typical spectra from a Cu implanted aluminum crystal are shown in Fig. 1 with the energy of the analysing particles as parameter. No disorder peak is observed except a "knee" well deeper than the measured projected range which is about 1100 Å. Similar results have been observed from the Ga, Ge and Cs implanted aluminum samples, however, with no well defined "knee" from the Ga implanted sample. On the contrary S and Ca implanted samples showed a well resolved peak within the measured projected range of the implanted impurities as the energy of the analysing beam was increased. Fig. 2 shows one of such spectra from a Ca implanted sample. This type of direct backscattering peak is exceptional in ion

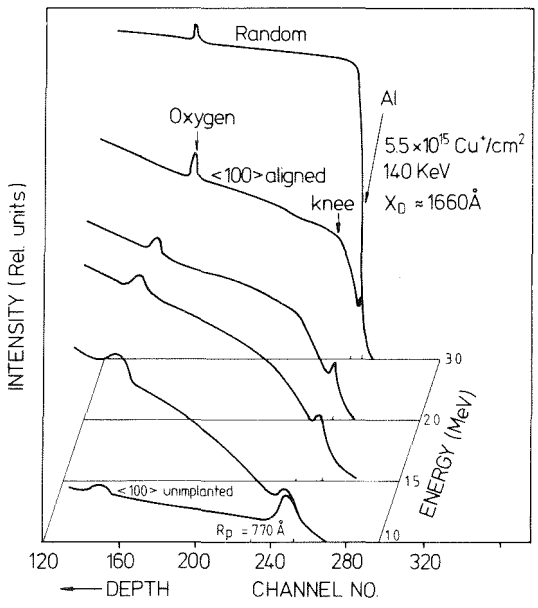


Fig. 1
Backscattering spectra of a <100> aligned Al crystal implanted with $5.5 \times 10^{15}$ $Cu^+/cm^2$, 140 keV at four different analyzing beam energies.

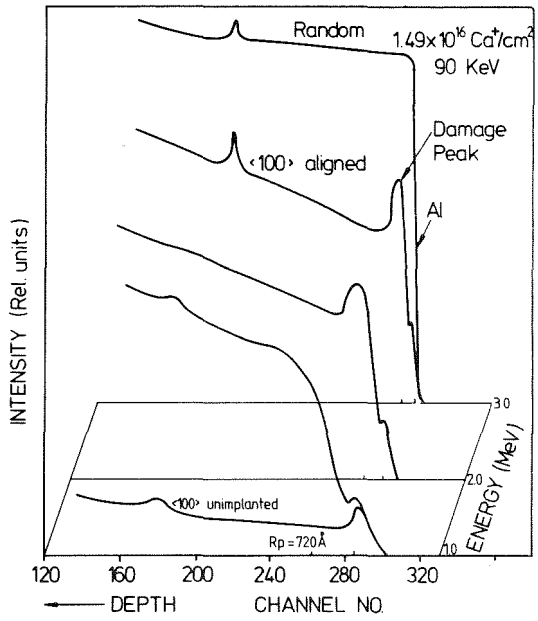


Fig. 2
Backscattering spectra at three different analyzing energies of a <100> aligned Al crystal implanted with $1.49 \times 10^{16}$ $Ca^+/cm^2$, 90 keV.

bombarded metals. It demonstrates the presence of local scattering centers i.e. largely displaced host lattice atoms.

Plots of the dechanneling cross-sections versus energy for the Cu, Ga, Ge and Cs implanted samples show a linear dependence on $\sqrt{E}$ with different slopes for Cs, Cu, Ga and Ge indicating the presence of dislocations with different concentrations. A slight decrease of the dechanneling yield determined behind the disorder peak has been observed for S and Ca implanted samples as the analyzing beam was increased. This is consistent with the presence of local scattering centres, however, the high absolute values of the dechanneling yield demonstrate, that additional defects were produced in the S and Ca implanted samples. It is difficult to determine the nature of this disorder as the true energy dependence may be shadowed by the presence of more than one kind of defect having energy dependences opposite in nature.

The results from the present study showed that different types of defects are stabilized in aluminum by the implantation of different ions.

Reference

/1/ Y. Quéré, Rad. Eff. 28, 253 (1976)

## 4.2 Lattice Location of Implanted Ions in Aluminum Single Crystals

*T. Hussain[a], G. Linker and M. Kraatz*

[a] *On leave from Physics Department, University of Dacca, Bangladesh.*

In comparison to other methods (such as neutron and X-ray scattering) used for the determination of impurity location, the channeling technique has some advantages. This technique gives the location of impurities relative to the lattice atoms and concentrations as low as $10^{-2}$ atomic % can be studied. Again, since this technique probes only the near surface region rather than throughout the bulk of a solid, it is quite amenable to surface related methods of impurity introduction such as ion-implantation.

Here we studied the lattice position of S,Ca,Cu,Ga,Ge and Cs ions implanted into aluminum single crystals. The implantations were performed at room temperature and along random directions. Angular scans were performed along both <100> and <110> directions to obtain an unambiguous lattice site determination. Fig. 1 shows a typical angular scan relative to <110> axis from a Ga implanted sample. An increase of the minimum yield and a narrowing of the yield curve for the impurity is observed in comparison to the yield curve for the host lattice. The substitutional fraction of the implanted ions have been determined from the normalized minimum yield values of the impurity and the host. High substitutional fractions have been observed for Cu(.73) and for Ga(.87). However, the narrowing of the angular widths observed for both impurity atoms, Cu and Ga, indicates slight displacements of these atoms from the ideal lattice position. Values of about 0.02nm for Cu and 0.016nm for Ga have been estimated for the <100> direction for these displacements using Barrett's formula /1/. Ge showed a substitutionality of about 28% whereas S, Ca and Cs were found to be distributed almost randomly as observed in the <100> direction. The angular scan relative to <100> direction from a Ca implanted sample ($6.5 \times 10^{15}$ $Ca^+/cm^2$, 90keV) shown in Fig. 2, however, revealed oscillations in the Ca yield which indicate different defined non-substitutional positions of Ca in the Al host-lattice. The distribution of Ca may be associated with different defects.

From this lattice location studies together with the disorder in Al described in the previous report it may be concluded that maximum distortions of the Al host lattice are caused by atoms which are nonsubstitutionaly distributed in the lattice.

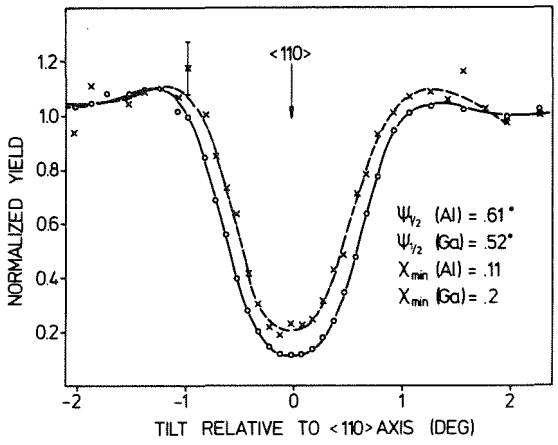


Fig. 1
Angular scan of the backscattered $^4He^+$ yield relative to <110> from a Ga implanted ($5.3x10^{15}Ga^+/cm^2$, 150keV) aluminium crystal. Ga(x--x) and Al(o—o). Incident beam of 2.0 MeV $^4He^+$.

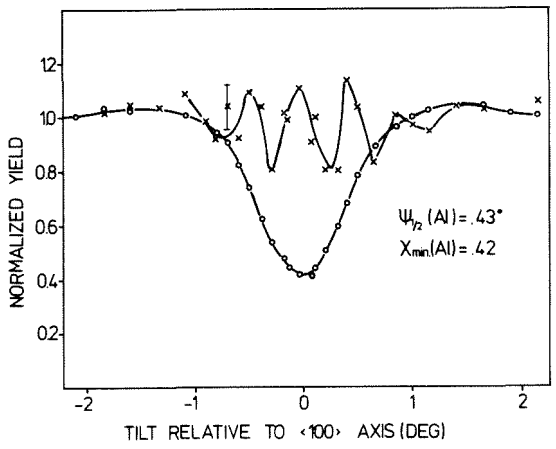


Fig. 2
Angular yield curves relative to <100> from a Ca implanted Al crystal showing oscillation of the Ca (x--x) yield. Incident beam: 2.0 MeV, $^4He^+$

Reference

/1/ J.H. Barrett, Phys. Rev. B3, 1527 (1971)

## 4.3 Annealing Studies of Ion Implanted Al-Crystals

*T. Hussain[a] and G. Linker*

*[a]On leave from Physics Department, University of Dacca, Bangladesh*

The annealing behaviour of aluminum single crystals implanted with S,Ca, Cu,Ga,Ge and Cs ions has been studied in isochronal cycles (60 min) in the temperature range of 100°C up to 500°C. The impurity distribution and the lattice disorder were studied by using channeling and backscattering of 2MeV $^4He^+$ ions along the <100> direction. All samples except the sulphur-implanted crystal showed annealing of the damage with increasing temperature. The annealing of the disorder was connected with a change of the distribution of the implanted ions. Cu,Ga and Ge impurities showed indiffusion starting at about 400°C while for Ca

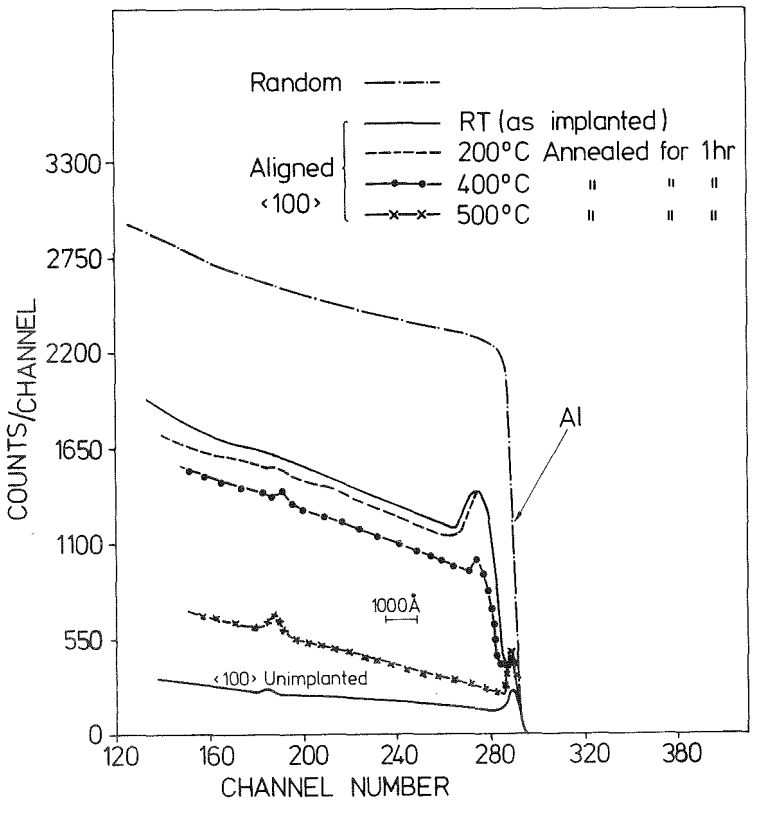


Fig. 1
<100> aligned backscattering from spectra from a Ca implanted sample (RT implantation with $1.49 \times 10^{16} Ca^{+}/cm^{2}$, 90keV) at different annealing temperatures. Analyzing beam of 2 MeV $^{4}He^{+}$.

and Cs outdiffusion was observed at the same temperature. The outdiffusion of Ca and Cs was associated with a recrystallization of the Al host lattice. This behaviour is demonstrated in Fig. 1 and Fig. 2. In Fig. 1 backscattering spectra from Al of a Ca implanted Al sample ($1.5 \cdot 10^{16} Ca^{+}/cm^{2}$, 90keV) are shown after annealing at different temperatures. It can be seen that the disorder peak is completely vanished at 500°C however some disorder is remained as judged from the dechanneling yield. In Fig. 2 backscattering spectra reflecting the Ca distribution for the sample are shown. The Ca redistribution starts at 400°C and a considerable change of the distribution with a sharp peak growing at the sample surface is observed at 500°C. This final distribution indicates that almost all Ca ions are accumulated at the surface. A similar type of behaviour was found for Cs ions while the sulphur distribution and the disorder created by the sulphur im-

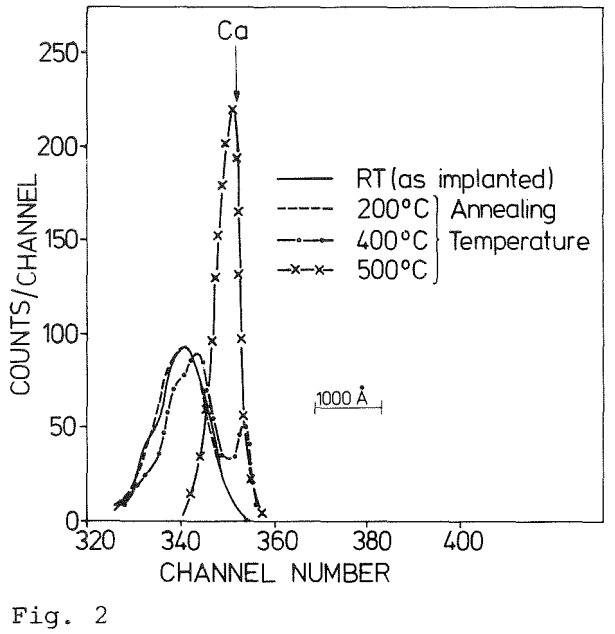


Fig. 2
Ca distributions from the sample of Fig. 1 at different-annealing temperatures.

plantation were stable in the annealing treatment in the quoted temperature range.

The results of these annealing studies demonstrate a close relationship between the annealing of disorder and impurity redistribution in implanted Al single crystals. The annealing of the disorder is correlated with an outdiffusion of the impurities from the disordered regions. While ions occupying substitutional lattice positions probably diffuse into the Al bulk, ions with large atomic radius and distributed nonsubstitutionally seem to move to the sample surface.

## 4.4 Correlation between Oxygen Content $c_o$ and $T_c$ of Granular and Quench Condensed Al-Films Evaporated from Alumina Boats

*M. Nittmann[a], P. Ziemann[a], and G. Linker*

[a] *Phys. Institut, Uni Karlsruhe*

Al-films evaporated at room temperature in an oxygen atmosphere exhibit enhanced transition temperatures to superconductivity $T_c$ up to approximately 2.3 K. The dependence of $T_c$ on the oxygen content $c_o$ of such granular Al-films has been studied in an earlier work /1/ and conclusions on the oxide barrier thickness were drawn /2/. Supplementary to this previous work we report here on the relationship between $T_c$ and oxygen concentration in Al-films evaporated from $Al_2O_3$-crucibles. These crucibles are used, since for Al-films evaporated in this way onto substrates held at 4.2 K, $T_c$-values up to 5.8 K were observed /3/. Thus the question arises whether this type of crucible only acts as an internal source for oxygen, and which oxygen concentration is needed to stabilize the high $T_c$-values of quench condensed Al-films.

To answer this question films were first evaporated at room temperature. In this way one can compare the results with those obtained for films evaporated at room temperature in an oxygen atmosphere. This is shown in Fig. 1, where $T_c$ and the residual resistivity ratio r = R (R.T.)/R (L He) are plotted against the oxygen content $c_o$. This latter quantity was determined by Rutherford backscat-

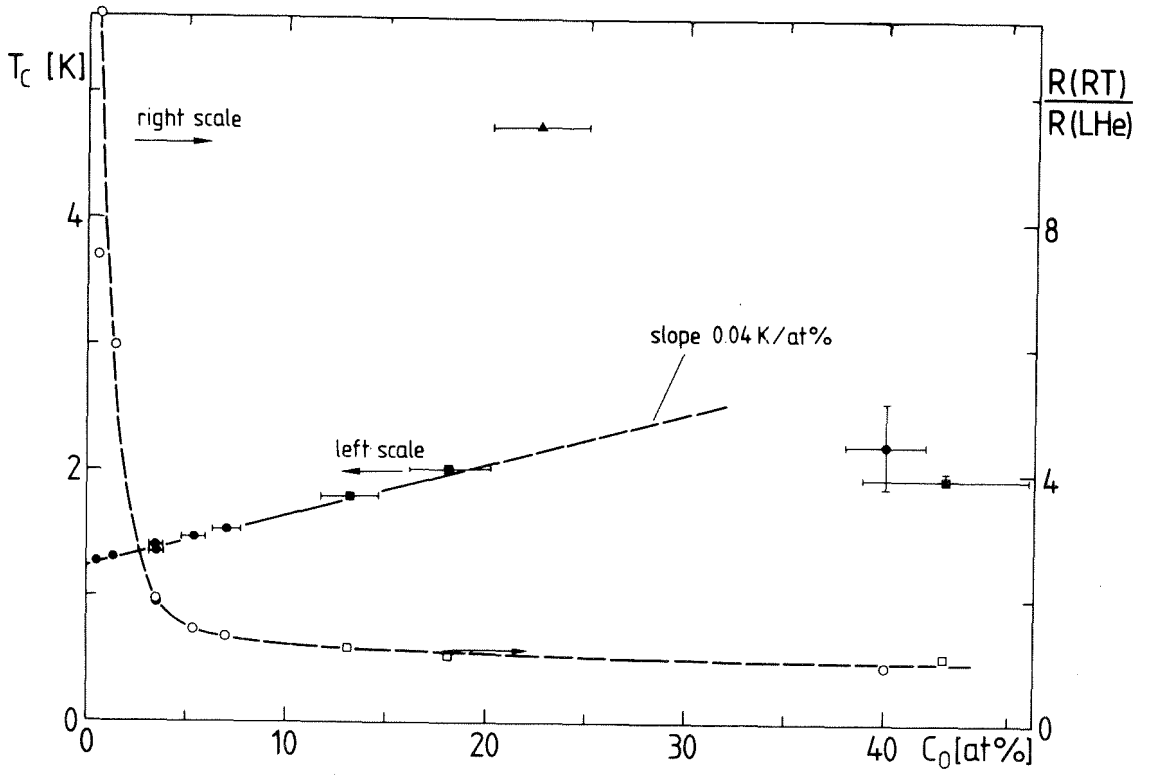


Fig. 1 Transition temperature $T_c$ and residual resistivity ratio as a function of oxygen content in Al layers prepared at various conditions.

- ● $T_c$ value and o resistivity ratio r of films evaporated at room temperature in an oxygen atmosphere /1/.
- ■ $T_c$ value and □ r of films evaporated at room temperature from an $Al_2O_3$ crucible.
- Δ $T_c$ of films evaporated at 4.2 K from an $Al_2O_3$ crucible.

tering of 2 MeV α-particles from films evaporated onto carbon substrates. $T_c$ was measured resistively by means of a standard four-point dc-technique.

From Fig. 1 one can see that the films evaporated from the $Al_2O_3$-crucibles at room temperature show exactly the same behaviour as films evaporated in an oxygen atmosphere. We therefore conclude that the $Al_2O_3$-crucible indeed acts only as an internal oxygen source.

At the present state of investigation we have only analyzed one film, which was quench condensed from an $Al_2O_3$-crucible. The result is included in Fig. 1. The oxygen content of this layer of about 23 at. % corresponds to a $T_c$-value of 4.7 K. This result shows that similar to the room temperature evaporations also for quenched condensed layers high oxygen contents are necessary to stabilize superconducting phases with enhanced $T_c$-values.

References

/1/ P. Ziemann, KfK 2562, (1978)

/2/ P. Ziemann, G. Heim, W. Buckel, Sol. State Comm. 27, 1131 (1978)

/3/ G. v. Minnigerode, J. Rothenberg, Z. Phys. 213, 397 (1968)

## 4.5 Structural Distortions in Nitrogen Implanted Niobium Layers

*G. Linker and M. Kraatz*

In a previous report the influence of ion bombardment on the superconducting transition temperature $T_c$ and the structure of thin evaporated niobium layers was investigated /1/. X-ray analysis of nitrogen implanted samples showed that the Nb bcc-structure was preserved up to an impurity concentration of about 15 at%, however, also a considerable increase of the lattice parameter together with line weakening in particular at high angles was observed. This line weakening suggests a defect model consisting of small static displacements of the lattice atoms.

Here results are reported from a quantitative analysis which has been performed to obtain an estimate of these displacements by treating them like a temperature factor in conventional crystal structure analysis.

In the experiments a niobium layer has been successively implanted homogeneously with 2,4,6,10,15 and 20 at% nitrogen. Diffractometer traces from the sample have been taken before and after each implantation employing a Guinier thin film diffractometer. The intensity of the primary X-ray beam has been controlled with a reference Au sample. The integral line intensities have been determined by planimetry of slow diffractometer traces and the line width was defined as the full width at half peak height.

Together with the intensity reduction an increase of the line width has been observed. Both parameters were found to be a function of implanted nitrogen concentration.

The analysis of the intensity data has been performed with the help of a modified Wilson plot. In an original Wilson plot /2/ the natural logarithm of the ratio of measured and calculated intensities is plotted vs. $\sin^2\Theta/\lambda^2$ ($\Theta$ = glancing angle, $\lambda$-wavelength) and the temperature factor B is determined from the slope of the straight lines through the data points. Here the measured in-

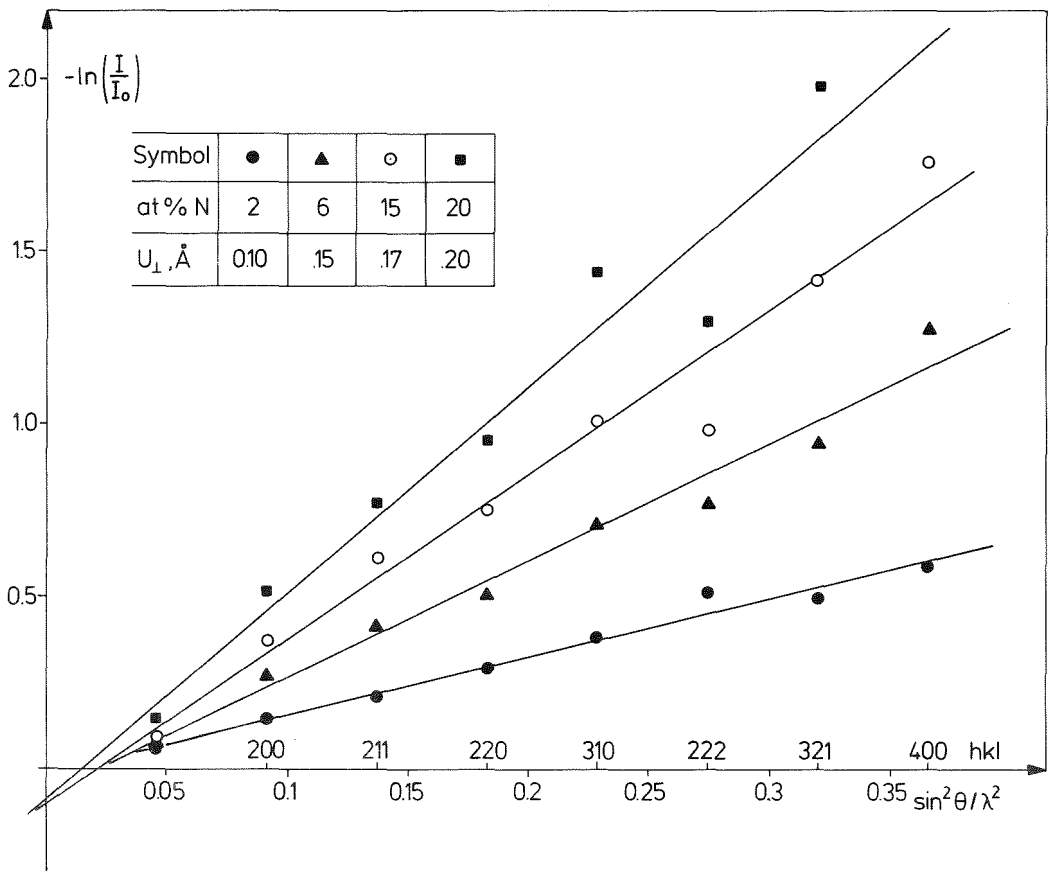


Fig. 1 Wilson plots for four different nitrogen concentrations in an implanted Nb layer.

tensities of the implanted samples, $I_d$, have been referred to the intensities of the not implanted sample, $I_o$, rather than to calculated values. This procedure has two main advantages: firstly, effects of preferred orientation which readily occur in evaporated layers are avoided, secondly, on this relative scale only the static effects arising from the implantation process are taken into account while temperature effects compensate. In this procedure, however, it is assumed, that the dynamical behaviour of the Nb atoms is not changed in the implanted system.

Wilson plots for four different concentrations are shown in Fig. 1. Straight lines from a least squares procedure were fitted through the experimental points. The reasonable linearity between $\ln(I_d/I_o)$ and $\sin^2\theta/\lambda$ is considered to be a justification for the procedure and the suggested defect model. The deviation of the intersection values of the straight lines on the abszissa from the origin is within experimental error. Rms displacements of the atoms $\sqrt{u_\perp^2}$ have been calculated from the relationship $B = 8\,\pi^2 u_\perp^2$ and are given for the different nitrogen concentrations in table 1.

Table 1

| at% N | 2 | 4 | 6 | 10 | 15 | 20 |
|---|---|---|---|---|---|---|
| B, ($\AA^2$) | 0.84 | 1.23 | 1.70 | 2.10 | 2.40 | 3.02 |
| $\sqrt{u_\perp^2}$, ($\AA$) | 0.10 | 0.12 | 0.15 | 0.16 | 0.17 | 0.20 |

The assumption of increasing distortion of the Nb bcc-structure with nitrogen concentration is supported by the numbers. Preliminary analysis of the line widths indicated that line broadening is due to a distribution in the lattice parameter values rather than to crystallite size effects.

References

/1/ G. Linker, Int. Conf. Ion Beam Modification of Materials, Budapest, Sept. 1978

/2/ see e.g. M.M. Woolfson, An Introduction to X-Ray Crystallography, Cambridge University Press, 1970

## 4.6 A Lattice Location Study of Ion Implanted Vanadium Single Crystals

*H.W. Alberts[a] and O. Meyer*

*[a]On leave from Physics Department, University of Pretoria, South Africa*

Vanadium single crystals were implanted with $Ga^+$ and $Se^+$ ions at an energy of 200 keV and a fluence of 1 x $10^{16}$ ions/cm$^2$. This fluence was chosen to correspond to low dose implantations ($\leq 10^{16}$ ions/cm$^2$) where only a narrow surface peak was detected and no polycrystalline layer was observed either on annealing or after implantation /1/. The implantations were performed at room temperature and along random directions.

All channeling and backscattering experiments were performed with 2 MeV $^4He^+$ ions. Typically backscattering spectra for a random and <100> aligned vanadium single crystal are shown in Fig. 1 for the unimplanted as well as implanted (1 x $10^{16}$ $Ga^+$ ions/cm$^2$, 200 keV) case. All spectra are normalized to the same random height. A relative damage-free region is observed behind the surface disorder peak. The dechanneling yield increases monotonically behind this surface disorder peak and extends to a characteristic "knee" well behind the ions projected range, in accordance with earlier measurements /1/.

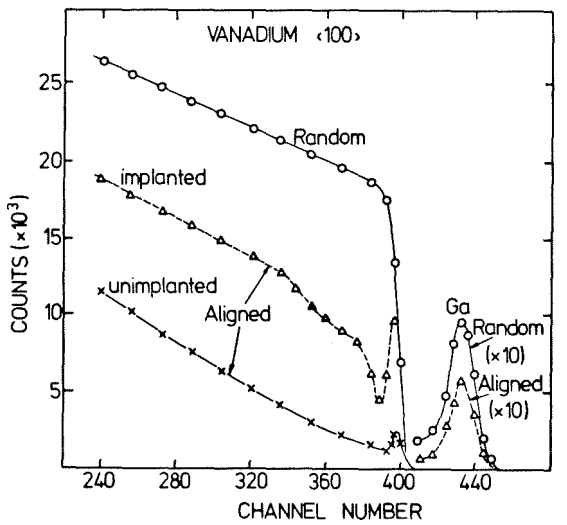


Fig. 1
Backscattering spectra of a <100> aligned V crystal bombarded with 1 x $10^{16}$ $Ga^+/cm^2$, 200 keV. A random and an aligned spectrum from an unbombarded crystal are included in the figure. Incident beam: 2.0 MeV $^4He^+$.

Angular scans were performed along both <100> and <111> directions to obtain an unambiguous lattice site determination after implantation. In all cases the signals from the impurity and host lattice atoms have been selected to correspond to the same depth within the crystal. The measured angular half-angle $\Psi_{1/2}$ for the unimplanted vanadium crystals are equal to those determined for the implanted vanadium crystals and are in agreement with the calculated values ($\Psi_{1/2}^{<100>} = 0.68^o$ and $\Psi_{1/2}^{<111>} = 0.73^o$) obtained by using Barrett's formula /2/ with $\Theta_D = 360^oK$.

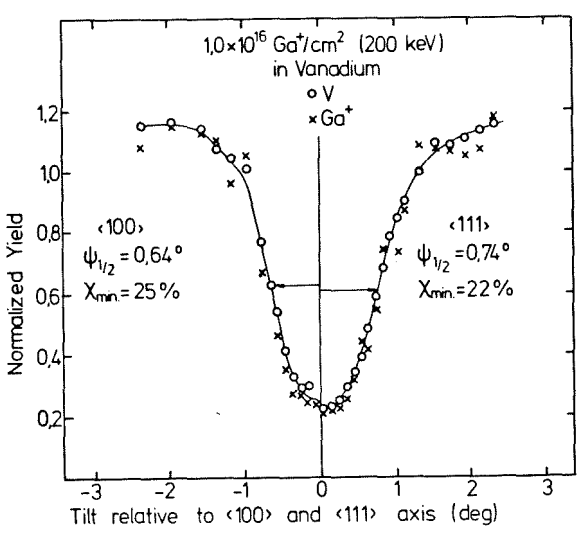


Fig. 2
Angular yield curves relative to <100> and <111> from a Ga implanted (1 x $10^{16}$ $Ga^+/cm^2$, 200 keV) vanadium crystal. Incident beam: 2.0 MeV $^4He^+$.

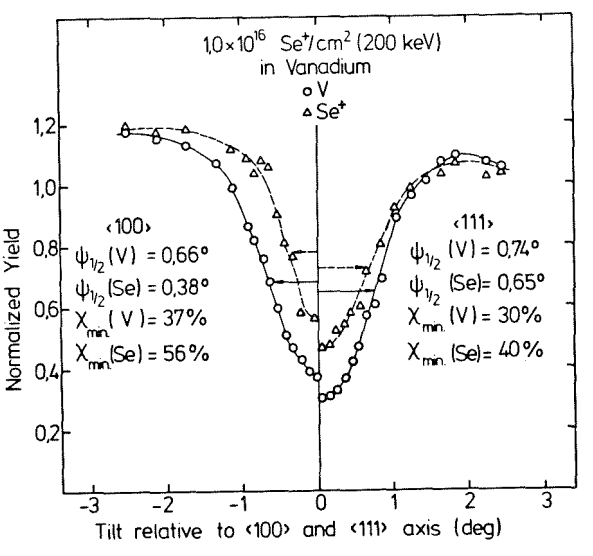


Fig. 3
Angular yield curves relative to <100> and <111> from a Se implanted (1 x $10^{16}$ $Se^+/cm^2$, 200 keV) vanadium crystal. Incident beam: 2.0 MeV $^4He^+$.

For the determination of the lattice position of the implanted ions the data from the angular scans have been used to calculate the substitutional fraction $f_s$, using the definition

$$f_s = \frac{1 - \chi_i}{1 - \chi_h}$$

where $\chi_i$ is the normalized minimum yield from the impurity and $\chi_h$ that for the host at the position of the implanted atoms. From the data presented in Fig. 2 it is seen that the Ga exactly duplicate the distribution of the host within experimental errors. The Ga impurity is found to be 100 % substitutional in both axial directions of the V lattice for this room-temperature implanted species with no annealing.

In contrast to the above result a uniform narrowing of the angular distribution can be seen in Fig. 3 for the implanted Se-atoms in both axial directions. This indicates that the Se-atoms are slightly displaced from their substitutional lattice site. In both directions the substitutional fractions are in the order of 70 %.

References

/1/ M. Gettings, O. Meyer and G. Linker, Rad. Eff. 21 (1974) 51.

/2/ J.H. Barrett, Phys. Rev. B3 (1971) 1527.

## 4.7 Preparation and Analysis of Evaporated Rhenium Superconducting Thin Films

*A. ul Haq, O. Meyer and R. Smithey*

Increases of the superconducting transition temperature, $T_c$ has been reported in rhenium films prepared by different evaporation conditions /1/. These higher transition temperatures ($T_c$ = 2-3 K) as compared to bulk material ($T_c$ = 1.7 K) were attributed to structural distortions and not to impurity effects. The purpose of this investigation was to obtain films having the properties of the bulk material.

Rhenium films were deposited onto quartz and sapphire substrates using different evaporation rates and different substrate temperatures. The pressure

in the evaporation chamber before deposition was typically of $10^{-8}$ torr and rose during deposition to about $10^{-7}$ torr or remained unchanged.

Film thickness, purity, homogeneity and impurity content has been analysed by Rutherford back-scattering of 2 MeV He ions. The structure of the polycrystalline layers has been analysed using a thin film X-ray camera. The superconducting transition temperature $T_c$ was measured resistively and the residual resistivity ratio r, defined as the ratio of the resistances at room temperature and just before transition into the superconducting state, was determined as a measure of the layer quality.

Table 1

Electrical and superconducting properties of Re-single crystal films at $T_s$ = 1100°C or above

| Resistivity at room temp. $\rho_{RT}$ [μΩcm] | Residual resistivity $\rho_o$ [μΩcm] | Thermal resistivity $\rho_{Th}$ [μΩcm] | $r=\frac{\rho_{RT}}{\rho_o}$ | Rate of evaporation [Å/sec] | $T_c$ [K] | $\Delta T_c$ [K] | Thickness [Å] |
|---|---|---|---|---|---|---|---|
| 16.4 | 0.7 | 15.7 | 23.4 | 1.4 | 2.0 | 0.14 | 1100 |
| 18.6 | 4.0 | 14.6 | 4.6 | 4.6 | 2.0 | 0.22 | 1370 |
| 25.4 | 0.58 | 23.1 | 43.8 | 4.8 | 1.7 | 0.12 | 2180 |
| 18.3 | 1.2 | 17.1 | 15.2 | 5.1 | 1.8 | 0.04 | 1120 |
| 17.1 | 1.4 | 15.7 | 12.2 | 6.7 | 1.3 | 0.06 | 1000 |

Bulk properties of Re /1/ $\rho_{RT}$ = 18.7 μΩcm and $T_c$ = 1.7°K

The properties of the layers were depending on the deposition conditions. The layers deposited on sapphire below 1100°C substrate temperature and on quartz substrates had $T_c$ values between 2.3K and 2.7K and r varied from 2.7 to 11.4. The residual resistivity was 2.6 μΩcm and resistivity at room temperature was about 30 μΩcm. These properties are quite different from that of the bulk material /1/ with $T_c$ = 1.7K and $\rho_{RT} \tilde{=}$ 19 μΩcm.

The Re-films deposited at and above 1100°C onto sapphire substrate showed epitaxial growth which was confirmed from Laue patterns and channeling measurements. The electrical and superconducting properties of these films are similar to those of bulk material and are summarized in table 1.

Reference

/1/ P.E. Frieberthauser and H.A. Notarys, J.Vac.Sc.Techl. 7, 485 (1970)

## 4.8 The Influence of Ion Irradiation on Resistivity and Superconducting Transition Temperature of Re-Films

*A. ul Haq, O. Meyer and M. Kraatz*

In previous experiments /1/ it has been observed that implantation of various ions in Re caused an increase of the superconducting transition temperature $T_c$ from 2.2 to about 10 K, depending on the ion species and fluence. In order to investigate the influence of intrinsic defects on $T_c$, pure Re-films were irradiated with various fluences of Ar- and N-ions with energies of 750 keV and 350 keV respectively at room- and liquid nitrogen-temperature. The energies chosen allowed the ions to penetrate the Re-films of thickness up to 200 nm.

In Fig. 1 $T_c$-values of single- and poly-crystalline Re-films are given as a function of Ar-ion fluence. For the single crystalline film $T_c$ decreases and the transition width $\Delta T_c$ strongly increases with fluences up to $2 \times 10^{12}$ Ar/cm$^2$. At higher fluences $T_c$ is found to increase and $\Delta T_c$ to decrease. Polycrystalline layers irradiated either at room temperature or at 77 K in contrast show no large variations neither in $T_c$ nor in $\Delta T_c$ as in the low fluence region. $T_c$ increases monotonously with fluence and saturates for fluences above $2 \times 10^{16}$ Ar/cm$^2$ with a saturation value of 3.1 ± 0.1K. A unique dependence of resisitivity ratio r (defined as the ratio of the resistivities at room temperature $\rho_{RT}$ to the residual resistivity $\rho_o$) on fluence is observed which is independent of growth conditions, irradiating ion mass and irradiation temperature. The resistivity ratio was found to decrease from 24 to 1.5 in the fluence region from $1 \times 10^{12}$ to $2 \times 10^{17}$ ions/cm$^2$. This decrease of r is mainly due to an increase of $\rho_o$ which ranges from 0.7 to 26.8 μΩcm.

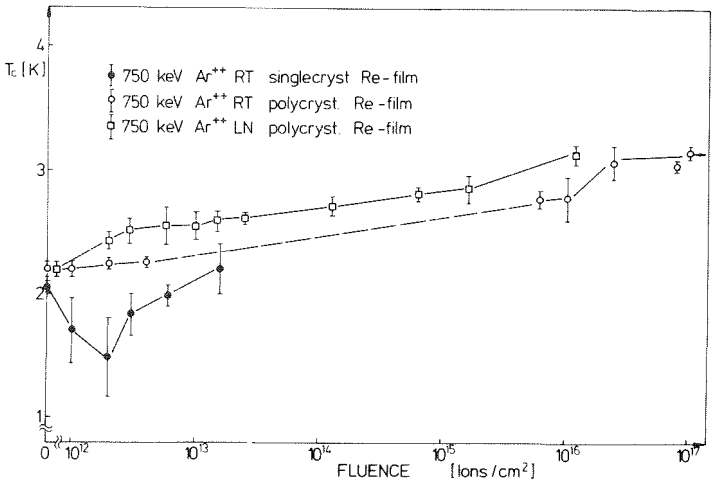


Fig. 1
$T_c$ of single- and polycrystalline Re-films as function of the Ar-ion fluence

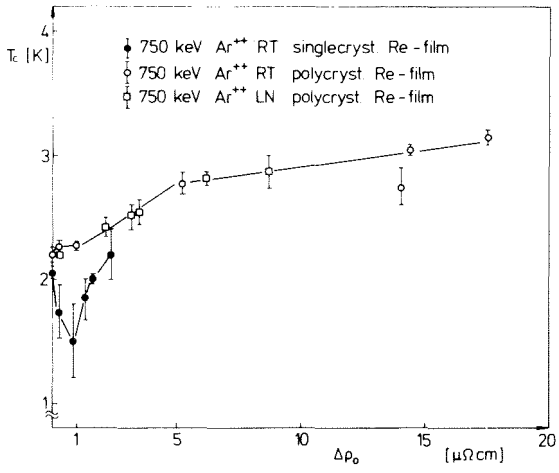


Fig. 2
$T_c$ of single- and polycrystalline Re-films as function of the change of $\Delta\rho_o$

In Fig. 2 $T_c$ is plotted as a function of $\Delta\rho_o$ for poly- and single-crystalline layers. At low fluences, the $T_c$ is observed to decrease with $\Delta\rho_o$ for the single crystalline film. This may be due to the release of the inhomogenous strains which were produced during the film growth and caused high $T_c$ values as compared to the bulk material. However, for higher fluences, $T_c$ is found to increase monotonously with increasing $\Delta\rho_o$ independent of irradiation temperature and ion mass and saturates at about 3.1 K and no difference is observed for poly- and single-crystalline layers. As saturation with fluence occurs for $T_c$ as well as for $\Delta\rho_o$ we believe that only one type of intrinsic defect is produced during irradiation which is responsible for the $T_c$-enhancement.

Reference

/1/ O. Meyer in "New Uses of Ion Accelerators", Ed. J. F. Ziegler, Plenum Press N. Y. (1975)

## 4.9 The Superconducting Transition Temperature of Ion Bombarded VN Layers

*G. Linker, O. Meyer and M. Kraatz*

Theoretical calculations of the superconducting transition temperature $T_c$ of the transition metals V and Nb and the interstitial compound VN resulted in values well above the experimental findings /1/. It was suggested that this discrepancy was due to magnetic effects (paramagnons) competing with supercon-

ductivity in these materials and thus depressing $T_c$. Higher $T_c$-values could be expected if the detrimental influence of magnetism could be compensated e.g. by alloying with hydrogen.

For this reason we have performed implantation and irradation experiments on VN layers with $H^+$ and $He^+$ ions. The VN layers with thicknesses of about 400nm and with pure NaCl structure were obtained previously in a reactive sputtering process /2/. A homogeneous doping with hydrogen was obtained by implantation with different ion energies of 10, 20, 40, 60 and 90 keV and fluences corresponding to concentrations ranging from 0.01 to 50 at% $H^+$ were used. Irradiation experiments with the ions penetrating the layers were performed with 300 keV $H^+$ and 360 keV $He^+$ and fluences in the range of $1 \times 10^{14}$ ions/cm$^2$ - $1 \times 10^{18}$ ions/cm$^2$ and $1 \times 10^{16}$ ions/cm$^2$ - $1 \times 10^{18}$ ions/cm$^2$ for hydrogen and helium respectively. The experiments were carried out at room temperature, however, layers were also bombarded at elevated temperatures and cooled with liquid nitrogen.

All $T_c$ values from these preliminary measurements are summarized in Fig. 1 in a plot vs the resistance ratio r (defined as the ratio of the resistivities at room temperature and above the transition to the superconducting state) which was considered as a measure of the amount of disorder produced during ion bombardement. Results from annealing of a layer doped with 50 at% $H^+$ are included in Fig. 1.

From this figure it can be seen that $T_c$ in VN is rather insensitive to disorder. While the resistance ratio changed from 2 to 1.2 only small effects were observed for $T_c$ with $H^+$ implantation or irradiation.

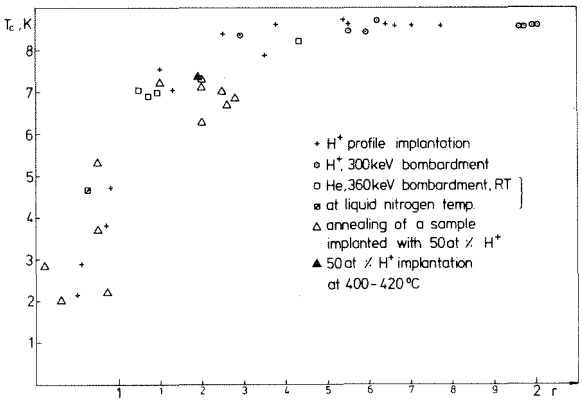


Fig. 1
The superconducting transition temperature $T_c$ of VN layers after different ion bombardment treatments as a function of the residual resistance ratio r.

For small hydrogen contents of about 0.1 at% a $T_c$ increase of about 0.13K occured. It cannot be decided, however, at the present state of investigation whether this effect is due to the presence of hydrogen or to radiation disorder. For higher hydrogen contents (>1 at%) or high fluence $He^+$ irradiation at liquid nitrogen temperature, large $T_c$ depressions and transition widths were observed. X-ray patterns from the bombarded samples showed that these depressions correlate with heavy distortions of the NaCl-structure of VN.

Therefore a 50 at% $H^+$ implantation was performed at an elevated substrate temperature of 400°C. Here the $T_c$ value (midpoint = 7.4 K, onset = $T_c$ of the unimplanted layer) corresponded to the maximum value obtained in an annealing experiment of a layer doped with 50 at% $H^+$ at room temperature. It is not known if at the end of the experiments at elevated temperatures the hydrogen was still present in the layers. Further experiments including hydrogen profiling are necessary to establish appropriate implantation parameters which allow to introduce hydrogen into VN without destroying the superconducting NaCl-phase.

References

/1/ H. Rietschel, H. Winter, G. Riess, Verhandl. DPG (VI) 14, 405 (1979)

/2/ B. Hofmann-Kraeft, KfK 2524, (1977)

## 4.10 Monte-Carlo Channeling Studies on C-Implanted NbC-Single-Crystals

*R. Kaufmann and O. Meyer*

In implantation experiments of understoichiometric NbC-single crystals a maximum $T_c$-value of 11.8 K was reached after C-implantation at substrate temperatures of about 800°C or after room temperature implantation and annealing to 900°C /1/. Channeling measurements in implanted crystals indicated that a partial annealing of the disturbed Nb-sublattice occured in that temperature region, however, in the C-sublattice, as can be seen from the $^{12}C$ (d,p) $^{13}C$ reaction yield, no channeling behaviour could be observed at all. /2/. In order to explain the measured high $T_c$-values it is believed that all C-atoms should stay on their lattice sites. Thus the question about the real structure of the disorder in the implanted crystals arose.

For the analysis of the channeling data a Monte-Carlo-program previously developed for studying damage structures in $V_3Si$-single-crystals was used /3/. The computer simulation was started with a defect model consisting of displaced C-atoms randomly distributed across the channels. The total damage depth was 300 nm. The calculated backscattering spectra indicated that for 50% C-atoms displaced from their lattice sites channeling does no longer occur in the C-sublat-

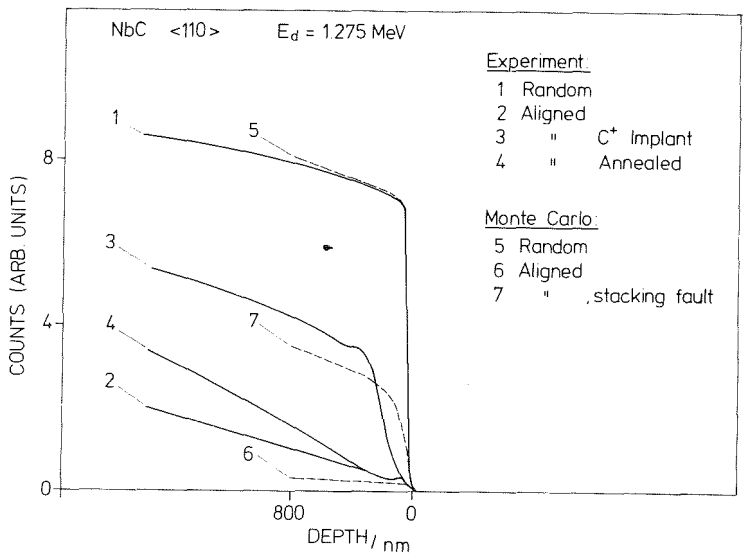


Fig. 1
Calculated aligned spectra (dashed lines) for the Nb-sublattice using a displacement vector of a/6 $<11\bar{2}>$ and a stacking fault length of 7 nm compared to experimental results (solid lines)

tice. This amount of displaced C-atoms, however, causes only a small increase of the dechanneling in the Nb-sublattice in contrast to the experimental results.

Therefore as a second defect structure a stacking fault model was used with two parameters: 1. the length of the stacking fault, 2. the displacement vector describing the shift of the atomic rows parallel to the previous position.

From experiments with plastic deformation in refractory materials it is known that a <111> <110> slip system exists similar to those observed for fcc-metals /4/. Partial dislocations will form and stabilize a faulted area with a displacement vector a/2$<10\bar{1}>$ → a/6$<11\bar{2}>$ + a/6$<2\bar{1}\bar{1}>$ + fault. A vector of a/6 $<11\bar{2}>$ used in the calculation has been found to be in good agreement with experiment as can be seen in Fig. 1 for the Nb-sublattice and in Fig. 2 for the C-sublattice. In this case the metal atoms have to move through carbon sites and a carbon diffusion process must occur. Annealing of the stacking fault occurs at temperatures above 1200°C where carbon diffusion is observed.

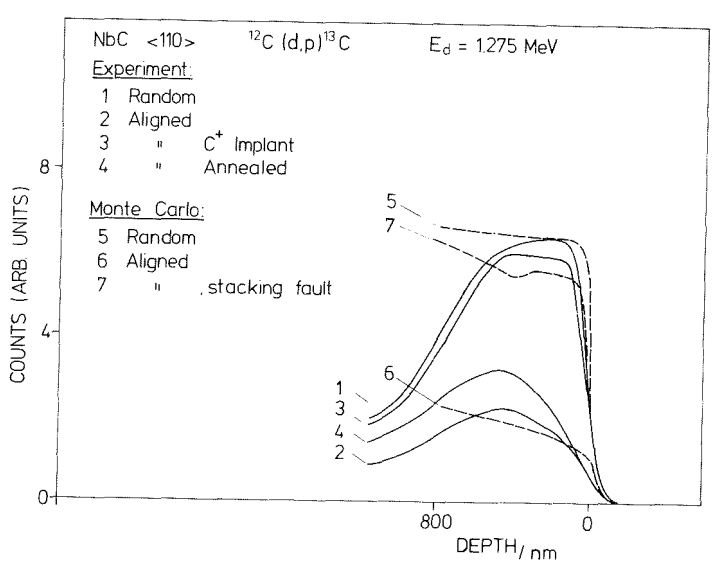


Fig. 2
Calculated aligned spectra for the C-sublattice using the same model compared to experimental results.

From these preliminary investigations on C-implantation results of understoichiometric NbC-single crystals it is concluded that the damage structure existing after the implantation process is consisting of stacking faults.

References

/1/ J. Geerk and K.G. Langguth, Sol. State Comm. 23, 83 (1977)

/2/ J.M. Lombaard and O. Meyer, Rad. Eff. 36, 83 (1978)

/3/ R. Kaufmann and O. Meyer, Rad. Eff. 40, 161 (1979)

/4/ A Summary is given by L.E. Toth: Refractory Materials Vol. 7, Academic Press 1971

## 4.11 The Influence of Light and Heavy Ion Irradiation on the Structure, Resistivity and Superconducting Transition Temperature of $V_3Si$ - A Comparative Study

*O. Meyer, G. Linker, M. Kraatz, R. Smithey*

Different defect structures such as disordered regions, antisite defects and static displacements of atoms have been observed after irradiation with electrons, light and heavy ions and neutrons in materials with A15 structure. It is suggested that only one type of defect is responsible for the large depressions of $T_c$ and this "universal defect" might as well ultimately limit the highest $T_c$-values obtainable in these materials.

$V_3Si$ poly- and single crystalline thin films and a $V_3Si$ single crystal have been irradiated with various fluences of He- and Kr- ions at room temperature. Quite different damage structures are produced for He- and Kr - irradiation in the fluence region where the $T_c$-depression occurs. This can be seen from channeling results /1/ /2/ and from integrated X-ray intensity measurement where it has been shown that in $V_3Si$ films where $T_c$ has been reduced by the same amount with He- and Kr-ion irradiation a stronger intensity reduction and a larger increase of the lattice parameter is found for Kr-irradiated samples.

This additional damage component in Kr-irradiated $V_3Si$ consists of strongly disordered regions which will lead to complete amorphization of the irradiated

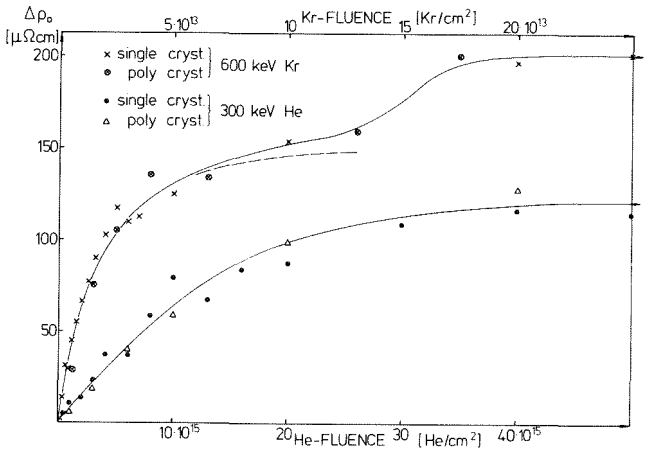


Fig. 1
Change of the residual resistivity of single- and polycrystalline $V_3Si$-layers as function of the He- and Kr- ion fluence

volume at fluences above 2 x $10^{14}$ $Kr/cm^2$ in agreement with the channeling results. As this disorder is not observed for He- irradiated layers it is not preferentially responsible for the $T_c$ depression.

This damage component does also influence the residual resistivity as can be seen in Fig. 1 where the influence of He- and Kr-ion fluence on the residual resistivity $\Delta\rho_o$ is given. ($\Delta\rho_o = \rho_o^{irr} - \rho_o$, the residual resitivity to irradiation is subtracted). The $\Delta\rho_o$-dependence on He-fluence F exhibits an exponential behaviour of the form $\Delta\rho_o = A(1-\exp(-BF))$ where A the saturation value is equal to 130 μΩcm. Applying a similar saturation formula to the $\Delta\rho_o$ (F) dependence for Kr-irradiated layers it is seen that a second damage component contributes to $\Delta\rho_o$ in the fluence region where the disordered regions start to overlap and $T_c$ has reached its saturation value.

$T_c$ is found to decrease exponentially with Kr- and with He-fluence and a saturation value of 1.3 K has been observed for He- as well as for Kr-ions. The dependence of $T_c$ on fluence is described by an exponential term with B similar to that given above, indicating that the $T_c$-change is determined by the process of damage production and saturation. As $T_c(F)$ and $\Delta\rho_o(F)$ have similar exponential dependences one expects a linear correlation between $T_c$ and $\Delta\rho_o$. In Fig.2

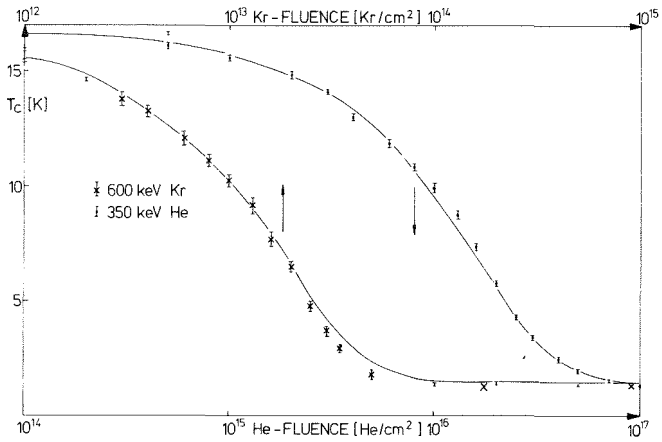


Fig. 2
$T_c$ as function of $\Delta\rho_o$ after He- and Kr- irradiation. Included are results from a n-irradiated $V_3Si$-single crystal /3/ and theoretical results (solid lines /4/)

it can be seen that $\Delta\rho_o$ increases with decreasing $T_c$ independently of the kind of radiation (data for n-radiation have been included /3/). Deviations from this linear behaviour do not occur because the enhanced damage contribution to $\Delta\rho_o$ for heavy ion irradiation happens to take place when $T_c$ has reached the saturation value. Results from a theoretical model calculation /4/ have been included in Fig. 2 and a good agreement is reached between measured and calculated values.

References

/1/ O. Meyer and B. Seeber, Solid State Commun. 22, 603 (1977)

/2/ R. Kaufmann and O. Meyer, this issue, p. 105

/3/ R. Viswanathan and R. Caton, Phys. Rev. B18, 15 (1978)

/4/ L.R. Testardi and L.F. Mattheiss, Phys. Rev. Lett. 41, 1612 (1978)

## 4.12 Low Temperature Irradiation of $Nb_3Sn$ and $V_3Si$ with High Energy Sulphur Ions

*H. Adrian[a], G. Ischenko[a], M. Lehmann[a], P. Müller[a], H. Braun[a] and G. Linker*

[a] *Physikalisches Institut der Universität Erlangen-Nürnberg, D 8520 Erlangen (F.R.G.)*

[b] *Institut für Angewandte Physik der Universität Giessen, D 6300 Giessen (F.R.G.)*

Journal of the Less-Common Metals, 62 (1978) 99-110

Abstract

The critical temperature $T_c$, the transition width $T_\phi$ and the residual resistance $R^o$ of $Nb_3Si$ and $V_3Si$ have been measured as functions of the fluence of 20 MeV sulphur ions below 20 K and isochronal annealing up to 290 K. The temperature dependence of the resistivity is reported for samples with different irradiation-induced states of damage. $T_\phi$ and the thermal part of the resistivity are unambiguously correlated to the $T_c$ versus fluence behavior. At high fluences the $T_c$ of $Nb_3Sn$ again shows a minimum as a function of fluence, as reported ear-

lier for oxygen irradiation. The temperature coefficient of the resisitivity changes from positive to negative when the $T_c$ of $Nb_3Sn$ passes through the minimum. A qualitatively different annealing behavior of $T_c$ and $R^o$ is observed for samples irradiated to $T_c$ values before and after the minimum. Highly damaged $Nb_3Sn$ shows an increase of $R^o$ with increasing annealing temperature. The results are compared with A15 irradiations with different projectiles and with heavy ion irradiations of superconducting elements.

## 4.13 Analysis of the Defect Structure in Kr-Bombarded $V_3Si$ - Single Crystals

*R. Kaufmann and O. Meyer*

In order to simulate the effect of neutron bombardment on the defect structure in $V_3Si$ irradiations with 600 keV-Kr-ions were carried out. Backscattering spectra from the bombarded sample showed a peak structure growing with increasing Kr-fluence. The depth position of this structure is in accordance with the primary energy deposition profile whose maximum was calculated to be at a depth of 100 nm /1/ (Fig. 1).

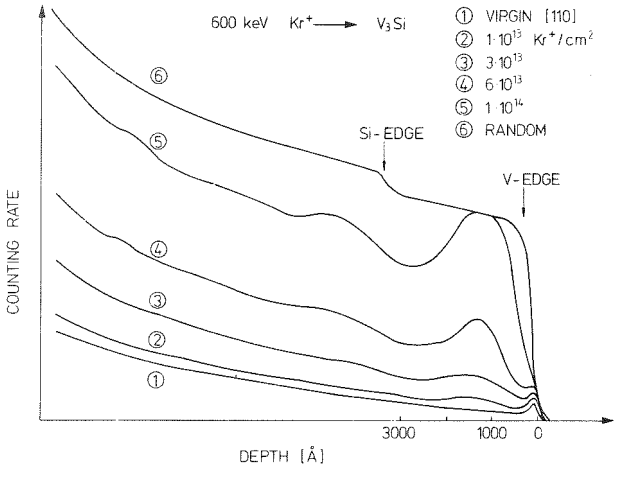


Fig. 1
Random and aligned backscattering spectra with 2 MeV-He-ions before and after $Kr^+$-irradiation with various fluences.

The direct backscattering component is probably due to V-atoms having large displacement values. Angular yield curves measured after 3 x $10^{13}$ and 6 x $10^{13}$ $Kr^+/cm^2$ irradiation showed a parallel narrowing of the curves. A similar behaviour is normally found in measurements at higher temperatures where the thermal vibration amplitudes are enlarged.
Computer simulations were performed in order to get quantitative results about the $Kr^+$-irradiation-induced defect structure. As a damage depth distribution a primary energy depo-

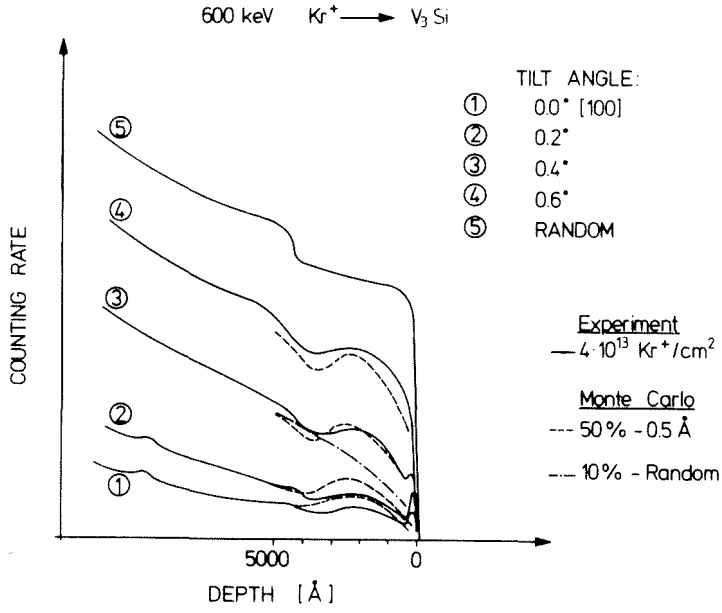


Fig. 2
Experimental and calculated spectra at different tilt angles to the <100>-direction.

sition profile calculated with a program from D.K. Brice /1/ was chosen. Two models were used in the calculation: in the first one 50% of the V-atoms (at the maximum of the depth distribution) were displaced according to a Gaussian distribution with a mean displacement of 0.5 Å, in the second one 10% of the V-atoms were randomly displaced. Backscattering spectra and angular yield curves were calculated for both models.

The spectra for both models agree at tilt angles of $0.0^{\circ}$ and $0.2^{\circ}$ whereas at greater angles no peak structure is developed with the random displacement model. From this result the Gaussian distribution of the displacements seems to be more probable.

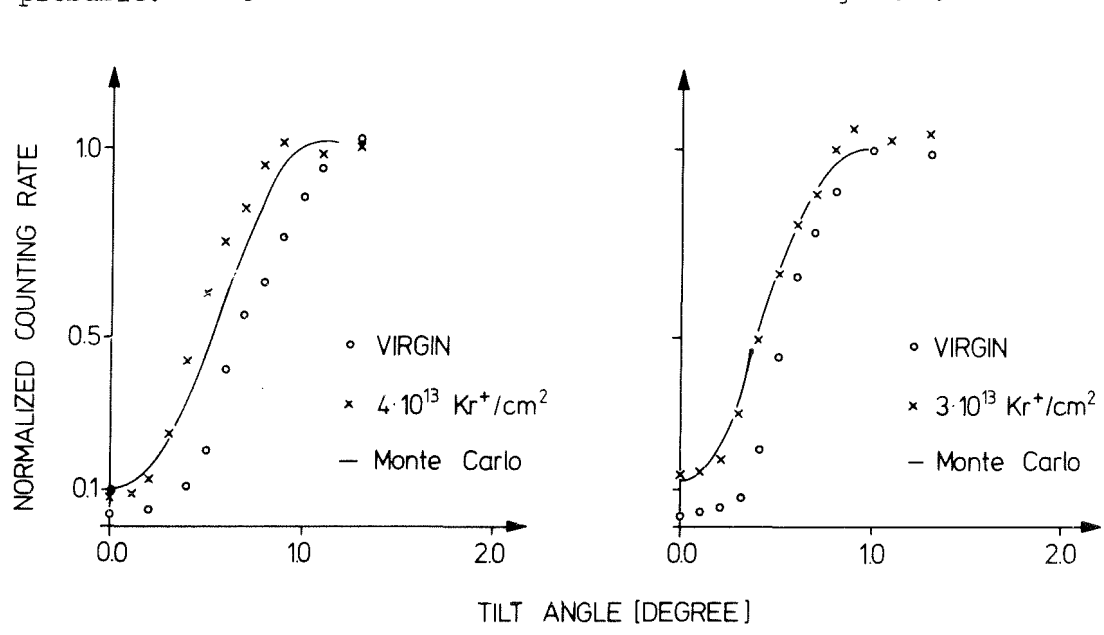


Fig. 3 Experimental and calculated angular yield curves for the <100> and the <110>-direction.

The angular yield curves simulated with both models show significant differences (Fig. 3). In the curve calculated with the random displacement model only the minimum yield is raised whereas the half-width of the curve does not change. In the Gaussian displacement model the minimum yield increases and also a decrease of the half-width is observed which is in good agreement with the experimental result.

Summarizing, the comparison between experiment and Monte-Carlo-simulation leads to the following conclusions:

The development of a peak structure in the experimental spectrum shows that the defect structure here is completely different from that in the transmission region of He-ions. This phenomenon probably is due to the higher collision densities with Kr-ions. The simulation tells that the atoms are probably distributed according to a Gaussian probability function with a displacement length large as compared to a thermal vibration amplitude.

Reference

/1/ D.K. Brice, Sandia Lab. Res. Report SAND 75-0622, July 1977

## 4.14 Computer Simulation of Channelling Measurements on $V_3Si$ Single Crystals

*R. Kaufmann and O. Meyer*

Radiation Effects 1979, Vol. 40, pp. 97-104

Abstract

A computer program has been developed to simulate the channelling process of He-ions in $V_3Si$ with A15 crystal structure. The program considers the anisotropy of the thermal vibrations of the V-atoms and takes into account the interactions of an ion with all neighboured atoms in a plane. Angular scan curves through the <100>- and the <110>-channelling directions in the V- and the Si-sublattices are calculated with this computer program and found to be in good agreement with measured values. Calculated depth dependences of the critical angle and the minimum yield are in reasonable agreement with the measured results. Analytical treatments have also been applied but fail to describe the measured data.

## 4.15 Computer Simulation of Channelling Measurements in He-Irradiated $V_3Si$ Single Crystals

*R. Kaufmann and O. Meyer*

Radiation Effects 1979, Vol. 40, pp. 161-166

Abstract

A previously developed computer program has been extended to simulate the channeling process in $V_3Si$ after irradiation at room temperature with $4 \times 10^{16}$ and $1.5 \times 10^{16}$ $He/cm^2$ at energies of 300 and 50 keV respectively. The best agreement with measured results in the transmission region of the ions with 300 keV was obtained by assuming an average static displacement of 0.05 Å of all V-atoms from their lattice sites. In order to study the radiation damage in the region where the 50 keV He-ions came to rest depth profiles of defects as well as lateral profiles perpendicular to the channels have been simulated in the program. The number and the lateral distribution of the defects have been varied until the measured back-scattering aligned yields in dependence of the incident beam angle could be reproduced by the calculation. By this method the assumption is preferred that about 50% of the V-atoms are displaced with a maximum displacement length of 0.5 Å.

## 4.16 X-Ray Diffraction Studies on He- and Ar-Irradiated $Nb_3Ge$ Thin Films

*J. Pflüger, O. Meyer and M. Kraatz*

Statistically distributed static displacements of atoms in He- and Kr-irradiated $V_3Si$-single crystals have been determined by channeling experiments and are believed to be responsible for the large decrease of $T_c$ with ion fluence in superconductors with A15 structures /1/ /2/. In order to get information on the existence of static displacements in irradiated polycrystalline material with A15 structure we have performed measurements of relative integrated X-ray inten-

sities on superconducting $Nb_3Ge$-layers before and after irradiation with 350 keV He- and 650 keV Ar-ions. Intensity measurements were carried out with a Seemann-Bohlin focusing diffractometer. A Ge-monochromator was used to select Cu - $K_{\alpha 1}$ radiation. The area irradiated with ions was larger (about 10 mm in diameter) than the X-ray beam diameter (about 3 x 5 $mm^2$). Intensities of 13 lines were measured prior and after irradiation at different fluences. The intensity ratio $I/I_o$, where $I_o$ and I is the intensity of a particular line prior and after irradiation, respectively, is altered due to irradiation effects only.

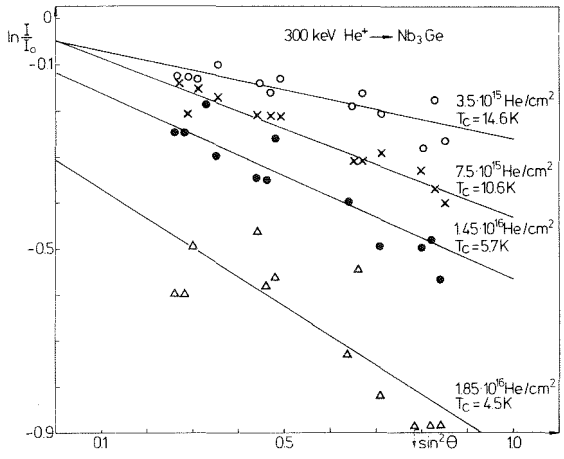


Fig. 1a
$\ln(I/I_o)$ as function of $\sin^2\theta$. $T_c$-values after He-irradiation at various fluences are indicated

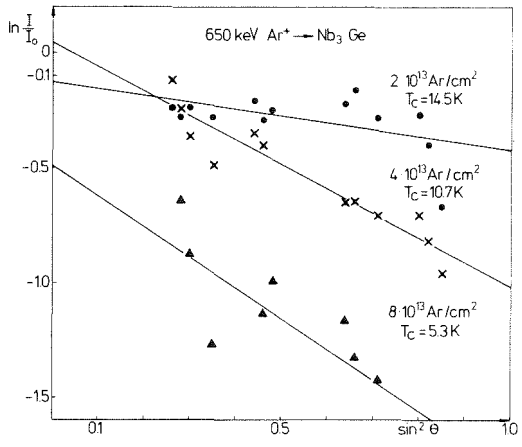


Fig. 1b
$\ln(I/I_o)$ as function of $\sin^2\theta$ with the Ar-ion fluence as parameter

In Figs. 1a and 1b $\ln(I/I_o)$ is given as function of $\sin^2\theta$ after irradiation with various fluences of He- and Ar- ions. Fluences used and $T_c$-values obtained after irradiation are indicated in the figures. The slopes of the least square fit straight lines are equal to $2B/\lambda^2$, where B is equal to $8\pi^2 \langle u^2 \rangle$ and $\langle u^2 \rangle$ is the mean square displacement of atoms. With increasing ion fluence $\langle u^2 \rangle$ is found to increase for He- as well as for Ar-irradiation. The most simple explanation for this result is the assumption of the existence of static displacements which now seem to be a common defect in irradiated A15 materials. The displacement amplitudes as determined from these X-ray experiments have been correlated to the observed relative $T_c$ decrease $(\Delta T_c + T_c^s) / T_{c_o}$ in Fig. 2, where $\Delta T_c$ is equal to $T_{c_o} - T_c^{irr}$ with $T_{c_o}$ and $T_c^{irr}$ being the $T_c$-values for the ion-irradiated and the irradiated layer, respectively, and $T_c^s$ is the saturation value at high fluences. Displacement amplitudes as measured by the channeling technique /1/ /2/ for He- and Kr-irradiated $V_3Si$ single crystals have been included in Fig.2 together with the value determined by Cox and Tarvin /3/ for a neutron irradiated $V_3Si$ single crystal. For similar reduced $T_c$ values the mean displacement amplitude

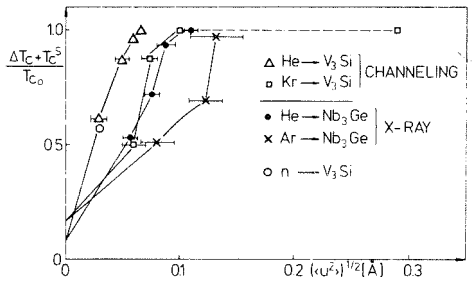


Fig. 2
Relative $T_c$-decrease as function of the average displacement amplitude

is larger for Ar- and Kr- than for He-irradiated $Nb_3Ge$ and $V_3Si$. This result can be explained by assuming that different defect structures are produced by light and heavy ion irradiation: a) displacements with small amplitudes homogeneously distributed in the irradiated volume are preferentially produced by light ion irradiation b) amorphous zones and regions with large displacement amplitudes inhomogeneously distributed in the irradiated volume are mainly produced by heavy ion irradiation and will completely shadow small displacements in the total volume. This damage model is supported by X-ray intensity measurements, channelling measurements and from the functional dependence of $\Delta\rho_o$ on ion fluence. In He-irradiated material strongly disordered regions do not exist and are not responsible for the $T_c$ decrease. In heavy ion irradiated A15 material the presence of strongly disordered regions shadow the possible existence of small displacements homogeneously distributed in the irradiated layer. From channelling results the total volume of strongly disordered regions has been determined and it was concluded that these defects are not responsible for the observed $T_c$-depression in $V_3Si$ and $Nb_3Ge$ irradiated with heavy ions.

References

/1/ O. Meyer and B. Seeber, Solid State Commun. 22, 603 (1977)

/2/ R. Kaufmann and O. Meyer, Rad. Effects 40, 161 (1979)

/3/ D.E. Cox and J.A. Tarvin, Phys. Rev. B18, 22 (1978)

## 4.17 On the Correlation of the Superconducting Transition Temperature and the Residual Resistivity in Irradiated $Nb_3Ge$-Layers

*J. Pflüger, O. Meyer and M. Kraatz*

The superconducting transition temperature, $T_c$, of A15 materials is strongly depressed by particle and neutron irradiation /1/. For irradiated $V_3Si$-films

the decrease of $T_c$ is correlated with an increase of the residual resistivity, $\rho_o$, independent of the kind of irradiating particles /2/.

$Nb_3Ge$-layers have been irradiated with 350 keV He-and 650 keV Ar-ions at various fluences at room temperature in order to test this universal behaviour.

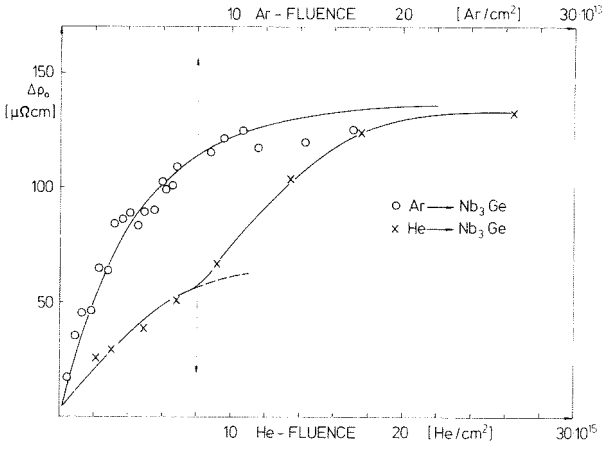


Fig. 1
The change of the residual resistivity of $Nb_3Ge$-layers as function of the He- and Ar-fluence

In Fig. 1 the dependence of $\Delta\rho_o(\rho_o$, the residual resistivity prior to irradiation has been subtracted) on the He- and Ar-ion fluence is shown. $\Delta\rho_o$ saturates at similar values of $\Delta\rho_o$ equal to 130 μΩcm irrespective of irradiating particle mass, however the functional dependence is different for He- and Ar-ion fluences. For $V_3Si$ /2/ different saturation values have been observed for Kr- and He-ion irradiation. The dependence of $\Delta\rho_o$ on Kr-fluence in $V_3Si$ is similar to the dependence of $\Delta\rho_o$ on He-fluence in $Nb_3Ge$ indicating, that $Nb_3Ge$ is more sensitive to radiation damage than $V_3Si$, where the amorphous state can not be reached with He-irradiation. In $V_3Si$ strongly disordered regions produced by Kr-irradiation influence $\Delta\rho_o$ at fluences where $T_c$ had already reached it's saturation value /2/. For Ar-irradiated $Nb_3Ge$ however, strongly disordered regions contribute to $\Delta\rho_o$ at fluences, where the $T_c$-depression occurs. From this, we expect that for $Nb_3Ge$ the correlation between $T_c$ and $\Delta\rho_o$ does depend on irradiating particle mass. In Fig. 2 it is seen that for the same reduction of $T_c$, $\Delta\rho_o$ is larger in Ar- than in He-irradiated $Nb_3Ge$-layers. This result can be interpreted simply by a reduction of the areal cross section of the irradiated layer due to the presence of disordered zones of high resistivity. The measured resistance from the lightly damaged part of the layer is increased due to the reduced areal cross section and an enhanced $\Delta\rho_o$-value is deceived. The conclusion would be that the universal dependence of $T_c$ on $\rho_o$ is not violated.

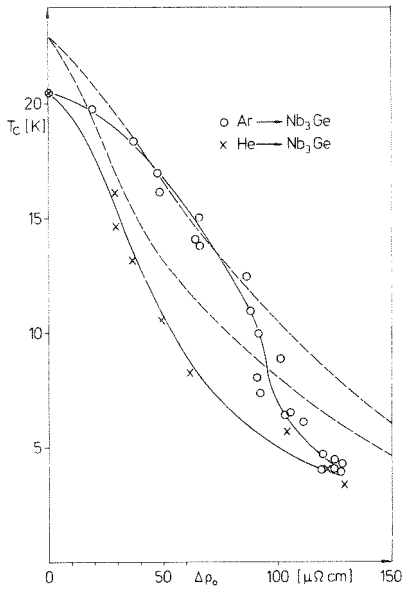


Fig. 2
The correlation of $T_c$ and the residual resistivity for He- and Ar-ion irradiation $Nb_3Ge$-layers

References

/1/ Proc. International Discussion Meeting on Radiation Effects on Superconductors J. Nucl. Materials 72,1-300 (1978)

/2/ O. Meyer, G. Linker, M. Kraatz, R. Smithey (this issue), p. 102

## 4.18 X-Ray Analysis of Implanted Surface Layers on Bulk Samples of the Niobium-Germanium A15 Phase

*J. Geerk and G. Linker*

The modification of structural and superconducting properties of bulk samples by ion implantation is a subject of increasing interest in our laboratory. The determination of the composition of the implanted surface layers is possible with Rutherford backscattering. The characterization of the crystallographic structure seems to be difficult due to the penetration depth of the X-ray radiation which e.g. for CuKα and for materials of interest like Nb, NbC, $Nb_3Ge$ is of the order of 10 µm which has to be compared to the typical depth of implanted layers of 1000 to 2000 Å. It is obvious that most of the diffracted intensity then originates from unimplanted material. One possibility to increase the ratio Γ of the X-ray intensity diffracted from the implanted layer to the intensity of the backing material is to use small incident angles resulting in smaller effective penetration depths. Fig. 1 shows Γ as a function of the depth of the implanted layer for $Nb_3Ge$ calculated using the absorption coefficients listed in /1/ for an incident angle of 10°. As can be read from the figure an implanted layer of for instance 2000 Å thickness yields 30 % of the intensity diffracted from the backing material.

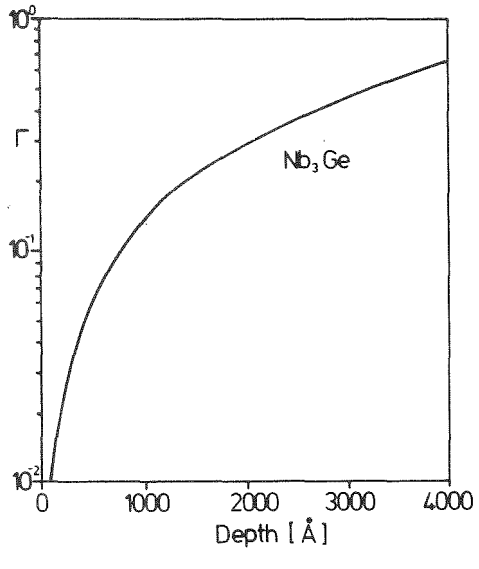


Fig. 1
The ratio Γ of X-ray intensity diffracted from an implanted surface layer to the intensity of the backing material as a function of the depth of the implanted layer.

High $T_c$ surface layers of 2000 Å thickness on low $T_c$ bulk material of the niobium germanium A15 phase have been produced by implantation of Ge-ions as described in /2/. X-ray measurements were carried out using a thin film Guinier Camera adjusted to an incident angle of 10°. As the sample was of polycrystalline composition with crystallites of about 0.01 mm Ø instead of continuous diffraction lines with unimplanted samples intense diffraction points at the line position were observed on the film. The implanted and annealed samples showed also these distinct points but additionally with satellites situated at slightly higher diffraction angles. These are caused by diffraction from the implanted surface layer. We conclude that the implanted high $T_c$ surface layer is grown to a high extend epitaxially on the single crystallites of the bulk sample as otherwise we would observe continuous lines but no satellites reflecting the form of the intense diffraction points. Fig. 2 shows a photometric scan across such a diffraction point with a satellite. The implanted surface layer of this sample showed a sharp superconducting transition at 14.6 K measured resistively. As can be deduced from Fig. 2 the lattice constant $a_o$ of the implanted layer is reduced by 0.020 Å with respect to the bulk material with $a_o$ = 5.168 Å. This reduction in $a_o$ is stronger than expected from the transition temperature of the implanted surface layers. Thus we conclude, that a certain sort of defects which effect $T_c$ survives the thermal annealing.

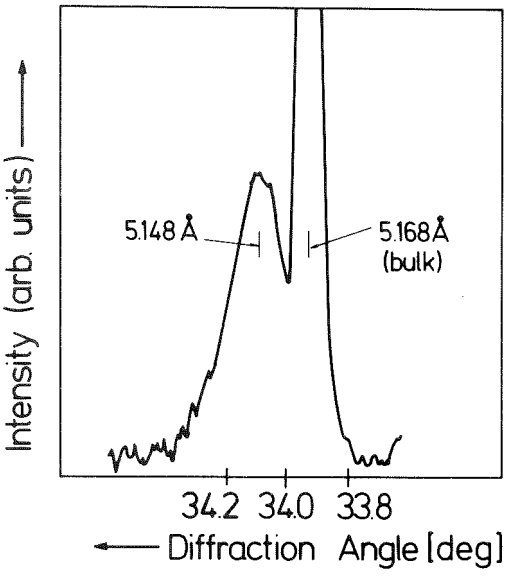


Fig. 2
Photometric scan across a diffraction point showing a satellite resulting from the implanted surface layer with a $T_c$ of 14.6K.

References

/1/ International Tables for Crystallography Vol. 3 Kynoch Press Birmingham 1968

/2/ Progress Report Teilinstitut Nukleare Festkörperphysik KFK 2670, p 104 (1978)

## 4.19 The Determination of Lattice Parameter and $T_c$ for Stressed $Nb_3Ge$-Layers

*Ernst L. Haase, Isa G. Khubeis[a] and R. Smithey*

[a] *Inst. f. Kernphysik, KfK, On leave of absence from the Phys. Dept., University of Jordan, Amman, Jordan*

Discrepancies exist in the literature between the dependence of the lattice parameter and the superconducting transition temperature ($T_c$) for bulk and splat-cooled samples, and those of samples prepared by unconventionel methods like co-evaporation, sputtering and chemical vapour deposition.

It will be shown that the origin of the discrepancies lies in stresses and disappears, when a lattice parameter determination method is used that takes care of stresses.

Fig. 1 shows both the lattice parameter $a_o$ /1/ and $T_c$ as a function of at % Ge for mostly co-evaporated and some sputtered $Nb_3Ge$ layers.

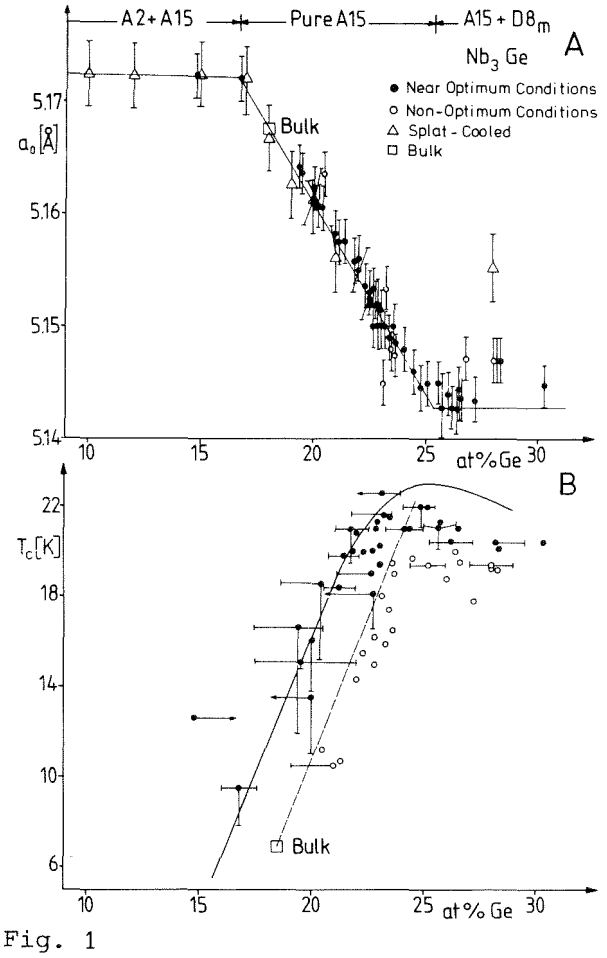


Fig. 1

Fig. 1A shows the lattice parameter $a_o$ as a function of at % Ge. Below 16.7 at %, one has a mixture of the A2-(Nb) and A15-phases with a constant lattice parameter of 5.1722 Å. Between 16.7 and 25.4 at % Ge samples having pure A15 phase can be produced when the preparation conditions are optimal. As the larger Nb atoms are replaced successively by the smaller Ge-atoms, the lattice parameter decreases linearly with a slope of $3.38 \times 10^{-3}$ Å/at % Ge. Beyond 25.4at%, a phase mixture of A15 and $D8_m$ coexists and the A15-lattice parameter stays constant at a value of 5.143 Å. Asymptotically $a_o$ could approach an estimated value of 5.141 Å for optimal layers.

Shown as triangles are results of splat-cooled samples /2/. There is an excellent agreement between the two sets of data.

The triangle point at 28 at % Ge indicates the minimum value for the lattice parameter of 5.155 Å reached by the authors.

The bulk values are given as squares also. Similar curves have been obtained by other groups, see for instance the convincing work of A.H. Dayem et al. /3/, but usually without considering the effects of stresses, and hence are not shown in Fig. 1.

In Fig. 1 b the dashed line shows the expected values of $T_c$ for bulk or optimally prepared splat-cooled samples. Due to microscopic variations in the composition caused by rapid vapour rate variations the $T_c$ vs. $a_o$ curve broadens for co-evaporated or sputtered layers as indicated by the solid line. The maximum $T_c$ of 22.6 K is reached, as expected, near stoichiometry.

Fig. 2 shows for two co-evaporated $Nb_3Ge$-layers prepared simultaneously under identical conditions, but deposited on a sapphire and a silicon substrate, the lattice parameter values as a function of cos 2 $\phi$, where $\phi$ is the angle between the normals to the layer and the lattice plane, as determined with a Guinier film camera using Seemann-Bohlin focussing /4/. As the Bragg-Brentano arrangement gives reflections only from lattice planes parallel to the surface, lattice parameters thus determined do not allow the determination of stresses, and hence that arrangement is unsuitable for determining stresses.

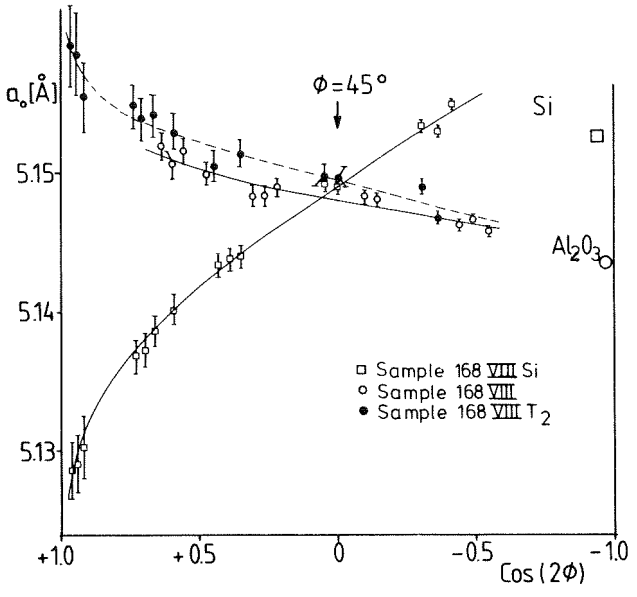


Fig. 2. Lattice parameter values for two $Nb_3Ge$ films on $Al_2O_3$ ($T_c$ = 21.3 K) and silicon ($T_c$ = 19.4 K) samples plotted as a function of cos 2 $\phi$, $\phi$ being the angle between the normals to the layer and the lattice plane. The dashed curve shows the result after two isochronal anneals at 820° and 880°C, which lowered $T_c$ to 19.9 K, and increased the lattice parameter to 5.1494 Å.

The curves should, and within the experimental error, do intercept at $\phi$ = 45°, where the effect of stresses disappears /4/. The mean value of the lattice parameter is taken to be the value of a least-squares fit through the data points at $\phi$ = 45° /1/. The lattice parameter $a_o$ is plotted as function of cos 2$\phi$. The fitted curves are definitely non-linear, giving evidence for intrinsic stresses /5/.

The layer deposited on sapphire is compressively stressed, reducing the Nb-chain distance parallel to the surface, thus raising $T_c$ probably due to anisotropy.

The layer on the Si-substrate has a lower $T_c$ of 19.4° K, attributed to the anisotropic dilatation of the Nb-chains. Annealing the sapphire layer reduced $T_c$ to 19.9 K, and correspondingly increased the lattice parameter.

It has been shown that excellent agreement is obtained for the lattice parameter values for bulk and for stressed layers; but for stressed layers, a lattice parameter determination method that considers stresses must be used. It was observed that stresses affect $T_c$ by about 1K also.

References

/1/ E.L. Haase, KfK Report 2670, p. 100 (1978), also to be submitted to J. Appl. Cryst.

/2/ J.L. Jorda, R. Flückiger and J. Müller, J. Less Common Metals, 62, 25 (1978)

/3/ A.H. Dayem et al., J. Phys. Chem. Solids, 39, 529 (1978)

/4/ R. Feder and B.S. Berry, J. Appl. Cryst. 3, 372 (1970)

/5/ R.W. Hofmann in "Physics of Non-metallic Thin Films", ed. C.H.S. Dupuy and A. Cachard, Plenum Press, N.Y., 273 (1976)

## 4.20 Towards the Solution of the $Nb_3Si$-Puzzle

*Ernst L. Haase, I.G. Khubeis[a], R. Smithey, and O. Meyer*

*[a]Inst. f. Kernphysik, KfK; on leave of absence from the Physics Department, Univ. of Jordan, Amman, Jordan*

During the past decade numerous attempts have been undertaken to produce A15 $Nb_3Si$ because of its allegedly high $T_c$. A good survey of the status last fall was published Jan. 1979 /1/. Here we will compare our results only with those having $T_c$-values above 9K.

When carefully examining the available data, it becomes apparent that the results cannot solely be accounted for on the basis of the A15-phase but that a second high $T_c$ phase must exist.

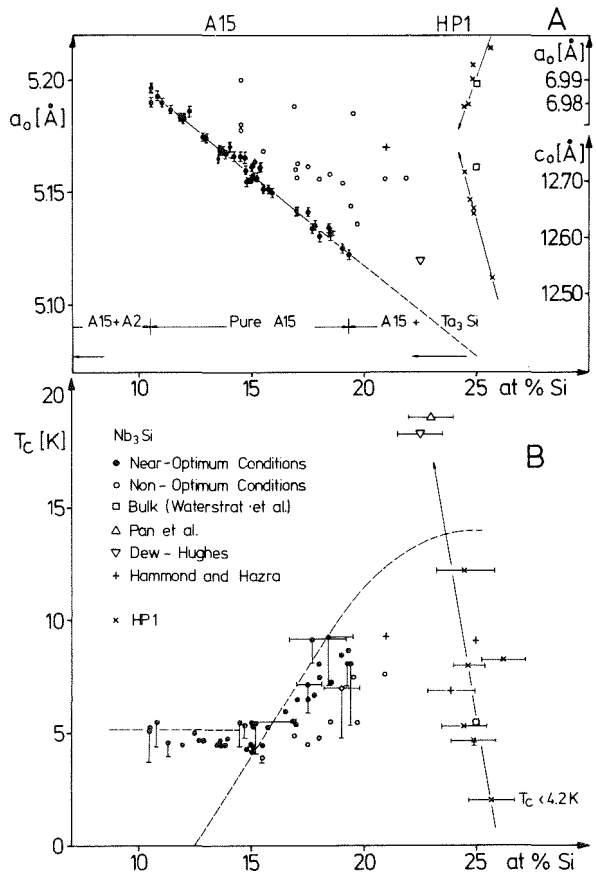


Fig. 1 shows lattice parameter and $T_c$ as a function of at.%Si for A15 (left) and HP1 /2/ (right) $Nb_3Si$. The upper half shows data points for A15 $Nb_3Si$ over its range of the stability from 10.5 to 19.3 at.%Si. The slope is $8.0 \times 10^{-3}$ Å/at.%Si. When extrapolated to stoichiometric composition the $a_o$-value of 5.076 Å is obtained, which is in good agreement with founded semiempirical estimates of 5.06 to 5.08 Å. The bottom half shows $T_c$ vs. at.%Si for the same samples. As for $Nb_3Ge$, $T_c$ rises linearly with increasing Si-contents above 15 at.%Si, as indicated by the solid line. Below 15 at.% the lattice parameter continues to increase, but the $T_c$ is dominated by the amorphous Nb-Si system. At 19.4 at.%Si or a little beyond the limit of pure A15-phase stability is reached, with a $T_c$ of about 10 K /6/. Beyond about 20 at.%Si a mixture of A15 and the $Ta_3Si$-phase is formed with no further increase in $T_c$. The two points shown as crosses /3/ confirm this. Following the trend of $Nb_3Ge$ /9/, an extrapolated value for $T_c$ for stoichiometric $Nb_3Si$ is indicated by the dashed curve. The extrapolation presumes the absence of rapid variations in the electronic density of states. The low value of $T_c$ of about 14 K is in agreement with the low value of the density of states predicted by energy band calculations /4/.

Around 25 at.%Si we have made numerous metastable samples showing predominantly the HP1- /2/ with no detectable A15-phase. The $T_c$-value and lattice parameter from the d-values of Ref. /2/ are shown as squares. For this phase both $T_c$ and the lattice parameters $a_o$ and $c_o$ of the tetragonal phase vary extremely rapidly with composition. The lattice parameter values are given, but have not yet been corrected for stresses. Our data points for $T_c$ and $a_o$ and $c_o$ vs. at.%Si extrapolate to the results of Pan et al. and Dew-Hughes /5/ where phase identifications have been extremely difficult due to the many phases present. Their stated A15-lattice parameters are now inconsistent with an A15-phase assignment. The 10 K point of Levchenko /6/ is stated to be pure A15-phase within the detec-

tion limit of 3-5 at%, but no at.%Si is given. The samples with $T_c$ up to 14 K produced by Somekh and Evetts /7/ were prepared at temperatures where the $Nb_3Si$ A15 phase neither forms nor survives from our and Hammonds experience. The assignment to the HP1 phase appears likely as there is a fairly good match in line-position and -intensity of their diffractometer peaks. At the temperatures given in Ref. /7/ and /8/, we have observed reactions with the $Al_2O_3$ substrate, permitting the formation of $Nb_3Al$ or more likely the $Nb_3Al_{1-x}Si_x$ ternary compound.

In Fig. 2 the ranges of stability of the $Nb_3B$ systems are shown. As the Z of the B-element decreases, there is a definite trend towards lower at.%. In fact it is surprising that A15 $Nb_3Si$ exists in a metastable phase over such a wide range of composition ceasing around 20 at.%.

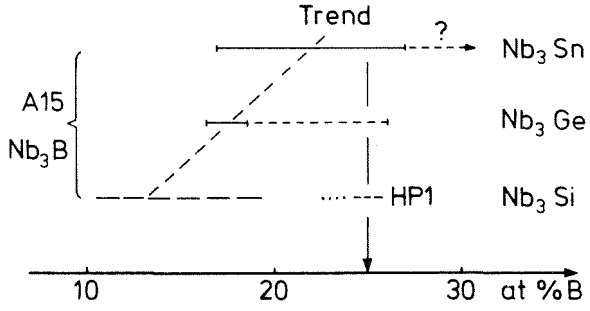


Fig. 2
Range of stability (solid line) and metastability (dashed line) for $Nb_3Sn$, $Nb_3Ge$ and $Nb_3Si$ for the A15- and the HP1-phases. The B-elements belong to the the IVb group and are plotted in ascending order.

Near 25 at.%Si the new HP1 phase is metastable, and is forming at substrate temperatures of about 800 to 1000°C, while the A15-phase already decomposes starting around 750°C. See /3/ and present annealing tests.

It has been shown that $Nb_3Si$ in the A15-phase cannot be prepared with the present techniques much beyond 20 at.%Si, and even if it could be prepared, it is unlikely to have $T_c$ much beyond 14 K. Instead near stoichiometry there exists a new tetragonal high $T_c$ phase. We have prepared in the $Nb_3Ge_{1-x}Si_x$ dozens of samples showing this phase with $T_c$'s as high as 19.5 K but have not yet evaluated these data. After the A15-phase, the HP1 phase is now the phase with the highest $T_c$.

References

/1/ R.H. Hammond in ONR-NRL Superconducting Materials Symposium, T.L. Francavilla, D.U. Gubser and S.A. Wolf, eds., NRL Report No. 3906, (Jan. 1979)

/2/ R.M. Waterstrat et al., J. Appl. Phys. 49, 1143 (1978)

/3/ R.H. Hammond and S. Hasra in Proc.13th Int. Conf. on Low Temperature Physics, Boulder/Colorado. Eds.: K.D. Timmerhaus et al. (Plenum Press, N.Y.) 3,465(1972)

/4/ B.M. Klein, L.L. Boyer and D.A. Papaconstantopoulos, Phys. Rev. B18, 6411(1978)

/5/ V.M. Pan et al., JETP Letters 21, 228 (1975). D. Dew-Hughes in Ref. /1/

/6/ I.S. Levchenko, Soviet Physics - Lebedev Institute Rep. Nr. 12, p. 6., Allerton Press Inc. (1976)

/7/ R.E. Somekh and J.E. Evetts, Solid State Com. 24, 733 (1977)

/8/ R.E. Somekh in Ref. /1/

/9/ E.L. Haase, I.G. Khubeis and R. Smithey, this report p. 114

## 4.21 A Low Energy Pulsed Electron Beam Generator for Solid State Applications

*J. Geerk and F. Ratzel*

It is now well established, that high energy lasers offer a very efficient tool in annealing the disorder in ion implanted or deposited layers on crystalline semiconductor surfaces. However an application of this new processing technology to metals is difficult because of the small absorption depth of the electromagnetic radiation and the high reflectivity of metals.

A better control of energy deposition with respect to depth and fluence can be achieved by use of short duration pulsed beams of low energy electrons (10 - 30 keV). Machines which are so far in use for these applications /1/ are of quite complex construction and not easily adjustable with respect to electron energy. It was our aim to build up a small electron beam generator suited for laboratory use which allows an easy variation of the important parameters which are the deposited energy density and the electron energy.

The electron pulse was generated by a triggered vacuum discharge initiated between two flat electrodes connected coaxially to an industrial short pulse capacitor acting as energy store. The samples are placed behind the anode which consists of a high transparent metallic mesh.

The pulse lenght was measured with a storage oscilloscope and was found to vary between 0.2 and 2 µs depending on the charging voltage of the capacitor and the anode - cathode spacing. The diameter of the electron beam is about 5 cm. On sample areas of 4 x 4 $mm^2$ which are typical in our experiments the deposited energy density is uniform to ± 10 %. Fig. 1 shows the calorimetrically determined energy density per pulse as a function of the charging voltage of the storage ca-

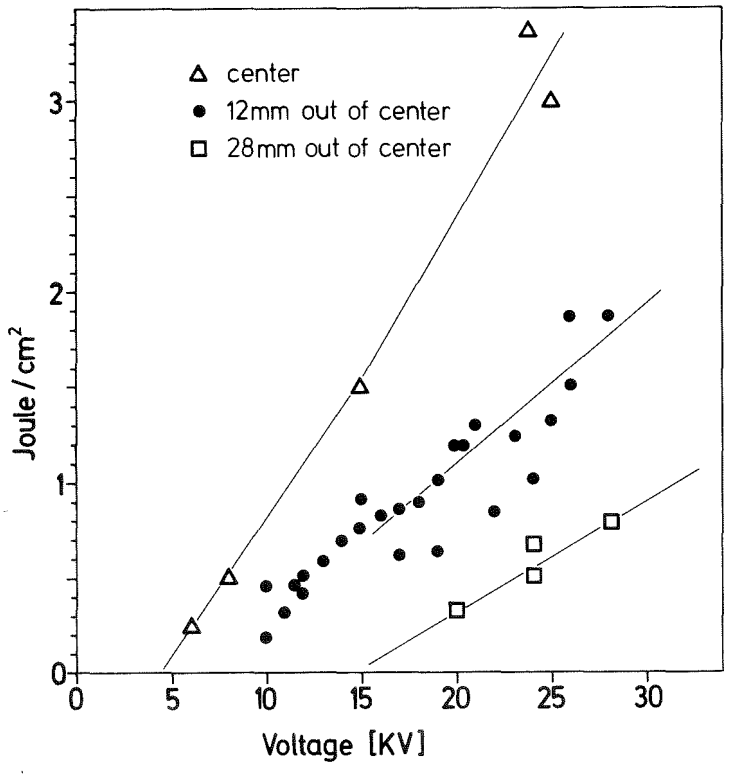


Fig. 1
The energy density per pulse as a function of the charging voltage of the storage capacitor. Parameter is the sample distance from center of the discharge.

pacitor. The curve parameter is the distance of the sample from the center of the discharge. As the figure shows the variation of the sample distance from the center provides the possibility to adjust independently the electron energy and the deposited energy density (fluence). Fig. 1 shows further that the maximum energy density the apparatus can supply is about 3.5 $J/cm^2$, which is far enough for our projected solid state applications.

Reference

/1/ Proceedings of Laser Effects in Ion Implanted Semiconductors, Catania, 1978 Corso Italia

## 4.22 Pulsed Electron Beam Annealing of Te-implanted Silicon Single Crystals

*J. Geerk, O. Meyer and M. Kraatz*

Annealing of ion implanted silicon by short, high power laser pulses has been shown to result in layers of high structural perfection and high substitutional solubility with special dopants /1/. Instead of laser pulses we use low

energy (5 - 30 keV) electron pulses for our annealing experiments. The electron beam generator is described in /2/. An interesting dopant for short duration annealing is Te. Previously it was found, that low dose implants of Te into silicon result in only 50 % substitutional fraction after thermal annealing /3/.

We implanted 1.4 x $10^{15}$ $Te^+$ at 260 keV into silicon wafers and analyzed the radiation damage and the distribution of the implanted tellurium atoms by Rutherford backscattering (RBS). Fig. 1 shows the area of the RBS silicon damage peak as a function of the deposited electron energy. The steplike behavior is typical for this type of experiments. The threshold value of 1.2 J/$cm^2$ where the damage drops to very low values agrees well with the threshold values observed in laser annealing experiments.

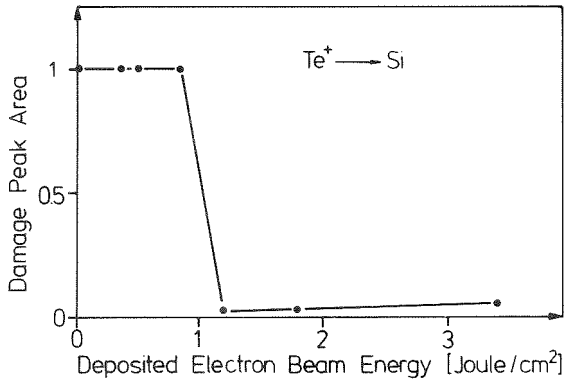


Fig. 1
The area of the silicon damage peak as a function of deposited electron energy density.

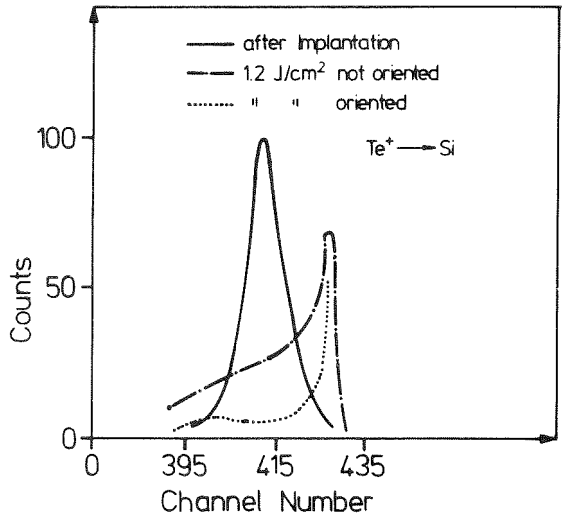


Fig. 2
The depth profile of tellurium implanted into silicon before and after application of an electron pulse of 1.2 J/$cm^2$

Fig. 2 shows the tellurium distribution before and after application of an electron pulse of 1.2 J/$cm^2$. After annealing the tellurium profile has changed considerably. It shows some similarity to a diffusion profile starting at the surface. As can be deduced from the difference in the profiles measured in oriented and random crystal directions a substitutional fraction of 87 % of the implanted tellurium has been achieved by electron pulse annealing. This is a substantially higher fraction than that obtained after conventional annealing /3/.

References

/1/ Proc. on Laser Effects in Ion Implanted Superconductors Ed. E. Rimini, Univ. Catania (Italy) 1978

/2/ J. Geerk, F. Ratzel, this issue, p. 119

/3/ O. Meyer, N.G.E. Johansson, S.T. Picraux, J.W. Mayer, Solid State Communications 8, (1970) 529

## 4.23 Pile-up Rejection Circuit to Improve the Detection Sensitivity for the Measurement of Depth Profiles Using Nuclear Reactions

*Ernst L. Haase and I.G. Khubeis*[a]

[a]*Institut für Kernphysik; on leave of absence from the Physics Dept., University of Jordan, Amman, Jordan*

One of the major problems in material analysis using nuclear reactions is the interference from competing reactions and the identification of peaks. The solution of this problem is much facilitated by using a more selective analysis technique. There is a simple way to reduce such interferences. Protons have a lower specific energy loss than alpha-particles. The detector thickness can be chosen in such a way, that proton, deuterons and tritons pass through, their resulting pulse heights being much lower.

To lower the detection sensitivity, or to make measurements in the presence of high Z-elements possible, an effective pile-up rejection circuit is needed. Commercial pile-up rejection circuits having a pulse-pair resolution of about 0.5 µsec are inadequate when one is trying to achieve low detection sensitivities.

To improve the detection limit substantially, a pulse pile-up circuit has been assembled and tested which improves the detection sensitivity by much more than an order of magnitude in comparison with commercial circuits (see Fig. 1).

To improve the pulse-pair rejection time of commercially available circuits, parallel to the energy processing string, a fast time rejection circuit has been set up, which consists of commercially available NIM units. By suitable

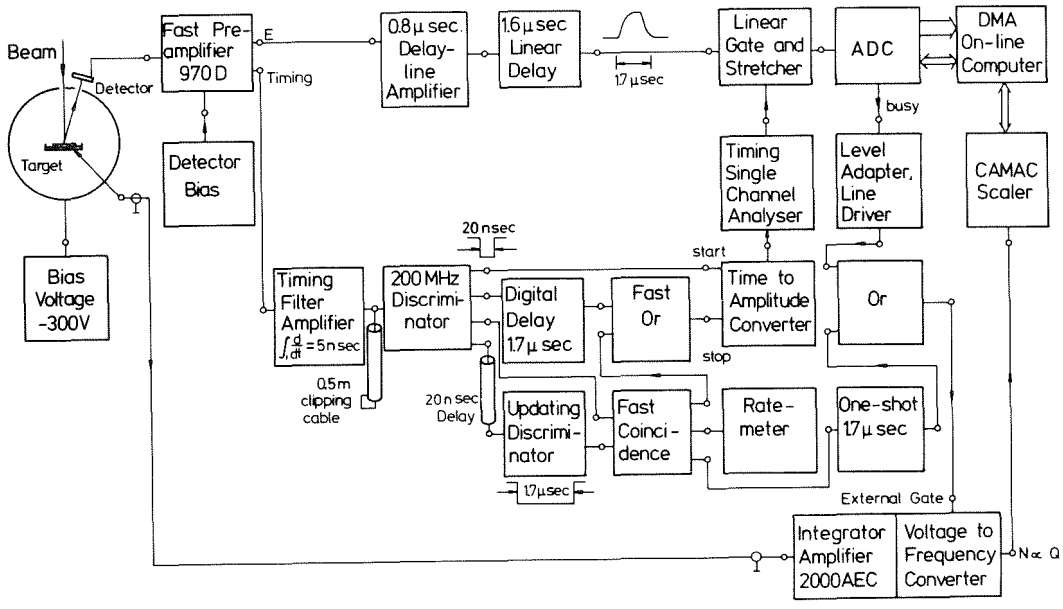


Fig. 1 Block diagram of pile-up rejection circuit.

shaping the timing information, a pulse-pair resolution of 30 nsec is reached. When there is no pile-up event within ± 1.7 μsec, the time to amplitute converter TAC and its following timing single channel analyser TSCA open the linear gate and thus the event passes on unhibited. As soon as there is a second event preceding or following the actual event within 1.7 μsec, the fast coincidence will respond and a TAC pulse height laying outside the set TSCA window is generated, thus preventing the passage of the pile-up event through the linear gate. A simpler, but more inconveniently adjustable alternative would be the use of a fast coincidence. For double pile-up, a non-updating discriminator would be adequate, when the timing is carefully adjusted. For the rare, but most cumbersome triple pile-up events, the updating discriminator appears to be the better solution.

The dead time of the ADC and the pile-up circuit are automatically corrected by gating the voltage to frequency converter. By measuring with different beam currents and checking for identical counts per channel, proper adjustment can be checked. If necessary, the one-shot duration must be corrected. The result of a severe pile-up test is shown in Fig. 2.

The O-peak sits on a strong triple pile-up tail, as the Ta-edge has an energy of about 1 MeV and the alpha-particles from oxygen have an energy of 2.6 MeV. Fig. 2B shows the same measurement, but with the pile-up circuit on. There is little background near the oxygen peak. To push the pile-up rejection

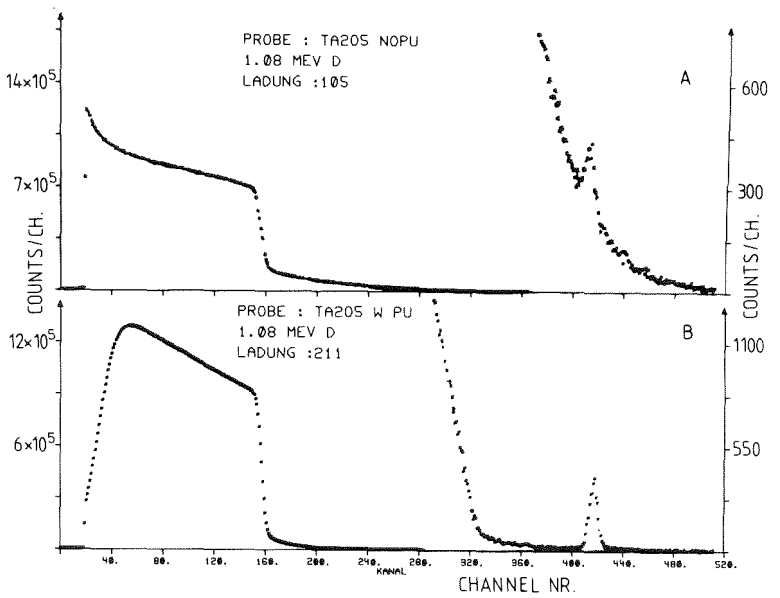


Fig. 2. Measuring the oxygen of a thin $Ta_2O_5$-layer on a solid Ta-substrate (Z=73) constitutes a severe test on any pile-up circuit due to the unfavourable ratio of elastic scattering counts to the $^{16}O(d,\alpha)$ events. Fig. 2A, with 2 cfs-scales, shows the elastic scattering and the oxygen peak of a measurement with the pile-up circuit off.
Fig. 2B shows the same measurement but with the pile-up circuit on.

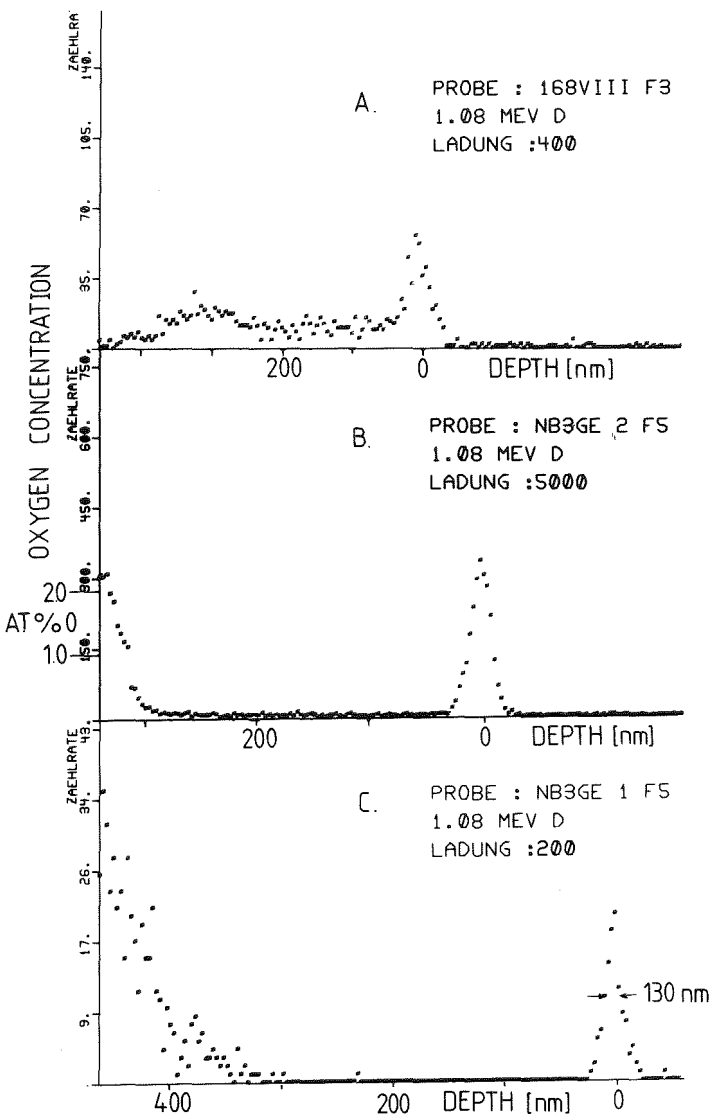


Fig. 3A shows the oxygen profile of a $Nb_3Ge$-layer on a Si-substrate, showing the surface and the substrate surface oxygen peaks, and a small amount of oxygen in the layer using a tilting factor of three.
Fig. 3B shows a similar measurement, but from a layer on a sapphire ($Al_2O_3$)-substrate. Besides the surface peak there is very little oxygen in the layer. There appears to be a small amount of oxygen near the substrate. This is difficult to analyse because of the oxygen in the substrate. The at.% oxygen scale is shown.
Fig. 3C shows the same from a sapphire substrate but for a layer practically free of oxygen, except for the surface and substrate interface peaks, with one event due to the oxygen in the layer. The surface peak demonstrates the depth resolution of 13 nm.

circuit to its limits, a beam current of about 6 nA was used for both measurements, resulting in an acquired data rate of about 38 000 cps. This is 4 times higher than the maximum count-rate normally employed and pushes the pile-up to $4^3 = 64$ times its maximum normal rate, as the probability for triple pile-up goes with the third power of the count rate. Thus the present pile-up rejection circuit has demonstrated superior performance.

The use of the above pile-up circuit for the $^{16}O(d,\alpha)$ reaction and the use of a thin detector has permitted to push the detection sensitivity to below 0.02 at.% and the depth resolution to 13 nm. 5 nm appears feasonable. The techniques described in this paper will generally facilitate the use of nuclear reactions for non-destructive material analysis.

Fig. 3, as an application, shows the oxygen depth profiles for three $Nb_3Ge$-layers. The corresponding parts of the raw data have been converted to depth scales and the depth dependent cross-section correction has been applied. A tilt angle of $\alpha = 63.5^{o}$ was used in the latter measurements to improve the depth resolution by about a factor of 5.

## 4.24 Formation of Tritium through Nuclear Reactions and the Measurement of Oxygen in Zircaloy.

*H. Münzel[a,b], M. Merkel[a], F. Michel[b], A. Schwierczinski[a], and E.L. Haase*

[a] *TH Darmstadt, Fachbereich f. Anorg. Chemie u. Kernchemie*

[b] *Institut f. Radiochemie, Kernforschungszentrum Karlsruhe*

Abstract

The investigations of the formation cross-sections for tritium in nuclear reactions with light charged projectiles were continued. The excitation function for the $^{197}Au(\alpha,t...)$ reaction has a maximum at 80 MeV. For $^{3}He$ induced reactions less tritium was formed than expected.

Oxygen depth profiling based on the $^{16}O(d,\alpha)$ reaction is described. First

investigations of the behavior of $ZrO_2$-layers on Zircaloy are discussed. Our measured diffusion-coefficient of oxygen in the $ZrO_2$/Zircaloy system is in agreement with literature values.

## 4.25 Preparation of NbN Single Crystals

*B. Scheerer*

KfK 2815, to be published in Journal of Crystal Growth

NbN single crystals were prepared for measurements of the phonon dispersion by inelastic neutron scattering and as starting material for ion implantation experiments. Series of experiments have been done to study three different possibilities to obtain crystals of the required size i) RF-zone melting of NbN-powder rods, ii) nitriding of Nb single crystals by a graphite heating element under a $N_2$-pressure up to 100 bar, iii) nitriding of Nb single crystals in a tungsten crucible by RF-heating. The crystals were characterized by chemical analysis, X-ray- and neutron diffraction and also by determination of the superconducting transition temperature.

## 4.26 Phase Relationships in the Nb-N and Ta-N System

*C. Politis*

As the constitution of the Nb-N and Ta-N systems has not been completely clarified, some investigations were carried out on these systems.

After equilibrium annealing the samples were investigated by X-ray diffractometry (with Si and NaCl as a calibration substance) as well as by metallography and chemical analysis. The cubic B1 type $\delta$-NbN and $\delta$-TaN have some interesting properties, for example the microhardness increases strongly upon transition

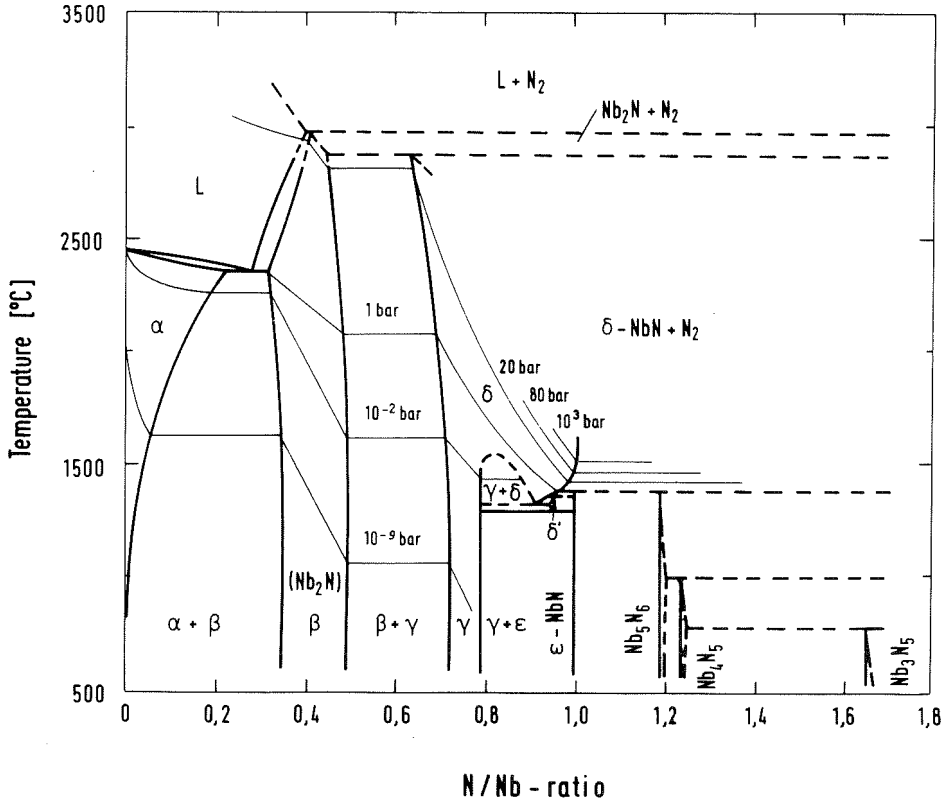


Fig. 1 Proposed phase diagram for Nb-N /1/ /2/ /3/ /4/ /7/

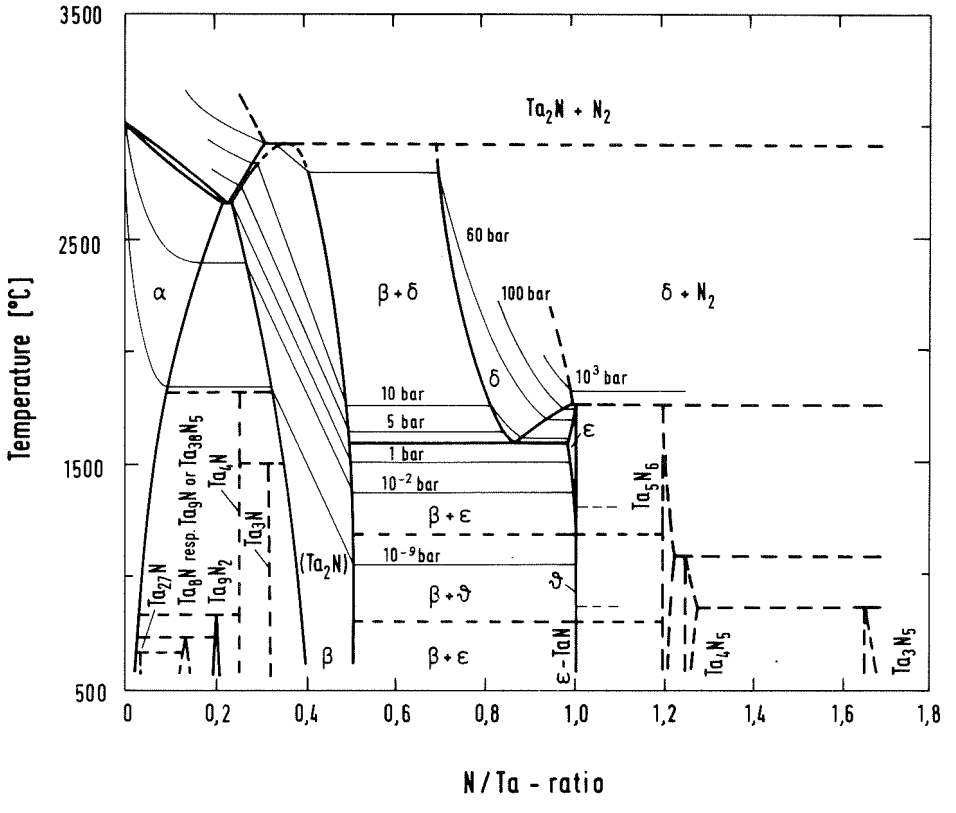


Fig. 2 Proposed phase diagram for Ta-N /1/ /5/ /6/ /7/

from the hexagonal to the cubic structure. Within the range of homogeneity of the δ-phase the microhardness decreases rapidly with increasing N/Me ratio /1/.

Fig. 1 gives a phase diagramm based on our measurements /1/ /7/ as well as on literature data, in particular the phase diagrams by Brauer and Esselborn /2/, Gebhardt and co-workers /3/ as well as by Guard and others /4/. This diagram is characterized by giving the phase width of the δ-phase and by taking into account the higher nitrides $Nb_5N_6$, $NbN_4N_5$, and $Nb_3N_5$. Some isobars are also given. The lower phase boundary of the range of homogeneity of δ-NbN is at N/Nb= 0.7 at T = 1900 K and a nitrogen pressure of 1 bar.

The phase relations for the systems Ta-N are given in Fig. 2. The phase diagram was established on the basis of our measurements together with some data from the relevant literature /5/ /6/. According to these measurements the lower phase boundary of the range of homogeneity of δ-TaN is at N/Ta = 0.70 while the upper phase boundary may be as high as N/T $\sim$ 1.0 at T = 2020 K and high nitrogen pressure (10 to $10^3$ bar $N_2$).

References

/1/ C. Politis, G. Rejman, KfK-Ext. 6/78-1 (1978)

/2/ G. Brauer, R. Esselborn, Z. anorg. Chem., 309 151 (1961)

/3/ E. Gebhardt, E. Fromm, D. Jacob, Z. Metallkunde 55, 423 (1964)

/4/ R.W. Guard, J.W. Savage, D.G. Swarthout, Trans. TMS-AIME 239, 643 (1967)

/5/ C. Ortiz, S. Steeb, J. Less-Common Metals 42, 51 (1975)

/6/ I. Gatterer, G. Dutek, P. Ettmayer, R. Kieffer, Mh. Chem. 106, 1137 (1975)

/7/ C. Politis, VI. Intern. Conf. on Solid Compounds of Transition Elements, Stuttgart, 1979

## 4.27 Preparation and Superconducting Transition Temperature of TiN, TiC and $TiC_xN_y$ Single Crystals Prepared by CVD

*Th. Wolf, H. Schneider[a], C. Politis*

[a] *Institut für Material- und Festkörperforschung, KfK*

The cubic transition metal compounds TiN and TiC and the carbonitrides $TiC_xN_y$ are still the subject of continuing attention, not only because of their

practical importance as protective coatings and wear resistant materials, but also because they serve as suitable and interesting model systems which supply valuable information about the electron structure, chemical bonding, superconductivity and other physical properties.

TiN crystallizes in a cubic phase with the B1 (NaCl)-structure. This cubic phase exists over a broad range of homogeneity where the N/Ti ratio extends from 0.42 to 1.05. Deviations from stoichiometry are usually interpreted as vacancies in the non-metallic sublattice. For the investigation of most physical properties homogeneous, single-phase, dense, and stoichiometric samples are required. Compared with zone melted single crystals, the crystals prepared by chemical vapor deposition (CVD) are less disturbed and have well structured growth areas. For determination of the superconducting parameters and for reflection measurements, Raman scattering, XPS, and neutron-scattering experiments, several $TiN_{1\pm x}$, TiC and $TiC_xN_y$-single crystals with various compositions were prepared by CVD.

The chemical vapor deposition of TiN, TiC, and $TiC_xN_y$ is carried out in a simple apparatus consisting of a quartz tube and a molybdenum susceptor heated to temperatures between 1200 and 2500 K by means of radio-frequency /1/. A schematic presentation of the deposition apparatus is shown in Fig. 1. Depending on the experimental conditions, skeleton or hollow crystals, twin cubes, and needle-shaped crystals (Fig. 2) are obtained. The stoichiometry of the single crystals investigated was determined by chemical analysis. The determination of the nitrogen and oxygen content was performed by means of vacuum hot-extractions /2/. Precise determinations of the lattice parameter were carried out, both by Guinier-

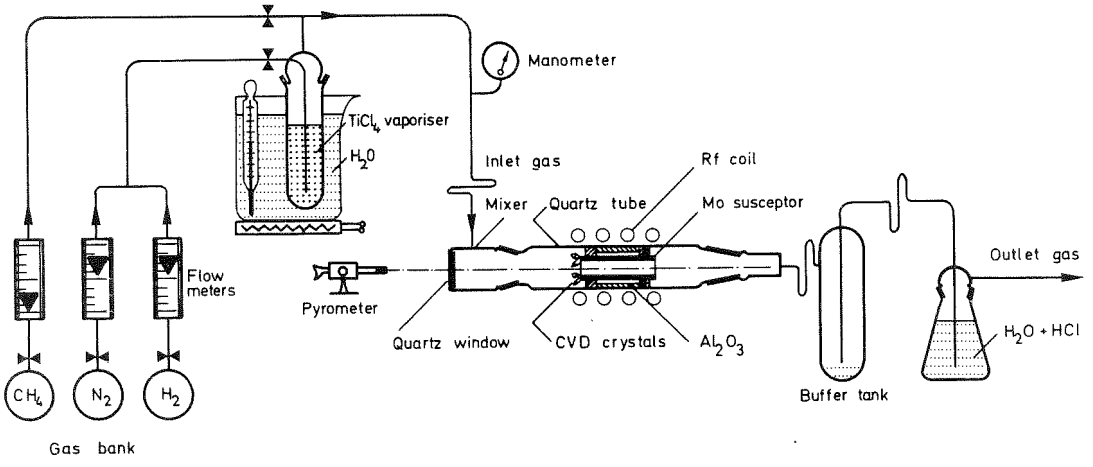


Fig. 1 Experimental apparatus for crystal growth of TiN, TiC and $TiC_xN_y$ by chemical vapor deposition in a quartz tube

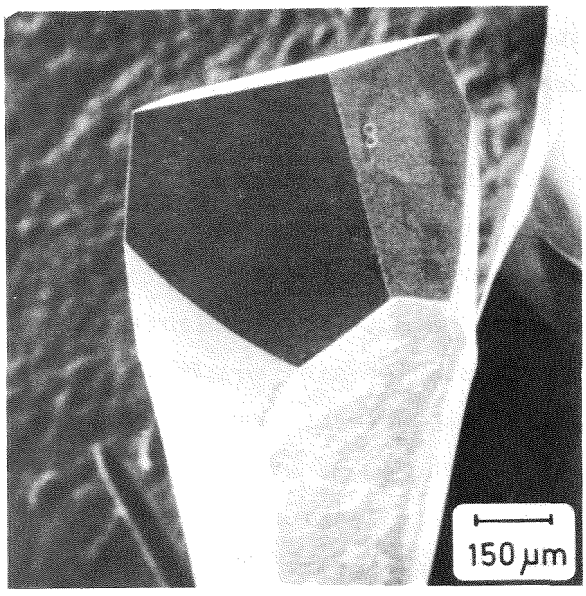


Fig. 2
Typical TiN needle prepared by chemical vapor deposition

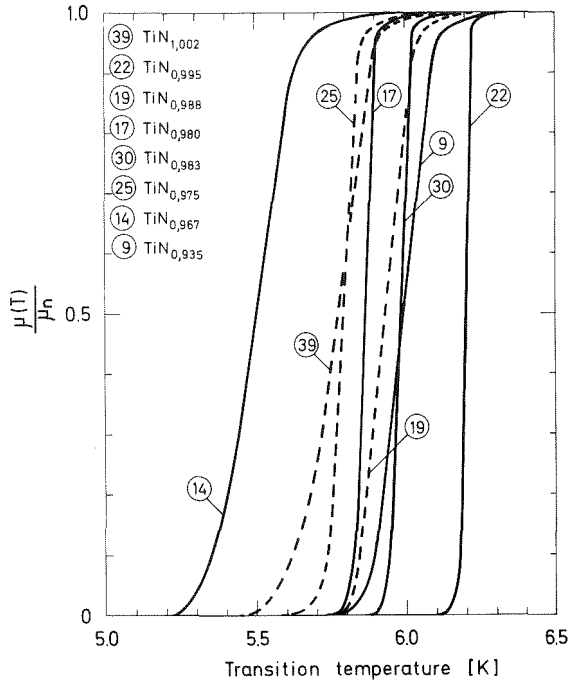


diffraction exposer (using Cu-$K\alpha_1$-radiation with NaCl as a calibration substance) and with a X-ray diffractometer (with Si as a calibration substance).

Measurements of $T_c$ using the inductive technique on TiN single crystals indicated that the transition to the superconducting phase, depending on stoichiometry, vacancies and oxygen content, is between $T_c$ = 5.8 K and $T_c$ = 6.2 K /3/. In Fig. 3 the transition curves are plotted for some TiN single crystals. The $\mu(T)/\mu_n$ ratio was determined by the use of the $\mu_n$ value at 10 K.

In nearly stoichiometric TiN single crystals the transition to superconductivity is found to be at higher temperatures than reported previously. This may be due to the high N/Ti ratio but also to the low oxygen and carbon content of the crystals. This confirms that the preparation of these stoichiometric compounds using the CVD technique furnishes new information about important physical phenomena.

Fig. 3
Transition curves of TiN single crystals. The permeability ratio $\mu(T)/\mu_n$ was determined by the use of the $\mu_n$ value at 10 K

References

/1/ Th. Wolf, Diplomarbeit University of Karlsruhe, (1977)

/2/ H. Schneider, E. Nold, Z. Analyt. chem. 260, 1 (1972)

/3/ C. Politis, Th. Wolf, H. Schneider, VII. Intern. Conf. on Chemical Vapor Deposition, Los Angeles, USA, October 14-19, 1979

## 4.28 Preparation and Superconducting Transition Temperature of Cubic δ-$TaC_xN_y$ and δ-$(Nb,Ta)C_xN_y$ Crystals

*M. Dietrich*[a], *C. Politis*

[a]*Institut für Technische Physik, KfK*

Single-phase δ-NbN, δ-$TaC_xN_y$, and δ-$(Nb, Ta)C_xN_y$ pellets of different composition have been produced by annealing in 1 to 20 bar $N_2$ at a temperature of about 2000 K. The production of single-phase δ-TaN was more problematic. The first attempts to produce δ-TaN were carried out in a high-pressure apparatus, keeping ε-TaN pellets under 3 to 20 bar nitrogen pressure at 1800 to 2300 K for up to 24h /1/. Although the quenching rate of this apparatus was high, compact single-phase δ-TaN was not obtained. Therefore a special small high-pressure apparatus was constructed for the production of low-oxygen coarse-grained δ-NbN and δ-TaN /2/ /3/. The Nb or Ta wire to be nitrided is suspended on the electrodes and is directly heated by the electric current. The wires thus nitrided retained their initial diameter and became very coarse-grained. On applying a slight pressure with the fingers, they broke into grains with lengths of 5 to 7mm. Some of these δ-NbN and δ-TaN grains were oriented small monocrystals. The microstructure of the surface is very fine and consists partly of twin grains, while the center of the sample is rather coarse-grained. The surface as well as the center of all the samples are single-phased. X-ray analysis, metallography and chemical analysis were carried out on the specimens.

Table I Composition and superconducting properties of $TaC_xN_yO_z$ and Ta

| Proben-Nr. | Chem. Zusammensetzung | Gitterkonst. [Å] | $\frac{dT_c}{dp}$ [mK/Kbar] | ρ [μΩcm] | $\frac{R_{300}}{R_{Rest}}$ | $T_c$ [K] |
|---|---|---|---|---|---|---|
| V108 | $TaC_{0.002}N_{0.937}O_{0.001}$ | 4.340 | + 7.2 | 162 | 0.92 | 8.91 |
| V136 | $TaC_{0.083}N_{0.938}O_{0.024}$ | 4.3439 | + 8.2 | 248 | 0.95 | 8.41 |
| V105 | $TaC_{0.030}N_{0.855}O_{0.001}$ | 4.385 | + 3.7 | 198 | 0.96 | 10.99 |
| V 51 | $TaC_{0.198}N_{0.747}O_{0.001}$ | 4.3733 | + 5.2 | 166 | 0.98 | 10.74 |
| V 86 | $TaC_{0.148}N_{0.638}O_{0.006}$ | 4.364 | + 2.9 | 199 | 1.04 | 12.01 |
| V109 | $TaC_{0.017}N_{0.632}O_{0.002}$ | 4.3741 | + 5.0 | 233 | 0.95 | 11.84 |
| V107 | $TaC_{0.600}N_{0.278}O_{0.002}$ | 4.4555 | - 11.3 | 75 | 1.53 | 12.10 |
| V 56 | $TaC_{0.671}N_{0.271}O_{0.004}$ | 4.4309 | - 6.7 | 117 | 1.12 | 10.92 |
| V 88 | $TaC_{0.532}N_{0.234}O_{0.006}$ | 4.4550 | - 13.2 | 76 | 1.58 | 9.96 |
| V 1 | $TaC_{0.970}N_{0.004}O_{0.005}$ | 4.452 | - 11.0 | — | — | 8.37 |
| V 21 | $TaC_{0.980}$ | 4.4548 | - 15.0 | — | — | 9.46 |
| | Ta | 3.3033 | - 26.0 | 12 | 23.7 | 4.41 |

Table II Composition and superconducting properties of $(Nb,Ta)C_xN_yO_z$

| Proben-Nr. | Stöchiometrie $(Nb_uTa_v)C_xN_yO_z$ | x+y+z | $\varrho$ [μΩcm] | $\frac{R_{300}}{R_{Rest}}$ | $T_c$ [K] Mitte |
|---|---|---|---|---|---|
| 243 | $(Nb_{0.650}Ta_{0.350})\ C_{0.813}N_{0.106}\ O_{0.014}$ | 0.933 | 88 | 1.07 | 12.30 |
| 248 | $(Nb_{0.650}Ta_{0.350})\ C_{0.596}N_{0.289}\ O_{0.008}$ | 0.893 | 153 | 0.97 | 11.85 |
| 233 | $(Nb_{0.650}Ta_{0.350})\ C_{0.006}N_{0.886}\ O_{0.014}$ | 0.906 | 117 | 0.91 | 11.30 |
| 242 | $(Nb_{0.822}Ta_{0.178})\ C_{0.844}N_{0.077}\ O_{0.010}$ | 0.931 | 88 | 1.07 | 12.60 |
| 249 | $(Nb_{0.822}Ta_{0.178})\ C_{0.560}N_{0.334}\ O_{0.010}$ | 0.904 | 85 | 1.07 | 14.70 |
| 225 | $(Nb_{0.822}Ta_{0.178})\ C_{0.005}N_{0.856}\ O_{0.013}$ | 0.874 | 98 | 1.02 | 12.90 |
| 241 | $(Nb_{0.941}Ta_{0.059})\ C_{0.842}N_{0.066}\ O_{0.012}$ | 0.920 | 86 | 1.08 | 12.96 |
| 246 | $(Nb_{0.941}Ta_{0.059})\ C_{0.396}N_{0.355}\ O_{0.011}$ | 0.762 | 91 | 1.09 | 16.22 |
| 223 | $(Nb_{0.941}Ta_{0.059})\ C_{0.004}N_{0.845}\ O_{0.010}$ | 0.859 | 77 | 0.65 | 14.40 |
| 247 | $NbN_{0.319}\ C_{0.482}\ O_{0.010}$ | 0.811 | 80 | 1.06 | 17.12 |

While the hexagonal phases ε-NbN and ε-TaN are not superconducting above 2 K, the cubic phases δ-NbN and δ-TaN become superconducting with the same N/Me ratio with relatively high transition temperature, e.g. $T_c$ = 17 K for $\delta$-$NbN_{0.96}$ and $T_c$ = 9 K for $\delta$-$TaN_{0.94}$ /4/ /5/. These high transition temperatures are regarded as a measure for the purity of the samples produced. Table I and II show some of the physical properties of superconducting cubic δ-TaN, $\delta$-$TaC_xN_y$ and $\delta$-$(Nb,Ta)C_xN_y$.

References

/1/ C. Politis, KfK 2168 (1975)

/2/ C. Politis, G. Rejman, KfK-Ext. 6/78-1 (1978)

/3/ C. Politis, Contemporary Inorganic Materials 1978, Proceedings of the 3rd German-Yugoslav Meeting on Materials Science and Development, Stuttgart, 1978

/4/ E. Thorwarth, M. Dietrich, C. Politis, Solid State Commun. 20, 171 (1976)

/5/ C. Politis, VI. Intern. Conf. on Solid Compounds of Transition Elements, Stuttgart, 1979

## 4.29 Preparation and Superconducting Transition Temperature of Some Quenched Cubic $\delta$-$(Mo,X)C_{1-x}$ Polycrystalline Samples (X = Ti,Zr,Hf,Ta)

*W. Krauss, C. Politis*

In the Mo-C system there exist the compounds $\alpha$-$Mo_2C$ (orthorhombic, $D_{2h}^{14}$), $\beta$-$Mo_2C$(hcp, L'3), $Mo_3C_2$ (hexagonal, $D_{6h}^{4}$) and $\delta$-$MoC_{1-x}$(fcc, B1). Only $\alpha$-$Mo_2C$ is stable at room temperature /1/. The cubic phase $\delta$-$MoC_{1-x}$ is stable above 2230 K with a C/Mo ratio in the range $0.64 \leq C/Mo \leq 0.75$. Thus, only by extremely rapid quenching from high temperatures it is possible to obtain metastable cubic $\delta$-$MoC_{1-x}$. $\delta$-$MoC_{1-x}$ forms an extended cubic solid solution with various carbides of transition elements such as TiC, ZrC, HfC, NbC and TaC. The Mo-rich mixtures are also stable at high temperatures only, but the $\delta$-$(Mo,X)C_{1-x}$ phase can be retained at room temperature by quenching more easily than pure $\delta$-$MoC_{1-x}$.

Table I Composition and superconducting transition temperature of some cubic $\delta$-$MoC_{1-x}$ polycrystalline samples

| Sample No. | Composition | onset $T_c$ [K] | $\Delta T_c$ [K] |
|---|---|---|---|
| V 503 | $(Mo_{0.90}Hf_{0.10})C_{0.66}$ | 9.1 | 0.2 |
| V 44,1 | $(Mo_{0.90}Hf_{0.10})C_{0.68}$ | 8.5 | 1.5 |
| V 45,1 | $(Mo_{0.90}Hf_{0.10})C_{0.68}$ | 8.5 | 0.7 |
| V 44 | $(Mo_{0.90}Hf_{0.10})C_{0.72}$ | 12.0 | 1.2 |
| V 441 | $(Mo_{0.95}Ti_{0.05})C_{0.77}$ + 3.7 wt.% free C | 11.4 | 2.0 |
| V 442 | $(Mo_{0.95}Zr_{0.05})C_{0.77}$ + 4.6 " " | 10.5 | 1.6 |
| V 443 | $(Mo_{0.95}Hf_{0.05})C_{0.77}$ + 2.3 " " | 11.4 | 1.4 |
| V 47 | $(Mo_{0.95}Ta_{0.05})C_{0.77}$ + 0.5 " " | 12.0 | 1.2 |
| V 45 | $(Mo_{0.90}Hf_{0.10})C_{0.77}$ + 0.1 " " | 10.7 | 0.7 |
| V 447 | $(Mo_{0.90}Ta_{0.10})C_{0.77}$ + 3.7 " " | 10.9 | 1.6 |

For investigations of the superconductivity and for neutron-scattering experiments a number of $\delta$-$MoC_{1-x}$ samples has been produced. About 50 grams of a mixture of $\alpha$-$Mo_2C$ + graphite + Ti, Zr, Hf or Ta has been pressed into pellets and melted in an electric arc furnace under argon atmosphere. Melting has been continued for 1 min, then the electric arc was stopped and the melt quenched.

The composition of the metastable cubic $\delta$-$MoC_{1-x}$ samples investigated has been determined by chemical analysis. Determinations of the lattice parameter (e.g. $a_o$ = 0.4292±0.0002nm for $\delta$-$MoC_{0.66}$) and metallographic investigations were carried out. Measurements of $T_c$ using the inductive technique on $\delta$-$MoC_{1-x}$ samples indicated -as evident from Table I- that the transition to the superconducting state, depending on composition and quenching rate, is between $T_c$ = 8.5 K and $T_c$ = 12.0 K.

Reference

/1/ E.K. Storms, in Solid State Chemistry, Vol. 10, edited by L.E.J. Roberts, Butterworths, Univ. Park Press, (1972)

## 4.30 Preparation and Optical Properties of $HfC_xN_{1-x}$

*F.-W. Fluck[a], H.P. Geserich[a], C. Politis*

[a] *Institut für Angewandte Physik, Universität Karlsruhe*

A systematic study of the optical properties of a large range of $HfC_xN_{1-x}$ compounds has been performed. Using a new technique /1/, highly dense, homogeneous and single phase $HfC_xN_{1-x}$ samples (with low oxygen content) were prepared in the whole concentration range of the pseudo-binary system HfC-HfN. All the samples were characterized by density measurements, chemical analysis, metallography and precise determinations of the lattice parameter. Fig. 1 shows the reflectivity obtained for mechanically polished $HfC_xN_{1-x}$ polycrystalline samples plotted over the photon energy on a logarithmic scale. The $HfC_xN_{1-x}$ samples studied show the steep plasma edge in the reflection typical for metals. At low energies there is a relatively high plateau. In the transition from $HfN_{1.0}$ to $HfC_{1.0}$ a shift in the plasma edge from $\hbar\omega$ = 3.2eV to $\hbar\omega$ = 1.2eV is observed /2/.

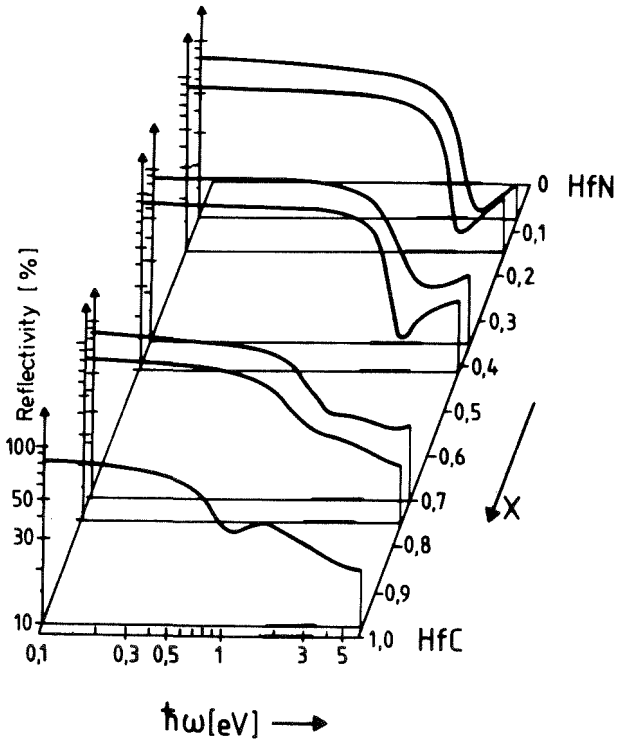


Fig. 1
Reflectivity of polycrystalline low-oxygen $HfC_xN_{1-x}$ crystals

References

/1/ DE-AS 2258 305

/2/ F.-W. Fluck, Dissertation, Fakultät für Physik, Universität Karlsruhe, (1978)

## 4.31 Raman Spectra and Superconductivity of Various Phases of a High-$T_c$ Superconductor: NbN

*R. Kaiser*[a], *W. Spengler*[a], *S. Schicktanz*[a], *C. Politis*

[a] *Physik-Department der Technischen Universität München*

Phys. stat. sol. (b) 87, 565 (1978)

Abstract

The first-order Raman spectra of β-, γ-, and ε-NbN and the defect-induced first-order Raman scattering of cubic $NbN_x$ are determined. In nearly stoichiomet-

ric δ-NbN the centre of the Raman spectrum after division by the Bose factor is at the same frequency of 150 $cm^{-1}$ as the centre of the phonon density from neutron scattering. With increasing deviation from stoichiometry the lowest Raman peak in $\delta$-$NbN_x$ due to acoustic phonons shifts to higher frequencies and $T_c$ decreases sharply. This behaviour indicates the existence of phonon anomalies.

## 4.32 The XPS Valence Band Spectra of Hf Metal and $HfC_xN_yO_z$ Compounds and the Correlation to their Superconductivity

*P. Steiner[a], H. Höchst[a], J. Schneider[a], S. Hüfner[a], C. Politis*

[a]*Fachbereich Physik, Universität des Saarlandes, Saarbrücken*

Z. Physik B 33, 241-250 (1979)

Abstract

The x-ray photoemission spectra of the valence bands of Hf metal and of several $HfC_xN_yO_z$ compounds have been measured and are compared to existing band structure calculations. The density of states at the Fermi energy of the $HfC_xN_yO$ compounds correlates strongly to their superconducting transition temperature $T_c$. A calculation of the $T_c$ values within the frame work of strong coupling superconductors indicates that the phonon spectrum and the electron phonon interaction is approximately constant within the series $HfC_xN_yO_z$.

## 4.33 Young's Modulus, Surface Energy and Fracture Properties of Polycrystalline $NbC_{1-x}$

*Hj. Matzke[a], C. Politis*

[a]*European Institut for Transuranium Elements, Commission of the European Communities, Karlsruhe.*

The question of fracture properties and of the surface energy of transition metal carbides, nitrides and carbonitrides gains increasing importance with

the more extensive use of these materials experience in technology. To understand their elastic and cracking behaviour, their surface energies, elastic moduli and fracture properties must be known.

In an attempt to determine these properties, a number of $NbC_{1-x}$ and $NbC_xN_y$ compounds was tested to get first data on the effects of deviations from stoichiometric non-metal/metal ratio and on the effect of replacing carbon atoms by nitrogen atoms. $NbC_{1-x}$ and $NbC_xN_y$ are in addition of interest due to both their hardness and their high $T_c$.

The specimens were investigated both in the as-sintered step, following a surface relaxation treatment at 1000 K for 1h to anneal surface damage introduced by diamond-paste polishing the surfaces to a mirror-like finish, and thirdly following a homogenization treatment at 2300 K under 0.8 bar argon for 50h.

Young's moduli E of polycrystalline $NbC_{1-x}$ samples were measured employing the ultrasonic transit-time method. An ultrasonic pulse originating from a quartz-oscillator is sent through the crystal and its arrival-time on the other side of the crystal is measured with a receiver. The set up was tested with Al and $Al_2O_3$ standards. The values obtained for the velocity of sound for longitudinal waves ($v_l$ = 5970 m/sec for Al and $v_l$ = 10250 m/sec for $Al_2O_3$) agreed favorably with literature results on these materials /1/. The Young's moduli of three $NbC_{1-x}$ samples are summarized in Table I. For the calculations of E for $NbC_{1-x}$, a porosity and composition independent value of the Poisson ratio, of $\nu$ = 0.21 was used. The Debye temperature of $NbC_{1-x}$ and $NbC_xN_y$ was also obtained from the simplified ultrasonic method described above /2/. Also the method of Hertzian indentation was used to obtain information on fracture properties and surface energy of some $NbC_{1-x}$, $NbN_{1-x}$ and $NbC_xN_y$ compounds /3/.

Table I

Longitudinal velocity of sound and Young's modulus of $NbC_{1-x}$ at T = 298 K. The $E_o$-value for theoretical density was calculated using a relation between the fractional porosity and the E-modulus.

| Sample | Composition | Lattice parameter a[nm] | Density $\rho \cdot 10^3$[Kg/m$^3$] | Velocity of sound $v_l$ [m/sec] | E-modulus x10$^{11}$ [N/m$^2$] | $E_o$-modulus x10$^{11}$ [N/m$^2$] |
|---|---|---|---|---|---|---|
| I | $NbC_{0.964}$ | 0.4467 | 7.14 | 8090 | 4.16±0.01 | 4.79 |
| II | $NbC_{0.885}$ | 0.4465 | 7.17 | 7880 | 3.96±0.01 | 4.09 |
| III | $NbC_{0.849}$ | 0.4459 | 7.36 | 7560 | 3.74±0.01 | 4.09 |

References

/1/ E. Schreiber, O.L. Anderson, N. Soga, Elastic Constants and their Measurement, McGraw-Hill, (1973)

/2/ C. Politis, to be published

/3/ Hj. Matzke, C. Politis, to be published (1979)

## 4.34 A Comment to the Homogeneity Range of the $Nb_3Ge$ Phase

*E. Aker, D. Ewert, C. Politis*

The Nb-Ge equilibrium phase diagram has been investigated by V.M. Pan et al. /1/ and J.L. Jorda et al. /2/. Since there were some doubts about the position of the homogeneity range of the A 15 phase we made our experiments with the view, to fix the range of the A 15 phase up to 1600°C.

Nb-Ge alloys were prepared by arc melting in a water cooled copper crucible under an argon pressure of 0.5 bar. The starting materials were 99.999% Ge ingots and 99.99% Nb wire. The ingots have been homogenized by annealing for over 100h at high temperature in an W-mesh furnace under an argon pressure of 1 bar. The samples were analysed by microscopic observations after chemical etching with a : $H_2O$:1 $HNO_3$: 1 HF solution.

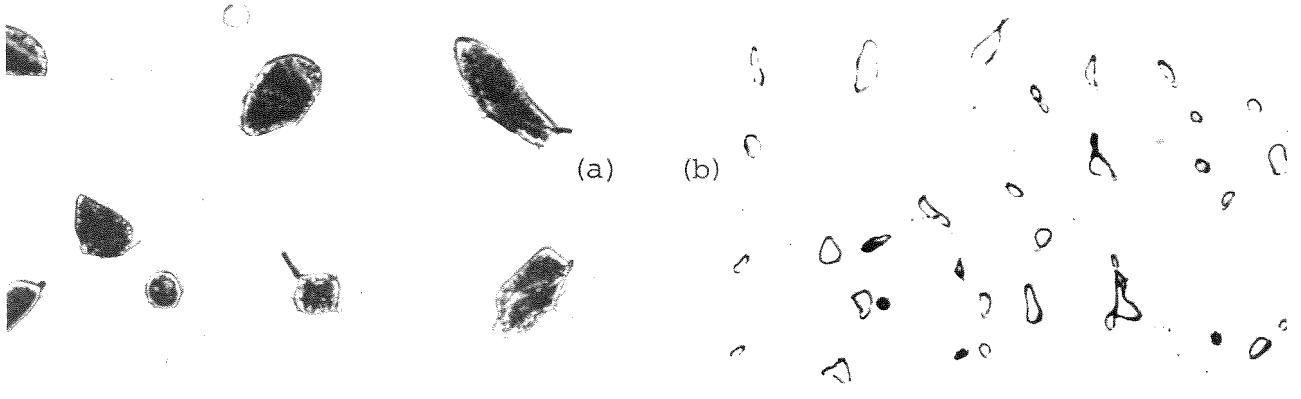


Fig. 1 Microstructure of Nb-Ge alloys after annealing at 1600°C/120h, 500x;
(a) 15 at.% Ge, precipitations of α-(Nb-Ge) solid solutions;
(b) 19 at.% Ge, precipitations of $Nb_5Ge_3$

The microstructure of some Nb-Ge alloys are shown in Fig. 1. We found that the homogeneity range of the A 15 phase extends from 18 to 19±0.5 at.% Ge at 1600°C /3/.

References

/1/ V.M. Pan, V.I. Latyesheva, E.A. Shishkin, Metall.-Phys. Chem. and Metal Phys. of Superconductors, Nauka, Moscow 157 (1967)

/2/ J.L. Jorda, R. Flukiger, J. Müller, J. Less-Common Met., 62, 25 (1978)

/3/ C. Politis, to be published, 1979

## 4.35 $V_3Si$ as a Model System for the Volume Pinning Force in A 15 Superconductors

*H. Küpfer[a], R. Meier-Hirmer[b], T. Reichert[a], C. Politis*

[a] *Institut für Experimentelle Kernphysik, Universität Karlsruhe*

[b] *Institut für Technische Physik, KfK*

$V_3Si$ is prepared as a model system for the investigation of the dependence of the volume pinning force on the defect structure of A 15 superconductors with high Ginzburg-Landau Parameter. A microstructure with single pinning forces (dislocation loops) smaller than the threshold force was produced by neutron irradiation. The corresponding volume pinning force is not proportional to the concentration of the pinning centres and shows a saturation with increasing concentration in the high field region. This unexpected behaviour is explained by a lowered threshold with increasing flux line lattice defects. It should disappear if strong single pinning centres i.e. precipitations determine the volume pinning force.

For the preperation of such a microstructure a series of V-Si-N and V-Si-C alloys were prepared by arc melting under argon and annealing at high temperatures and following precipitation hardening. The samples were characterized by measurements of the microscopic and superconducting properties.

# 5. DATA PROCESSING

## 5.1 A Simple Way of Variable Dimensioning in IBM FORTRAN IV

*W. Abel*

Programs written, for example, in Honywell FORTRAN IV may contain a so-called PARAMETER statement, which allows to vary array dimensions very easily. This useful statement does not exist in IBM FORTRAN IV. The problem was to incorporate such Honywell programs without changing them. Therefore, a macro facility for the evaluation of the PARAMETER statement has been written. Of course, all IBM FORTRAN IV programs may now be modified to take advantage of this variable dimensioning possibility. The preprocessor is based on a PL/I-FORMAC program. Due to FORMAC (FORmula MAnipulation Compiler) parameter expressions may also be coded; however, only integer constants or integer variables are allowed. The syntax of a PARAMETER statement is given by:

PARAMETER <variable> = <expression>|<integer constant>

Example for using the PARAMETER statement

```
C     MAIN PROGRAM ( or subprogram)
C
      PARAMETER  N = 2
      PARAMETER  IRR=N*(N+1)/2
      PARAMETER  NK = 26
      PARAMETER  NE=NK*N
C
      DIMENSION A(N,5),B(IRR),C(IRR,N),D(NK,N)
      DIMENSION E(NK),F(NE,NE,NE),H(3,2,NK)
```

Specification statements beginning with the keywords COMMON, REAL, INTEGER, LOGICAL, COMPLEX and DOUBLE are also evaluated. Also the operation field following the keyword PARAMETER will be converted to a legal FORTRAN statement. So the problem parameters are known for further use during execution time. After replacement the above statements have the form as indicated below.

```
      N = 2
      IRR=N*(N+1)/2
      NK = 26
      NE=NK*N
C
      DIMENSION A(2,5),B(3),C(3,2),D(26,2)
      DIMENSION E(26),F(52,52,52),H(3,2,26)
```

The preprocessor is called by the following JCL cards. After conversion the FORTRAN program then resides on a temporary data set, which is passed to the next step.

```
// EXEC PLG,NAME=TEMPNAME
//G.STEPLIB DD DSN=TSO352.SETALL.LOAD,DISP=SHR
//G.OUT DD DSN=&&PRE,UNIT=SYSDA,DISP=(NEW,PASS),
// DCB=(LRECL=80,RECFM=FB,BLKSIZE=3120),SPACE=(TRK,100)
//G.TSOIN DD *

   ... FORTRAN IV source code ...

// EXEC FGC
//C.SYSIN DD DSN=&&PRE,UNIT=SYSDA,DISP=(OLD,DELETE)
```

## 5.2 Tape Catalog Facility for Improving Data Transfer between TSO and Tape

*W. Abel*

Usually the TSO user is provided with the TSO command TAPE for producing a back up copy of all of his TSO data sets at a time. In order to have a more automated algorithm a method has been developed which enables the user to facilitate the data transfer from tape or to tape by applying a pseudo tape catalog facility.

With respect to an efficient use of the TSO contingent the user has the possibility to treat many data sets in a more simple way, because non used data sets may be temporarily placed on tape. According to the data set organization as indicated in the catalog entry a suitable batch job will be created automatically. In processing partitioned data sets a select option is available to write selected members on tape only.

No input data are needed from the user to describe the data set characteristics as mentioned below, because the most important descriptive parameters are held in each catalog entry.

The main command for performing the input/output operations is the TX.CLIST(AR) command. The tape catalog must be, of course, created before a first call. This can be done by using the TX.CLIST(ARC) command. The catalog is then

allocated as a sequential data set identified by the name of the tape (volume serial number).

In the input mode (transfer to a TSO data set) the appropriate file number of the saved data set is identical with the number of the catalog entry. In cases, where a data set was often copied on tape, the user is requested to enter the file number after examining the displayed list of all catalog entries of the data set specified.

In the output mode the new file number will be determined by taking the number of the end indication (EOF) of the tape catalog. This record will be then overwritten with the new entry, another EOF is placed at the end. Because the data sets reside on direct access devices, the related data set labels contain information about the data sets, for example, the number of tracks used and some DCB characteristics. In order to get these informations the TX.CLIST(RDDSCB) command serves to read out the VOLUME parameter, space requirements and the DCB keyword subparameters RECFM, LRECL, BLKSIZE and DSORG from the F1-DSCB or the specific data set using an IBM/370 ASSEMBLER written routine. These quantities are used to complete the tape catalog entry. In the following a tape catalog for the tape DV0247 is given as an example (one entry only):

```
DV0247ABEL*143P0A5A
TFINTER.TEXT.S070679.$06$FB 100 1600
EOF
```

The heading line contains the volume serial number and some accounting information needed for a user specific JOB card. In the period after the qualified name the data set organization is symbolically represented (S for sequential) followed by the creation date of the output file. This part of the entry before the dollar sign serves as DSNAME parameter for tape output. The remaining information describes the amount of space required by the data set and the DCB information as mentioned above.

## 5.3 SOS Power-Fail Handler

*G. Ehret, H. Hanak, H. Sobiesiak*

The latest releases of the Stand-Alone Operating System (SOS) and the BASIC Interpretersystem fixed all known bugs, but did no longer fit together in

the powerfail handlers. The result was a breakdown of the complete BASIC-system including the loss of the user's program and data in the case of a power failure. Additionally the usual procedure a) to load the systems into the computer, b) to switch off the grid, c) to send the computer to a remote station, and d) to plug it into the grid in order to have a working BASIC system, no longer was operational.

Because the manufacturer reduced the priority of the SOS-system and its fitting BASIC interpreter (resulting in an indefinite delay of error corrections) we bought the source programs. We corrected them as necessary for a Single-User-System. We also added the feature, that a message is sent to the user program. Thus the user may write code to set up his experiment automatically after power has been re-installed. The message is handled by our general BASIC interrupt processor /1/.

Reference

/1/ G. Ehret et al in Annual Report Teilinst. Kernphysik Gesellschaft für Kernforschung KfK 2223, 126 (1975)

## 5.4 The Adaptation of the Increment/List Processor to NOVA 3 Computers.

*H. Hanak, L. Schröder*[a]

[a]*Fachhochschule Karlsruhe*

The Increment/List-mode card has been developped for the NOVA2-computers /1/. It allowed to equip these computers with additional 128 K Byte of data memory along with the standard 64 K Byte of the standard program memory. Furthermore it had three direct memory channels programmable each in the block-input or in the memory-increment mode /2/.

Newer Data General computer models like NOVA3, NOVA4, or ECLISPE no longer support the memory-increment mode. They only have the two simple direct memory access modes: input or output. This restriction is now common to all computer manufacturer. We have not enough information about the CPU's microprograms of all

these Data General computers. Thus it is impossible in the moment to expand the CPU functions to our needs, as we did it with the NOVA2 CPU /3/.

Therefore we decided to change the microprogram of our Increment/List mode card. Within the mainframe given, additional feature only could be implemented on dispense of some other. We retained the listmode feature with a maximum of 96 bits, but reduced the number of increment input paths from 3 to only one. This needs the smallest number of accompanying hardware changes. The decision was also done with respect to the mapping feature of the NOVA3 computers, which allows only about 40 K Byte - 56 K Byte of increment space.

References

/1/ G. Ehret Progress Report KfK 2183, p. 99 (1975)

/2/ G. Ehret Documentation of the Call routines, unpublished

/3/ H. Hanak Progress Report KfK 2183, p.100 (1975)

## 5.5 Software for the NOVA Computer to Use the IBM Computer

*H. Sobiesiak, G. Ehret*

In order to have a simple and comfortable access to the central IBM computers four console commands have been implemented on the NOVA computer.

1.) IBMPRINT|V/S/R/I| NAME1 NAME2 ... NAMEn

This command prints textfiles which reside on NOVA-disks magnetic tapes, paper tape, or ECMA-cassettes on an IBM printer.
Modifications of the program are controlled by the switches /V /S /R and /I which may be used in any legal combination and may be omitted at all or partially.

2.) IBMGET|/V/A/T| IBMNAME NOVANAME

This command transports a catalogued IBM-data set to a NOVA device (disc,

magnetic tape, paper tape, ECMA-casette, printer, or display).

3.) IBMJOB|/V| NAME1 NAME2 ... NAMEn

This command submits jobs to the IBM

4.) IBMSTAT JOBNAME

This command prints the status of an IBM job on the NOVA console.

## 5.6 Tayloring of BASIC Interpreter Systems for the Experimentator

*G. Ehret, H. Klas[a], H. Sobiesiak*

[a] *Institut für Informatik und Formale Beschreibungsverfahren der Universität Karlsruhe*

The generation of taylored BASIC interpreters for the NOVA computers is now done as a dialogue on the system console. The dialogue is written on disk. It may be used to tune the interpreter system during a second generation.

The separation of the BASIC call-routines into a core resident part and an overlay part is completed.

According to the console dialogue overlays of the call-routines may be put into the virtual (core-resident) overlay module.

The work has been done in collaboration with the Institut für Angewandte Informatik und Formale Beschreibungsverfahren der Universität Karlsruhe /1/.

Reference

/1/ H. Klas, Diplomarbeit, Universität Karlsruhe (1979)

# 6. DEVELOPMENT OF INSTRUMENTS

## 6.1 Installation of a Two Axis Diffractometer at the R7 Beam

*G. Geibel*

Last year the R1 beam was no longer available for our high resolution two axis diffractometer, since the whole beam was needed for another experiment. Therefore, we transferred this spectrometer to the R7 beam tube, where we already had a simple two axis diffractometer for the orientation of single crystals. Now the two instruments were set one behind the other and use the same monochromatic beam.

A Cu monochromator cut perpendicular to the <01$\bar{1}$> plane is used in reflection or in transmission at a take off angle of $2\theta_M = 76^\circ$. Different wavelengths can be selected with appropriate reflecting planes. Most time we use the <311> plane since it allows rather high intensities with only a small high order contamination. The different possibilities are:

| Reflecting plane | wavelength Å | Si(111) Peak Intensity c.p.m. |
|---|---|---|
| <111> | 2.561 | 1900 |
| | 1.280 | 1550 |
| | 0.854 | 210 |
| <200> | 2.218 | 1450 |
| | 1.109 | 380 |
| <022> | 1.568 | 1300 |
| | 0.784 | 50 |
| <311> | 1.338 | 2200 |
| | 0.669 | 20 |
| <133> | 1.018 | 450 |
| <422> | 0.906 | 400 |

The white beam has an horizontal divergence of 35'. The collimator between monochromator and sample is accessible. Thus the divergence can be choosen to lie

between 17' and 45'. The counter aperture may also be varied between 24' and $1.5^{o}$. The resolution, $5 \times 10^{-3}$ with minimal divergence is not as good as at the R1 beam, due to the greater primary collimation and the lower take-off-angle. The size of the beam is $8 \times 4$ $cm^2$ and the maximum scattering angle is $2\theta = 138^{o}$.

Positioning and data acquisition is controlled by a NOVA 820 minicomputer with 64 K bytes memory. The system can performe the following functions:

i) $2\theta$ and $\omega - 2\theta$ scans
ii) Monochromator-, sample- and counter - positioning
iii) Plot of the data on a TV-screen or on the typewriter

## 6.2 Sollerkollimatoren kleiner Bauart (Soller-Collimators of Small Size)

*K. Weber*

Bei Spektrometern mit kurzen Abständen der einzelnen Achsen ist es notwendig, die Kollimatoren ebenfalls in Kleinbauweise herzustellen, wobei ein etwas größerer Intensitätsverlust in Kauf genommen wird.

Der in Bild 1 dargestellte Kleinkollimator ist aus folgenden Teilen aufgebaut:

a) 2 seitliche Stüzplatten aus Al
b) Al-Rahmen gefüllt mit Al-Waben
c) Absorberblech aus Stahl verkadmet
d) Spanndraht aus Al.

Zwischen den beiden 5mm starken Al-Seitenplatten werden die im Rahmen befindlichen Al-Waben /1/ im Wechsel mit den Absorberblechen bis zur gewünschten Strahlbreite aufgeschichtet und mit dem Spanndraht verschraubt. Dabei übernehmen die Al-Waben die parallele Abstandhaltung der Absorberbleche. Wird der Kollimator in Rechteckgeometrie hergestellt, so erhält man durch Drehen um $90^{o}$ zwei verschiedene Kollimationsmöglichkeiten.

Der bisher kleinste Abstand der Absorberbleche betrug 1 mm, dabei betrug der gesamte Intensitätsverlust 35 % bei 34' Kollimation.

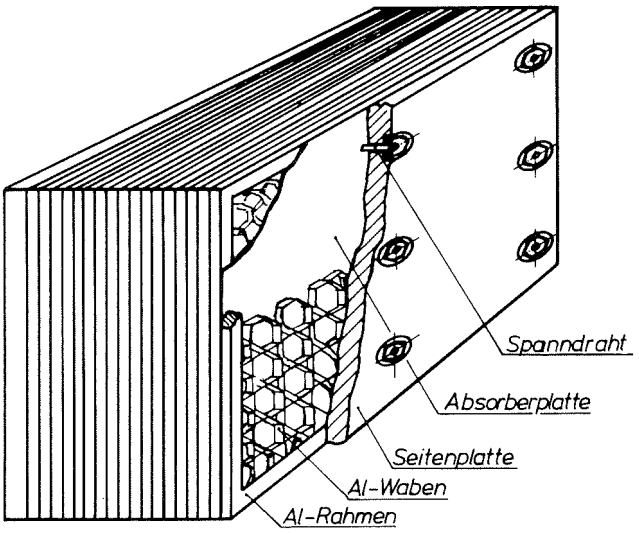


Bild 1

Abmessungen und Kollimation von bisher eingesetzten Kollimatoren

| äußere Abm. [mm] | Strahldurchlass [mm] | Abst. d. Absorberbl. | Kollimation |
|---|---|---|---|
| 100x90x40 | 100x30/90x30 | 1 mm | 34'/38 |
| 100x70x50 | 100x40/70x40 | 1,2 mm | 42'/60' |
| 100x70x50 | 100x40/70x40 | 2,5 mm | 86'/125' |

Reference

/1/ K. Weber, in Progress Report Teilinst. Nukl. Festkörperphysik, Ges. f. Kernforschung, KfK 2670, 121 (1978)

## 6.3 Design of an Electron Energy-Loss Spectrometer and Electron Optical Calculations

*J. Fink, G. Crecelius[a], R. Manzke[a], P. Johnen[a], and F. Schmidt[a]*

[a] *Institut für Festkörperforschung, KFA Jülich*

Electron energy loss spectroscopy is attracting increased attention in solid state physics. In the very low-lying energy-loss region ($\Delta E < 50meV$) investiga-

tions of optical and surface phonons have been reported. At intermediate energy loss (0.05 eV<$\Delta$E<50 eV) interband transitions and collective excitations (plasmons) have been observed, yielding the real and imaginary parts of the dielectric response function. In the high energy loss region with $\Delta$E greater than about 50-100 eV, phenomena related to core-loss excitations such as edge singularities, the density of unoccupied states and EXAFS have been investigated.

We have designed an electron energy-loss spectrometer featuring a 250 keV electron beam at the sample, a variable energy resolution ranging between less than 80 meV (low beam current) and 0.5 eV (high beam current) and a variable momentum transfer resolution ($\Delta k$=0.1 $\mathring{A}^{-1}$ to 0.01 $\mathring{A}^{-1}$). The electrons emitted from a tungsten dispenser cathode pass a Kuyatt-Simpson monochromator. The beam is then focussed onto the sample by a multielement zoom lens and an accelerator tube. After passing through the sample, the beam is decelerated by a deceleration tube and another multielement zoom lens. The energy of the beam is determined by a Kuyatt-Simpson analyzer, similar to the monochromator and the electrons are detected by an electron multiplier. Monochromator and analyzer are at the 250 keV potential whereas the sample is at ground potential. This allows the sample preparation chamber to be fixed directly to the electron energy loss spectrometer and thus the sample can be prepared, transfered and measured under UHV conditions.

During the design of the spectrometer considerable attention was paid to the calculation of electron trajectories in the various electron optical systems like zoom lenses, accelerator tubes and matching lenses at the monochromator. All lenses were made from cylindrical electrodes and also the acceleration tubes have cylindrical geometry. A computer program of E. Kisker /1/ was further developed to calculate and optimize electron trajectories in a potential of cylindrical symmetry. Using Bertrams method /2/ for expressing the potential inside cylindrical lenses in a unified way it is possible to calculate the field distribution in a multielement lens much faster than with other methods. After the set up of the potential the electron coordinates are calculated by integrating the equations of motion /3/. The focal properties of a two element lens derived with our program agree within 1 % with those calculated by E. Harting and F.H. Read /4/.

Besides the calculation of electron trajectories, the program is able to adjust any two given lens element voltages to find an image for the entrance window at a desired position and with a desired magnification. The adjustment of a given voltage in a field lens to put the exit pupil near to infinity is also incorporated in the program. Fig. 1 and Fig. 2 show typical calculations of electron trajectories used for the design of the spectrometer.

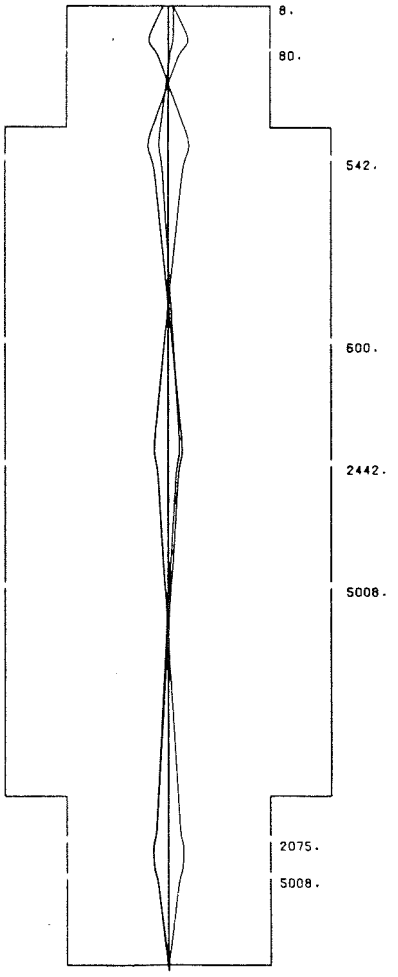


Fig. 1
Electron trajectories in a multi-element lens, consisting of an acceleration lens, a zoom lens and a field lens. The lenssystem lies between monochromator and accelerator tube. The numbers given at the lens elements give voltages for a given energy resolution and a given momentum resolution.

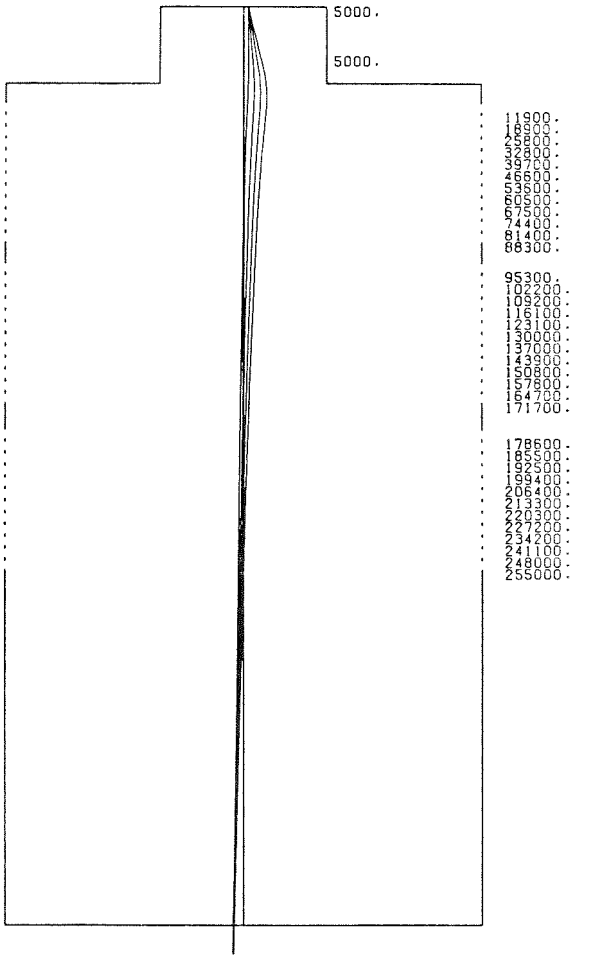


Fig. 2
Electron trajectories in an acceleration tube, starting at the midpoint of the field lens and ending at the sample. The numbers given indicate voltages at the electrodes of the acceleration tube.

References

/1/ E. Kisker, Diplomarbeit, Universität Hamburg 1969

/2/ S. Bertram, J. of Appl. Phys. 13, 496 (1942)

/3/ R. Lapeyre and M. Laudet, C.R. Acad. Sci. Paris 251, 679 (1960)

/4/ E. Harting and F.H. Read in Electrostatic Lenses, Elsevier Scientific Publishing Company, Amsterdam 1976

# 7. PUBLICATIONS, CONFERENCE CONTRIBUTIONS, AND SEMINARS

## 7.1 PUBLICATIONS

*Adrian, H.; Ischenko, G.; Lehmann, M.; Müller, P.; Braun, H.; Linker, G.*
Low temperature irradiation of $Nb_3Sn$ and $V_3Si$ with high energy sulphur ions
J. Less. Comm. Metals 62, 99 (1978)

*Blanckenhagen, P. von; Happel, H.; Knorr, K.*
Crystal fields in (Y,Er)$Al_2$ and (La,Er)$Al_2$
Journal of Magnetism and Magnetic Materials 9, 20 (1978)

*Götz, F.; Czjzek, G.; Fink, J.; Schmidt, H.; Fulde, P.*
Magnetic interactions in Pr:Eu alloys
J. Phys. (Paris) Colloque 40, C5 - 19 (1979)

*Gauss, C.*
Übergangstemperatur zur Supraleitung von metastabilen, kristallinen Blei-Wismut Legierungen.
Dissertation, Univ. Karlsruhe 1979
KfK 2814 (1979)

*Haase, E.L.; Bassalleck, B.; Klotz, W.D.; Takentchi, F.; Ullrich, H.; Furic, M.; Sakamoto, Y.*
Two-neutron emission in the absorption of stopped pions on lithium isotopes
Physical Review C 19, 1893 (1979)

*Heger, G.; Weitzel, H.; [HRSG.]*
Nukleare Festkörperforschung am FR2:
Ergebnisbericht 1977/78 der externen Arbeitsgruppen
KfK 2719 (1978)

*Jung, V.*
Realisierbarkeit des Gravitationsantriebes
ZEV Glas. Ann. 102, 265 (1978)

*Jung, V.*
Paßt die Cyclobahn in eine gewachsene Stadt
Nahverkehrspraxis 27, 104 (1979)

*Jung, V.*
Energieeinsparung im öffentlichen Personennahverkehr durch Schwerkraftantrieb
Wimatika, Karlsruhe 1979, S. 61-65, Hersg. Univ. Karlsruhe

*Käfer, K.*
Phonon dispersion and neutron scattering law $S(\underline{k},\omega)$ for a quasi-one-dimensional Peierls-system
Proc. of Internat. Conf. on Quasi-One-Dimensional Conductors, Dubrovnik, Yugoslavia, September 4-8, p. 219 (1978)

*Käfer, K. [HRSG.]*
Progress Report: Teilinstitut Nukleare Festkörperphysik 1.6.1977 - 31.5.1978, KfK 2670 (1978)

*Kaiser, R.; Spengler, W.; Schicktanz, S.; Politis, C.*
Raman spectra and superconductivity of various phases of a high - $T_c$ superconductor: NbN
Phys. stat. sol. (b) 87, 565 (1978)

*Lehner, H.*
Neutronenstreuuntersuchungen an $(CD_3ND_3)_2\ MnCl_4$
Dissertation, Univ. Würzburg 1978
KfK 2720 (1978)

*Kaufmann, R.; Meyer, O.*
Computer simulation of channelling measurements on $V_3Si$ single crystals
Radiation Effects 40, 97 (1979)

*Kaufmann, R.; Meyer, O.*
Computer simulation of channelling measurements in He irradiated $V_3Si$ single crystals
Radiation Effects 40, 161 (1979)

*Mereiter, K.; Preisinger, A.; Guth, H.*
Hydrogen bonds in Schlippe's salt: Refinement of the crystal structures of $Na_3SbS_4 \cdot 9H_2O$ by X-ray diffraction and $Na_3SbS_4 \cdot 9D_2O$ by neutron diffraction at room temperature
Acta Cryst. B 35, 19 (1979)

*Mullen, D.; Heger, G.; Treutmann, W.*
Refinement of the structure of thiourea: A neutron diffraction study at 293 K
Zeitschrift für Kristallographie 148, 95 (1978)

*Nägele, W.; Blanckenhagen, P. von; Knorr, K.; Suck, J.B.*
Spin relaxation in the amorphous spin glas $Al_2Mn_3Si_3O_{12}$
Z. Physik B 33, 251 (1979)

*Pintschovius, L.*
Polysulphur nitride $(SN)_x$, the first example of a polymeric metal
Colloid and Polymer Science 256, 883 (1979)

*Pintschovius, L.; Prynn, R.*
Kohn anomalies in the phonon dispersion on polysulphur nitride $(SN)_x$
Proc. of Internat. Conf. on Quasi One-Dimensional Conductors, Dubrovnik, Yugoslavia, September 4-8, p. 421 (1978)

*Politis, C.*
Structure and properties of cubic NbN and TaN
Proceedings of the 3rd German-Yugoslav Meeting on Materials Science and Development, Stuttgart 1978

*Rietschel, H.*
A non-local extension of the Gaspari-Gyorffy theory for superconductors
Z. Physik B 30, 271 (1978)

*Schwahn, D.; Schmatz, W.*
Neutron small angle scattering from the alloy Al-Zn above the critical point
Acta Metallurgica 26, 1571 (1978)

*Schweiss, P.; Renker, B.; Suck, J.B.*
Phonon density of states of molybdenum chalcogenides
J. Phys. (Paris) Colloque 39, C6 - 356 (1978)

*Steiner, P.; Höchst, H.; Schneider, J.; Hüfner, S.; Politis, C.*
The XPS valence band spectra of Hf metal and $HfC_xN_yO_z$ compounds and the correlation to their superconductivity
Z. Physik B 33, 241 (1979)

*Werner, K.; Schmatz, W.; Bauer, G.S.; Seitz, E.; Fenzl, J.H.; Baratoff, A.*
Long-range solute-host interactions in dilute Al-Mg alloys
J. Phys. F 8, L207 (1978)

*Winter, H.; Rietschel, H.; Ries, G.; Reichardt, W.*
Calculation of the superconducting transition temperature in refractory compounds
J. Phys. (Paris) Colloque 39, C6 - 474 (1978)

## 7.2 CONFERENCE CONTRIBUTIONS AND SEMINARS

*Blanckenhagen, P. von; Scheerer, B.*
Spinwellendispersion in teilgeordnetem $Ni_3Mn$
Verhandl. DPG (VI) 14, 178 (1979)

*Bohnen, K.-P.*
Selbstkonsistente Berechnung von elektronischen Oberflächeneigenschaften
Vortrag, Universität Regensburg, 7. Mai 1979

*Czjzek, G.; Fink, J.; Götz, F.; Schmidt, H.; Rebouillat, J.P.; Lienard, A.; Coby, J.D.M.*
Untersuchungen von amorphen Gd-Ni-Legierungen durch Mössbauerspektroskopie
Verhandl. DPG (VI) 14, 173 (1979)

*Czjzek, G.; Fink, J.; Götz, F.; Schmidt, H.; Rebouillat, J.P.; Lienard, A.; Coby, J.D.M.*
An investigation of amorphous Gd-Ni alloys by Mössbauer spectroscopy
Internat. C.N.R.S. Colloqu. on Physics of Metallic Rare Earths,
Saint Pierre de Chartreuse, France, September 4-7, 1978

*Ehret, G.; Hanak, H.; Richelsen, H.*
Speicher für Mega-Kanal-Analysatoren
Verhandl. DPG (VI) 13, 1201 (1978)

*Ehret, G.; Nücker, N.*
Integriertes Experimentier- und Auswertungssystem für inelastische Neutronenstreuung am Reaktor FR2
Verhandl. DPG (VI) 13, 1201 (1978)

*Ehret, G.; Hanak, H.*
File Struktur in einem Mega-Kanal-Analysator
Studiengruppe Nukleare Elektronik, Herbsttagung, Braunschweig, 6.-8.November 1978

*Ernst, A.*
Überwachungs- und Steuerungssystem für den 3,75 MV Van-de-Graaf-Beschleuniger
Verhandl. DPG (VI) 13, 1202 (1978)

*Geerk, J.*
The superconducting transition temperature of niobium carbide single crystals after implantation of light elements
Internat. Conf. on Ion Beam Modification of Materials,
Budapest, September 4-8, 1978

*Geerk, J.*
Die Übergangstemperatur zur Supraleitung von $Nb_3(Ge_{0.8}Nb_{0.2})$ nach Implantation von Ge- und Si-Ionen
Verhandl. DPG (VI) 14, 419 (1979)

*Götz, F.; Fink, J.; Schmidt, H.; Czjzek, G.; Fulde, P.*
Magnetic interactions in Pr: Eu alloys
Internat. C.N.R.S. Colloquium on Physics of Metallic Rare Earths, Saint Pierre de Chartreuse, France, September 4-7, 1978

*Götz, F.; Fink. J.; Schmidt, H.; Czjzek, G.; Fulde, P.*
Magnetische Wechselwirkung in verdünnten Pr: Eu Legierungen
Verhandl. DPG (VI) 14, 180 (1979)

*Gompf, F.; Schell, G.; Winter, H.*
Phononen Zustandsdichten von supraleitenden Hexaboriden
Verhandl. DPG (VI) 14, 414 (1979)

*Gompf, F.; Jönsson, S.*
Vergleich der Phononenzustandsdichte von Be mit der von $Be_{22}Re$
Verhandl. DPG (VI) 14, 415 (1979)

*Gompf, F.*
Comparison of the phonon density of states of trigonal, vitreous and red amorphous selenium
Internat. Conf. Physics of Selenium and Tellurium, Königstein, May 28-31, 1979

*Guth, H.; Mereiter, K.; Preisinger, A.; Mikenda, W.; Hiebl, K.*
Hydrogen-bonds in Schlippe's salt: X-ray and neutron diffraction, vibrational and resonance spectroscopic studies of $Na_3SbS_4 \cdot 9H_2O$ and $Na_3SbS_4 \cdot 9D_2O$ in the temperature range of 75 K to 295 K
11. General Assembly and Internat. Congress of Crystallography, Warschau, August 3-12, 1978

*Guth, H.; Heger, G.*
Temperature dependence of the crystal structure of β-eucryptite ($LiAlSiO_4$) investigated by means of neutron diffraction
11. General Assembly and Internat. Congress of Crystallography, Warschau, August 3-12, 1978

*Guth, H.*
Strukturelle Untersuchungen des eindimensioalen Li-Ionenleiters β-Eukryptit mit Hilfe von Neutronenstreuung
Vortrag, Techn. Univ. Wien, 30. Oktober 1978

*Guth, H.; Heger, G.*
Temperature dependence of the crystal structure of the 1-dim. $Li^+$-conductor β-eucryptite ($LiAlSiO_4$)
Fast Ion Transport in Solids, Conf., Lake Geneva, Wisc., USA, May 21-25, 1979

*Heger, G.*
Wasserstoff-Bindungen und strukturelle Phasenübergänge am Beispiel der perowskitähnlichen Schichtstrukturen vom Typ $(C_nH_{2n+1}NH_3)_2MeCl_4$
Vortrag, Techn. Univ. Wien, 30. Oktober 1978

*Hussain, T.; Linker, G.; Meyer, O.*
Correlation between $T_c$ and defect structure in ion implanted aluminum
Verhandl. DPG (VI) 14, 419 (1979)

*Jung, V.*
Untersuchung von Phasenumwandlungen in austenitischen Stählen mit Hilfe der Neutronenbeugung
Verhandl. DPG (VI) 14, 267 (1979)

*Käfer, K.*
Phonon dispersion and neutron scattering law $S(k,\omega)$ for a quasi-one-dimensional Peierls-system
Meeting on Quasi-One-Dimensional Conductors,
Dubrovnik, Yugoslavia, September 4-8, 1978

*Kaufmann, R.; Meyer, O.*
Untersuchung der Defektstruktur an ionenbeschossenen $V_3Si$-Einkristallen
Verhandl. DPG (VI) 14, 417 (1979)

*Knorr, K.; Renker, B.; Lüthi, B.; Assmus, W.; Takke, R.*
Akustische Phononen in $LaAg_{1-x}In_x$
Verhandl. DPG (VI) 14, 248 (1979)

*Kotai, E.; Nagy, T.; Meyer, O.; Gynlai, J.; Revesz, P.; Mezey, G.; Lehner, T.; Manuaba, A.*
Diffusion measurement of implanted Sb into Si using $SiO_2$ encapsulation
Internat. Conf. on Ion Beam Modification of Materials, Budapest,
September 4-8, 1978

*Kuhs, W.F.; Heger, G.*
Neutron diffraction study of $Cu_6PS_5Br$ at 293 K and 473 K
Fast Ion Transport in Solids, Conf., Lake Geneva, Wisc., USA, May 21-25, 1979

*Linker, G.*
Superconducting properties and structure of ion bombarded niobium layers
Internat. Conf. on Ion Beam Modification of Materials, Budapest,
September 4-8, 1978

*Linker, G.*
Einfluß von Defekten auf $T_c$ in aufgedampften und ionenbeschossenen Niobschichten
Verhandl. DPG (VI) 14, 417 (1979)

*Meyer, O.*
Application of ion beams for material modification and analysis
23. Annual Conf. of the South Africa Institute of Physics, Pretoria, July 13-17, 1978

*Meyer, O.*
Ion implantation in superconductors
NATO Advanced Study Institute: The Physics and Applications of Ion Beam Interactions with Solids, Albany, N.Y., July 24 - August 5, 1978

*Meyer, O.*
Defect analysis by channelling
Vortrag, Witwatersrand University, Johannesburg, 14. Juni, 1978

*Meyer, O.*
Radiation damage and superconductivity in $V_3Si$
Vortrag, University of Pretoria, 28. Juni, 1978

*Meyer, O.*
Ion-implantation in superconductors
Southern Universities Nuclear Institute, Capetown, 29. Juni 1978

*Meyer, O.*
Application of ion beams for modification and analysis of superconductors
Vortrag, Council for Scientific and Industrial Resarch, Pretoria, 5. July, 1978

*Meyer, O.*
Ion implantation in superconductors
VI. Internat. Conf. on Ion Beam Modification of Materials, Budapest, September 4-8, 1978

*Meyer, O.; Linker, G.*
Einfluß von Strahlendefekten auf $T_c$ und $\rho$ von $V_3Si$-Schichten
Verhandl. DPG (VI) 14, 418 (1979)

*Müller, P.; Ischenko, G.; Adrian, H.; Bieger, H.; Lehmann, H.; Haase, E.L.*
Folgeerscheinungen von Schwerionenstrahlenschäden auf die supraleitenden Eigenschaften von Hochtemperatursupraleitern mit A15-Struktur
Verhandl. DPG (VI) 14, 418 (1979)

*Mullen, D.; Hellner, E.; Treutmann, W.; Scheringer, C.; Klein, S.; Heger, G.*
Determination of reliable atomic parameters for electron density calculations: X-ray and neutron diffraction studies on urea
11. General Assembly and Internat. Congress of Crystallography, Warschau, August 3-12, 1978

*Nägele, W.; Knorr, K.; Prandl, W.; Renard, J.P.; Pommin, J.; Ferre, J.; Blanckenhagen, P. von; Suck, J.B.*
Magnetisierung, magnetische Nahordnung und Dynamik in Mangan-Silikat-Gläsern
Verhandl. DPG (VI) 13, 1188 (1978)

*Nägele, W.; Blanckenhagen, P. von; Knorr, K.; Suck, J.B.*
Spin Relaxation in dem amorphen Spinglas $Al_2Mn_3Si_3C_{12}$
Verhandl. DPG (VI) 14, 187 (1979)

*Nücker, N.; Reichardt, W.*
Phononenzustandsdichte von $Nb_3(Ge_{0.8}Nb_{0.2})$
Verhandl. DPG (VI) 14, 415 (1979)

*Pintschovius, L.; Holland-Moritz, E.; Wohlleben, D.; Stähr, S.; Liebertz, J.*
Suche nach Phononenanomalien in der Zwischenvalenzverbindung $CeSn_3$
Verhandl. DPG (VI) 14, 197 (1979)

*Pintschovious, L.; Roedhammer, P.; Christensen, A.N.*
Gitterschwingungen in einem Niobnitrid-Titankarbid-Mischkristall
Verhandl. DPG (VI) 14, 414 (1979)

*Reichardt, W.; Scheerer, B.; Weber, W.*
Die Gitterschwingungen des NbN
Verhandl. DPG (VI) 14, 414 (1979)

*Renker, B.; Käfer, K.; Buerkin, J.*
Akustische Phononen in $UAl_2$
Verhandl. DPG (VI) 14, 248 (1979)

*Rietschel, H.; Winter, H.; Ries, G.*
Supraleitung in Vanadiumnitrid
Verhandl. DPG (VI) 14, 405 (1979)

*Rietschel, H.*
Supraleitung und Paramagnetismus
DPG-Diskussionstagung, Bad Honnef, 22. Mai 1979

*Schell, G.; Winter, H.; Rietschel, H.*
Elektronenstruktur und Supraleitung in Hexaboriden
Verhandl. DPG (VI) 14, 407 (1979)

*Schmatz, W.*
Phasenumwandlung 1. Ordnung - Experimente
Institut für Festkörperforschung, Physik der Legierungen, KFA Jülich, 19.-30. März, 1979

*Schmatz, W.*
Neutron and X-ray scattering by disordered crystals
11. General Assembly and International Congress of Crystallography, Warschau, August 3-12, 1978

*Schmatz, W.*
General aspects of diffuse neutron scattering
Workshop for Instrumentation in Diffuse Scattering at the ILL Grenoble, Oct. 1978

*Schmatz, W.*
Neutronenstreuung zur Untersuchung biologischer Substanzen
Seminarvortrag am Institut für Genetik und Toxilogie des KfK, April 1979

*Schommers, W.*
Structural and dynamical behavior of $\alpha$-AgI
Fast Ion Transport in Solids, Conf., Lake Geneva, Wisc., USA, May 21-25, 1979

*Schommers, W.*
Molekulardynamisches Modell zur Untersuchung von Orts- und Zeitkorrelationen in $\alpha$-AgI
Vortrag, Univ. Freiburg, 2. Februar 1979

*Schröder, B.; Wagner, V.; Lehner, N.; Geick, R.*
Spin wave analysis of the two dimensional Heisenberg antiferromagnets $Rb_2MnCl_4$ and $(CH_3NH_3)_2MnCl_4$
15. Internat. Conf. on Low Temperature Physics, Grenoble, August 23-29, 1978

*Vogt, K.; Reichardt, W.; Prandl, W.*
Niedrig liegende Librationsmoden in $K_2SnCl_6$
Verhandl. DPG (VI) 14, 364 (1979)

*Weber, W.*
Phonon dispersion in transition metals
Vortrag, Univ. Aarhus, Dänemark, 23. Juni 1978

*Weber, W.*
Eine Berechnung der Eliashbergfunktion $\alpha^2(\omega)F(\omega)$ für NbC
Verhandl. DPG (VI) 14, 406 (1979)

*Weber, W.*
Electron-phonon coupling in transition metal compounds: the dormant interactions
Vortrag, Bell Laboratories, Murray Hill, N.J., 16. Oktober 1978

# 8. LIST OF THE NEUTRON SPECTROMETERS AT THE FR2 AT KARLSRUHE OPERATED BY THE IAK I

DIF 1 : Four circle diffractometer, $\lambda = 1.024$ Å

DIF 2 : Two circle diffractometer, $0.7$ Å $\leq \lambda < 2.6$ Å

DIF 3 : Two circle diffractometer, $\lambda = 1.28$ Å or $1.09$ Å

DIF 4 : Four circle diffractometer, $\lambda = 0.922$ Å or $2.41$ Å

DIF 5 : Four circle diffractometer, $\lambda = 0.89$ Å or $1.26$ Å

TAS 1 : Three-axis spectrometer, $13$ meV $\leq E_o < 120$ meV

TAS 2 : Three-axis spectrometer, $8$ meV $\leq E_o < 64$ meV

TOF 1 : Time-of-flight spectrometer with Fermi-chopper, 140 detectors, thermal neutrons

TOF 2 : Time-of-flight spectrometer with rotating crystal, 60 detectors, cold neutrons

TOF 3 : Time-of-flight spectrometer with Fermi-chopper, 120 detectors, thermal neutrons

TOF 4 : Time-of-flight spectrometer with rotating crystal, 6 detectors, cold neutrons

MAG 1 : Spectrometer for diffuse scattering, 40 detectors, thermal neutrons

MAG 2 : Multipurpose spectrometer, 40 detectors, cold neutrons.

# 9. STAFF MEMBERS (June 1, 1979)

Head of Institute: W. Schmatz

## Professional Staff

| | | | |
|---|---|---|---|
| *Blanckenhagen, P.v.* | *Haase, E.L.* | *Nücker, N.* | *Rietschel, H.* |
| *Bohnen, K.-P.* | *Heger, G.* | *Oestreich, V.* | *Schmidt, H.* |
| *Czjzek, G.* | *Jung, V.* | *Pintschovius, L.* | *Schmidt, H.-J.* |
| *Fink, J.** | *Kobbelt, M.* | *Politis, C.* | *Schommers, W.* |
| *Geerk, J.* | *Linker, G.* | *Reichardt, W.* | *Suck, J.-B.** |
| *Gompf, F.* | *Meyer, O.* | *Renker, B.* | *Weber, W.* |

## Technical Staff

| | | | |
|---|---|---|---|
| *Abel, W.*[+] | *Hanak, H.*[+] | *Ratzel, F.* | *Schreiber, H.*[+] |
| *Ehret, G.*[+] | *Kraatz, M.* | *Richelsen, H.*[+] | *Smithey, R.* |
| *Ernst, A.*[+] | *Kuhn, R.*[+] | *Roller, H.*[+] | *Sobiesiak, H.*[+] |
| *Ewert, D.* | *Nadasdy, J.*[+] | *Scheerer, B.* | *Weber, K.* |

## Visiting Scientists

*Alberts, H.W.; Guest from South Africa*
*Hussain, T.; Guest from Bangladesh*
*Łatka, K.; Guest from Poland*
*Lehner, N.; Guest from Würzburg*
*Mattheiss, L.F.; Guest from USA*
*Schweiß, P.; Guest from Frankfurt*
*Turos, A.; Guest from Poland*

## Research Students

*Aker, E.*[++]
*Bletzer, H.*[++]
*Geibel, C.*[++]
*Guth, H.*[++]
*Götz, F.*[+++]
*Härdle, H.*[++]
*Haq, Al ul.*[++]
*Kaufmann, R.*[++]
*Kieselmann, G.*[++]
*Krauss, W.*[++]
*Schell, G.*[++]
*Schneider, U.*[++]
*Pflüger, J.*[++]

*On leave of absence at KfA, Jülich
**On leave of absence at ILL, Grenoble
[+]Member of infrastructure
[++]Universität Karlsruhe
[+++]Universität Heidelberg